

MIT **OPEN** COURSEWARE

Ultrafast Optics

by Franz X. Kaertner



6.977 Ultrafast Optics

Franz X. Kaertner

Spring Term 2005

Contents

1	Introduction	1
1.1	Course Mission	1
1.2	Pulse Characteristics	1
1.3	Applications	3
1.4	Review of Laser Essentials	7
1.5	History	12
1.6	Laser Materials	15
2	Maxwell-Bloch Equations	21
2.1	Maxwell's Equations	21
2.2	Linear Pulse Propagation in Isotropic Media	22
2.2.1	Plane-Wave Solutions (TEM-Waves)	23
2.2.2	Complex Notations	24
2.2.3	Poynting Vectors, Energy Density and Intensity for Plane Wave Fields	25
2.2.4	Dielectric Susceptibility	25
2.3	Bloch Equations	27
2.3.1	The Two-Level Model	27
2.3.2	The Atom-Field Interaction In Dipole Approximation	30
2.3.3	Rabi-Oscillations	32
2.3.4	The Density Operator	35
2.3.5	Energy- and Phase-Relaxation	37
2.3.6	The Two-Level Atom with a Coherent Classical Exter- nal Field	39
2.4	Dielectric Susceptibility	41
2.5	Rate Equations	44
2.6	Pulse Propagation with Dispersion and Gain	45

2.6.1	Dispersion	48
2.6.2	Loss and Gain	52
2.7	Kramers-Kroenig Relations	55
2.8	Pulse Shapes and Time-Bandwidth Products	57
3	Nonlinear Pulse Propagation	63
3.1	The Optical Kerr-effect	63
3.2	Self-Phase Modulation (SPM)	64
3.3	The Nonlinear Schrödinger Equation	67
3.3.1	The Solitons of the NSE	67
3.3.2	The Fundamental Soliton	68
3.3.3	Higher Order Solitons	70
3.3.4	Inverse Scattering Theory	73
3.4	Universality of the NSE	77
3.5	Soliton Perturbation Theory	77
3.6	Soliton Instabilities by Periodic Perturbations	84
3.7	Pulse Compression	89
3.7.1	General Pulse Compression Scheme	89
3.7.2	Spectral Broadening with Guided Modes	91
3.7.3	Dispersion Compensation Techniques	92
3.7.4	Dispersion Compensating Mirrors	97
3.7.5	Hollow Fiber Compression Technique	112
3.8	Appendix: Sech-Algebra	113
3.9	Summary	114
4	Laser Dynamics (single-mode)	127
4.1	Rate Equations	127
4.2	Built-up of Laser Oscillation and Continuous Wave Operation	132
4.3	Stability and Relaxation Oscillations	133
4.4	Q-Switching	136
4.4.1	Active Q-Switching	137
4.4.2	Single-Frequency Q-Switched Pulses	140
4.4.3	Theory of Active Q-Switching	142
4.4.4	Passive Q-Switching	146
4.5	Example: Single Mode CW-Q-Switched Microchip Lasers	155
4.5.1	Set-up of the Passively Q-Switched Microchip Laser	155
4.5.2	Dynamics of a Q-Switched Microchip Laser	157
4.6	Q-Switched Mode Locking	163

4.7	Summary	167
5	Active Mode Locking	173
5.1	The Master Equation of Mode Locking	174
5.2	Active Mode Locking by Loss Modulation	177
5.3	Active Mode-Locking by Phase Modulation	182
5.4	Active Mode Locking with Additional SPM	183
5.5	Active Mode Locking with Soliton Formation	186
5.5.1	Stability Condition	188
5.5.2	Numerical simulations	196
5.5.3	Experimental Verification	201
5.6	Summary	203
5.7	Active Modelocking with Detuning	207
5.7.1	Dynamics of the Detuned Actively Mode-locked Laser .	212
5.7.2	Nonnormal Systems and Transient Gain	215
5.7.3	The Nonnormal Behavior of the Detuned Laser	217
6	Passive Modelocking	225
6.1	Slow Saturable Absorber Mode Locking	227
6.2	Fast Saturable Absorber Mode Locking	232
6.2.1	Without GDD and SPM	233
6.2.2	With GDD and SPM	237
6.3	Soliton Mode Locking	241
6.4	Dispersion Managed Soliton Formation	246
7	Kerr-Lens and Additive Pulse Mode Locking	257
7.1	Kerr-Lens Mode Locking (KLM)	257
7.1.1	Review of Paraxial Optics and Laser Resonator Design	258
7.1.2	Two-Mirror Resonators	261
7.1.3	Four-Mirror Resonators	270
7.1.4	The Kerr Lensing Effects	275
7.2	Additive Pulse Mode Locking	280
8	Semiconductor Saturable Absorbers	289
8.1	Carrier Dynamics and Saturation Properties	291
8.2	High Fluence Effects	295
8.3	Break-up into Multiple Pulses	299
8.4	Summary	306

9	Noise and Frequency Control	309
9.1	The Mode Comb	310
9.2	Noise in Mode-locked Lasers	314
9.2.1	The Optical Spectrum	317
9.2.2	The Microwave Spectrum	320
9.2.3	Example: Yb-fiber laser:	321
9.3	Group- and Phase Velocity of Solitons	324
9.4	Femtosecond Laser Frequency Combs	326
10	Pulse Characterization	333
10.1	Intensity Autocorrelation	333
10.2	Interferometric Autocorrelation (IAC)	336
10.2.1	Interferometric Autocorrelation of an Unchirped Sech- Pulse	341
10.2.2	Interferometric Autocorrelation of a Chirped Gaussian Pulse	342
10.2.3	Second Order Dispersion	342
10.2.4	Third Order Dispersion	343
10.2.5	Self-Phase Modulation	345
10.3	Frequency Resolved Optical Gating (FROG)	347
10.3.1	Polarization Gate FROG	349
10.3.2	FROG Inversion Algorithm	351
10.3.3	Second Harmonic FROG	354
10.3.4	FROG Geometries	355
10.4	Spectral Interferometry and SPIDER	357
10.4.1	Spectral Interferometry	357
10.4.2	SPIDER	359
10.4.3	Characterization of Sub-Two-Cycle Ti:sapphire Laser Pulses	365
10.4.4	Pros and Cons of SPIDER	367
11	Ultrafast Measurement Techniques	371
11.1	Pump Probe Measurements	371
11.1.1	Non-Colinear Pump-Probe Measurement:	371
11.1.2	Colinear Pump-Probe Measurement:	372
11.1.3	Heterodyne Pump Probe	374
11.2	Electro-Optic Sampling:	376
11.3	THz Spectroscopy and Imaging	378

<i>CONTENTS</i>	i
11.4 Four-Wave Mixing	380
12 Pulse Amplification	385

Chapter 1

Introduction

1.1 Course Mission

- Generation of ultrashort pulses: Nano-, Pico-, Femto-, Attosecond Pulses
- Propagation of ultrashort pulses
- Linear and nonlinear effects.
- Applications in high precision measurements, nonlinear optics, optical signal processing, optical communications, x-ray generation,....

1.2 Pulse Characteristics

Most often, there is not an isolated pulse, but rather a pulse train.

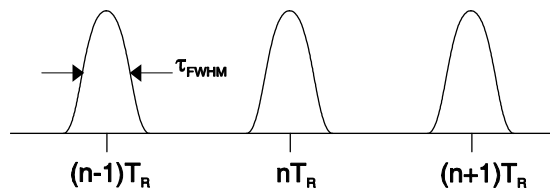


Figure 1.1: Periodic pulse train

T_R : pulse repetition time

W : pulse energy

$P_{ave} = W/T_R$: average power

τ_{FWHM} is the Full Width at Half Maximum of the intensity envelope of the pulse in the time domain.

The peak power is given by

$$P_p = \frac{W}{\tau_{FWHM}} = P_{ave} \frac{T_R}{\tau_{FWHM}}, \quad (1.1)$$

and the peak electric field is given by

$$E_p = \sqrt{2Z_{F_0} \frac{P_p}{A_{eff}}}. \quad (1.2)$$

A_{eff} is the beam cross-section and $Z_{F_0} = 377 \Omega$ is the free space impedance.

Time scales:

1 ns	\sim	30 cm	(high-speed electronics, GHz)
1 ps	\sim	300 μm	
1 fs	\sim	300 nm	
1 as = 10^{-18} s	\sim	0.3 nm = 3 \AA	(typ-lattice constant in metal)

The shortest pulses generated to date are about 4 – 5 fs at 800 nm ($\lambda/c = 2.7$ fs), less than two optical cycles and 250 as at 25 nm. For few-cycle pulses, the electric field becomes important, not only the intensity!

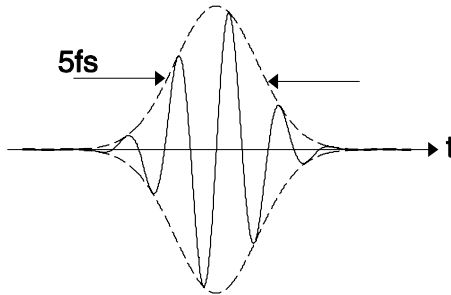


Figure 1.2: Electric field waveform of a 5 fs pulse at a center wavelength of 800 nm. The electric field depends on the carrier-envelope phase.

average power:

$$P_{ave} \sim 1W, \text{ up to } 100 \text{ W in progress.}$$

$$kW \text{ possible, not yet pulsed}$$

repetition rates:

$$T_R^{-1} = f_R = \text{mHz} - 100 \text{ GHz}$$

pulse energy:

$$W = 1\text{pJ} - 1\text{kJ}$$

pulse width:

$$\tau_{\text{FWHM}} = \begin{array}{ll} 5 \text{ fs} - 50 \text{ ps}, & \text{modelocked} \\ 30 \text{ ps} - 100 \text{ ns}, & \text{Q-switched} \end{array}$$

peak power:

$$P_p = \frac{1 \text{ kJ}}{1 \text{ ps}} \sim 1 \text{ PW},$$

obtained with Nd:glass (LLNL - USA, [1][2][3]).

For a typical lab pulse, the peak power is

$$P_p = \frac{10 \text{ nJ}}{10 \text{ fs}} \sim 1 \text{ MW}$$

peak field of typical lab pulse:

$$E_p = \sqrt{2 \times 377 \times \frac{10^6 \times 10^{12}}{\pi \times (1.5)^2} \frac{\text{V}}{\text{m}}} \approx 10^{10} \frac{\text{V}}{\text{m}} = \frac{10 \text{ V}}{\text{nm}}$$

1.3 Applications

- High time resolution: Ultrafast Spectroscopy, tracing of ultrafast physical processes in condensed matter (see Fig. 1.3), chemical reactions, physical and biological processes, influence chemical reactions with femtosecond pulses: Femto-Chemistry (Noble Prize, 2000 to A. Zewail), high speed electric circuit testing and sampling of electrical signals, see Fig. 1.4.

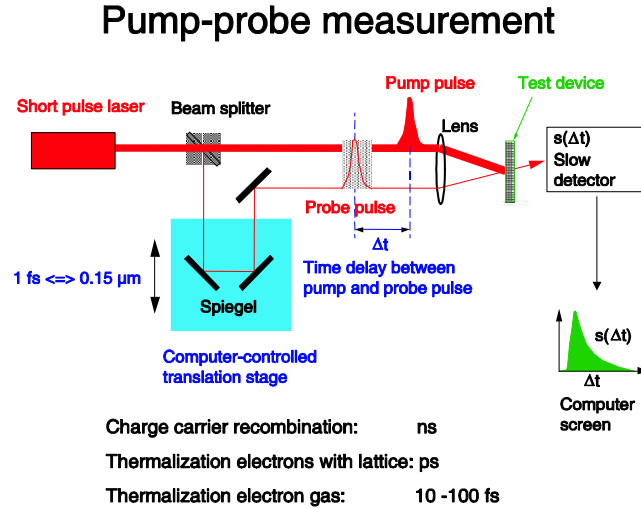


Figure 1.3: Pump-probe setup to extract time constants relevant for the carrier dynamics in semiconductors.

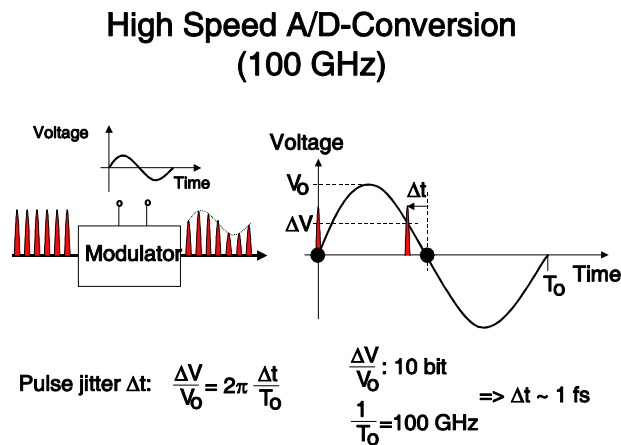


Figure 1.4: High speed A/D conversion with a high repetition rate pico- or femtosecond laser.

- High spatial resolution: $c\tau_{FWHM}$; optical imaging, e.g. optical coherence tomography, see Figs. 1.5-1.8).

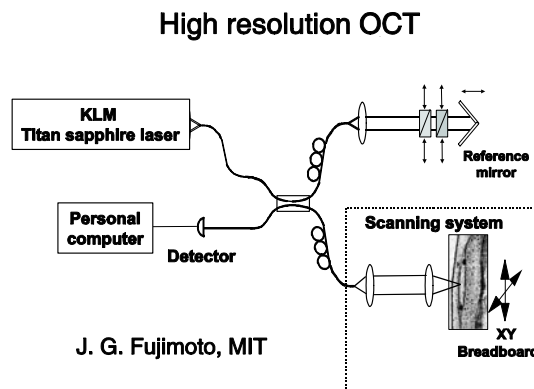


Figure 1.5: Setup for optical coherence tomography.
 Courtesy of James Fujimoto. Used with permission.

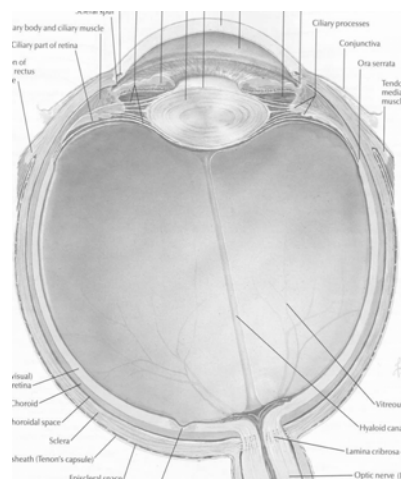


Figure 1.6: Cross section through the human eye.
 Courtesy of James Fujimoto. Used with permission.

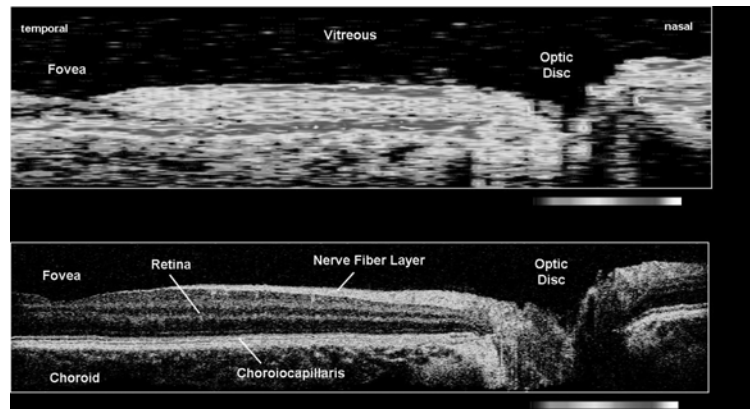


Figure 1.7: Comparison of retinal images taken with a superluminescence diode (top) versus a broadband Ti:sapphire laser (below).

Courtesy of James Fujimoto. Used with permission.

- Imaging through strongly scattering media:

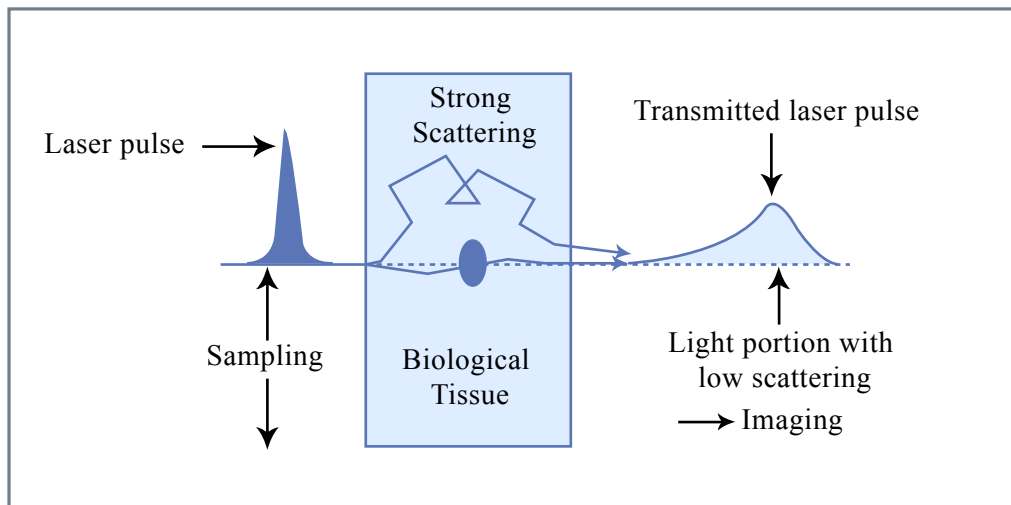


Figure 1.8: Imaging of the directly transmitted photons results in an un-blurred picture. Substitution for x-ray imaging; however, transmission is very low.

Figure by MIT OCW.

- High bandwidth: massive WDM - optical communications, many channels from one source or massive TDM, high bit-rate stream of short pulses.

- High intensities: Large intensities at low average power \Rightarrow Nonlinear frequency conversion, laser material processing, surgery, high intensity physics: x-ray generation, particle acceleration, ...

1.4 Review of Laser Essentials

Linear and ring cavities:

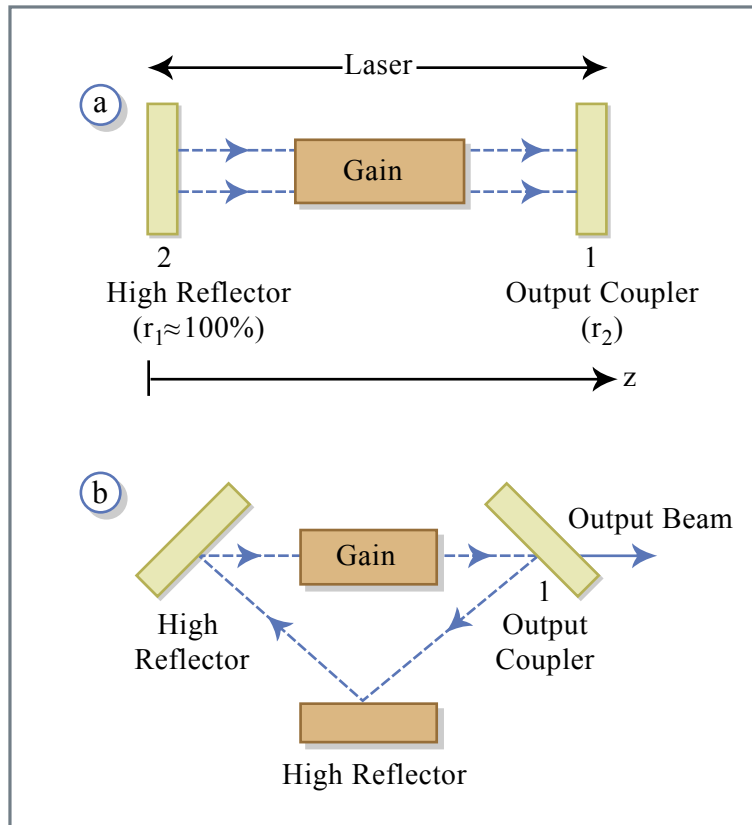


Figure 1.9: Possible cavity configurations. (a) Schematic of a linear cavity laser. (b) Schematic of a ring laser. [1]

Figure by MIT OCW.

Steady-state operation: Electric field must repeat itself after one roundtrip. Consider a monochromatic, linearly polarized field

$$E(z, t) = \Re \{ E_0 e^{j(\omega t - kz)} \}, \quad (1.3)$$

where

$$k = \frac{\omega}{c}n \quad (1.4)$$

is the propagation constant in a medium with refractive index n .

Consider linear resonator in Fig. 1.9a. Propagation from (1) to (2) is determined by $n = n' + jn''$ (complex refractive index), with the electric field given by

$$E = \Re \left\{ E_0 e^{\frac{\omega}{c}n''_g \ell_g} e^{j\omega t} e^{-j\frac{\omega}{c}(n'_g \ell_g + \ell_a)} \right\}, \quad (1.5)$$

where n_g is the complex refractive index of the gain medium (outside the gain medium $n = 1$ is assumed), ℓ_g is the length of the gain medium, ℓ_a is the outside gain medium, and $\ell = n_g \ell_g + \ell_a$ is the optical path length in the resonator.

Propagation back to (1), i.e. one full roundtrip results in

$$E = \Re \left\{ r_1 r_2 e^{2\frac{\omega}{c}n''_g \ell_g} E_0 e^{j\omega t - j2\frac{\omega}{c}\ell} \right\} \Rightarrow r_1 r_2 e^{2\frac{\omega}{c}n''_g \ell_g} = 1, \quad (1.6)$$

i.e. the gain equals the loss, and furthermore, we obtain the phase condition

$$\frac{2\omega\ell}{c} = 2m\pi. \quad (1.7)$$

The phase condition determines the resonance frequencies, i.e.

$$\omega_m = \frac{m\pi c}{\ell} \quad (1.8)$$

and

$$f_m = \frac{mc}{2\ell}. \quad (1.9)$$

The mode spacing of the longitudinal modes is

$$\Delta f = f_m - f_{m-1} = \frac{c}{2\ell} \quad (1.10)$$

(only true if there is no dispersion, i.e. $n \neq n(\omega)$). Assume frequency independent cavity loss and bell shaped gain (see Fig. 1.10).

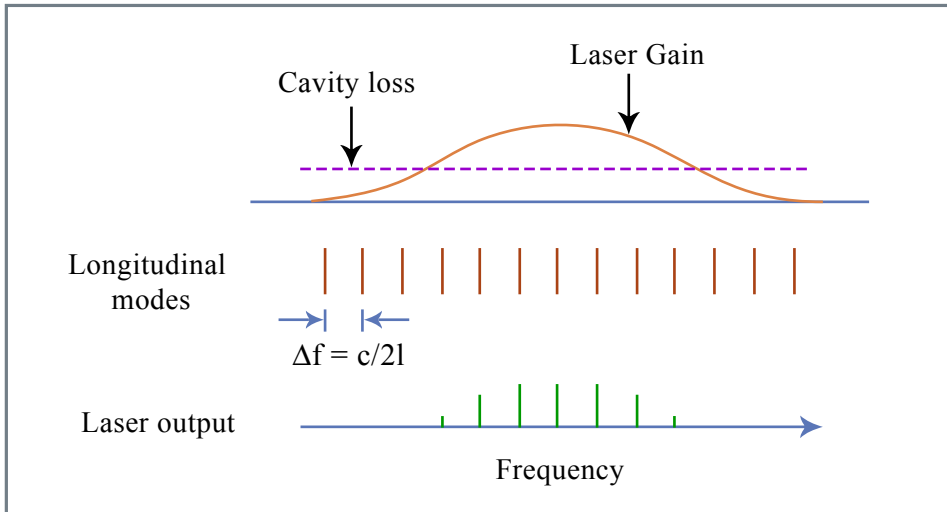


Figure 1.10: Laser gain and cavity loss spectra, longitudinal mode location, and laser output for multimode laser operation.

Figure by MIT OCW.

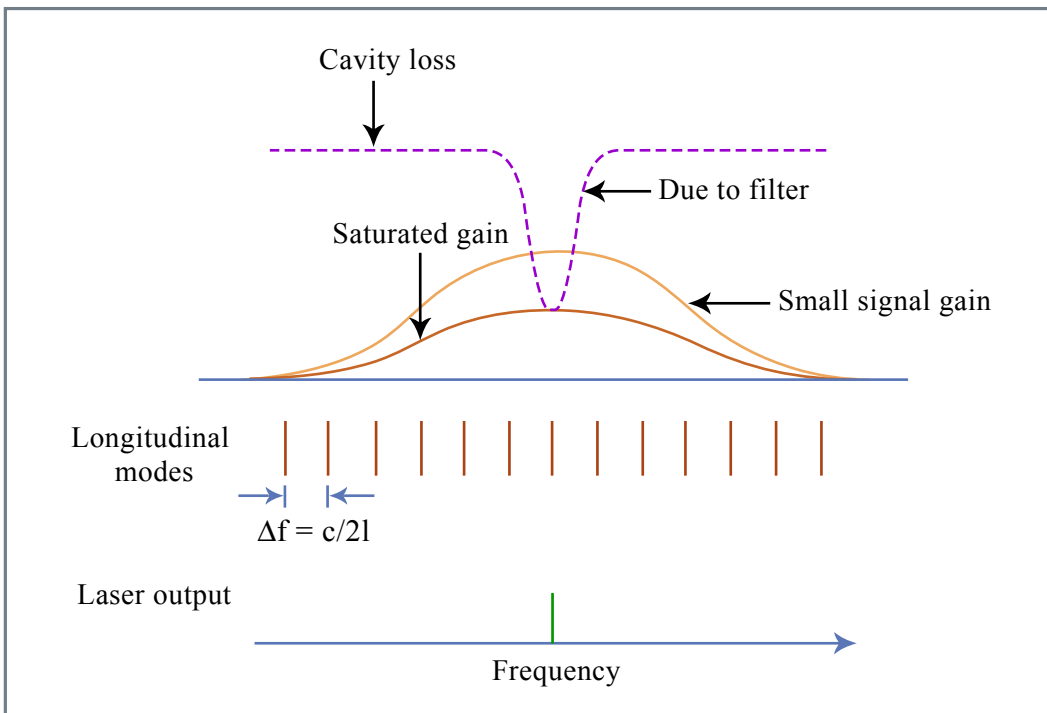


Figure 1.11: Gain and loss spectra, longitudinal mode locations, and laser output for single mode laser operation.

Figure by MIT OCW.

To assure single frequency operation use filter (etalon); distinguish between homogeneously and inhomogeneously broadened gain media, effects of spectral hole burning! Distinguish between small signal gain g_0 per roundtrip,

i.e. gain for laser intensity $I \rightarrow 0$, and large signal gain, most often given by

$$g = \frac{g_0}{1 + \frac{I}{I_{\text{sat}}}}, \quad (1.11)$$

where I_{sat} is the saturation intensity. Gain saturation is responsible for the steady state gain (see Fig. 1.11), and homogeneously broadened gain is assumed.

To generate short pulses, i.e. shorter than the cavity roundtrip time, we wish to have many longitudinal modes running in steady state. For a multimode laser the laser field is given by

$$E(z, t) = \Re \left[\sum_m \hat{E}_m e^{j(\omega_m t - k_m z + \phi_m)} \right], \quad (1.12a)$$

$$\omega_m = \omega_0 + m\Delta\omega = \omega_0 + \frac{m\pi c}{\ell}, \quad (1.12b)$$

$$k_m = \frac{\omega_m}{c}, \quad (1.12c)$$

where the symbol $\hat{}$ denotes a frequency domain quantity. Equation (1.12a) can be rewritten as

$$E(z, t) = \Re \left\{ e^{j\omega_0(t-z/c)} \sum_m \hat{E}_m e^{j(m\Delta\omega(t-z/c) + \phi_m)} \right\} \quad (1.13a)$$

$$= \Re [A(t - z/c) e^{j\omega_0(t-z/c)}] \quad (1.13b)$$

with the complex envelope

$$A\left(t - \frac{z}{c}\right) = \sum_m E_m e^{j(m\Delta\omega(t-z/c) + \phi_m)} = \text{complex envelope (slowly varying)}. \quad (1.14)$$

$e^{j\omega_0(t-z/c)}$ is the carrier wave (fast oscillation). Both carrier and envelope travel with the same speed (no dispersion assumed). The envelope function is periodic with period

$$T = \frac{2\pi}{\Delta\omega} = \frac{2\ell}{c} = \frac{L}{c}. \quad (1.15)$$

L is the roundtrip length (optical)!

Examples:

Examples:

We assume N modes with equal amplitudes $E_m = E_0$ and equal phases $\phi_m = 0$, and thus the envelope is given by

$$A(z, t) = E_0 \sum_{m=-(N-1)/2}^{(N-1)/2} e^{j(m\Delta\omega(t-z/c))}. \quad (1.16)$$

With

$$\sum_{m=0}^{q-1} a^m = \frac{1 - a^q}{1 - a}, \quad (1.17)$$

we obtain

$$A(z, t) = E_0 \frac{\sin \left[\frac{N\Delta\omega}{2} \left(t - \frac{z}{c} \right) \right]}{\sin \left[\frac{\Delta\omega}{2} \left(t - \frac{z}{c} \right) \right]}. \quad (1.18)$$

The laser intensity I is proportional to $E(z, t)^2$, averaged over one optical cycle: $I \sim |A(z, t)|^2$. At $z = 0$, we obtain

$$I(t) \sim |E_0|^2 \frac{\sin^2 \left(\frac{N\Delta\omega t}{2} \right)}{\sin^2 \left(\frac{\Delta\omega t}{2} \right)}. \quad (1.19)$$

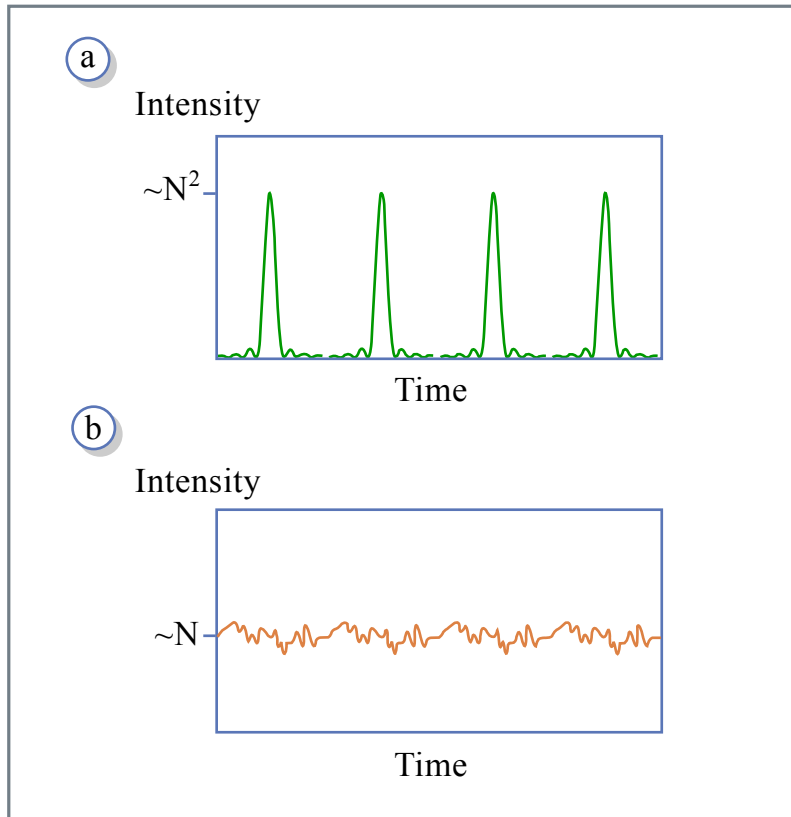


Figure 1.12: (a) mode-locked laser output with constant mode phase. (b) Laser output with randomly phased modes.

(a) Periodic pulses given by Eq. (1.19), period $T = 1/\Delta f = L/c$

- pulse duration

$$\Delta t = \frac{2\pi}{N\Delta\omega} = \frac{1}{N\Delta f} \quad (1.20)$$

- peak intensity $\sim N^2|E_0|^2$
- average intensity $\sim N|E_0|^2 \Rightarrow$ peak intensity is enhanced by a factor N .

(b) If phases of modes are not locked, i.e. ϕ_m random sequence

- Intensity fluctuates randomly about average value ($\sim N|E_0|^2$), same as modelocked case
- correlation time is $\Delta t_c \approx \frac{1}{N\Delta f}$
- Fluctuations are still periodic with period $T = 1/\Delta f$.

In a usual multimode laser, ϕ_m varies over t .

1.5 History

1960: First laser, ruby, Maiman [4].

1961: Proposal for Q-switching, Hellwarth [5].

1963: First indications of mode locking in ruby lasers, Guers and Mueller [6],[7], Statz and Tang [8]. on He-Ne lasers.

1964: Activemodelocking (HeNe, Ar, etc.), DiDomenico [9], [10] and Yariv [11].

1966: Passive modelocking with saturable dye absorber in ruby by A. J. Dellaria, Mocker and Collins [12].

1966: Dye laser, F. P. Schäfer, et al. [13].

1968: mode-locking (Q-Switching) of dye-lasers, Schmidt, Schäfer [14].

1972: cw-passive modelocking of dye laser, Ippen, Shank, Dienes [15].

1972: Analytic theories on active modelocking [21, 22].

1974: Sub-ps-pulses, Shank, Ippen [16].

1975: Theories for passive modelocking with slow [1], [24] and fast saturable absorbers [25] predicted hyperbolic secant pulse.

1981: Colliding-pulse mode-locked laser (CPM), [17].

1982: Pulse compression [20].

1984: Soliton Laser, Mollenauer, [26].

1985: Chirped pulse amplification, Strickland and Morou, [27].

1986: Ti:sapphire (solid-state laser), P. F. Moulton [28].

1987: 6 fs at 600 nm, external compression, Fork et al. [18, 19].

1988: Additive Pulse Modelocking (APM), [29, 30, 31].

1991: Kerr-lens modelocking, Spence et al. [32, 33, 34, 35, 36].

1993: Stretched pulse laser, Tamura et al [37].

1994: Chirped mirrors, Szipoecs et al. [38, 39]

1997: Double-chirped mirrors, Kaertner et al.[40]

2001: 5 fs, sub-two cycle pulses, octave spanning, Ell et al.[42]

2001: 250 as by High-Harmonic Generation, Krausz et al.[43]

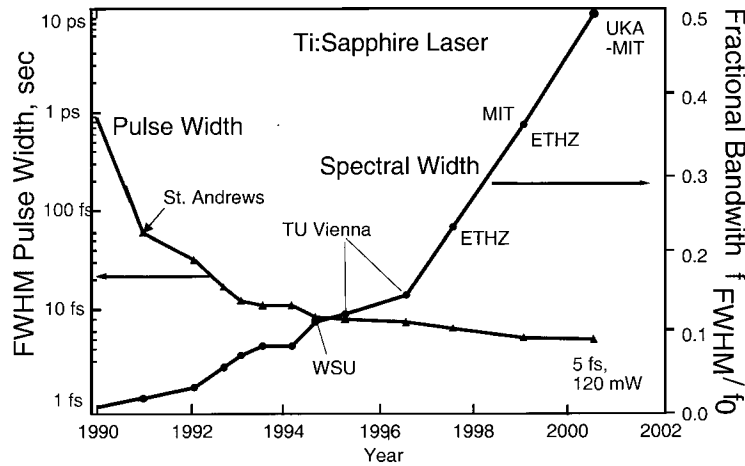


Figure 1.14: Pulse width of Ti:sapphire lasers by year.

1.6 Laser Materials

Laser Material	Absorption Wavelength	Average Emission λ	Band Width	Pulse Width
Nd:YAG	808 nm	1064 nm	0.45 nm	~ 6 ps
Nd:YLF	797 nm	1047 nm	1.3 nm	~ 3 ps
Nd:LSB	808 nm	1062 nm	4 nm	~ 1.6 ps
Nd:YVO ₄	808 nm	1064 nm	2 nm	~ 4.6 ps
Nd:fiber	804 nm	1053 nm	22-28 nm	~ 33 fs
Nd:glass	804 nm	1053 nm	22-28 nm	~ 60 fs
Yb:YAG	940, 968 nm	1030 nm	6 nm	~ 300 fs
Yb:glass	975 nm	1030 nm	30 nm	~ 90 fs
Ti:Al ₂ O ₃	480-540 nm	796 nm	200 nm	~ 5 fs
Cr ⁴⁺ :Mg ₂ SiO ₄ :	900-1100 nm	1260 nm	200 nm	~ 14 fs
Cr ⁴⁺ :YAG	900-1100 nm	1430 nm	180 nm	~ 19 fs

Transition metals: (Cr³⁺, Ti³⁺, Ni²⁺, CO²⁺, etc.) (outer $3d$ -electrons)
 → broadband

Rare earth: (Nd³⁺, Tm³⁺, Ho³⁺, Er³⁺, etc.) (shielded $4f$ -electrons)
 → narrow band.

Bibliography

- [1] M. D. Perry and G. Mourou, "Terawatt to Petawatt Subpicosecond Lasers," *Science*, Vol. 264 (1994), p. 917.
- [2] M. D. Perry et al., "Petawatt Laser Pulses," *Optics Letters*, Vol. 24 (1999), p. 160.
- [3] T. Tajima and G. Mourou, *Phys. Rev. Spec. Topics-Accelerators and Beams* 5(031301) 1 (2002).
See also www.wapr.apr.jaeri.go.jp/aprc/e/index_e.html,
www.eecs.umich.edu/CUOS/HERCULES/index, www.clf.rl.ac.uk
- [4] T. H. Maimann, "Stimulated optical radiation in ruby", *Nature* **187**, 493-494, (1960).
- [5] R. W. Hellwarth, Ed., *Advances in Quantum Electronics*, Columbia Press, NY (1961).
- [6] K. Gürs, R. Müller: "Breitband-modulation durch Steuerung der emission eines optischen masers (Auskoppel-modulation)", *Phys. Lett.* **5**, 179-181 (1963).
- [7] K. Gürs (Ed.): "Beats and modulation in optical ruby laser," in *Quantum Electronics III* (Columbia University Press, New York 1964).
- [8] H. Statez, C.L. Tang (Eds.): "Zeeman effect and nonlinear interactions between oscillating laser modes", in *Quantum Electronics III* (Columbia University Press, New York 1964).
- [9] M. DiDomenico: "Small-signal analysis of internal (coupling type) modulation of lasers," *J. Appl. Phys.* **35**, 2870-2876 (1964).

- [10] L.E. Hargrove, R.L. Fork, M.A. Pollack: "Locking of He-Ne laser modes induced by synchronous intracavity modulation," *Appl. Phys. Lett.* **5**, 4-5 (1964).
- [11] A. Yariv: "Internal modulation in multimode laser oscillators," *J. Appl. Phys.* **36**, 388-391 (1965).
- [12] H.W. Mocker, R.J. Collins: "Mode competition and self-locking effects in a Q-switched ruby laser," *Appl. Phys. Lett.* **7**, 270-273 (1965).
- [13] F. P. Schäfer, F. P. W. Schmidt, J. Volze: "Organic Dye Solution Laser," *Appl. Phys. Lett.* **9**, 306 – 308 (1966).
- [14] F. P. W. Schmidt, F. P. Schäfer: "Self-mode-locking of dye-lasers with saturable absorbers," *Phys. Lett.* **26A**, 258-259 (1968).
- [15] E.P. Ippen, C.V. Shank, A. Dienes: "Passive mode locking of the cw dye laser," *Appl. Phys. Lett.* **21**, 348-350 (1972).
- [16] C.V. Shank, E.P. Ippen: "Sub-picosecond kilowatt pulses from a mode-locked cw dye laser," *Appl. Phys. Lett.* **24**, 373-375 (1974).
- [17] R.L. Fork, B.I. Greene, C.V. Shank: "Generation of optical pulses shorter than 0.1 psec by colliding pulse mode-locking," *Appl. Phys. Lett.* **38**, 617-619 (1981).
- [18] W.H. Knox, R.L. Fork, M.C. Downer, R.H. Stolen, C.V. Shank, J.A. Valdmanis: "Optical pulse compression to 8 fs at a 5-kHz repetition rate," *Appl. Phys. Lett.* **46**, 1120-1122 (1985).
- [19] R.L. Fork, C.H.B. Cruz, P.C. Becker, C.V. Shank: "Compression of optical pulses to six femtoseconds by using cubic phase compensation," *Opt. Lett.* **12**, 483-485 (1987).
- [20] D. Grischowsky, A. C. Balant: TITLE, *Appl. Phys. Lett.* **41**, pp. (1982).
- [21] J. Kuizenga, A. E. Siegman: "FM und AM mode locking of the homogeneous laser - Part I: Theory, *IEEE J. Quantum Electron.* **6**, 694-708 (1970).

- [22] J. Kuizenga, A. E. Siegman: "FM und AM mode locking of the homogeneous laser - Part II: Experimental results, IEEE J. Quantum Electron. **6**, 709-715 (1970).
- [23] G.H.C. New: Pulse evolution in mode-locked quasicontinuous lasers, IEEE J. Quantum Electron. **10**, 115-124 (1974).
- [24] H.A. Haus: Theory of mode locking with a slow saturable absorber, IEEE J. Quantum Electron. **QE 11**, 736-746 (1975).
- [25] H.A. Haus, C.V. Shank, E.P. Ippen: Shape of passively mode-locked laser pulses, Opt. Commun. **15**, 29-31 (1975).
- [26] L.F. Mollenauer, R.H. Stolen: The soliton laser, Opt. Lett. **9**, 13-15 (1984).
- [27] D. Strickland and G. Morou: "Chirped pulse amplification," Opt. Comm. **56**,229-221,(1985).
- [28] P. F. Moulton: "Spectroscopic and laser characteristics of Ti:Al₂O₃", JOSA B **3**, 125-132 (1986).
- [29] K. J. Blow and D. Wood: "Modelocked Lasers with nonlinear external cavity," J. Opt. Soc. Am. B **5**, 629-632 (1988).
- [30] J. Mark, L.Y. Liu, K.L. Hall, H.A. Haus, E.P. Ippen: Femtosecond pulse generation in a laser with a nonlinear external resonator, Opt. Lett. **14**, 48-50 (1989).
- [31] E.P. Ippen, H.A. Haus, L.Y. Liu: Additive pulse modelocking, J. Opt. Soc. Am. B **6**, 1736-1745 (1989).
- [32] D.E. Spence, P.N. Kean, W. Sibbett: 60-fsec pulse generation from a self-mode-locked Ti:Sapphire laser, Opt. Lett. **16**, 42-44 (1991).
- [33] D.K. Negus, L. Spinelli, N. Goldblatt, G. Feugnet: TITLE, in *Advanced Solid-State Lasers* G. Dubé, L. Chase (Eds.) (Optical Society of America, Washington, D.C., 1991) pp. 120-124.
- [34] F. Salin, J. Squier, M. Piché: Mode locking of Ti:Al₂O₃ lasers and self-focusing: A Gaussian approximation, Opt. Lett. **16**, 1674-1676 (1991).

- [35] M. Piché: Beam reshaping and self-mode-locking in nonlinear laser resonators, *Opt. Commun.* **86**, 156-160 (1991)
- [36] U. Keller, G.W. 'tHooft, W.H. Knox, J.E. Cunningham: TITLE, *Opt. Lett.* **16**, 1022-1024 (1991).
- [37] K. Tamura, E.P. Ippen, H.A. Haus, L.E. Nelson: 77-fs pulse generation from a stretched-pulse mode-locked all-fiber ring laser, *Opt. Lett.* **18**, 1080-1082 (1993)
- [38] A. Stingl, C. Spielmann, F. Krausz: "Generation of 11-fs pulses from a Ti:sapphire laser without the use of prism," *Opt. Lett.* **19**, 204-206 (1994)
- [39] R. Szipöcs, K. Ferencz, C. Spielmann, F. Krausz: Chirped multilayer coatings for broadband dispersion control in femtosecond lasers, *Opt. Lett.* **19**, 201-203 (1994)
- [40] F.X. Kärtner, N. Matuschek, T. Schibli, U. Keller, H.A. Haus, C. Heine, R. Morf, V. Scheuer, M. Tilsch, T. Tschudi: Design and fabrication of double-chirped mirrors, *Opt. Lett.* **22**, 831-833 (1997)
- [41] Y. Chen, F.X. Kärtner, U. Morgner, S.H. Cho, H.A. Haus, J.G. Fujimoto, E.P. Ippen: Dispersion-managed mode locking, *J. Opt. Soc. Am. B* **16**, 1999-2004 (1999)
- [42] R. Ell, U. Morgner, F.X. Kärtner, J.G. Fujimoto, E.P. Ippen, V. Scheuer, G. Angelow, T. Tschudi: Generation of 5-fs pulses and octave-spanning spectra directly from a Ti:Sapphire laser, *Opt. Lett.* **26**, 373-375 (2001)
- [43] H. Hentschel, R. Kienberger, Ch. Spielmann, G. A. Reider, N. Milošević, T. Brabec, P. Corkum, U. Heinzmann, M. Drescher, F. Krausz: "Attosecond Metrology," *Nature* **414**, 509-513 (2001).

Chapter 2

Maxwell-Bloch Equations

2.1 Maxwell's Equations

Maxwell's equations are given by

$$\vec{\nabla} \times \vec{H} = \vec{j} + \frac{\partial \vec{D}}{\partial t}, \quad (2.1a)$$

$$\vec{\nabla} \times \vec{E} = -\frac{\partial \vec{B}}{\partial t}, \quad (2.1b)$$

$$\vec{\nabla} \cdot \vec{D} = \rho, \quad (2.1c)$$

$$\vec{\nabla} \cdot \vec{B} = 0. \quad (2.1d)$$

The material equations accompanying Maxwell's equations are:

$$\vec{D} = \epsilon_0 \vec{E} + \vec{P}, \quad (2.2a)$$

$$\vec{B} = \mu_0 \vec{H} + \vec{M}. \quad (2.2b)$$

Here, \vec{E} and \vec{H} are the electric and magnetic field, \vec{D} the dielectric flux, \vec{B} the magnetic flux, \vec{j} the current density of free carriers, ρ is the free charge density, \vec{P} is the polarization, and \vec{M} the magnetization. By taking the curl of Eq. (2.1b) and considering $\vec{\nabla} \times (\vec{\nabla} \times \vec{E}) = \vec{\nabla} (\vec{\nabla} \cdot \vec{E}) - \Delta \vec{E}$, we obtain

$$\Delta \vec{E} - \mu_0 \frac{\partial}{\partial t} \left(\vec{j} + \epsilon_0 \frac{\partial \vec{E}}{\partial t} + \frac{\partial \vec{P}}{\partial t} \right) = \frac{\partial}{\partial t} \vec{\nabla} \times \vec{M} + \vec{\nabla} (\vec{\nabla} \cdot \vec{E}) \quad (2.3)$$

and hence

$$\left(\Delta - \frac{1}{c_0^2} \frac{\partial^2}{\partial t^2}\right) \vec{E} = \mu_0 \left(\frac{\partial \vec{j}}{\partial t} + \frac{\partial^2 \vec{P}}{\partial t^2}\right) + \frac{\partial}{\partial t} \vec{\nabla} \times \vec{M} + \vec{\nabla} (\vec{\nabla} \cdot \vec{E}). \quad (2.4)$$

The vacuum velocity of light is

$$c_0 = \sqrt{\frac{1}{\mu_0 \epsilon_0}}. \quad (2.5)$$

2.2 Linear Pulse Propagation in Isotropic Media

For dielectric non magnetic media, with no free charges and currents due to free charges, there is $\vec{M} = \vec{0}$, $\vec{j} = \vec{0}$, $\rho = 0$. We obtain with $\vec{D} = \epsilon(\vec{r}) \vec{E} = \epsilon_0 \epsilon_r(\vec{r}) \vec{E}$

$$\vec{\nabla} \cdot (\epsilon(\vec{r}) \vec{E}) = 0. \quad (2.6)$$

In addition for homogeneous media, we obtain $\vec{\nabla} \cdot \vec{E} = 0$ and the wave equation (2.4) greatly simplifies

$$\left(\Delta - \frac{1}{c_0^2} \frac{\partial^2}{\partial t^2}\right) \vec{E} = \mu_0 \frac{\partial^2 \vec{P}}{\partial t^2}. \quad (2.7)$$

This is the wave equation driven by the polarization in the medium. If the medium is linear and has only an induced polarization described by the susceptibility $\chi(\omega) = \epsilon_r(\omega) - 1$, we obtain in the frequency domain

$$\hat{P}(\omega) = \epsilon_0 \chi(\omega) \hat{E}(\omega). \quad (2.8)$$

Substituted in (2.7)

$$\left(\Delta + \frac{\omega^2}{c_0^2}\right) \hat{E}(\omega) = -\omega^2 \mu_0 \epsilon_0 \chi(\omega) \hat{E}(\omega), \quad (2.9)$$

where $\hat{D} = \epsilon_0 \epsilon_r(\omega) \hat{E}(\omega)$, and thus

$$\left(\Delta + \frac{\omega^2}{c_0^2} (1 + \chi(\omega))\right) \hat{E}(\omega) = 0, \quad (2.10)$$

with the refractive index n and $1 + \chi(\omega) = n^2$

$$\left(\Delta + \frac{\omega^2}{c^2}\right) \hat{\vec{E}}(\omega) = 0, \quad (2.11)$$

where $c = c_0/n$ is the velocity of light in the medium.

2.2.1 Plane-Wave Solutions (TEM-Waves)

The complex plane-wave solution of Eq. (2.11) is given by

$$\hat{\vec{E}}^{(+)}(\omega, \vec{r}) = \hat{\vec{E}}^{(+)}(\omega) e^{-j\vec{k}\cdot\vec{r}} = E_0 e^{-j\vec{k}\cdot\vec{r}} \cdot \vec{e} \quad (2.12)$$

with

$$|\vec{k}|^2 = \frac{\omega^2}{c^2} = k^2. \quad (2.13)$$

Thus, the dispersion relation is given by

$$k(\omega) = \frac{\omega}{c_0} n(\omega). \quad (2.14)$$

From $\vec{\nabla} \cdot \vec{E} = 0$, we see that $\vec{k} \perp \vec{e}$. In time domain, we obtain

$$\vec{E}^{(+)}(\vec{r}, t) = E_0 \vec{e} \cdot e^{j\omega t - j\vec{k}\cdot\vec{r}} \quad (2.15)$$

with

$$k = 2\pi/\lambda, \quad (2.16)$$

where λ is the wavelength, ω the angular frequency, \vec{k} the wave vector, \vec{e} the polarization vector, and $f = \omega/2\pi$ the frequency. From Eq. (2.1b), we get for the magnetic field

$$-j\vec{k} \times E_0 \vec{e} e^{j(\omega t - \vec{k}\cdot\vec{r})} = -j\mu_0 \omega \vec{H}^{(+)}, \quad (2.17)$$

or

$$\vec{H}^{(+)} = \frac{E_0}{\mu_0 \omega} e^{j(\omega t - \vec{k}\cdot\vec{r})} \vec{k} \times \vec{e} = H_0 \vec{h} e^{j(\omega t - \vec{k}\cdot\vec{r})} \quad (2.18)$$

with

$$\vec{h} = \frac{\vec{k}}{|\vec{k}|} \times \vec{e} \quad (2.19)$$

and

$$H_0 = \frac{|k|}{\mu_0 \omega} E_0 = \frac{1}{Z_F} E_0. \quad (2.20)$$

The natural impedance is

$$Z_F = \mu_0 c = \sqrt{\frac{\mu_0}{\epsilon_0 \epsilon_r}} = \frac{1}{n} Z_{F_0} \quad (2.21)$$

with the free space impedance

$$Z_{F_0} = \sqrt{\frac{\mu_0}{\epsilon_0}} = 377 \Omega. \quad (2.22)$$

For a backward propagating wave with $\vec{E}^{(+)}(\vec{r}, t) = E_0 \vec{e} \cdot e^{j\omega t + j\vec{k} \cdot \vec{r}}$ there is $\vec{H}^{(+)} = H_0 \vec{h} e^{j(\omega t - \vec{k} \cdot \vec{r})}$ with

$$H_0 = -\frac{|k|}{\mu_0 \omega} E_0. \quad (2.23)$$

Note that the vectors \vec{e} , \vec{h} and \vec{k} form an orthogonal trihedral,

$$\vec{e} \perp \vec{h}, \quad \vec{k} \perp \vec{e}, \quad \vec{k} \perp \vec{h}. \quad (2.24)$$

2.2.2 Complex Notations

Physical \vec{E} , \vec{H} fields are real:

$$\vec{E}(\vec{r}, t) = \frac{1}{2} \left(\vec{E}^{(+)}(\vec{r}, t) + \vec{E}^{(-)}(\vec{r}, t) \right) \quad (2.25)$$

with $\vec{E}^{(-)}(\vec{r}, t) = \vec{E}^{(+)}(\vec{r}, t)^*$. A general temporal shape can be obtained by adding different spectral components,

$$\vec{E}^{(+)}(\vec{r}, t) = \int_0^\infty \frac{d\omega}{2\pi} \widehat{\vec{E}}^{(+)}(\omega) e^{j(\omega t - \vec{k} \cdot \vec{r})}. \quad (2.26)$$

Correspondingly, the magnetic field is given by

$$\vec{H}(\vec{r}, t) = \frac{1}{2} \left(\vec{H}^{(+)}(\vec{r}, t) + \vec{H}^{(-)}(\vec{r}, t) \right) \quad (2.27)$$

with $\vec{H}^{(-)}(\vec{r}, t) = \vec{H}^{(+)}(\vec{r}, t)^*$. The general solution is given by

$$\vec{H}^{(+)}(\vec{r}, t) = \int_0^\infty \frac{d\omega}{2\pi} \widehat{\vec{H}}^{(+)}(\omega) e^{j(\omega t - \vec{k} \cdot \vec{r})} \quad (2.28)$$

with

$$\widehat{\vec{H}}^{(+)}(\omega) = \frac{E_0}{Z_F} \vec{h}. \quad (2.29)$$

2.2.3 Poynting Vectors, Energy Density and Intensity for Plane Wave Fields

Quantity	Real fields	Complex fields $\langle \rangle_t$
Energy density	$w = \frac{1}{2} (\epsilon_0 \epsilon_r \vec{E}^2 + \mu_0 \mu_r \vec{H}^2)$	$w = \frac{1}{4} \left(\begin{array}{l} \epsilon_0 \epsilon_r \vec{E}^{(+)} ^2 \\ + \mu_0 \mu_r \vec{H}^{(+)} ^2 \end{array} \right)$
Poynting vector	$\vec{S} = \vec{E} \times \vec{H}$	$\vec{T} = \frac{1}{2} \vec{E}^{(+)} \times (\vec{H}^{(+)*})$
Intensity	$I = \vec{S} = cw$	$I = \vec{T} = cw$
Energy Cons.	$\frac{\partial w}{\partial t} + \vec{\nabla} \cdot \vec{S} = 0$	$\frac{\partial w}{\partial t} + \vec{\nabla} \cdot \vec{T} = 0$

For $\vec{E}^{(+)}(\vec{r}, t) = E_0 \vec{e}_x e^{j(\omega t - kz)}$ we obtain the energy density

$$w = \frac{1}{2} \epsilon_r \epsilon_0 |E_0|^2, \quad (2.30)$$

the poynting vector

$$\vec{T} = \frac{1}{2Z_F} |E_0|^2 \vec{e}_z \quad (2.31)$$

and the intensity

$$I = \frac{1}{2Z_F} |E_0|^2 = \frac{1}{2} Z_F |H_0|^2. \quad (2.32)$$

2.2.4 Dielectric Susceptibility

The polarization is given by

$$\vec{P}^{(+)}(\omega) = \frac{\text{dipole moment}}{\text{volume}} = N \cdot \langle \vec{p}^{(+)}(\omega) \rangle = \epsilon_0 \chi(\omega) \vec{E}^{(+)}(\omega), \quad (2.33)$$

where N is density of elementary units and $\langle \vec{p} \rangle$ is the average dipole moment of unit (atom, molecule, ...).

Classical harmonic oscillator model

The damped harmonic oscillator driven by an electric force in one dimension, x , is described by the differential equation

$$m \frac{d^2 x}{dt^2} + 2 \frac{\omega_0}{Q} m \frac{dx}{dt} + m \omega_0^2 x = e_0 E(t), \quad (2.34)$$

where $E(t) = \hat{E}e^{j\omega t}$. By using the ansatz $x(t) = \hat{x}e^{j\omega t}$, we obtain for the complex amplitude of the dipole moment $p = e_0x(t) = \hat{p}e^{j\omega t}$

$$\hat{p} = \frac{\frac{e_0^2}{m}}{(\omega_0^2 - \omega^2) + 2j\frac{\omega_0}{Q}\omega} \hat{E}. \quad (2.35)$$

For the susceptibility, we get

$$\chi(\omega) = \frac{N \frac{e_0^2}{m} \frac{1}{\epsilon_0}}{(\omega_0^2 - \omega^2) + 2j\omega \frac{\omega_0}{Q}} \quad (2.36)$$

and thus

$$\chi(\omega) = \frac{\omega_p^2}{(\omega_0^2 - \omega^2) + 2j\omega \frac{\omega_0}{Q}}, \quad (2.37)$$

with the plasma frequency ω_p , determined by $\omega_p^2 = Ne_0^2/m\epsilon_0$. Figure 2.1 shows the real part and imaginary part of the classical susceptibility (2.37).

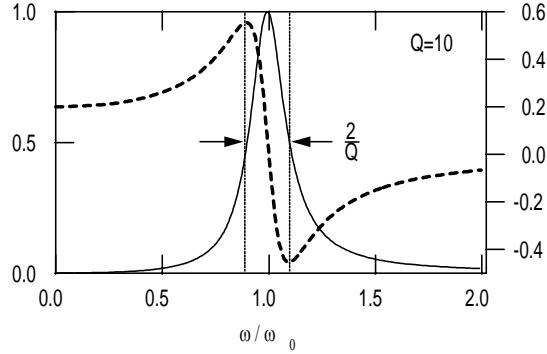


Figure 2.1: Real part and imaginary part of the susceptibility of the classical oscillator model for the electric polarizability.

Note, there is a small resonance shift due to the loss. Off resonance, the imaginary part approaches very quickly zero. Not so the real part, it approaches a constant value ω_p^2/ω_0^2 below resonance, and approaches zero for above resonance, but slower than the real part, i.e. off resonance there is still a contribution to the index but practically no loss.

2.3 Bloch Equations

Atoms in low concentration show line spectra as found in gas-, dye- and some solid-state laser media. Usually, there are infinitely many energy eigenstates in an atomic, molecular or solid-state medium and the spectral lines are associated with allowed transitions between two of these energy eigenstates. For many physical considerations it is already sufficient to take only two of the possible energy eigenstates into account, for example those which are related to the laser transition. The pumping of the laser can be described by phenomenological relaxation processes into the upper laser level and out of the lower laser level. The resulting simple model is often called a two-level atom, which is mathematically also equivalent to a spin $1/2$ particle in an external magnetic field, because the spin can only be parallel or anti-parallel to the field, i.e. it has two energy levels and energy eigenstates. The interaction of the two-level atom or the spin with the electric or magnetic field is described by the Bloch equations.

2.3.1 The Two-Level Model

An atom having only two energy eigenvalues is described by a two-dimensional state space spanned by the two energy eigenstates $|e\rangle$ and $|g\rangle$. The two states constitute a complete orthonormal system. The corresponding energy eigenvalues are E_e and E_g (Fig. 2.2).

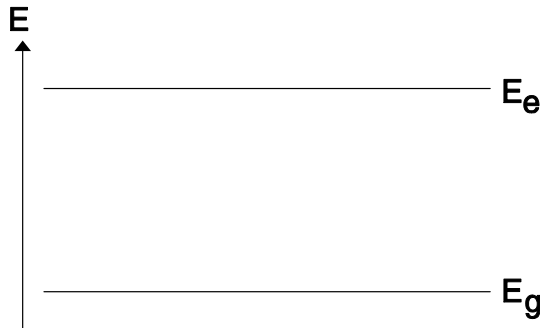


Figure 2.2: Two-level atom

In the position-, i.e. x -representation, these states correspond to the wave

functions

$$\psi_e(x) = \langle x|e \rangle, \quad \text{and} \quad \psi_g(x) = \langle x|g \rangle. \quad (2.38)$$

The Hamiltonian of the atom is given by

$$H_A = E_e|e \rangle \langle e| + E_g|g \rangle \langle g|. \quad (2.39)$$

In this two-dimensional state space only $2 \times 2 = 4$ linearly independent linear operators are possible. A possible choice for an operator base in this space is

$$\mathbf{1} = |e \rangle \langle e| + |g \rangle \langle g|, \quad (2.40)$$

$$\sigma_z = |e \rangle \langle e| - |g \rangle \langle g|, \quad (2.41)$$

$$\sigma^+ = |e \rangle \langle g|, \quad (2.42)$$

$$\sigma^- = |g \rangle \langle e|. \quad (2.43)$$

The non-Hermitian operators σ^\pm could be replaced by the Hermitian operators $\sigma_{x,y}$

$$\sigma_x = \sigma^+ + \sigma^-, \quad (2.44)$$

$$\sigma_y = -j\sigma^+ + j\sigma^-. \quad (2.45)$$

The physical meaning of these operators becomes obvious, if we look at the action when applied to an arbitrary state

$$|\psi \rangle = c_g|g \rangle + c_e|e \rangle. \quad (2.46)$$

We obtain

$$\sigma^+|\psi \rangle = c_g|e \rangle, \quad (2.47)$$

$$\sigma^-|\psi \rangle = c_e|g \rangle, \quad (2.48)$$

$$\sigma_z|\psi \rangle = c_e|e \rangle - c_g|g \rangle. \quad (2.49)$$

The operator σ^+ generates a transition from the ground to the excited state, and σ^- does the opposite. In contrast to σ^+ and σ^- , σ_z is a Hermitian operator, and its expectation value is an observable physical quantity with expectation value

$$\langle \psi|\sigma_z|\psi \rangle = |c_e|^2 - |c_g|^2 = w, \quad (2.50)$$

the inversion w of the atom, since $|c_e|^2$ and $|c_g|^2$ are the probabilities for finding the atom in state $|e \rangle$ or $|g \rangle$ upon a corresponding measurement.

If we consider an ensemble of N atoms the total inversion would be $\sigma = N \langle \psi | \sigma_z | \psi \rangle$. If we separate from the Hamiltonian (2.38) the term $(E_e + E_g)/2 \cdot \mathbf{1}$, where $\mathbf{1}$ denotes the unity matrix, we rescale the energy values correspondingly and obtain for the Hamiltonian of the two-level system

$$\mathbf{H}_A = \frac{1}{2} \hbar \omega_{eg} \sigma_z, \quad (2.51)$$

with the transition frequency

$$\omega_{eg} = \frac{1}{\hbar} (E_e - E_g). \quad (2.52)$$

This form of the Hamiltonian is favorable. There are the following commutator relations between operators (2.41) to (2.43)

$$[\sigma^+, \sigma^-] = \sigma_z, \quad (2.53)$$

$$[\sigma^+, \sigma_z] = -2\sigma^+, \quad (2.54)$$

$$[\sigma^-, \sigma_z] = 2\sigma^-, \quad (2.55)$$

and anti-commutator relations, respectively

$$[\sigma^+, \sigma^-]_+ = \mathbf{1}, \quad (2.56)$$

$$[\sigma^+, \sigma_z]_+ = \mathbf{0}, \quad (2.57)$$

$$[\sigma^-, \sigma_z]_+ = \mathbf{0}, \quad (2.58)$$

$$[\sigma^-, \sigma^-]_+ = [\sigma^+, \sigma^+]_+ = \mathbf{0}. \quad (2.59)$$

The operators $\sigma_x, \sigma_y, \sigma_z$ fulfill the angular momentum commutator relations

$$[\sigma_x, \sigma_y] = 2j\sigma_z, \quad (2.60)$$

$$[\sigma_y, \sigma_z] = 2j\sigma_x, \quad (2.61)$$

$$[\sigma_z, \sigma_x] = 2j\sigma_y. \quad (2.62)$$

The two-dimensional state space can be represented as vectors in \mathbb{C}^2 according to the rule:

$$|\psi \rangle = c_e |e \rangle + c_g |g \rangle \rightarrow \begin{pmatrix} c_e \\ c_g \end{pmatrix}. \quad (2.63)$$

The operators are then represented by matrices

$$\boldsymbol{\sigma}^+ \rightarrow \begin{pmatrix} 0 & 1 \\ 0 & 0 \end{pmatrix}, \quad (2.64)$$

$$\boldsymbol{\sigma}^- \rightarrow \begin{pmatrix} 0 & 0 \\ 1 & 0 \end{pmatrix}, \quad (2.65)$$

$$\boldsymbol{\sigma}_z \rightarrow \begin{pmatrix} 1 & 0 \\ 0 & -1 \end{pmatrix}, \quad (2.66)$$

$$\mathbf{1} \rightarrow \begin{pmatrix} 1 & 0 \\ 0 & 1 \end{pmatrix}. \quad (2.67)$$

2.3.2 The Atom-Field Interaction In Dipole Approximation

The dipole moment of an atom $\vec{\mathbf{p}}$ is essentially determined by the position operator $\vec{\mathbf{x}}$ via

$$\vec{\mathbf{p}} = -e_0 \vec{\mathbf{x}}. \quad (2.68)$$

Then the expectation value for the dipole moment of an atom in state (2.46) is

$$\begin{aligned} \langle \psi | \vec{\mathbf{p}} | \psi \rangle &= -e_0 (|c_e|^2 \langle e | \vec{\mathbf{x}} | e \rangle + c_e c_g^* \langle g | \vec{\mathbf{x}} | e \rangle \\ &+ c_g c_e^* \langle e | \vec{\mathbf{x}} | g \rangle + |c_g|^2 \langle g | \vec{\mathbf{x}} | g \rangle). \end{aligned} \quad (2.69)$$

For simplicity, we may assume that the medium is an atomic gas. The atoms possess inversion symmetry, therefore, energy eigenstates must be symmetric or anti-symmetric, i.e. $\langle e | \vec{\mathbf{x}} | e \rangle = \langle g | \vec{\mathbf{x}} | g \rangle = 0$. We obtain

$$\langle \psi | \vec{\mathbf{p}} | \psi \rangle = -e_0 (c_e c_g^* \langle g | \vec{\mathbf{x}} | e \rangle + c_g c_e^* \langle g | \vec{\mathbf{x}} | e \rangle^*). \quad (2.70)$$

(Note, this means, there is no permanent dipole moment in an atom, which is in an energy eigenstate. Note, this might not be the case in a solid. The atoms constituting the solid are oriented in a lattice, which may break the symmetry. If so, there are permanent dipole moments and consequently the matrix elements $\langle e | \vec{\mathbf{x}} | e \rangle$ and $\langle g | \vec{\mathbf{x}} | g \rangle$ would not vanish. If so, there are also crystal fields, which then imply level shifts, via the linear Stark effect.) Thus an atom does only exhibit a dipole moment in the average, if the product $c_e c_g^* \neq 0$, i.e. the state of the atom is in a superposition of states $|e\rangle$ and $|g\rangle$.

With the dipole matrix elements

$$\vec{M} = e_0 \langle g | \vec{x} | e \rangle \quad (2.71)$$

the expectation value for the dipole moment can be written as

$$\langle \psi | \vec{p} | \psi \rangle = -(c_e c_g^* \vec{M} + c_g c_e^* \vec{M}^*) = -\langle \psi | (\boldsymbol{\sigma}^+ \vec{M}^* + \boldsymbol{\sigma}^- \vec{M}) | \psi \rangle. \quad (2.72)$$

Since this is true for an arbitrary state, the dipole operator (2.68) is represented by

$$\vec{p} = \vec{p}^+ + \vec{p}^- = -\vec{M}^* \boldsymbol{\sigma}^+ - \vec{M} \boldsymbol{\sigma}^-. \quad (2.73)$$

Therefore, the operators $\boldsymbol{\sigma}^+$ and $\boldsymbol{\sigma}^-$ are proportional to the complex dipole moment operators \vec{p}^+ and \vec{p}^- , respectively.

The energy of an electric dipole in an electric field is

$$\mathbf{H}_{A-F} = -\vec{p} \cdot \vec{E}(\vec{x}_A, t). \quad (2.74)$$

The electric field at the position of the atom, \vec{x}_A , can be written as

$$\vec{E}(\vec{x}_A, t) = \frac{1}{2} \left(\vec{E}(t)^{(+)} + \vec{E}(t)^{(-)} \right) = \frac{1}{2} \left(\hat{E}(t)^{(+)} e^{j\omega t} + \hat{E}(t)^{(-)} e^{-j\omega t} \right), \quad (2.75)$$

where $\hat{E}(t)^{(\pm)}$ denotes the slowly varying complex field envelope with $\omega \approx \omega_{eg}$. In the Rotating-Wave Approximation (RWA), we only keep the slowly varying components in the interaction Hamiltonian. As we will see later, if there is no field the operator $\boldsymbol{\sigma}^+$ evolves like $\boldsymbol{\sigma}^+(t) = \boldsymbol{\sigma}^+(0) e^{j\omega_{eg}t}$, thus we obtain in RWA

$$\mathbf{H}_{A-F} = -\vec{p} \cdot \vec{E}(\vec{x}_A, t) \approx \quad (2.76)$$

$$\approx \mathbf{H}_{A-F}^{RWA} = \frac{1}{2} \vec{M}^* \vec{E}(t)^{(-)} \boldsymbol{\sigma}^+ + h.c.. \quad (2.77)$$

The Schrödinger Equation for the two-level atom in a classical field is then given by

$$j\hbar \frac{d}{dt} |\psi \rangle = (\mathbf{H}_A + \mathbf{H}_{A-F}) |\psi \rangle \quad (2.78)$$

$$\approx (\mathbf{H}_A + \mathbf{H}_{A-F}^{RWA}) |\psi \rangle. \quad (2.79)$$

Written in the energy representation, we obtain

$$\frac{d}{dt}c_e = -j\frac{\omega_{eg}}{2}c_e - j\Omega_r e^{-j\omega t}c_g, \quad (2.80)$$

$$\frac{d}{dt}c_g = +j\frac{\omega_{eg}}{2}c_g - j\Omega_r e^{+j\omega t}c_e, \quad (2.81)$$

with the Rabi-frequency defined as

$$\Omega_r = \frac{\vec{M}^* \hat{E}}{2\hbar}. \quad (2.82)$$

For the time being, we assume that the the Rabi-frequency is real. If this is not the case, a transformation including a phase shift in the amplitudes $c_{a,b}$ would be necessary to eliminate this phase. As expected the field couples the energy eigenstates.

2.3.3 Rabi-Oscillations

If the incident light has a constant field amplitude \hat{E} Eqs. (2.80) and (2.81) can be solved and we observe an oscillation in the population difference, the Rabi-oscillation [1]. To show this we introduce the detuning between field and atomic resonance

$$\Delta = \frac{\omega_{ab} - \omega}{2} \quad (2.83)$$

and the new probability amplitudes

$$C_e = c_e e^{j\frac{\omega}{2}t}, \quad (2.84)$$

$$C_g = c_g e^{-j\frac{\omega}{2}t}. \quad (2.85)$$

This leads to the new system of equations with constant coefficients

$$\frac{d}{dt}C_e = -j\Delta C_e - j\Omega_r C_g, \quad (2.86)$$

$$\frac{d}{dt}C_g = +j\Delta C_g - j\Omega_r C_e. \quad (2.87)$$

Note, these are coupling of mode equations in time. Now, the modes are electronic ones instead of photonic modes. But otherwise everything is the

same. For the case of vanishing detuning it is especially easy to eliminate one of the variables and we arrive at

$$\frac{d^2}{dt^2}C_e = -\Omega_r^2 C_e \quad (2.88)$$

$$\frac{d^2}{dt^2}C_g = -\Omega_r^2 C_g. \quad (2.89)$$

The solution to this set of equations are the oscillations we are looking for. If the atom is at time $t = 0$ in the ground-state, i.e. $C_g(0) = 1$ and $C_e(0) = 0$, respectively, we arrive at

$$C_g(t) = \cos(\Omega_r t) \quad (2.90)$$

$$C_e(t) = -j \sin(\Omega_r t). \quad (2.91)$$

Then, the probabilities for finding the atom in the ground or excited state are

$$|c_b(t)|^2 = \cos^2(\Omega_r t) \quad (2.92)$$

$$|c_a(t)|^2 = \sin^2(\Omega_r t), \quad (2.93)$$

as shown in Fig. 2.3. For the expectation value of the dipole operator under the assumption of a real dipole matrix element $\vec{M} = \vec{M}^*$ we obtain

$$\langle \vec{\mathbf{p}} \rangle = -\vec{M} c_e c_g^* + c.c. \quad (2.94)$$

$$= -\vec{M} \sin(2\Omega_r t) \sin(\omega_{eg} t). \quad (2.95)$$

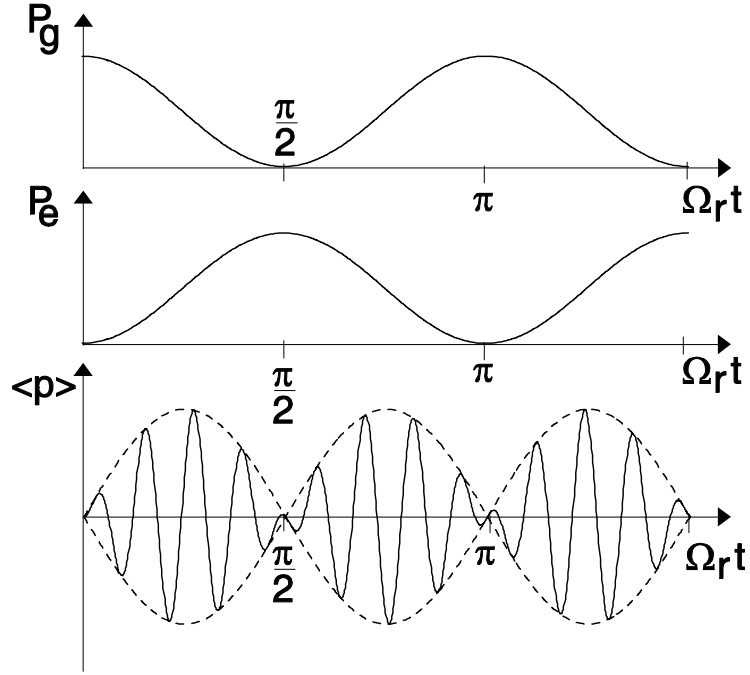


Figure 2.3: Evolution of occupation probabilities of ground and excited state and the average dipole moment of a two-level atom in resonant interaction with a coherent classical field.

The coherent external field drives the population of the atomic system between the two available states with a period $T_r = \pi/\Omega_r$. Applying the field only over half of this period leads to a complete inversion of the population. These Rabi-oscillations have been observed in various systems ranging from gases to semiconductors. Interestingly, the light emitted from the coherently driven two-level atom is not identical in frequency to the driving field. If we look at the Fourier spectrum of the polarization according to Eq.(2.95), we obtain lines at frequencies $\omega_{\pm} = \omega_{eg} \pm 2\Omega_r$. This is clearly a nonlinear output and the sidebands are called Mollow-sidebands [2]. Most important for the existence of these oscillations is the coherence of the atomic system over at least one Rabi-oscillation. If this coherence is destroyed fast enough, the Rabi-oscillations cannot happen and it is then impossible to generate inversion in a two-level system by interaction with light. This is the case for a large class of situations in light-matter interaction. So we are interested what happens in the case of loss of coherence due to additional interaction

of the atoms with a heat bath.

2.3.4 The Density Operator

To study incoherent or dissipative processes it is useful to switch to a statistical description using the density operator instead of deterministic wave functions similar to classical statistical mechanics, where the deterministic trajectories of particles are replaced by probability distributions.

The density operator of a pure state is defined by the dyadic product of the state with itself

$$\boldsymbol{\rho} = |\psi\rangle\langle\psi| \quad (2.96)$$

or in coordinate representation by a 2×2 -matrix

$$\boldsymbol{\rho} = \begin{pmatrix} \rho_{ee} & \rho_{eg} \\ \rho_{ge} & \rho_{gg} \end{pmatrix}. \quad (2.97)$$

In case of a pure state (2.46) this is

$$\boldsymbol{\rho} = \begin{pmatrix} c_e c_e^* & c_e c_g^* \\ c_g c_e^* & c_g c_g^* \end{pmatrix}. \quad (2.98)$$

It is obvious, that, for the rather simple case of a two-level system, each element of the density matrix corresponds to a physical quantity. The main diagonal contains the population probabilities for the levels and the off-diagonal element is the expectation value of the positive or negative frequency component of the dipole moment of the atom, i.e. its contribution to the medium polarization.

The expectation value of an arbitrary operator \mathbf{A} can be computed using the trace formula

$$\langle \mathbf{A} \rangle = \text{Tr}\{\boldsymbol{\rho}\mathbf{A}\} = \langle \psi|\mathbf{A}|\psi \rangle. \quad (2.99)$$

The advantage of the density operator is, that mixtures of pure states can also be treated in a statistical sense. For example, if the atom is in state $|e\rangle$ with probability p_e and in state $|g\rangle$ with probability p_g a density operator

$$\boldsymbol{\rho} = p_e |e\rangle\langle e| + p_g |g\rangle\langle g| \quad (2.100)$$

is defined, which can be used to compute the average values of observables in the proper statistical sense

$$\langle \mathbf{A} \rangle = \text{Tr}\{\boldsymbol{\rho}\mathbf{A}\} = p_e \langle e|\mathbf{A}|e \rangle + p_g \langle g|\mathbf{A}|g \rangle. \quad (2.101)$$

Since the matrices (2.64) to (2.67) build a complete base in the space of 2×2 -matrices, we can express the density matrix as

$$\boldsymbol{\rho} = \rho_{ee} \frac{1}{2}(\mathbf{1} + \boldsymbol{\sigma}_z) + \rho_{gg} \frac{1}{2}(\mathbf{1} - \boldsymbol{\sigma}_z) + \rho_{eg} \boldsymbol{\sigma}^+ + \rho_{ge} \boldsymbol{\sigma}^- \quad (2.102)$$

$$= \frac{1}{2} \mathbf{1} + \frac{1}{2}(\rho_{ee} - \rho_{gg}) \boldsymbol{\sigma}_z + \rho_{eg} \boldsymbol{\sigma}^+ + \rho_{ge} \boldsymbol{\sigma}^-, \quad (2.103)$$

since the trace of the density matrix is always one (normalization). Choosing the new base $\mathbf{1}, \boldsymbol{\sigma}_x, \boldsymbol{\sigma}_y, \boldsymbol{\sigma}_z$, we obtain

$$\boldsymbol{\rho} = \frac{1}{2} \mathbf{1} + \frac{1}{2}(\rho_{ee} - \rho_{gg}) \boldsymbol{\sigma}_z + d_x \boldsymbol{\sigma}_x + d_y \boldsymbol{\sigma}_y, \quad (2.104)$$

with

$$d_x = \frac{1}{2}(\rho_{eg} + \rho_{ge}) = \Re\{\langle \boldsymbol{\sigma}^{(+)} \rangle\}, \quad (2.105)$$

$$d_y = \frac{j}{2}(\rho_{eg} - \rho_{ge}) = \Im\{\langle \boldsymbol{\sigma}^{(+)} \rangle\}. \quad (2.106)$$

The expectation value of the dipole operator is given by (2.73)

$$\langle \vec{\mathbf{p}} \rangle = Tr\{\boldsymbol{\rho} \vec{\mathbf{p}}\} = -\vec{M}^* Tr\{\boldsymbol{\rho} \boldsymbol{\sigma}^+\} + c.c. = -\vec{M}^* \rho_{ge} + c.c. \quad (2.107)$$

From the Schrödinger equation for the wave function $|\psi\rangle$ we can easily derive the equation of motion for the density operator, called the von Neumann equation

$$\begin{aligned} \dot{\boldsymbol{\rho}} &= \frac{d}{dt} |\psi\rangle\langle\psi| + h.c. = \frac{1}{j\hbar} \mathbf{H} |\psi\rangle\langle\psi| - \frac{1}{j\hbar} |\psi\rangle\langle\psi| \mathbf{H} \quad (2.108) \\ &= \frac{1}{j\hbar} [\mathbf{H}, \boldsymbol{\rho}]. \end{aligned}$$

Due to the linear nature of the equation, this is also the correct equation for a density operator describing an arbitrary mixture of states. In case of a two-level atom, the von Neumann equation is

$$\dot{\boldsymbol{\rho}} = \frac{1}{j\hbar} [\mathbf{H}_A, \boldsymbol{\rho}] = -j \frac{\omega_{eg}}{2} [\boldsymbol{\sigma}_z, \boldsymbol{\rho}]. \quad (2.109)$$

Using the commutator relations (2.53) - (2.55), the result is

$$\dot{\rho}_{\in e} = 0, \quad (2.110)$$

$$\dot{\rho}_{gg} = 0, \quad (2.111)$$

$$\dot{\rho}_{eg} = -j\omega_{eg}\rho_{eg} \rightarrow \rho_{eg}(t) = e^{-j\omega_{eg}t}\rho_{eg}(0), \quad (2.112)$$

$$\dot{\rho}_{ge} = j\omega_{eg}\rho_{ge} \rightarrow \rho_{ge}(t) = e^{j\omega_{eg}t}\rho_{ge}(0). \quad (2.113)$$

Again the isolated two-level atom has a rather simple dynamics, the populations are constant, only the dipole moment oscillates with the transition frequency ω_{eg} , if there has been a dipole moment induced at $t = 0$, i.e. the system is in a superposition state.

2.3.5 Energy- and Phase-Relaxation

In reality, there is no isolated atom. Indeed in our case we are interested with a radiating atom, i.e. it has a dipole interaction with the field. The coupling with the infinitely many modes of the free field leads already to spontaneous emission, an irreversible process. We could treat this process by using the Hamiltonian

$$\mathbf{H} = \mathbf{H}_A + \mathbf{H}_F + \mathbf{H}_{A-F}. \quad (2.114)$$

Here, \mathbf{H}_A is the Hamiltonian of the atom, \mathbf{H}_F of the free field and \mathbf{H}_{A-F} describes the interaction between them. A complete treatment along these lines is beyond the scope of this class and is usually done in classes on Quantum Mechanics. But the result of this calculation is simple and leads in the von Neumann equation of the reduced density matrix, i.e. the density matrix of the atom. With the spontaneous emission rate $1/\tau_{sp}$, i.e. the inverse spontaneous life time τ_{sp} , the populations change according to

$$\frac{d}{dt}|c_e(t)|^2 = \frac{d}{dt}\rho_{ee} = -\Gamma_e\rho_{ee} + \Gamma_a\rho_{gg} \quad (2.115)$$

with the abbreviations

$$\Gamma_e = \frac{1}{\tau_{sp}}(n_{th} + 1), \quad (2.116)$$

$$\Gamma_a = \frac{1}{\tau_{sp}}n_{th}. \quad (2.117)$$

Here, n_{th} is the number of thermally excited photons in the modes of the free field with frequency ω_{eg} , $n_{th} = 1/(\exp(\hbar\omega_{eg}/kT) - 1)$, at temperature T .

The total probability of being in excited or ground state has to be maintained, that is

$$\frac{d}{dt}\rho_{gg} = -\frac{d}{dt}\rho_{ee} = \Gamma_e\rho_{ee} - \Gamma_a\rho_{gg}. \quad (2.118)$$

If the populations decay, so does the polarization too, since $\rho_{ge} = c_e^*c_g$, i.e.

$$\frac{d}{dt}\rho_{ge} = j\omega_{eg}\rho_{eg} - \frac{\Gamma_e + \Gamma_a}{2}\rho_{ge}. \quad (2.119)$$

Thus absorption as well as emission processes are also destructive to the phase, therefore, the corresponding rates add up in the phase decay rate.

Taking the coherent (2.113) and incoherent processes (2.118-2.119) into account results in the following equations for the normalized average dipole moment $d = d_x + jd_y$ and the inversion w

$$\dot{d} = \dot{\rho}_{ge} = (j\omega_{eg} - \frac{1}{T_2})d, \quad (2.120)$$

$$\dot{w} = \dot{\rho}_{ee} - \dot{\rho}_{gg} = -\frac{w - w_0}{T_1}, \quad (2.121)$$

with the time constants

$$\frac{1}{T_1} = \frac{2}{T_2} = \Gamma_e + \Gamma_a = \frac{2n_{th} + 1}{\tau_{sp}} \quad (2.122)$$

and equilibrium inversion w_0 , due to the thermal excitation of the atom by the thermal field

$$w_0 = \frac{\Gamma_a - \Gamma_e}{\Gamma_a + \Gamma_e} = \frac{-1}{1 + 2n_{th}} = -\tanh\left(\frac{\hbar\omega_{eg}}{2kT}\right). \quad (2.123)$$

The time constant T_1 denotes the energy relaxation in the two-level system and T_2 the phase relaxation. T_2 is the correlation time between amplitudes c_e and c_g . This coherence is destroyed by the interaction of the two-level system with the environment. In this model the energy relaxation is half the phase relaxation rate or

$$T_2 = 2T_1. \quad (2.124)$$

The atoms in a laser medium do not only interact with the electromagnetic field, but in addition also with phonons of the host lattice, they might collide with each other in a gas laser and so on. All these processes must be

considered when determining the energy and phase relaxation rates. Some of these processes are only destroying the phase, but do actually not lead to an energy loss in the system. Therefore, these processes reduce T_2 but have no influence on T_1 . In real systems the phase relaxation time is most often much shorter than twice the energy relaxation time,

$$T_2 \leq 2T_1. \quad (2.125)$$

If the inversion deviates from its equilibrium value w_0 it relaxes back into equilibrium with a time constant T_1 . Eq. (2.123) shows that for all temperatures $T > 0$ the inversion is negative, i.e. the lower level is stronger populated than the upper level. Thus with incoherent thermal light inversion in a two-level system cannot be achieved. Inversion can only be achieved by pumping with incoherent light, if there are more levels and subsequent relaxation processes into the upper laser level. Due to these relaxation processes the rate Γ_a deviates from the equilibrium expression (2.117), and it has to be replaced by the pump rate Λ . If the pump rate Λ exceeds Γ_e , the inversion corresponding to Eq. (2.123) becomes positive,

$$w_0 = \frac{\Lambda - \Gamma_e}{\Lambda + \Gamma_e}. \quad (2.126)$$

If we allow for artificial negative temperatures, we obtain with $T < 0$ for the ratio of relaxation rates

$$\frac{\Gamma_e}{\Gamma_a} = \frac{1 + \bar{n}}{\bar{n}} = e^{\frac{\hbar\omega_{eg}}{kT}} < 1. \quad (2.127)$$

Thus the pumping of the two-level system drives the system far away from thermal equilibrium, which has to be expected.

2.3.6 The Two-Level Atom with a Coherent Classical External Field

If there is in addition to the coupling to an external heat bath, which models the spontaneous decay, pumping, and other incoherent processes, a coherent external field, the Hamiltonian has to be extended by the dipole interaction with that field,

$$\mathbf{H}_E = -\vec{\mathbf{p}}\vec{E}(\vec{x}_A, t). \quad (2.128)$$

Again we use the interaction Hamiltonian in RWA

$$\mathbf{H}_E = \frac{1}{2} \vec{M}^* \vec{E}(t)^{(-)} \sigma^+ + h.c.. \quad (2.129)$$

This leads in the von Neumann equation to the additional term

$$\dot{\rho}|_E = \frac{1}{j\hbar} [H_E, \rho] \quad (2.130)$$

$$= \frac{1}{2j\hbar} \vec{M}^* \vec{E}(t)^{(-)} [\sigma^+, \rho] + h.c.. \quad (2.131)$$

or

$$\dot{\rho}_{ee}|_E = \frac{1}{2j\hbar} \vec{M}^* \vec{E}^{(-)} \rho_{ge} + c.c., \quad (2.132)$$

$$\dot{\rho}_{ge}|_E = \frac{1}{2j\hbar} \vec{M} \vec{E}^{(+)} (\rho_{ee} - \rho_{gg}), \quad (2.133)$$

$$\dot{\rho}_{gg}|_E = -\frac{1}{2j\hbar} \vec{M}^* \vec{E}^{(-)} \rho_{ge} + c.c.. \quad (2.134)$$

The evolution of the dipole moment and the inversion is changed by

$$\dot{d}|_E = \dot{\rho}_{ge}|_E = \frac{1}{2j\hbar} \vec{M} \vec{E}^{(+)} w, \quad (2.135)$$

$$\dot{w}|_E = \dot{\rho}_{ee}|_E - \dot{\rho}_{gg}|_E = \frac{1}{j\hbar} (\vec{M}^* \vec{E}^{(-)} d^* - \vec{M} \vec{E}^{(+)} d). \quad (2.136)$$

Thus, the total dynamics of the two-level system including the pumping and dephasing processes from Eqs.(2.120) and (2.121) is given by

$$\dot{d} = -\left(\frac{1}{T_2} - j\omega_{eg}\right)d + \frac{1}{2j\hbar} \vec{M} \vec{E}^{(+)} w, \quad (2.137)$$

$$\dot{w} = -\frac{w - w_0}{T_1} + \frac{1}{j\hbar} (\vec{M}^* \vec{E}^{(-)} d - \vec{M} \vec{E}^{(+)} d^*). \quad (2.138)$$

These equations are called Bloch-equations. They describe the dynamics of an atom interacting with a classical electric field. Together with Eq. (2.7) they build the Maxwell-Bloch equations.

2.4 Dielectric Susceptibility

If the incident field is monofrequent, i.e.

$$\vec{E}(t)^{(+) = \hat{E}e^{j\omega t}, \quad (2.139)$$

and assuming that the inversion w of the atom will be well represented by its time average w_s , then the dipole moment will oscillate with the same frequency in the stationary state

$$d = \hat{d}e^{j\omega t}, \quad (2.140)$$

and the inversion will adjust to a new stationary value w_s . With ansatz (2.139) and (2.140) in Eqs. (2.137) and (2.138), we obtain

$$\hat{d} = \frac{-j}{2\hbar} \frac{w_s}{1/T_2 + j(\omega - \omega_{eg})} \vec{M} \hat{E}, \quad (2.141)$$

$$w_s = \frac{w_0}{1 + \frac{T_1}{\hbar^2} \frac{1/T_2 |\vec{M} \hat{E}|^2}{(1/T_2)^2 + (\omega_{eg} - \omega)^2}}. \quad (2.142)$$

We introduce the normalized lineshape function, which is in this case a Lorentzian,

$$L(\omega) = \frac{(1/T_2)^2}{(1/T_2)^2 + (\omega_{eg} - \omega)^2}, \quad (2.143)$$

and connect the square of the field $|\hat{E}|^2$ to the intensity I of a propagating plane wave, according to Eq. (2.32), $I = \frac{1}{2Z_F} |\hat{E}|^2$,

$$w_s = \frac{w_0}{1 + \frac{I}{I_s} L(\omega)}. \quad (2.144)$$

Thus the stationary inversion depends on the intensity of the incident light, therefore, w_0 can be called the unsaturated inversion, w_s the saturated inversion and I_s , with

$$I_s = \left[\frac{2T_1 T_2 Z_F}{\hbar^2} \frac{|\vec{M} \hat{E}|^2}{|\hat{E}|^2} \right]^{-1}, \quad (2.145)$$

is the saturation intensity. The expectation value of the dipole operator is then given by

$$\langle \vec{p} \rangle = -(\vec{M}^* d + \vec{M} d^*). \quad (2.146)$$

Multiplication with the number of atoms per unit volume N relates the dipole moment of the atom to the complex polarization $\hat{\vec{P}}^+$ of the medium, and therefore to the susceptibility according to

$$\hat{\vec{P}}^{(+)} = -2N\vec{M}^*\hat{d}, \quad (2.147)$$

$$\hat{\vec{P}}^{(+)} = \epsilon_0\chi(\omega)\hat{\vec{E}}. \quad (2.148)$$

From the definitions (2.147), (2.148) and Eq. (2.141) we obtain for the linear susceptibility of the medium

$$\chi(\omega) = \vec{M}^*\vec{M}^T \frac{jN}{\hbar\epsilon_0} \frac{w_s}{1/T_2 + j(\omega - \omega_{eg})}, \quad (2.149)$$

which is a tensor. In the following we assume that the direction of the atom is random, i.e. the alignment of the atomic dipole moment \vec{M} and the electric field is random. Therefore, we have to average over the angle enclosed between the electric field of the wave and the atomic dipole moment, which results in

$$\overline{\begin{pmatrix} M_x M_x & M_x M_y & M_x M_z \\ M_y M_x & M_y M_y & M_y M_z \\ M_z M_x & M_z M_y & M_z M_z \end{pmatrix}} = \begin{pmatrix} \overline{M_x^2} & 0 & 0 \\ 0 & \overline{M_y^2} & 0 \\ 0 & 0 & \overline{M_z^2} \end{pmatrix} = \frac{1}{3}|\vec{M}|^2 \mathbf{1}. \quad (2.150)$$

Thus, for homogeneous and isotropic media the susceptibility tensor shrinks to a scalar

$$\chi(\omega) = \frac{1}{3}|\vec{M}|^2 \frac{jN}{\hbar\epsilon_0} \frac{w_s}{1/T_2 + j(\omega - \omega_{eg})}. \quad (2.151)$$

Real and imaginary part of the susceptibility

$$\chi(\omega) = \chi'(\omega) + j\chi''(\omega) \quad (2.152)$$

are then given by

$$\chi'(\omega) = -\frac{|\vec{M}|^2 N w_s T_2^2 (\omega_{eg} - \omega)}{3\hbar\epsilon_0} L(\omega), \quad (2.153)$$

$$\chi''(\omega) = \frac{|\vec{M}|^2 N w_s T_2}{3\hbar\epsilon_0} L(\omega). \quad (2.154)$$

If the incident radiation is weak enough, i.e.

$$T_1 T_2 \frac{|\vec{M}^* \hat{E}|^2}{\hbar^2} L(\omega) \ll 1 \quad (2.155)$$

we obtain $w_s \approx w_0$. Since $w_0 < 0$, and especially for optical transitions $w_0 = -1$, real and imaginary part of the susceptibility are shown in Fig. 2.4.

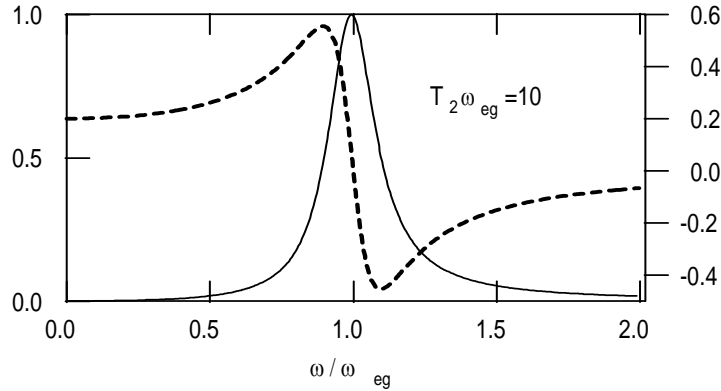


Figure 2.4: Real and imaginary part of the complex susceptibility.

The susceptibility computed quantum mechanically compares well with the classical susceptibility derived from the harmonic oscillator model close to the transition frequency for a transition with reasonably high $Q = T_2 \omega_{ab}$. Note, there is an appreciable deviation far away from resonance. Far off resonance the rotating wave approximation should not be used.

The physical meaning of the real and imaginary part of the susceptibility becomes obvious, when the propagation of a plane electro-magnetic wave through this medium is considered,

$$\vec{E}(z, t) = \Re \left\{ \hat{E} e^{j(\omega t - kz)} \right\}, \quad (2.156)$$

which is propagating in the positive z -direction. The propagation constant k is related to the susceptibility by

$$k = \omega \sqrt{\mu_0 \epsilon_0 (1 + \chi(\omega))} \approx k_0 \left(1 + \frac{1}{2} \chi(\omega) \right), \quad \text{with } k_0 = \omega \sqrt{\mu_0 \epsilon_0} \quad (2.157)$$

for $|\chi| \ll 1$. Under this assumption we obtain

$$k = k_0 \left(1 + \frac{\chi'}{2}\right) + jk_0 \frac{\chi''}{2}. \quad (2.158)$$

The real part of the susceptibility contributes to the refractive index $n = 1 + \chi'/2$. In case of $\chi'' < 0$, the imaginary part leads to an exponential damping of the wave. For $\chi'' > 0$ amplification takes place. Amplification of the wave is possible for $w_0 > 0$, i.e. an inverted medium.

The phase relaxation rate $1/T_2$ of the dipole moment determines the width of the absorption line or the bandwidth of the amplifier.

2.5 Rate Equations

With the wave equation Eq.(2.7) and the expression for the polarization induced by the electric field of the wave, we end up with the complete Maxwell-Bloch equations describing an electromagnetic field interacting with a statistical ensemble of atoms that are located at positions z_i

$$\left(\Delta - \frac{1}{c_0^2} \frac{\partial^2}{\partial t^2}\right) \vec{E}^{(+)}(z, t) = \mu_0 \frac{\partial^2}{\partial t^2} \vec{P}^{(+)}(z, t), \quad (2.159)$$

$$\vec{P}^{(+)}(z, t) = -2N \vec{M}^* d(z, t) \quad (2.160)$$

$$\dot{d}(z, t) = -\left(\frac{1}{T_2} - j\omega_{eg}\right)d + \frac{1}{2j\hbar} \vec{M} \vec{E}^{(+)} w, \quad (2.161)$$

$$\dot{w}(z, t) = -\frac{w - w_0}{T_1} + \frac{1}{j\hbar} (\vec{M}^* \vec{E}^{(-)} d - \vec{M} \vec{E}^{(+)} d) \quad (2.162)$$

In the following we consider a electromagnetic wave with polarization vector \vec{e} , frequency ω_{eg} and wave number $k_0 = \omega_{eg}/c_0$ with a slowly varying envelope propagating to the right

$$\vec{E}(z, t)^{(+)} = \sqrt{2Z_{F_0}} A(z, t) e^{j(\omega_{eg}t - k_0z)} \vec{e}, \quad (2.163)$$

with

$$\left| \frac{\partial A(z, t)}{\partial t} \right|, \left| c \frac{\partial A(z, t)}{\partial z} \right| \ll |\omega_{eg} A(z, t)|. \quad (2.164)$$

Note, we normalized the complex amplitude $A(t)$ such that its magnitude square is proportional to the intensity of the wave. This will also excite a wave of dipole moments in the atomic medium according to

$$d(z, t) = \hat{d}(z, t) e^{j(\omega_{eg}t - k_0z)}, \quad (2.165)$$

that is also slowly varying. In that case, we obtain from Eq.(2.159-d) in leading order

$$\left(\frac{\partial}{\partial z} + \frac{1}{c_0} \frac{\partial}{\partial t}\right) A(z, t) = jN\vec{e}^T \vec{M}^* \sqrt{\frac{Z_{F_0}}{2}} \hat{d}(z, t), \quad (2.166)$$

$$\frac{\partial}{\partial t} d(z, t) = -\frac{1}{T_2} \hat{d} + \frac{\sqrt{2Z_{F_0}}}{2j\hbar} (\vec{M}\vec{e}) A(t)w \quad (2.167)$$

$$\frac{\partial}{\partial t} w(z, t) = -\frac{w - w_0}{T_1} + \frac{\sqrt{2Z_{F_0}}}{j\hbar} ((\vec{M}^* \vec{e}^*) A^*(t) \hat{d} - (\vec{M}\vec{e}) A(t) \hat{d}) \quad (2.168)$$

Furthermore, in the limit, where the dephasing time T_2 is much faster than the variation in the envelope of the electric field, one can adiabatically eliminate the rapidly decaying dipole moment, i.e.

$$\hat{d} = T_2 \frac{\sqrt{2Z_{F_0}}}{2j\hbar} (\vec{M}\vec{e}) A(t)w, \quad (2.169)$$

$$\dot{w} = -\frac{w - w_0}{T_1} + \frac{|A(t)|^2}{E_s} w, \quad (2.170)$$

where $E_s = I_s T_1$, is called the saturation fluence, $[J/cm^2]$, of the medium.

Note, now we don't have to care anymore about the dipole moment and we are left over with a rate equation for the population difference of the medium and the complex field amplitude of the wave.

$$\left(\frac{\partial}{\partial z} + \frac{1}{c_0} \frac{\partial}{\partial t}\right) A(z, t) = \frac{N\hbar}{4T_2 E_s} w(z, t) A(z, t), \quad (2.171)$$

$$\dot{w} = -\frac{w - w_0}{T_1} + \frac{|A(z, t)|^2}{E_s} w(z, t) \quad (2.172)$$

Equation (2.171) clearly shows that we obtain gain for an inverted medium and that the gain saturates with the electromagnetic power density flowing through the medium.

2.6 Pulse Propagation with Dispersion and Gain

In many cases, mode locking of lasers can be most easily studied in the time domain. Then mode locking becomes a nonlinear, dissipative wave propaga-

tion problem. In this chapter, we discuss the basic elements of pulse propagation in linear and nonlinear media, as far as it is necessary for the following chapters. A comprehensive discussion of nonlinear pulse propagation can be found in [6].

We consider the electric field of a monochromatic electromagnetic wave with frequency Ω , which propagates along the z -axis, and is polarized along the x -axis, (Fig. 2.5).

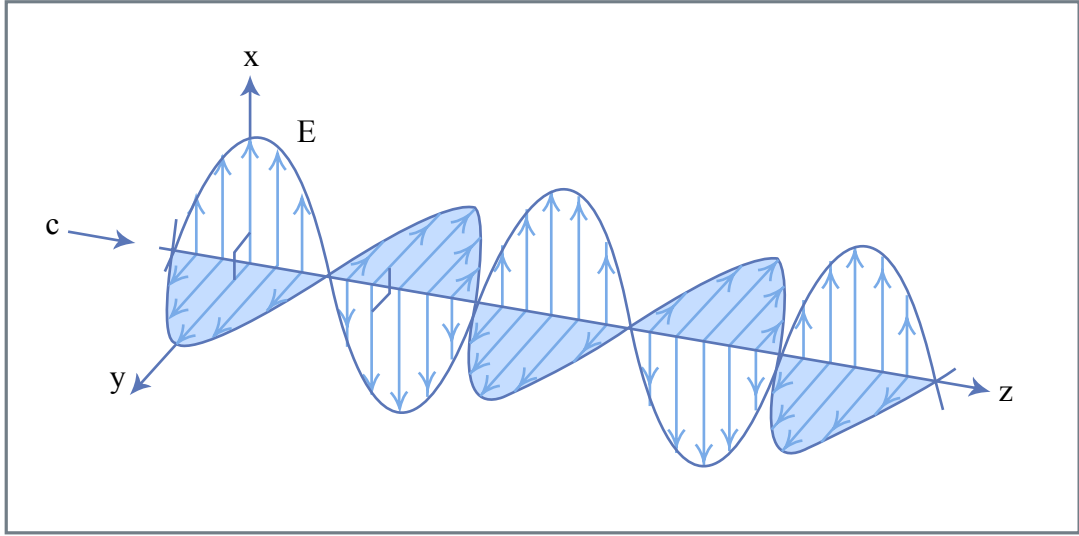


Figure 2.5: Transverse electro-magnetic wave.

Figure by MIT OCW.

In a linear, isotropic, homogeneous, and lossless medium the electric field of that electromagnetic wave is given by

$$\begin{aligned}\vec{E}(z, t) &= \vec{e}_x E(z, t), \\ E(z, t) &= \Re \left\{ \tilde{E}(\Omega) e^{j(\Omega t - Kz)} \right\} \\ &= |\tilde{E}| \cos(\Omega t - Kz + \varphi),\end{aligned}\tag{2.173}$$

where $\tilde{E} = |\tilde{E}|e^{j\varphi}$ is the complex wave amplitude of the electromagnetic wave at frequency Ω and wave number $K = \Omega/c = n\Omega/c_0$. Here, n is the refractive index, c the velocity of light in the medium and c_0 the velocity of light in vacuum, respectively. The planes of constant phase propagate with the phase velocity c of the wave. Usually, we have a superposition of many frequencies with spectrum shown in Fig. 2.6

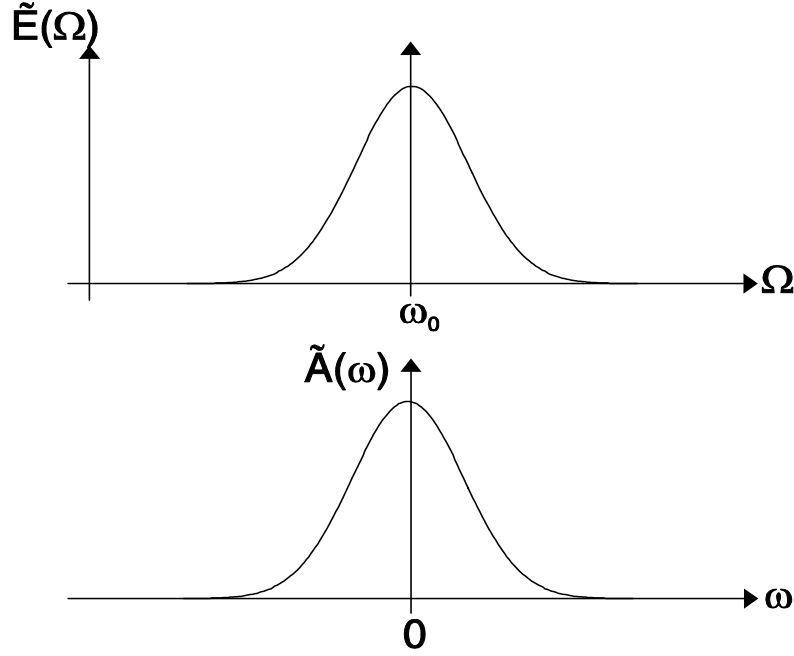


Figure 2.6: Electric field and pulse envelope in frequency domain.

In general, the refractive index is a function of frequency and one is interested in the propagation of a pulse, that is produced by a superposition of monochromatic waves grouped around a certain carrier frequency ω_0 (Fig. 2.6)

$$E(z, t) = \Re \left\{ \frac{1}{2\pi} \int_0^\infty \tilde{E}(\Omega) e^{j(\Omega t - K(\Omega)z)} d\Omega \right\}. \quad (2.174)$$

We can always separate the complex electric field in Eq. (2.174) into a carrier wave and an envelope $A(z, t)$

$$E(z, t) = \Re \left\{ A(z, t) e^{j(\omega_0 t - K(\omega_0)z)} \right\}. \quad (2.175)$$

The envelope is given by

$$A(z, t) = \frac{1}{2\pi} \int_{-\omega_0 \rightarrow -\infty}^{\infty} \tilde{A}(\omega) e^{j(\omega t - k(\omega)z)} d\omega, \quad (2.176)$$

where we introduced the offset frequency, offset wave vector and spectrum of

the envelope

$$\omega = \Omega - \omega_0, \quad (2.177)$$

$$k(\omega) = K(\omega_0 + \omega) - K(\omega_0), \quad (2.178)$$

$$\tilde{A}(\omega) = \tilde{E}(\Omega = \omega_0 + \omega), \quad (2.179)$$

(see Fig. 2.8).

Depending on the dispersion relation, the pulse will be reshaped during propagation.

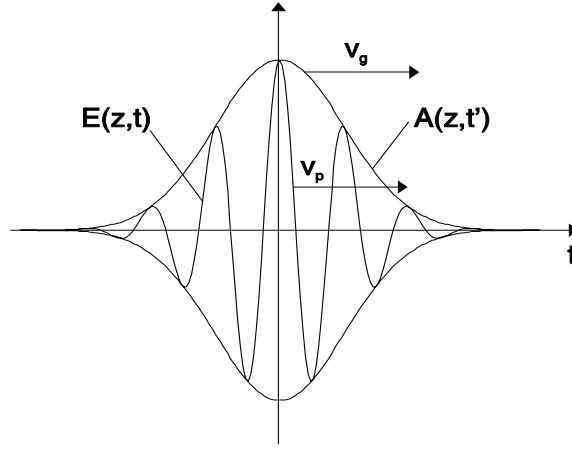


Figure 2.7: Electric field and pulse envelope in time domain.

2.6.1 Dispersion

If the spectral width of the pulse is small compared to the carrier frequency, the envelope is only slowly varying with time. Additionally, if the dispersion relation $k(\omega)$ is only slowly varying over the pulse spectrum, it is useful to represent the dispersion relation, $K(\Omega)$, see Fig. 2.8, by its Taylor expansion

$$k(\omega) = k'\omega + \frac{k''}{2}\omega^2 + \frac{k^{(3)}}{6}\omega^3 + O(\omega^4). \quad (2.180)$$

If the refractive index depends on frequency, the dispersion relation is no longer linear with respect to frequency, see Fig. 2.8.

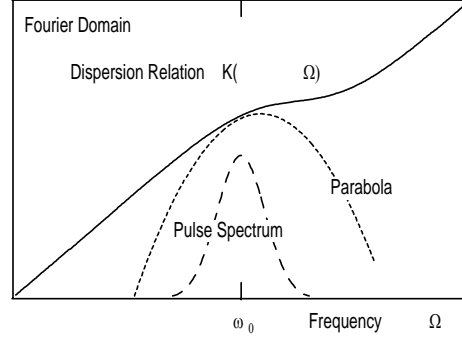


Figure 2.8: Taylor expansion of dispersion relation.

For the moment, we keep only the first term, the linear term, in Eq.(2.180). Then we obtain for the pulse envelope from (2.176) by definition of the group velocity $v_g = 1/k'$

$$A(z, t) = A(0, t - z/v_g). \quad (2.181)$$

Thus the derivative of the dispersion relation at the carrier frequency determines the velocity of the corresponding wave packet. We introduce the local time $t' = t - z/v_g$. With respect to this local time the pulse shape is invariant during propagation

$$A(z, t') = A(0, t'). \quad (2.182)$$

If the spectrum of the pulse becomes broad enough, so that the second order term in (2.180) becomes important, wave packets with different carrier frequencies propagate with different group velocities and the pulse spreads. When keeping in the dispersion relation terms up to second order it follows from (2.176)

$$\frac{\partial A(z, t')}{\partial z} = -j \frac{k''}{2} \frac{\partial^2 A(z, t')}{\partial t'^2}. \quad (2.183)$$

This is equivalent to the Schrödinger equation for a nonrelativistic free particle. Like in Quantum Mechanics, it describes the spreading of a wave packet. Here, the spreading is due to the first nontrivial term in the dispersion relation, which describes spreading of an electromagnetic wave packet via group velocity dispersion (GVD). Of course, we can keep all terms in the dispersion relation, which would lead to higher order derivatives in the equation for the

envelope

$$\frac{\partial A(z, t')}{\partial z} = j \sum_{n=2}^{\infty} \frac{k^{(n)}}{n!} \left(j \frac{\partial}{\partial t'} \right)^n A(z, t'). \quad (2.184)$$

Therefore, one usually calls the first term dispersion and the higher order terms higher order dispersion. In the following, we always work in the local time frame to get rid of the trivial motion of the pulse. Therefore, we drop the prime to simplify notation. Figure 2.9 shows the evolution of a Gaussian wave packet during propagation in a medium which has no higher order dispersion and $k'' = 2$ is given in normalized units. The pulse spreads continuously.

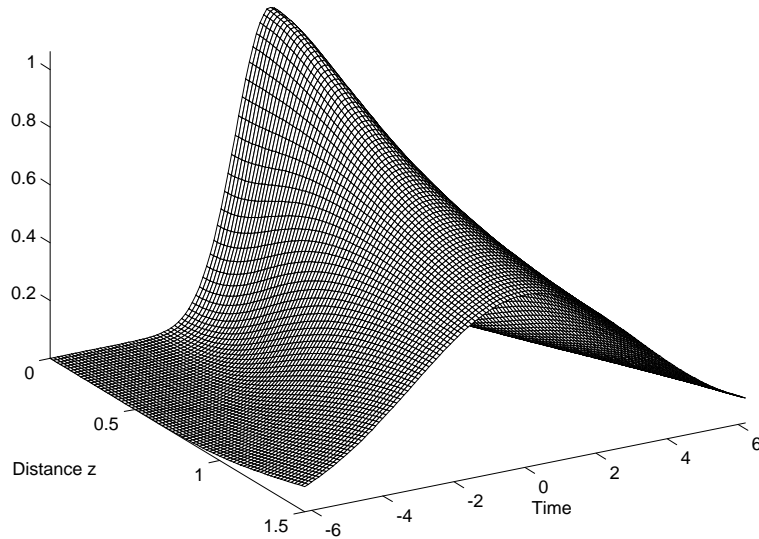


Figure 2.9: Amplitude of the envelope of a Gaussian pulse, $|A(z, t)|$, in a dispersive medium.

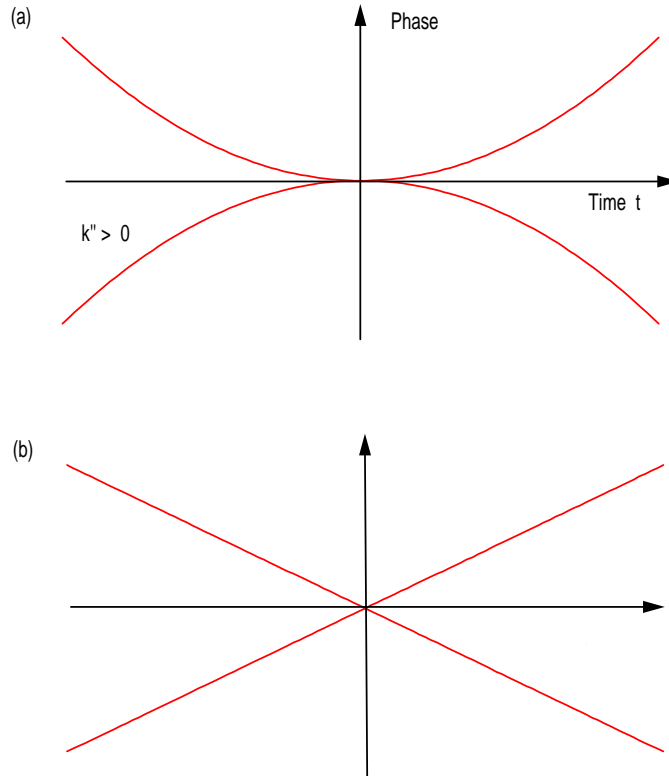


Figure 2.10: (a) Phase and (b) instantaneous frequency of a Gaussian pulse during propagation through a medium with positive or negative dispersion.

As shown in Fig. 2.10(a), during propagation in the dispersive medium, the pulse acquires a linear chirp, i.e. its phase becomes parabolic. The derivative of the phase with respect to time is the instantaneous frequency Fig. 2.10(b). It indicates, that the low frequencies are in the front of the pulse, whereas the high frequencies are in the back of the pulse. This is due to the positive dispersion $k'' > 0$, which causes, that wave packets with lower frequencies travel faster than wave packets with higher frequencies.

2.6.2 Loss and Gain

If the medium considered has loss, we can incorporate this loss into a complex refractive index

$$n(\Omega) = n_r(\Omega) + jn_i(\Omega). \quad (2.185)$$

The refractive index is determined by the linear response, $\chi(\Omega)$, of the polarization in the medium onto the electric field induced in the medium

$$n(\Omega) = \sqrt{1 + \chi(\Omega)}. \quad (2.186)$$

For an optically thin medium, i.e. $|\chi(\Omega)| \ll 1$ we obtain approximately

$$n(\Omega) \approx 1 + \frac{\chi(\Omega)}{2}. \quad (2.187)$$

For a two level atom with an electric dipole transition, the susceptibility is given, in the rotating wave approximation, by the complex Lorentzian lineshape

$$\chi(\Omega) = \frac{2j\alpha}{1 - j\frac{\Omega - \Omega_0}{\Delta\Omega}}, \quad (2.188)$$

where α will turn out to be the peak absorption or gain of the transition, which is proportional to the density of the atomic inversion, Ω_0 is the center frequency of the optical transition and $\Delta\Omega$ is the HWHM linewidth of the transition. Figure 2.11 shows the normalized real and imaginary part of the complex Lorentzian

$$\chi_r(\Omega) = \frac{-2\alpha\frac{(\Omega - \Omega_0)}{\Delta\Omega}}{1 + \left(\frac{\Omega - \Omega_0}{\Delta\Omega}\right)^2}, \quad (2.189)$$

$$\chi_i(\Omega) = \frac{2\alpha}{1 + \left(\frac{\Omega - \Omega_0}{\Delta\Omega}\right)^2}, \quad (2.190)$$

which are the real- and imaginary part of the complex susceptibility for a noninverted optical transition, i.e. loss.

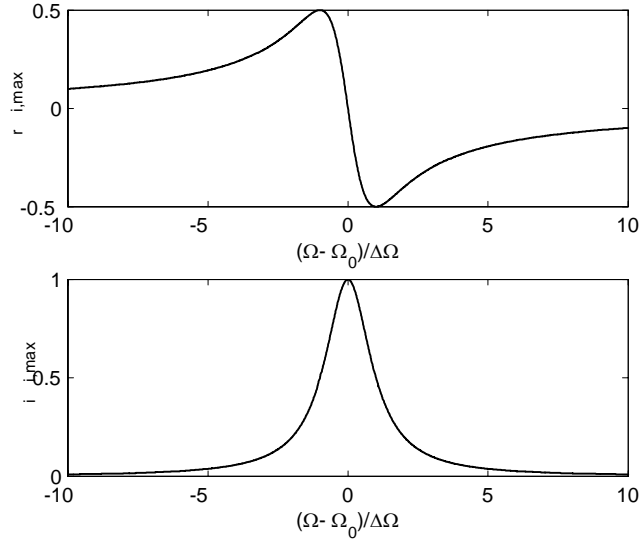


Figure 2.11: Normalized real and imaginary part of the complex Lorentzian.

The real part of the transition modifies the real part of the refractive index of the medium, whereas the imaginary part leads to loss in the case of a noninverted medium.

In the derivation of the wave equation for the pulse envelope (2.184) in section 2.6.1, there was no restriction to a real refractive index. Therefore, the wave equation (2.184) also treats the case of a complex refractive index. If we assume a medium with the complex refractive index (2.187), then the wave number is given by

$$K(\Omega) = \frac{\Omega}{c_0} \left(1 + \frac{1}{2} (\chi_r(\Omega) + j\chi_i(\Omega)) \right). \quad (2.191)$$

Since we introduced a complex wave number, we have to redefine the group velocity as the inverse derivative of the real part of the wave number with respect to frequency. At line center, we obtain

$$v_g^{-1} = \left. \frac{\partial K_r(\Omega)}{\partial \Omega} \right|_{\Omega_0} = \frac{1}{c_0} \left(1 - \alpha \frac{\Omega_0}{\Delta\Omega} \right). \quad (2.192)$$

Thus, for a narrow absorption line, $\alpha > 0$ and $\frac{\Omega_0}{\Delta\Omega} \gg 1$, the absolute value of the group velocity can become much larger than the velocity of light in

vacuum. The opposite is true for an inverted, and therefore, amplifying transition, $\alpha < 0$. There is nothing wrong with it, since the group velocity only describes the motion of the peak of a Gaussian wave packet, which is not a causal wave packet. A causal wave packet is identical to zero for some earlier time $t < t_0$, in some region of space. A Gaussian wave packet fills the whole space at any time and can be reconstructed by a Taylor expansion at any time. Therefore, the tachionic motion of the peak of such a signal does not contradict special relativity.

The imaginary part in the wave vector (2.191), due to gain and loss, has to be completely treated in the envelope equation (2.184). In the frequency domain this leads for a wave packet with a carrier frequency at line center, $\omega_0 = \Omega_0$ and $K_r(\Omega_0) = k_0$, to the term

$$\left. \frac{\partial \tilde{A}(z, \omega)}{\partial z} \right|_{(loss)} = \frac{-\alpha k_0}{1 + \left(\frac{\omega}{\Delta\Omega}\right)^2} \tilde{A}(z, \omega). \quad (2.193)$$

In the time domain, we obtain up to second order in the inverse linewidth

$$\left. \frac{\partial A(z, t)}{\partial z} \right|_{(loss)} = -\alpha k_0 \left(1 + \frac{1}{\Delta\Omega^2} \frac{\partial^2}{\partial t^2} \right) A(z, t), \quad (2.194)$$

which corresponds to a parabolic approximation of the Lorentzian line shape at line center, (Fig. 2.11). For an inverted optical transition, we obtain a similar equation, we only have to replace the loss by gain

$$\left. \frac{\partial A(z, t)}{\partial z} \right|_{(gain)} = g \left(1 + \frac{1}{\Omega_g^2} \frac{\partial^2}{\partial t^2} \right) A(z, t), \quad (2.195)$$

where $g = -\alpha k_0$ is the peak gain at line center per unit length and Ω_g is the HWHM linewidth of the gain transition. The gain is proportional to the inversion in the atomic system, see Eq.(2.149), which also depends on the field strength or intensity according to the rate equation (2.172)

$$\frac{\partial g(z, t)}{\partial t} = -\frac{g - g_0}{\tau_L} - g \frac{|A(z, t)|^2}{E_L}. \quad (2.196)$$

Here, E_L is the saturation fluence of the gain medium and τ_L the life time of the inversion, i.e. the upper-state life time of the gain medium.

	Fused Quartz	Sapphire
a_1	0.6961663	1.023798
a_2	0.4079426	1.058364
a_3	0.8974794	5.280792
λ_1^2	$4.679148 \cdot 10^{-3}$	$3.77588 \cdot 10^{-3}$
λ_2^2	$1.3512063 \cdot 10^{-2}$	$1.22544 \cdot 10^{-2}$
λ_3^2	$0.9793400 \cdot 10^2$	$3.213616 \cdot 10^2$

Table 2.1: Table with Sellmeier coefficients for fused quartz and sapphire.

2.7 Kramers-Kroenig Relations

The linear susceptibility is the frequency response of a linear system to an applied electric field, which is causal, and therefore real and imaginary parts obey Kramers-Kroenig Relations

$$\chi_r(\Omega) = \frac{2}{\pi} \int_0^{\infty} \frac{\omega \chi_i(\omega)}{\omega^2 - \Omega^2} d\omega = n^2(\Omega) - 1, \quad (2.197)$$

$$\chi_i(\Omega) = -\frac{2}{\pi} \int_0^{\infty} \frac{\Omega \chi_r(\omega)}{\omega^2 - \Omega^2} d\omega. \quad (2.198)$$

In transparent media one is operating far away from resonances. Then the absorption or imaginary part of the susceptibility can be approximated by

$$\chi_i(\Omega) = \sum_i A_i \delta(\omega - \omega_i) \quad (2.199)$$

and the Kramers-Kroenig relation results in a Sellmeier Equation for the refractive index

$$n^2(\Omega) = 1 + \sum_i A_i \frac{\omega_i}{\omega_i^2 - \Omega^2} \quad (2.200)$$

$$= 1 + \sum_i a_i \frac{\lambda}{\lambda^2 - \lambda_i^2}. \quad (2.201)$$

For an example Table 2.1 shows the sellmeier coefficients for fused quartz and sapphire.

A typical situation for a material having resonances in the UV and IR, such as glass, is shown in Fig. 2.12

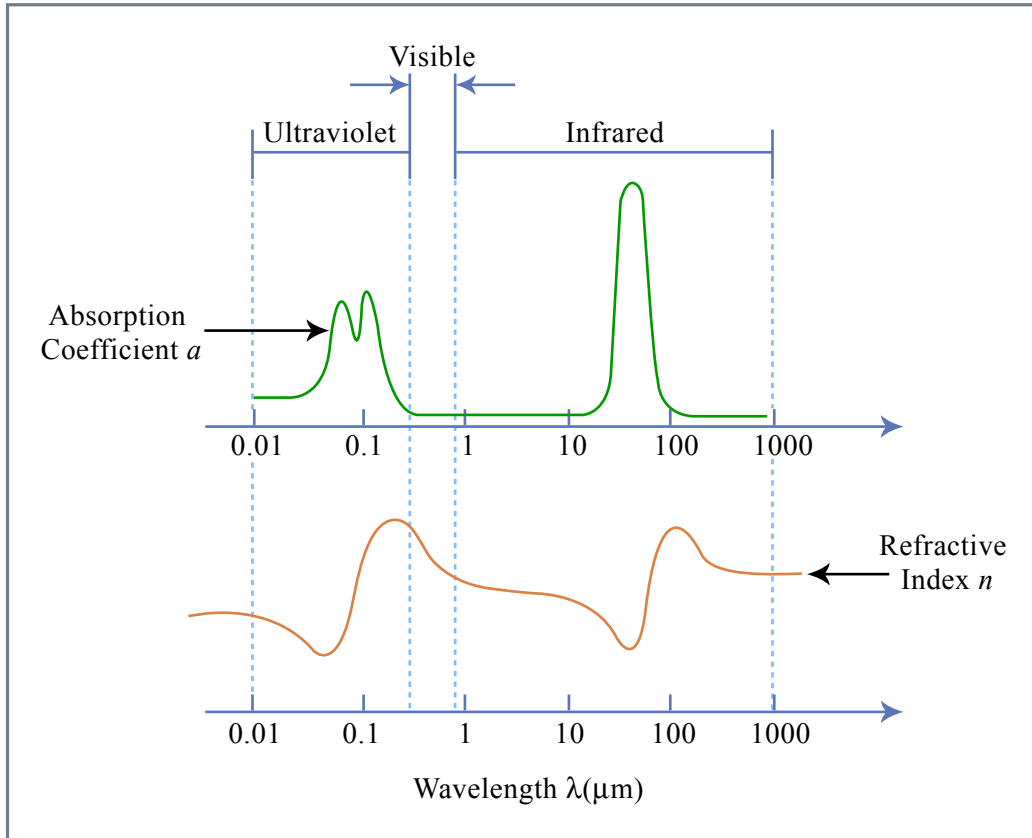


Figure 2.12: Typical distribution of absorption lines in a medium transparent in the visible.

Figure by MIT OCW.

The regions where the refractive index is decreasing with wavelength is usually called normal dispersion range and the opposite behavior anomalous dispersion

$$\frac{dn}{d\lambda} < 0 : \text{normal dispersion (blue refracts more than red)}$$

$$\frac{dn}{d\lambda} > 0 : \text{abnormal dispersion}$$

Fig.2.13 shows the transparency range of some often used media.

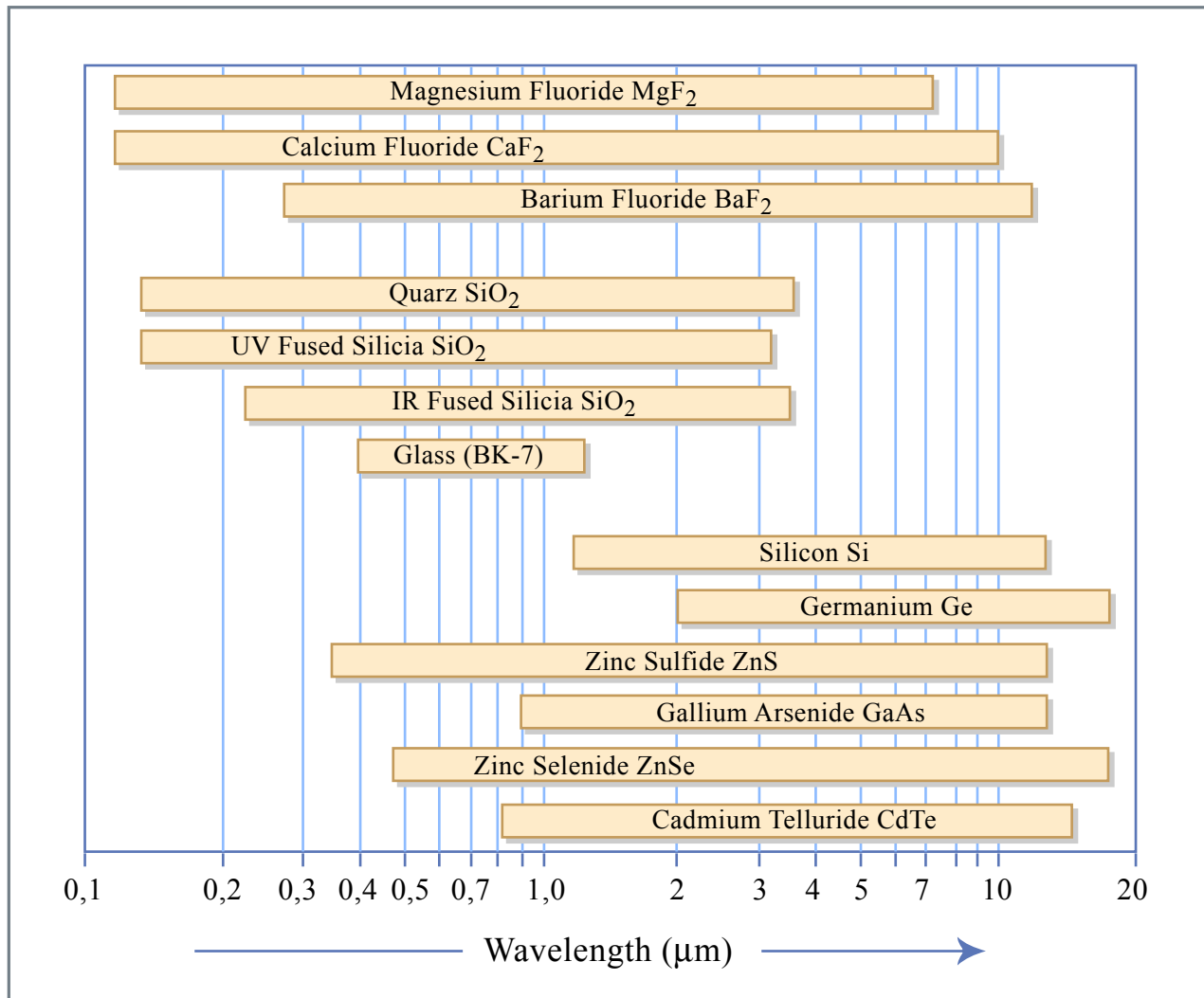


Figure 2.13: Transparency range of some materials.

Figure by MIT OCW.

2.8 Pulse Shapes and Time-Bandwidth Products

The following table 2.2 shows pulse shape, spectrum and time bandwidth products of some often used pulse forms.

$a(t)$	$\hat{a}(\omega) = \int_{-\infty}^{\infty} a(t)e^{-j\omega t} dt$	Δt	$\Delta t \cdot \Delta f$
Gauss: $e^{-\frac{t^2}{\tau^2}}$	$\sqrt{2\pi}\tau e^{-\frac{1}{2}\tau^2\omega^2}$	$2\sqrt{\ln 2}\tau$	0.441
Hyperbolicsecant: $\operatorname{sech}\left(\frac{t}{\tau}\right)$	$\frac{\tau}{2} \operatorname{sech}\left(\frac{\pi}{2}\tau\omega\right)$	1.7627τ	0.315
Rect-function: $= \begin{cases} 1, & t \leq \tau/2 \\ 0, & t > \tau/2 \end{cases}$	$\tau \frac{\sin(\tau\omega/2)}{\tau\omega/2}$	τ	0.886
Lorentzian: $\frac{1}{1+(t/\tau)^2}$	$2\pi\tau e^{- \tau\omega }$	1.287τ	0.142
Double-Exponential: $e^{- t/\tau }$	$\frac{\tau}{1+(\omega\tau)^2}$	$\ln 2 \tau$	0.142

Table 2.2: Pulse shapes, corresponding spectra and time bandwidth products.

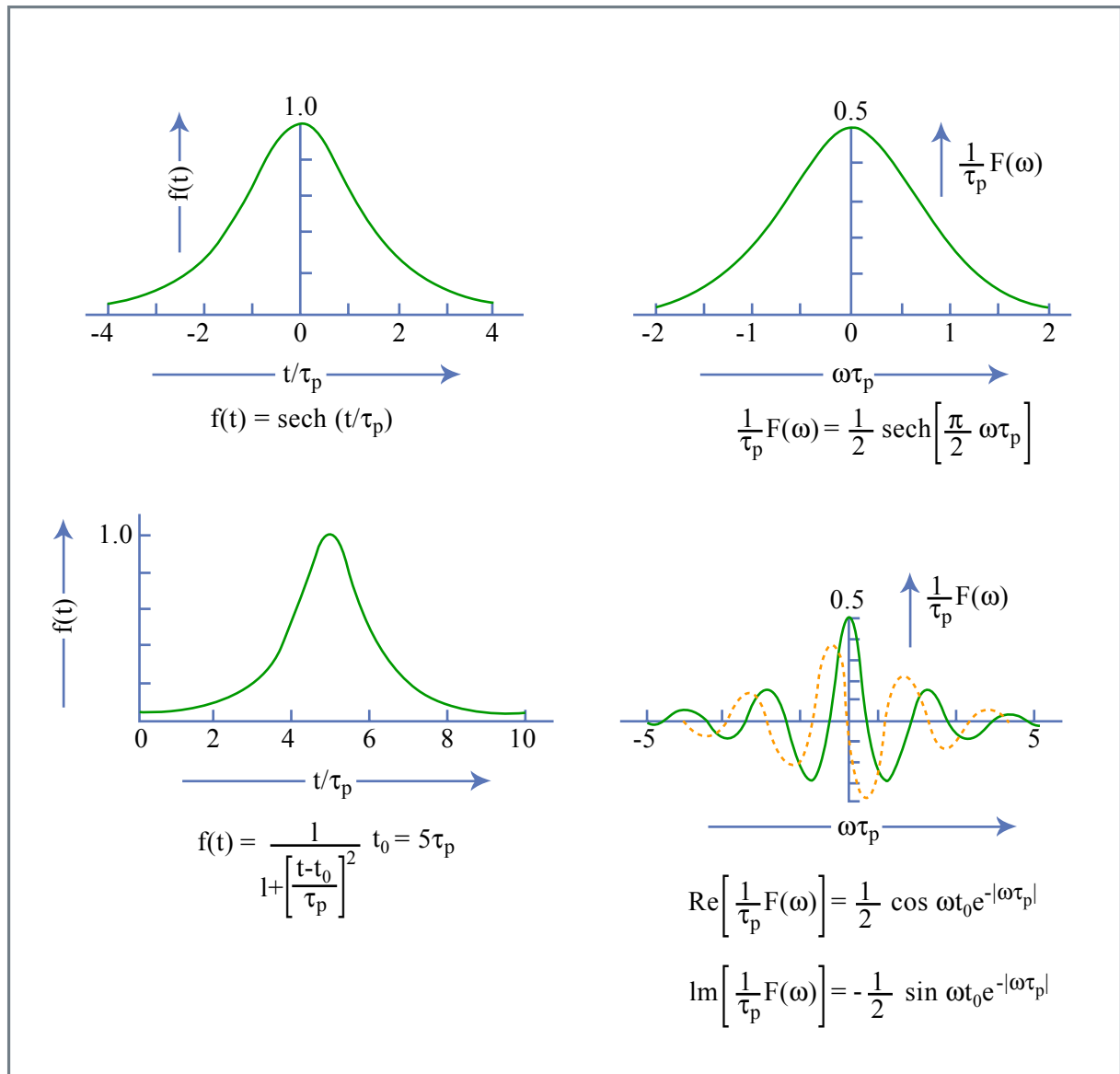


Figure 2.14: Fourier relationship to table above.

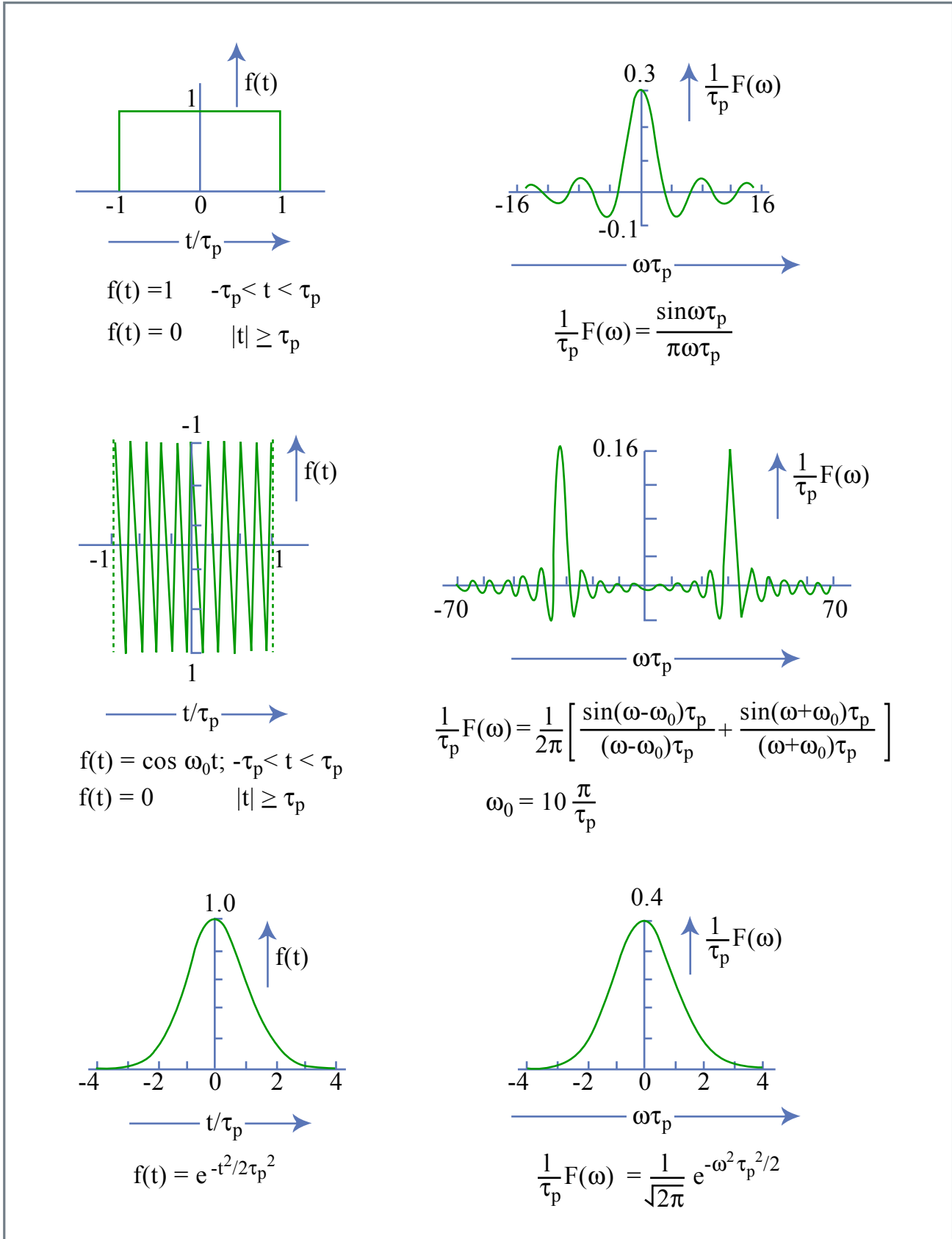


Figure 2.15: Fourier relationships to table above.

Bibliography

- [1] I. I. Rabi: "Space Quantization in a Gyating Magnetic Field,". Phys. Rev. **51**, 652-654 (1937).
- [2] B. R. Mollow, "Power Spectrum of Light Scattered by Two-Level Systems," Phys. Rev **188**, 1969-1975 (1969).
- [3] P. Meystre, M. Sargent III: Elements of Quantum Optics, Springer Verlag (1990).
- [4] L. Allen and J. H. Eberly: Optical Resonance and Two-Level Atoms, Dover Verlag (1987).
- [5] G. B. Whitham: "Linear and Nonlinear Waves," John Wiley and Sons, NY (1973).

Chapter 3

Nonlinear Pulse Propagation

There are many nonlinear pulse propagation problems worthwhile of being considered in detail, such as pulse propagation through a two-level medium in the coherent regime, which leads to self-induced transparency and solitons governed by the Sinus-Gordon-Equation. The basic model for the medium is the two-level atom discussed before with infinitely long relaxation times $T_{1,2}$, i.e. assuming that the pulses are much shorter than the dephasing time in the medium. In such a medium pulses exist, where the first half of the pulse fully inverts the medium and the second half of the pulse extracts the energy from the medium. The integral over the Rabi-frequency as defined in Eq.(2.39) is than a mutiple of 2π . The interested reader is refered to the book of Allen and Eberly [1]. Here, we are interested in the nonlinear dynamics due to the Kerr-effect which is most important for understanding pulse propagation problems in optical communications and short pulse generation.

3.1 The Optical Kerr-effect

In an isotropic and homogeneous medium, the refractive index can not depend on the direction of the electric field. Therefore, to lowest order, the refractive index of such a medium can only depend quadratically on the field, i.e. on the intensity [22]

$$n = n(\omega, |A|^2) \approx n_0(\omega) + n_{2,L}|A|^2. \quad (3.1)$$

Here, we assume, that the pulse envelope A is normalized such that $|A|^2$ is the intensity of the pulse. This is the optical Kerr effect and $n_{2,L}$ is called

Material	Refractive index n	$n_{2,L}[cm^2/W]$
Sapphire (Al_2O_3)	1.76 @ 850 nm	$3 \cdot 10^{-16}$
Fused Quartz	1.45 @ 1064 nm	$2.46 \cdot 10^{-16}$
Glass (LG-760)	1.5 @ 1064 nm	$2.9 \cdot 10^{-16}$
YAG ($Y_3Al_5O_{12}$)	1.82 @ 1064 nm	$6.2 \cdot 10^{-16}$
YLF ($LiYF_4$), n_e	1.47 @ 1047 nm	$1.72 \cdot 10^{-16}$
Si	3.3 @ 1550 nm	$4 \cdot 10^{-14}$

Table 3.1: Nonlinear refractive index coefficients for different materials. In the literature most often the electro-statitic unit system is in use. The conversion is $n_{2,L}[cm^2/W] = 4.19 \cdot 10^{-3} n_{2,L}[esu]/n_0$

the intensity dependent refractive index coefficient. Note, the nonlinear index depends on the polarization of the field and without going further into details, we assume that we treat a linearly polarized electric field. For most transparent materials the intensity dependent refractive index is positive.

3.2 Self-Phase Modulation (SPM)

In a purely one dimensional propagation problem, the intensity dependent refractive index imposes an additional self-phase shift on the pulse envelope during propagation, which is proportional to the instantaneous intensity of the pulse

$$\frac{\partial A(z,t)}{\partial z} = -jk_0 n_{2,L} |A(z,t)|^2 A(z,t) = -j\delta |A(z,t)|^2 A(z,t). \quad (3.2)$$

where $\delta = k_0 n_{2,L}$ is the self-phase modulation coefficient. Self-phase modulation (SPM) leads only to a phase shift in the time domain. Therefore, the intensity profile of the pulse does not change only the spectrum of the pulse changes, as discussed in the class on nonlinear optics. Figure (3.1) shows the spectrum of a Gaussian pulse subject to SPM during propagation (for $\delta = 2$ and normalized units). New frequency components are generated by the nonlinear process via four wave mixing (FWM). If we look at the phase of the pulse during propagation due to self-phase modulation, see Fig. 3.2 (a), we find, that the pulse redistributes its energy, such that the low frequency contributions are in the front of the pulse and the high frequencies in the back of the pulse, similar to the case of positive dispersion.

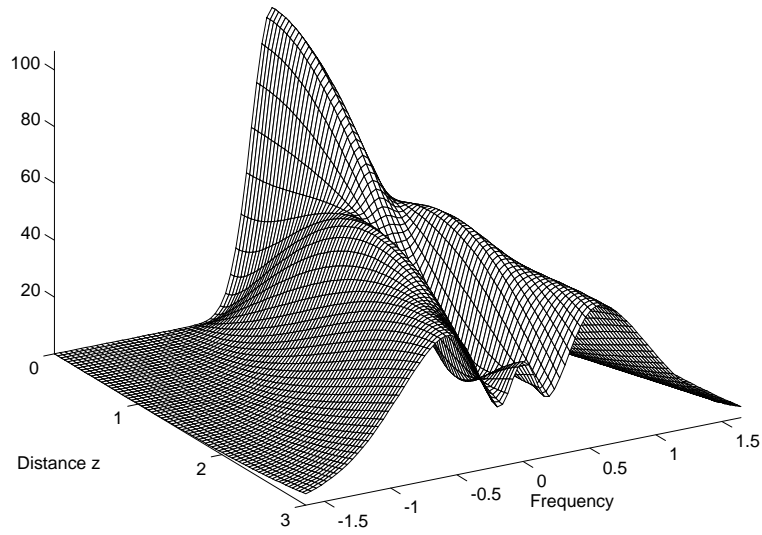


Figure 3.1: Spectrum $|\hat{A}(z, \omega = 2\pi f)|^2$ of a Gaussian pulse subject to self-phase modulation.

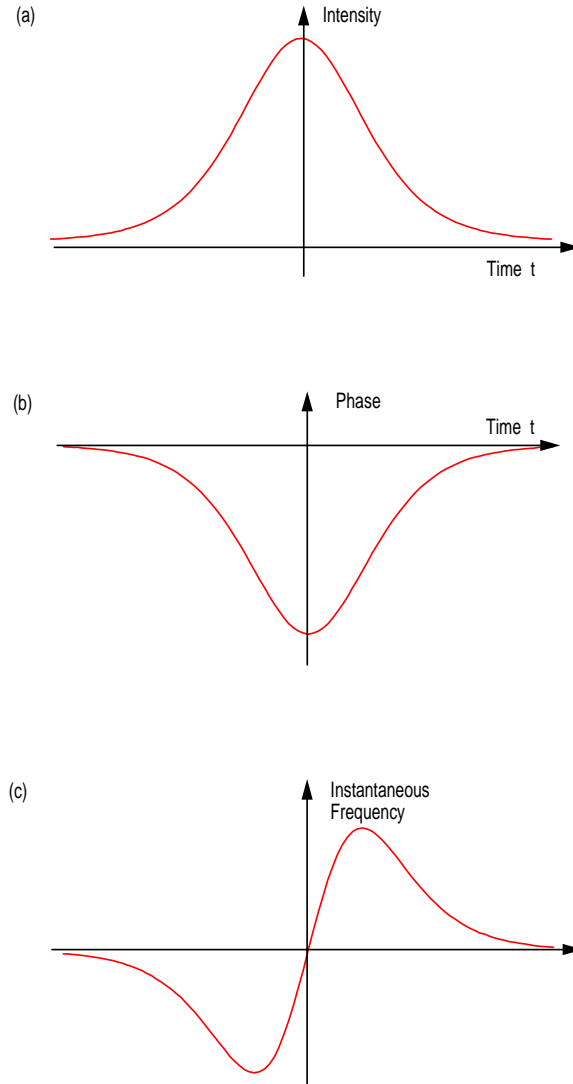


Figure 3.2: (a) Intensity, (b) phase and (c) instantaneous frequency of a Gaussian pulse during propagation through a medium with positive self-phase modulation.

3.3 The Nonlinear Schrödinger Equation

If both effects, dispersion and self-phase modulation, act simultaneously on the pulse, the field envelope obeys the equation

$$j \frac{\partial A(z, t)}{\partial z} = -D_2 \frac{\partial^2 A}{\partial t^2} + \delta |A|^2 A, \quad (3.3)$$

This equation is called the Nonlinear Schrödinger Equation (NSE) - if we put the imaginary unit on the left hand side -, since it has the form of a Schrödinger Equation. Its called nonlinear, because the potential energy is derived from the square of the wave function itself. As we have seen from the discussion in the last sections, positive dispersion and positive self-phase modulation lead to a similar redistribution of the spectral components. This enhances the pulse spreading in time. However, if we have negative dispersion, i.e. a wave packet with high carrier frequency travels faster than a wave packet with a low carrier frequency, then, the high frequency wave packets generated by self-phase modulation in the front of the pulse have a chance to catch up with the pulse itself due to the negative dispersion. The opposite is the case for the low frequencies. This arrangement results in pulses that do not disperse any more, i.e. solitary waves. That negative dispersion is necessary to compensate the positive Kerr effect is also obvious from the NSE (3.3). Because, for a positive Kerr effect, the potential energy in the NSE is always negative. There are only bound solutions, i.e. bright solitary waves, if the kinetic energy term, i.e. the dispersion, has a negative sign, $D_2 < 0$.

3.3.1 The Solitons of the NSE

In the following, we study different solutions of the NSE for the case of negative dispersion and positive self-phase modulation. We do not intend to give a full overview over the solution manifold of the NSE in its full mathematical depth here, because it is not necessary for the following. This can be found in detail elsewhere [4, 5, 6, 7].

Without loss of generality, by normalization of the field amplitude $A = \frac{A'}{\tau} \sqrt{\frac{2D_2}{\delta}}$, the propagation distance $z = z' \cdot \tau^2 / D_2$, and the time $t = t' \cdot \tau$, the NSE (3.3) with negative dispersion can always be transformed into the

normalized form

$$j\frac{\partial A(z, t)}{\partial z} = \frac{\partial^2 A}{\partial t^2} + 2|A|^2 A \quad (3.4)$$

This is equivalent to set $D_2 = -1$ and $\delta = 2$. For the numerical simulations, which are shown in the next chapters, we simulate the normalized eq.(3.4) and the axes are in normalized units of position and time.

3.3.2 The Fundamental Soliton

We look for a stationary wave function of the NSE (3.3), such that its absolute square is a self-consistent potential. A potential of that kind is well known from Quantum Mechanics, the sech^2 -Potential [8], and therefore the shape of the solitary pulse is a sech

$$A_s(z, t) = A_0 \text{sech}\left(\frac{t}{\tau}\right) e^{-j\theta}, \quad (3.5)$$

where θ is the nonlinear phase shift of the soliton

$$\theta = \frac{1}{2}\delta A_0^2 z \quad (3.6)$$

The soliton phase shift is constant over the pulse with respect to time in contrast to the case of self-phase modulation only, where the phase shift is proportional to the instantaneous power. The balance between the nonlinear effects and the linear effects requires that the nonlinear phase shift is equal to the dispersive spreading of the pulse

$$\theta = \frac{|D_2|}{\tau^2} z. \quad (3.7)$$

Since the field amplitude $A(z, t)$ is normalized, such that the absolute square is the intensity, the soliton energy fluence is given by

$$w = \int_{-\infty}^{\infty} |A_s(z, t)|^2 dt = 2A_0^2 \tau. \quad (3.8)$$

From eqs.(3.6) to (3.8), we obtain for constant pulse energy fluence, that the width of the soliton is proportional to the amount of negative dispersion

$$\tau = \frac{4|D_2|}{\delta w}. \quad (3.9)$$

Note, the pulse area for a fundamental soliton is only determined by the dispersion and the self-phase modulation coefficient

$$\text{Pulse Area} = \int_{-\infty}^{\infty} |A_s(z, t)| dt = \pi A_0 \tau = \pi \sqrt{\frac{|D_2|}{2\delta}}. \quad (3.10)$$

Thus, an initial pulse with a different area can not just develop into a pure soliton.

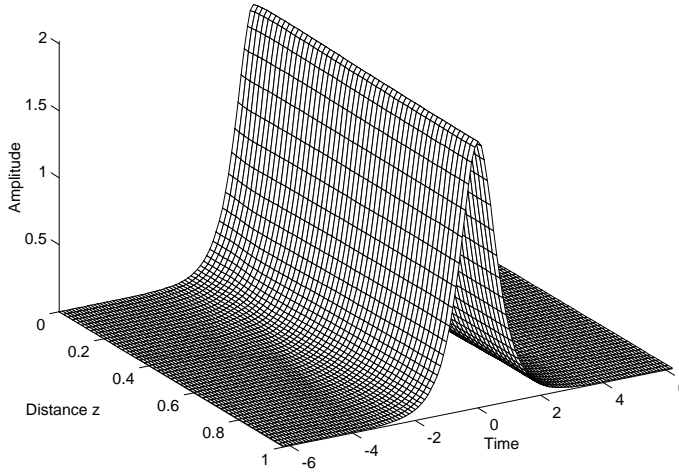


Figure 3.3: Propagation of a fundamental soliton.

Fig. 3.3 shows the numerical solution of the NSE for the fundamental soliton pulse. The distance, after which the soliton acquires a phase shift of $\pi/4$, is called the soliton period, for reasons, which will become clear in the next section.

Since the dispersion is constant over the frequency, i.e. the NSE has no higher order dispersion, the center frequency of the soliton can be chosen arbitrarily. However, due to the dispersion, the group velocities of the solitons with different carrier frequencies will be different. One easily finds by a Gallilei transformation to a moving frame, that the NSE possesses the following general fundamental soliton solution

$$A_s(z, t) = A_0 \text{sech}(x(z, t)) e^{-j\theta(z, t)}, \quad (3.11)$$

with

$$x = \frac{1}{\tau}(t - 2|D_2|p_0z - t_0), \quad (3.12)$$

and a nonlinear phase shift

$$\theta = p_0(t - t_0) + |D_2| \left(\frac{1}{\tau^2} - p_0^2 \right) z + \theta_0. \quad (3.13)$$

Thus, the energy fluence w or amplitude A_0 , the carrier frequency p_0 , the phase θ_0 and the origin t_0 , i.e. the timing of the fundamental soliton are not yet determined. Only the soliton area is fixed. The energy fluence and width are determined if one of them is specified, given a certain dispersion and SPM-coefficient.

3.3.3 Higher Order Solitons

The NSE has constant dispersion, in our case negative dispersion. That means the group velocity depends linearly on frequency. We assume, that two fundamental solitons are far apart from each other, so that they do not interact. Then this linear superposition is for all practical purposes another solution of the NSE. If we choose the carrier frequency of the soliton, starting at a later time, higher than the one of the soliton in front, the later soliton will catch up with the leading soliton due to the negative dispersion and the pulses will collide.

Figure 3.4 shows this situation. Obviously, the two pulses recover completely from the collision, i.e. the NSE has true soliton solutions. The solitons have particle like properties. A solution, composed of several fundamental solitons, is called a higher order soliton. If we look closer to figure 3.4, we recognize, that the soliton at rest in the local time frame, and which follows the $t = 0$ line without the collision, is somewhat pushed forward due to the collision. A detailed analysis of the collision would also show, that the phases of the solitons have changed [4]. The phase changes due to soliton collisions are used to built all optical switches [10], using backfolded Mach-Zehnder interferometers, which can be realized in a self-stabilized way by Sagnac fiber loops.

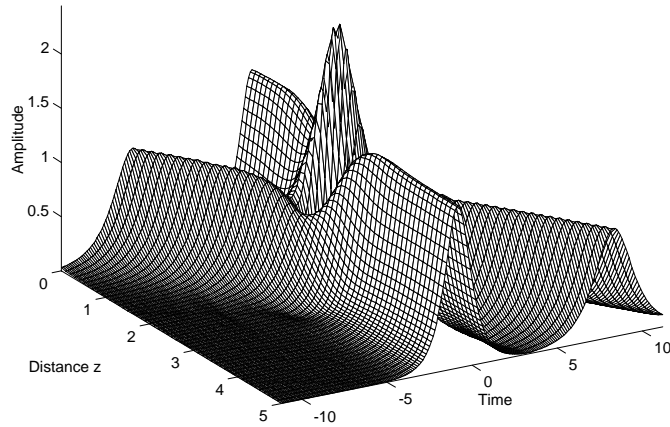


Figure 3.4: A soliton with high carrier frequency collides with a soliton of lower carrier frequency. After the collision both pulses recover completely.

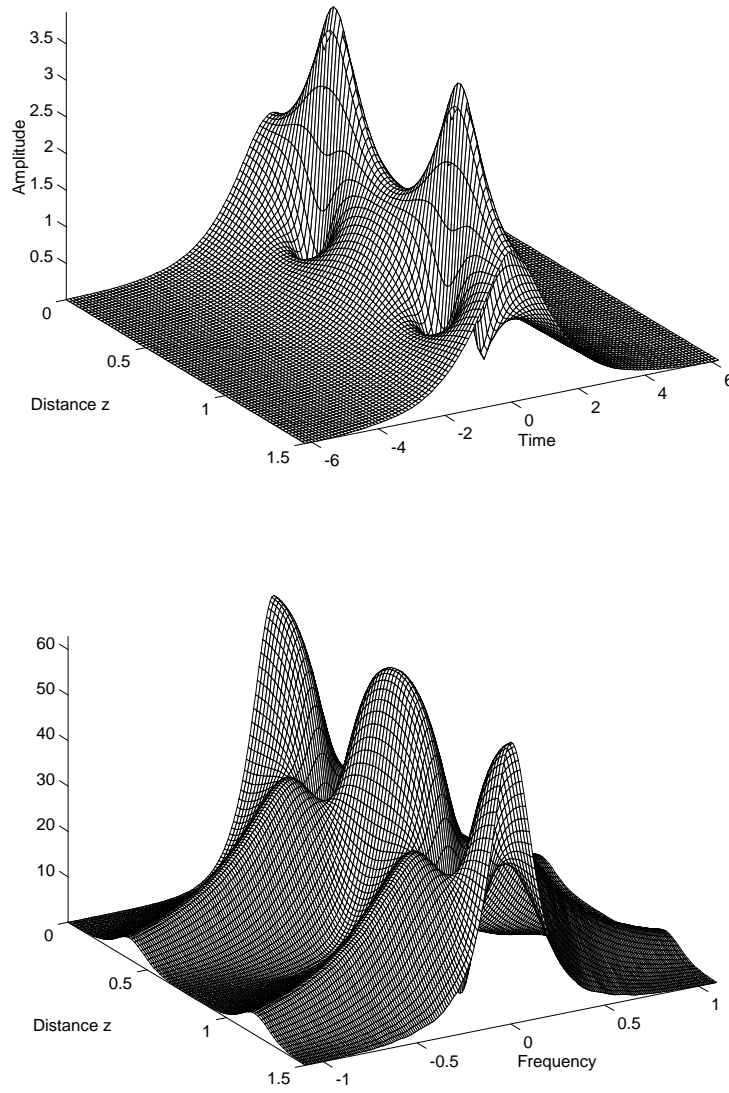


Figure 3.5: (a) Amplitude and, (b) Spectrum of a higher order soliton composed of two fundamental solitons with the same carrier frequency

The NSE also shows higher order soliton solutions, that travel at the same speed, i.e. they possess the same carrier frequency, the so called breather solutions. Figures 3.5(a) and (b) show the amplitude and spectrum of such a higher order soliton solution, which has twice the area of the fundamental soliton. The simulation starts with a sech-pulse, that has twice the area of the fundamental soliton, shown in figure 3.3. Due to the interaction of the two solitons, the temporal shape and the spectrum exhibits a complicated but periodic behaviour. This period is the soliton period $z = \pi/4$, as mentioned above. As can be seen from Figures 3.5(a) and 3.5(b), the higher order soliton dynamics leads to an enormous pulse shortening after half of the soliton period. This process has been used by Mollenauer, to build his soliton laser [11]. In the soliton laser, the pulse compression, that occurs for a higher order soliton as shown in Fig. 3.5(a), is exploited for modelocking. Mollenauer pioneered soliton propagation in optical fibers, as proposed by Hasegawa and Tappert [3], with the soliton laser, which produced the first picosecond pulses at $1.55 \mu\text{m}$. A detailed account on the soliton laser is given by Haus [12].

So far, we have discussed the pure soliton solutions of the NSE. But, what happens if one starts propagation with an input pulse that does not correspond to a fundamental or higher order soliton?

3.3.4 Inverse Scattering Theory

Obviously, the NSE has solutions, which are composed of fundamental solitons. Thus, the solutions obey a certain superposition principle which is absolutely surprising for a nonlinear system. Of course, not arbitrary superpositions are possible as in a linear system. The deeper reason for the solution manifold of the NSE can be found by studying its physical and mathematical properties. The mathematical basis for an analytic formulation of the solutions to the NSE is the inverse scattering theory [13, 14, 4, 15]. It is a spectral transform method for solving integrable, nonlinear wave equations, similar to the Fourier transform for the solution of linear wave equations [16].

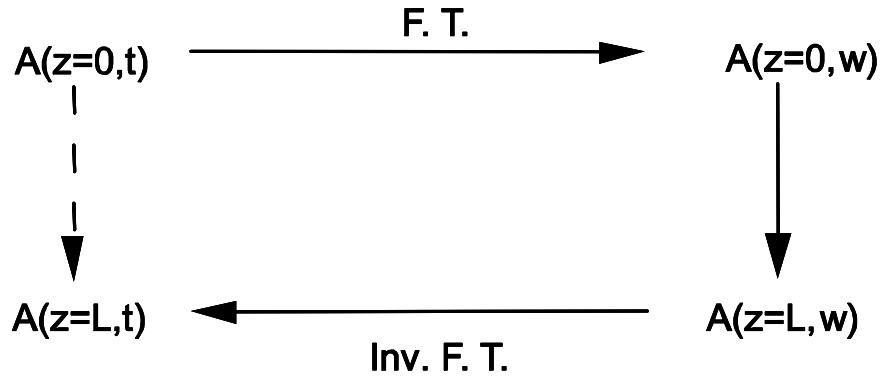


Figure 3.6: Fourier transform method for the solution of linear, time invariant partial differential equations.

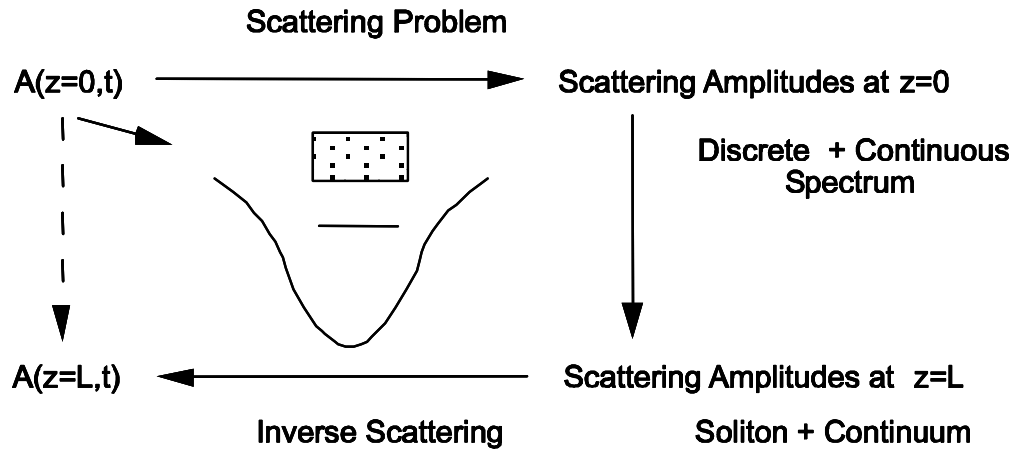


Figure 3.7: Schematic representation of the inverse scattering theory for the solution of integrable nonlinear partial differential equations.

Let's remember briefly, how to solve an initial value problem for a linear partial differential equation (p.d.e.), like eq.(2.184), that treats the case of a purely dispersive pulse propagation. The method is sketched in Fig. 3.6. We Fourier transform the initial pulse into the spectral domain, because, the exponential functions are eigensolutions of the differential operators with

constant coefficients. The right side of (2.184) is only composed of powers of the differential operator, therefore the exponentials are eigenfunctions of the complete right side. Thus, after Fourier transformation, the p.d.e. becomes a set of ordinary differential equations (o.d.e.), one for each partial wave. The excitation of each wave is given by the spectrum of the initial wave. The eigenvalues of the differential operator, that constitutes the right side of (2.184), is given by the dispersion relation, $k(\omega)$, up to the imaginary unit. The solution of the remaining o.d.e is then a simple exponential of the dispersion relation. Now, we have the spectrum of the propagated wave and by inverse Fourier transformation, i.e. we sum over all partial waves, we find the new temporal shape of the propagated pulse.

As in the case of the Fourier transform method for the solution of linear wave equations, the inverse scattering theory is again based on a spectral transform, (Fig.3.7). However, this transform depends now on the details of the wave equation and the initial conditions. This dependence leads to a modified superposition principle. As is shown in [7], one can formulate for many integrable nonlinear wave equations a related scattering problem like one does in Quantum Theory for the scattering of a particle at a potential well. However, the potential well is now determined by the solution of the wave equation. Thus, the initial potential is already given by the initial conditions. The stationary states of the scattering problem, which are the eigensolutions of the corresponding Hamiltonian, are the analog to the monochromatic complex oscillations, which are the eigenfunctions of the differential operator. The eigenvalues are the analog to the dispersion relation, and as in the case of the linear p.d.e's, the eigensolutions obey simple linear o.d.e's.

A given potential will have a certain number of bound states, that correspond to the discrete spectrum and a continuum of scattering states. The characteristic of the continuous eigenvalue spectrum is the reflection coefficient for waves scattered upon reflection at the potential. Thus, a certain potential, i.e. a certain initial condition, has a certain discrete spectrum and continuum with a corresponding reflection coefficient. From inverse scattering theory for quantum mechanical and electromagnetic scattering problems, we know, that the potential can be reconstructed from the scattering data, i.e. the reflection coefficient and the data for the discrete spectrum [?]. This is true for a very general class of scattering potentials. As one can almost guess now, the discrete eigenstates of the initial conditions will lead to soliton solutions. We have already studied the dynamics of some of these soliton so-

lutions above. The continuous spectrum will lead to a dispersive wave which is called the continuum. Thus, the most general solution of the NSE, for given arbitrary initial conditions, is a superposition of a soliton, maybe a higher order soliton, and a continuum contribution.

The continuum will disperse during propagation, so that only the soliton is recognized after a while. Thus, the continuum becomes an asymptotically small contribution to the solution of the NSE. Therefore, the dynamics of the continuum is completely described by the linear dispersion relation of the wave equation.

The back transformation from the spectral to the time domain is not as simple as in the case of the Fourier transform for linear p.d.e's. One has to solve a linear integral equation, the Marchenko equation [17]. Nevertheless, the solution of a nonlinear equation has been reduced to the solution of two linear problems, which is a tremendous success.

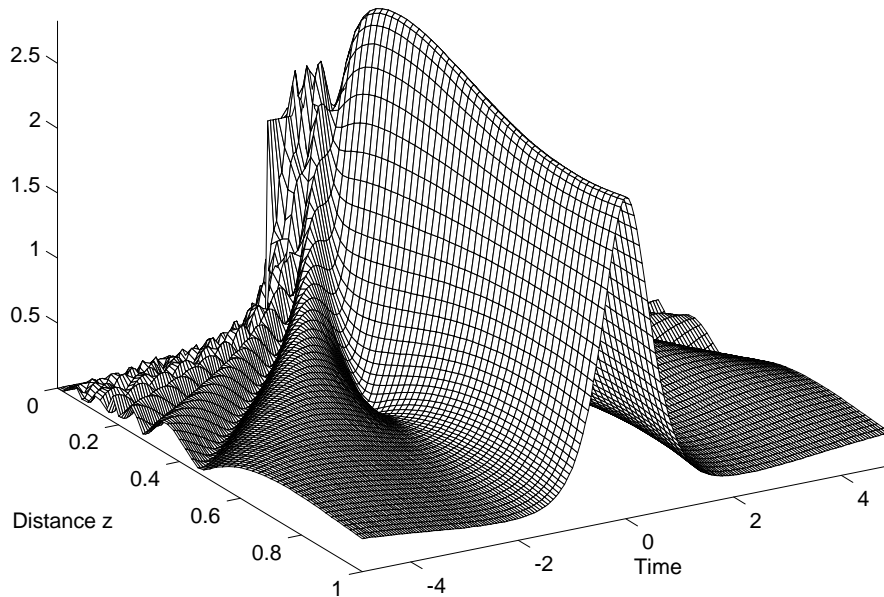


Figure 3.8: Solution of the NSE for an unchirped and rectangular shaped initial pulse.

To appreciate these properties of the solutions of the NSE, we solve the NSE for a rectangular shaped initial pulse. The result is shown in Fig. 3.8.

The scattering problem, that has to be solved for this initial condition, is the same as for a nonrelativistic particle in a rectangular potential box [32]. The depth of the potential is chosen small enough, so that it has only one bound state. Thus, we start with a wave composed of a fundamental soliton and continuum. It is easy to recognize the continuum contribution, i.e. the dispersive wave, that separates from the soliton during propagation. This solution illustrates, that soliton pulse shaping due to the presence of dispersion and self-phase modulation may have a strong impact on pulse generation [18]. When the dispersion and self-phase modulation are properly adjusted, soliton formation can lead to very clean, stable, and extremely short pulses in a modelocked laser.

3.4 Universality of the NSE

Above, we derived the NSE in detail for the case of dispersion and self-phase modulation. The input for the NSE is surprisingly low, we only have to admit the first nontrivial dispersive effect and the lowest order nonlinear effect that is possible in an isotropic and homogeneous medium like glass, gas or plasmas. Therefore, the NSE and its properties are important for many other effects like self-focusing [19], Langmuir waves in plasma physics, and waves in protein molecules [20]. Self-focusing will be treated in more detail later, because it is the basis for Kerr-Lens Mode Locking.

3.5 Soliton Perturbation Theory

From the previous discussion, we have full knowledge about the possible solutions of the NSE that describes a special Hamiltonian system. However, the NSE hardly describes a real physical system such as, for example, a real optical fiber in all its aspects [21, 22]. Indeed the NSE itself, as we have seen during the derivation in the previous sections, is only an approximation to the complete wave equation. We approximated the dispersion relation by a parabola at the assumed carrier frequency of the soliton. Also the instantaneous Kerr effect described by an intensity dependent refractive index is only an approximation to the real $\chi^{(3)}$ -nonlinearity of a Kerr-medium [23,

24]. Therefore, it is most important to study what happens to a soliton solution of the NSE due to perturbing effects like higher order dispersion, finite response times of the nonlinearities, gain and the finite gain bandwidth of amplifiers, that compensate for the inevitable loss in a real system.

The investigation of solitons under perturbations is as old as the solitons itself. Many authors treat the perturbing effects in the scattering domain [25, 26]. Only recently, a perturbation theory on the basis of the linearized NSE has been developed, which is much more illustrative than a formulation in the scattering amplitudes. This was first used by Haus [27] and rigorously formulated by Kaup [28]. In this section, we will present this approach as far as it is indispensable for the following.

A system, where the most important physical processes are dispersion and self-phase modulation, is described by the NSE complimented with some perturbation term F

$$\frac{\partial A(z, t)}{\partial z} = -j \left[|D_2| \frac{\partial^2 A}{\partial t^2} + \delta |A|^2 A \right] + F(A, A^*, z). \quad (3.14)$$

In the following, we are interested what happens to a solution of the full equation (3.14) which is very close to a fundamental soliton, i.e.

$$A(z, t) = \left[a\left(\frac{t}{\tau}\right) + \Delta A(z, t) \right] e^{-jk_s z}. \quad (3.15)$$

Here, $a(x)$ is the fundamental soliton according to eq.(3.5)

$$a\left(\frac{t}{\tau}\right) = A_0 \operatorname{sech}\left(\frac{t}{\tau}\right), \quad (3.16)$$

and

$$k_s = \frac{1}{2} \delta A_0^2 \quad (3.17)$$

is the phase shift of the soliton per unit length, i.e. the soliton wave vector.

A deviation from the ideal soliton can arise either due to the additional driving term F on the right side or due to a deviation already present in the initial condition. We use the form (3.15) as an ansatz to solve the NSE to first order in the perturbation ΔA , i.e. we linearize the NSE around the fundamental soliton and obtain for the perturbation

$$\begin{aligned} \frac{\partial \Delta A}{\partial z} = & -jk_s \left[\left(\frac{\partial^2}{\partial x^2} - 1 \right) \Delta A + 2 \operatorname{sech}^2(x) (2\Delta A + \Delta A^*) \right] \\ & + F(A, A^*, z) e^{jk_s z}, \end{aligned} \quad (3.18)$$

where $x = t/\tau$. Due to the nonlinearity, the field is coupled to its complex conjugate. Thus, eq.(3.18) corresponds actually to two equations, one for the amplitude and one for its complex conjugate. Therefore, we introduce the vector notation

$$\Delta \mathbf{A} = \begin{pmatrix} \Delta A \\ \Delta A^* \end{pmatrix}. \quad (3.19)$$

We further introduce the normalized propagation distance $z' = k_s z$ and the normalized time $x = t/\tau$. The linearized perturbed NSE is then given by

$$\frac{\partial}{\partial z'} \Delta \mathbf{A} = \mathbf{L} \Delta \mathbf{A} + \frac{1}{k_s} \mathbf{F}(A, A^*, z) e^{jz'} \quad (3.20)$$

Here, \mathbf{L} is the operator which arises from the linearization of the NSE

$$\mathbf{L} = -j\sigma_3 \left[\left(\frac{\partial^2}{\partial x^2} - 1 \right) + 2 \operatorname{sech}^2(x)(2 + \sigma_1) \right], \quad (3.21)$$

where $\sigma_i, i = 1, 2, 3$ are the Pauli matrices. For a solution of the inhomogeneous equation (3.20), we need the eigenfunctions and the spectrum of the differential operator \mathbf{L} . We found in section 3.3.2, that the fundamental soliton has four degrees of freedom, four free parameters. This gives already four known eigensolutions and mainsolutions of the linearized NSE, respectively. They are determined by the derivatives of the general fundamental soliton solutions according to eqs.(3.11) to (3.13) with respect to free parameters. These eigenfunctions are

$$\mathbf{f}_w(x) = \frac{1}{w}(1 - x \tanh x) a(x) \begin{pmatrix} 1 \\ 1 \end{pmatrix}, \quad (3.22)$$

$$\mathbf{f}_\theta(x) = -j a(x) \begin{pmatrix} 1 \\ -1 \end{pmatrix}, \quad (3.23)$$

$$\mathbf{f}_p(x) = -j x \tau a(x) \begin{pmatrix} 1 \\ -1 \end{pmatrix}, \quad (3.24)$$

$$\mathbf{f}_t(x) = \frac{1}{\tau} \tanh(x) a(x) \begin{pmatrix} 1 \\ 1 \end{pmatrix}, \quad (3.25)$$

and they describe perturbations of the soliton energy, phase, carrier frequency and timing. One component of each of these vector functions is shown in Fig. 3.9.

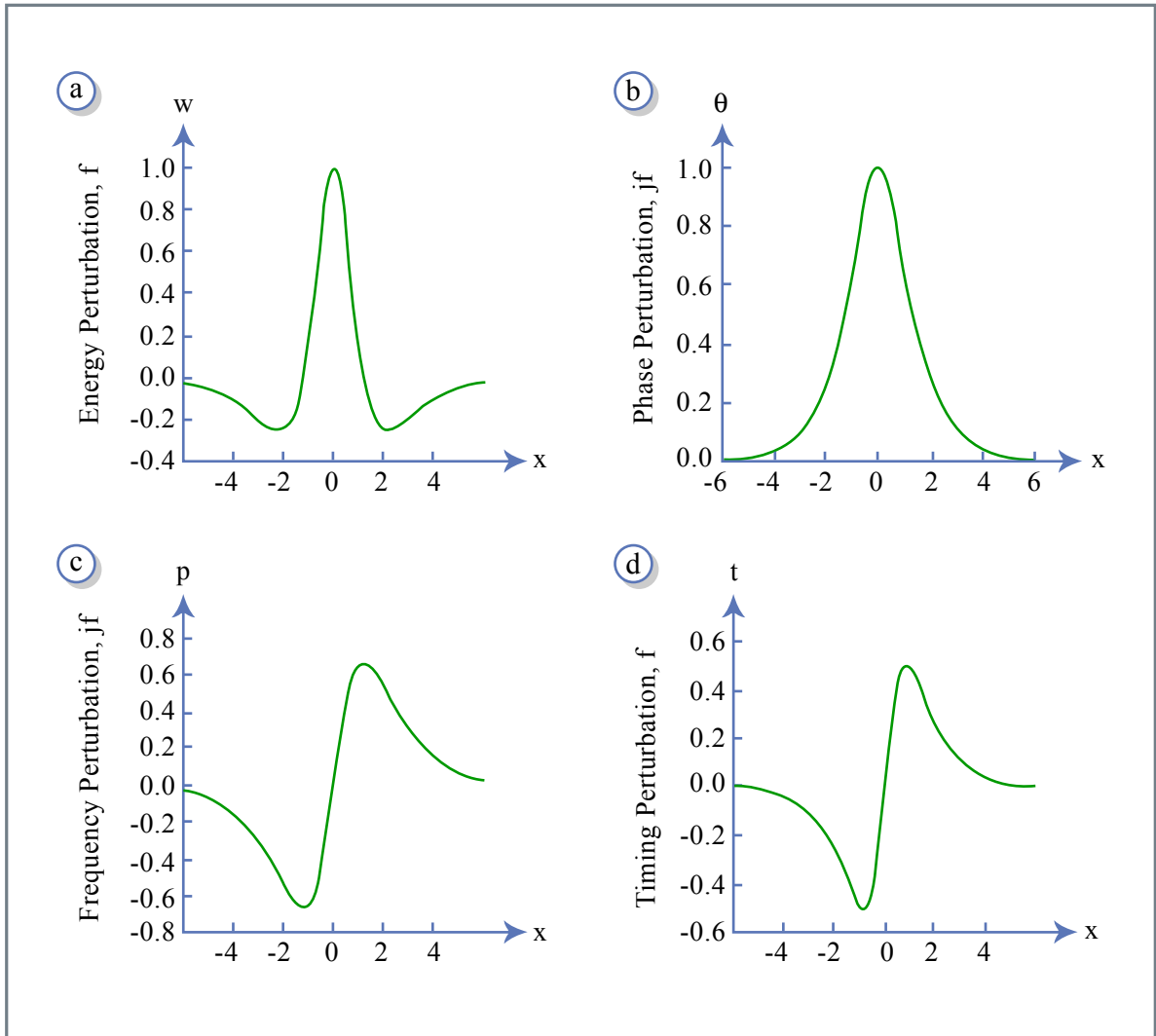


Figure 3.9: Perturbations in soliton amplitude (a), phase (b), frequency (c), and timing (d).

Figure by MIT OCW.

The action of the evolution operator of the linearized NSE on these soliton perturbations is

$$\mathbf{L}f_w = \frac{1}{w}f_\theta, \quad (3.26)$$

$$\mathbf{L}f_\theta = 0, \quad (3.27)$$

$$\mathbf{L}f_p = -2\tau^2 f_t, \quad (3.28)$$

$$\mathbf{L}f_t = 0. \quad (3.29)$$

Equations (3.26) and (3.28) indicate, that perturbations in energy and carrier frequency are converted to additional phase and timing fluctuations of the pulse due to SPM and GVD. This is the base for soliton squeezing in optical fibers [27]. The timing and phase perturbations can increase without bounds, because the system is autonomous, the origin for the Gordon-Haus effect, [29] and there is no phase reference in the system. The full continuous spectrum of the linearized NSE has been studied by Kaup [28] and is given by

$$\mathbf{L}\mathbf{f}_k = \lambda_k \mathbf{f}_k, \quad (3.30)$$

$$\lambda_k = j(k^2 + 1), \quad (3.31)$$

$$\mathbf{f}_k(x) = e^{-jkx} \begin{pmatrix} (k - j \tanh x)^2 \\ \operatorname{sech}^2 x \end{pmatrix}, \quad (3.32)$$

and

$$\mathbf{L}\bar{\mathbf{f}}_k = \bar{\lambda}_k \bar{\mathbf{f}}_k, \quad (3.33)$$

$$\bar{\lambda}_k = -j(k^2 + 1), \quad (3.34)$$

$$\bar{\mathbf{f}}_k = \sigma_1 \mathbf{f}_k. \quad (3.35)$$

Our definition of the eigenfunctions is slightly different from Kaup [28], because we also define the inner product in the complex space as

$$\langle \mathbf{u} | \mathbf{v} \rangle = \frac{1}{2} \int_{-\infty}^{+\infty} \mathbf{u}^+(x) \mathbf{v}(x) dx. \quad (3.36)$$

Adopting this definition, the inner product of a vector with itself in the subspace where the second component is the complex conjugate of the first component is the energy of the signal, a physical quantity.

The operator \mathbf{L} is not self-adjoint with respect to this inner product. The physical origin for this mathematical property is, that the linearized system does not conserve energy due to the parametric pumping by the soliton. However, from (3.21) and (3.36), we can easily see that the adjoint operator is given by

$$\mathbf{L}^+ = -\sigma_3 \mathbf{L} \sigma_3, \quad (3.37)$$

and therefore, we obtain for the spectrum of the adjoint operator

$$\mathbf{L}^+ \mathbf{f}_k^{(+)} = \lambda_k^{(+)} \mathbf{f}_k^{(+)}, \quad (3.38)$$

$$\lambda_k^{(+)} = -j(k^2 + 1), \quad (3.39)$$

$$\mathbf{f}_k^{(+)} = \frac{1}{\pi(k^2 + 1)^2} \sigma_3 \mathbf{f}_k, \quad (3.40)$$

and

$$\mathbf{L}^+ \bar{\mathbf{f}}_k^{(+)} = \bar{\lambda}_k^{(+)} \bar{\mathbf{f}}_k^{(+)}, \quad (3.41)$$

$$\bar{\lambda}_k^{(+)} = j(k^2 + 1), \quad (3.42)$$

$$\bar{\mathbf{f}}_k^{(+)} = \frac{1}{\pi(k^2 + 1)^2} \sigma_3 \bar{\mathbf{f}}_k. \quad (3.43)$$

The eigenfunctions to \mathbf{L} and its adjoint are mutually orthogonal to each other, and they are already properly normalized

$$\begin{aligned} \langle \mathbf{f}_k^{(+)} | \mathbf{f}_{k'} \rangle &= \delta(k - k'), & \langle \bar{\mathbf{f}}_k^{(+)} | \bar{\mathbf{f}}_{k'} \rangle &= \delta(k - k') \\ \langle \bar{\mathbf{f}}_k^{(+)} | \mathbf{f}_{k'} \rangle &= \langle \mathbf{f}_k^{(+)} | \bar{\mathbf{f}}_{k'} \rangle = 0. \end{aligned}$$

This system, which describes the continuum excitations, is made complete by taking also into account the perturbations of the four degrees of freedom of the soliton (3.22) - (3.25) and their adjoints

$$\mathbf{f}_w^{(+)}(x) = j2\tau\sigma_3\mathbf{f}_\theta(x) = 2\tau a(x) \begin{pmatrix} 1 \\ 1 \end{pmatrix}, \quad (3.44)$$

$$\begin{aligned} \mathbf{f}_\theta^{(+)}(x) &= -2j\tau\sigma_3\mathbf{f}_w(x) \\ &= \frac{-2j\tau}{w}(1 - x \tanh x)a(x) \begin{pmatrix} 1 \\ -1 \end{pmatrix}, \end{aligned} \quad (3.45)$$

$$\mathbf{f}_p^{(+)}(x) = -\frac{2j\tau}{w}\sigma_3\mathbf{f}_t(x) = \frac{2i}{w}\tanh xa(x) \begin{pmatrix} 1 \\ -1 \end{pmatrix}, \quad (3.46)$$

$$\mathbf{f}_t^{(+)}(x) = \frac{2j\tau}{w}\sigma_3\mathbf{f}_p(x) = \frac{2\tau^2}{w}xa(x) \begin{pmatrix} 1 \\ 1 \end{pmatrix}. \quad (3.47)$$

Now, the unity can be decomposed into two projections, one onto the continuum and one onto the perturbation of the soliton variables [28]

$$\begin{aligned} \delta(x - x') &= \int_{-\infty}^{\infty} dk \left[|\mathbf{f}_k \rangle \langle \mathbf{f}_k^{(+)}| + |\bar{\mathbf{f}}_k \rangle \langle \bar{\mathbf{f}}_k^{(+)}| \right] \\ &+ |\mathbf{f}_w \rangle \langle \mathbf{f}_w^{(+)}| + |\mathbf{f}_\theta \rangle \langle \mathbf{f}_\theta^{(+)}| \\ &+ |\mathbf{f}_p \rangle \langle \mathbf{f}_p^{(+)}| + |\mathbf{f}_t \rangle \langle \mathbf{f}_t^{(+)}|. \end{aligned} \quad (3.48)$$

Any deviation ΔA can be decomposed into a contribution that leads to a soliton with a shift in the four soliton parameters and a continuum contribution a_c

$$\Delta \mathbf{A}(z') = \Delta w(z')\mathbf{f}_w + \Delta \theta(z')\mathbf{f}_\theta + \Delta p(z')\mathbf{f}_p + \Delta t(z')\mathbf{f}_t + \mathbf{a}_c(z'). \quad (3.49)$$

Further, the continuum can be written as

$$\mathbf{a}_c = \int_{-\infty}^{\infty} dk [g(k)\mathbf{f}_k(x) + \bar{g}(k)\bar{\mathbf{f}}_k(x)]. \quad (3.50)$$

If we put the decomposition (3.49) into (3.20) we obtain

$$\begin{aligned} \frac{\partial \Delta w}{\partial z'} \mathbf{f}_w + \frac{\partial \Delta \theta}{\partial z'} \mathbf{f}_\theta + \frac{\partial \Delta p}{\partial z'} \mathbf{f}_p + \frac{\partial \Delta t}{\partial z'} \mathbf{f}_t + \frac{\partial}{\partial z'} \mathbf{a}_c = \\ \mathbf{L}(\Delta w(z')\mathbf{f}_w + \Delta p(z')\mathbf{f}_p + \mathbf{a}(z')_c) + \frac{1}{k_s} \mathbf{F}(A, A^*, z') e^{-iz'}. \end{aligned} \quad (3.51)$$

By building the scalar products (3.36) of this equation with the eigensolutions of the adjoint evolution operator (3.38) to (3.43) and using the eigenvalues (3.26) to (3.35), we find

$$\frac{\partial}{\partial z'} \Delta w = \frac{1}{k_s} \langle \mathbf{f}_w^{(+)} | \mathbf{F} e^{jz'} \rangle, \quad (3.52)$$

$$\frac{\partial}{\partial z'} \Delta \theta = \frac{\Delta W}{W} + \frac{1}{k_s} \langle \mathbf{f}_\theta^{(+)} | \mathbf{F} e^{jz'} \rangle, \quad (3.53)$$

$$\frac{\partial}{\partial z'} \Delta p = \frac{1}{k_s} \langle \mathbf{f}_p^{(+)} | \mathbf{F} e^{jz'} \rangle, \quad (3.54)$$

$$\frac{\partial}{\partial z'} \Delta t = 2\tau \Delta p + \frac{1}{k_s} \langle \mathbf{f}_t^{(+)} | \mathbf{F} e^{jz'} \rangle, \quad (3.55)$$

$$\frac{\partial}{\partial z'} g(k) = j(1+k^2)g(k) + \frac{1}{k_s} \langle \mathbf{f}_k^{(+)} | \mathbf{F}(A, A^*, z') e^{jz'} \rangle. \quad (3.56)$$

Note, that the continuum \mathbf{a}_c has to be in the subspace defined by

$$\sigma_1 \mathbf{a}_c = \mathbf{a}_c^*. \quad (3.57)$$

The spectra of the continuum $g(k)$ and $\bar{g}(k)$ are related by

$$\bar{g}(k) = g(-k)^*. \quad (3.58)$$

Then, we can directly compute the continuum from its spectrum using (3.32), (3.50) and (3.57)

$$a_c = -\frac{\partial^2 G(x)}{\partial x^2} + 2 \tanh(x) \frac{\partial G(x)}{\partial x} - \tanh^2(x) G(x) + G^*(x) \operatorname{sech}^2(x), \quad (3.59)$$

where $G(x)$ is, up to the phase factor $e^{iz'}$, Gordon's associated function [33]. It is the inverse Fourier transform of the spectrum

$$G(x) = \int_{-\infty}^{\infty} g(k) e^{ikx} dk. \quad (3.60)$$

Since $g(k)$ obeys eq.(3.56), Gordon's associated function obeys a pure dispersive equation in the absence of a driving term F

$$\frac{\partial G(z', x)}{\partial z'} = -j \left(1 + \frac{\partial^2}{\partial x^2} \right) G(z', x). \quad (3.61)$$

It is instructive to look at the spectrum of the continuum when only one continuum mode with normalized frequency k_0 is present, i.e. $g(k) = \delta(k - k_0)$. Then according to eqs. (3.59) and (3.60) we have

$$a_{c,k}(x) = [k_0^2 - 2jk_0 \tanh(x) - 1] e^{-jk_0x} + 2\text{sech}^2(x) \cos(x). \quad (3.62)$$

The spectrum of this continuum contribution is

$$\begin{aligned} \tilde{a}_{c,k}(\omega) = & 2\pi(k_0^2 - 1)\delta(\omega - k_0) + 2k_0 P.V. \left(\frac{2}{\omega - k_0} + \frac{\pi}{\sinh\left(\frac{\pi}{2}(\omega - k_0)\right)} \right) \\ & + \pi \frac{\omega - k_0}{\sinh\left(\frac{\pi}{2}(\omega - k_0)\right)} + \pi \frac{\omega + k_0}{\sinh\left(\frac{\pi}{2}(\omega + k_0)\right)}. \end{aligned} \quad (3.63)$$

3.6 Soliton Instabilities by Periodic Perturbations

Periodic perturbations of solitons are important for understanding ultrashort pulse lasers as well as long distance optical communication systems [30, 31]. Along a long distance transmission system, the pulses have to be periodically amplified. In a mode-locked laser system, most often the nonlinearity, dispersion and gain occur in a lumped manner. The solitons propagating in these systems are only average solitons, which propagate through discrete components in a periodic fashion, as we will see later.

The effect of this periodic perturbations can be modelled by an additional term F in the perturbed NSE according to Eq.(3.14)

$$F(A, A^*, z) = j\xi \sum_{n=-\infty}^{\infty} \delta(z - nz_A) A(z, t). \quad (3.64)$$

The periodic kicking of the soliton leads to shedding of energy into continuum modes according to Eq.(3.56)

$$\frac{\partial}{\partial z}g(k) = jk_s(1+k^2)g(k) + \langle \mathbf{f}_k^{(+)} \mathbf{F}(A, A^*, z) e^{jk_s z} \rangle. \quad (3.65)$$

$$\langle \mathbf{f}_k^{(+)} \mathbf{F}(A, A^*, z) e^{jk_s z} \rangle = j\xi \sum_{n=-\infty}^{\infty} \delta(z - nz_A) \frac{1}{2}. \quad (3.66)$$

$$\begin{aligned} & \int_{-\infty}^{+\infty} \frac{1}{\pi(k^2+1)^2} e^{jkx} \begin{pmatrix} (k + j \tanh x)^2 \\ -\operatorname{sech}^2 x \end{pmatrix} \cdot \begin{pmatrix} 1 \\ 1 \end{pmatrix} A_0 \operatorname{sech} x \, dx \\ &= j\xi \sum_{n=-\infty}^{\infty} \delta(z - nz_A) \cdot \\ & \int_{-\infty}^{+\infty} \frac{A_0}{2\pi(k^2+1)^2} e^{jkx} (k^2 + 2jk \tanh x - 1) \cdot \operatorname{sech} x \, dx \end{aligned} \quad (3.67)$$

Note, $\frac{d}{dx} \operatorname{sech} x = -\operatorname{sech} x \tanh x$, and therefore

$$\begin{aligned} & \langle \mathbf{f}_k^{(+)} \mathbf{F}(A, A^*, z) e^{jz} \rangle = -j\xi \sum_{n=-\infty}^{\infty} \delta(z - nz_A) \cdot \\ & \int_{-\infty}^{+\infty} \frac{A_0}{2\pi(k^2+1)} e^{jkx} \cdot \operatorname{sech} x \, dx \\ &= -j\xi \sum_{n=-\infty}^{\infty} \delta(z - nz_A) \frac{A_0}{4(k^2+1)} \operatorname{sech} \left(\frac{\pi k}{2} \right). \end{aligned} \quad (3.68)$$

Using $\sum_{n=-\infty}^{\infty} \delta(z - nz_A) = \frac{1}{z_A} \sum_{m=-\infty}^{\infty} e^{jm \frac{2\pi}{z_A} z}$ we obtain

$$\frac{\partial}{\partial z}g(k) = jk_s(1+k^2)g(k) - j \frac{\xi}{z_A} \sum_{m=-\infty}^{\infty} e^{jm \frac{2\pi}{z_A} z} \frac{A_0}{4(k^2+1)} \operatorname{sech} \left(\frac{\pi k}{2} \right). \quad (3.69)$$

Eq.(3.69) is a linear differential equation with constant coefficients for the continuum amplitudes $g(k)$, which can be solved by variation of constants with the ansatz

$$g(k, z) = C(k, z) e^{jk_s(1+k^2)z}, \quad (3.70)$$

and initial conditions $C(z = 0) = 0$, we obtain

$$\frac{\partial}{\partial z} C(k, z) = -j \frac{\xi}{z_A} \sum_{m=-\infty}^{\infty} \frac{A_0}{4(k^2 + 1)} \operatorname{sech} \left(\frac{\pi k}{2} \right) e^{-j(k_s(1+k^2) - m \frac{2\pi}{z_A} z)}, \quad (3.71)$$

or

$$\begin{aligned} C(k, z) &= -j \frac{\xi}{z_A} \frac{A_0}{4(k^2 + 1)} \operatorname{sech} \left(\frac{\pi k}{2} \right) \cdot \sum_{m=-\infty}^{\infty} \int_0^z e^{j(-k_s(1+k^2) + m \frac{2\pi}{z_A} z)} dz \\ &= -j \frac{\xi}{z_A} \frac{A_0}{4(k^2 + 1)} \operatorname{sech} \left(\frac{\pi k}{2} \right) \cdot \\ &\quad \sum_{m=-\infty}^{\infty} \frac{e^{j(-k_s(1+k^2) + m \frac{2\pi}{z_A} z)} - 1}{m \frac{2\pi}{z_A} - k_s(1 + k^2)}. \end{aligned} \quad (3.72)$$

There is a resonant denominator, which blows up at certain normalized frequencies k_m for $z \rightarrow \infty$. Those frequencies are given by

$$m \frac{2\pi}{z_A} - k_s(1 + k_m^2) = 0 \quad (3.73)$$

$$\text{or} \quad k_m = \pm \sqrt{\frac{m \frac{2\pi}{z_A}}{k_s} - 1}. \quad (3.74)$$

Removing the normalization by setting $k = \omega\tau$, $k_s = |D_2|/\tau^2$ and introducing the nonlinear phase shift of the soliton acquired over one periode of the perturbation $\phi_0 = k_s z_A$, we obtain a handy formula for the location of the resonant sidebands

$$\omega_m = \pm \frac{1}{\tau} \sqrt{\frac{2m\pi}{\phi_0} - 1}, \quad (3.75)$$

and the coefficients

$$\begin{aligned} C(\omega, z) &= -j \frac{\xi}{z_A} \frac{A_0}{4((\omega\tau)^2 + 1)} \operatorname{sech} \left(\frac{\pi\omega\tau}{2} \right) \\ &\quad \cdot \sum_{m=-\infty}^{\infty} z_A \frac{e^{j(-k_s(1+(\omega\tau)^2) + m \frac{2\pi}{z_A} z)} - 1}{2\pi m - \phi_0(1 + (\omega\tau)^2)}. \end{aligned} \quad (3.76)$$

The coefficients stay bounded for frequencies not equal to the resonant condition and they grow linearly with z_A , at resonance, which leads to a destruction of the pulse. To stabilize the soliton against this growth of resonant

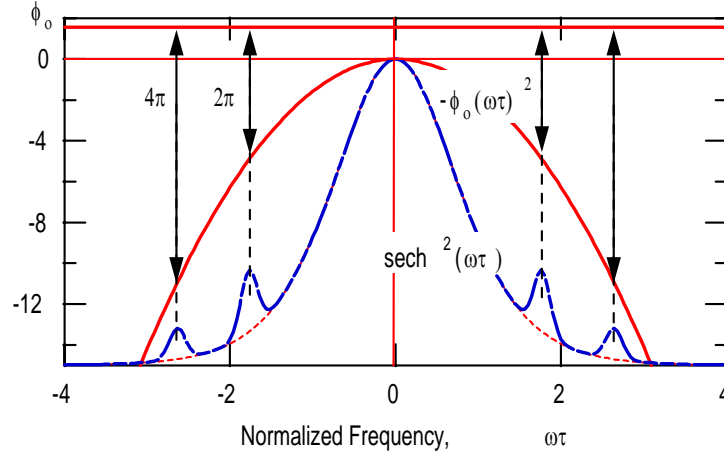


Figure 3.10: Phasematching between soliton and continuum due to periodic perturbations leads to resonant sideband generation. The case shown is for $\phi_0 = \pi/2$.

sidebands, the resonant frequencies have to stay outside the spectrum of the soliton, see Fig. 3.10, which feeds the continuum, i.e. $\omega_m \gg \frac{1}{\tau}$. This condition is only fulfilled if $\phi_0 \ll \pi/4$. This condition requires that the soliton period is much longer than the period of the perturbation. As an example Fig. 3.10 shows the resonant sidebands observed in a fiber laser. For optical communication systems this condition requires that the soliton energy has to be kept small enough, so that the soliton period is much longer than the distance between amplifiers, which constitute periodic perturbations to the soliton. These sidebands are often called Kelly-Sidebands, according to the person who first described its origin properly [30].

To illustrate its importance we discuss the spectrum observed from the longcavity Ti:sapphire laser system illustrated in Figure 3.11 and described in full detail in [37]. Due to the low repetitionrate, a rather large pulse energy builds up in the cavity, which leads to a large nonlinear phase shift per roundtrip. Figure 3.12 shows the spectrum of the output from the laser. The Kelly sidebands are clearly visible. It is this kind of instability, which limits further increase in pulse energy from these systems operating in the soliton pulse shaping regime. Energy is drained from the main pulse into the sidebands, which grow at the expense of the pulse. At some point the

Image removed due to copyright restrictions.

Please see:

Kowalewicz, A. M., et al. "Generation of 150-nJ pulses from a multiple-pass cavity Kerr-lens modelocked Ti:Al₂O₃ oscillator." *Optics Letters* 28 (2003): 1507-09.

Figure 3.11: Schematic layout of a high pulse energy laser cavity. All shaded mirrors are (Double-chirped mirrors) DCMs. The standard 100 MHz cavity with arms of 45 cm and 95 cm extends from the OC to M6 for the short and long arms respectively. The multiple pass cavity (MPC) is enclosed in the dotted box. The pump source is a frequency doubled Nd:Vanadate that produces up to 10W at 532 nm [37].

pulse shaping becomes unstable because of conditions to be discussed in later chapters.

Image removed due to copyright restrictions.

Please see:

Kowalewicz, A. M., et al. "Generation of 150-nJ pulses from a multiple-pass cavity Kerr-lens modelocked Ti:Al₂O₃ oscillator." *Optics Letters* 28 (2003): 1507-09.

Figure 3.12: Measured modelocked spectrum with a 16.5 nm FWHM centered at 788 nm

3.7 Pulse Compression

So far we have discussed propagation of a pulse in negative dispersive media and positive self-phase modulation. Then at large enough pulse energy a soliton can form, because the low and high frequency components generated by SPM in the front and the back of the pulse are slow and fast and therefore catch up with the pulse and stay together. What happens if the dispersion is positive? Clearly, the low and high frequency components generated by SPM in the front and back of the pulse are fast and slow and move away from the pulse in a continuous fashion. This leads to highly but linearly chirped pulse, which can be compressed after the nonlinear propagation by sending it through a linear negative dispersive medium or prism pair or grating pair. In that way, pulses can be compressed by large factors of 3 to 20. This pulse compression process can be formulated in a more general way.

3.7.1 General Pulse Compression Scheme

The general scheme for pulse compression of optical pulses was independently proposed by Gires and Tournois in 1964 [38] and Giordmaine *et al.* in 1968 [39]. The input pulse is first spectrally broadened by a phase modulator. The phase over the generated spectrum is hopefully in a form that can be conveniently removed afterwards, i.e. all spectral components can be rephased to generate a short as possible pulse in the time domain. To compress femtosecond pulses an ultrafast phase modulator has to be used, that is the pulse has to modulate its phase itself by self-phase modulation. In 1969 Fisher *et al.* [40] proposed that picosecond pulses can be compressed to femtosecond duration using the large positive chirp produced around the peak of a short pulse by SPM in an optical Kerr liquid. In the same year Laubereau [41] used several cells containing CS₂ and a pair of diffraction gratings to compress, by approximately ten times, 20-ps pulses generated by a mode-locked Nd:glass laser.

As discussed in section 3.2, the optical Kerr effect in a medium gives rise to an intensity dependent change of the refractive index $\Delta n = n_{2,L}I(t)$, where $n_{2,L}$ is the nonlinear-index coefficient and $I(t)$ is the optical intensity. The self-induced intensity-dependent nonlinear phase shift experienced by an optical field during its propagation in a Kerr medium of length ℓ is given by $\Delta\phi(t) = -(\omega_0/c)n_2I(t)\ell$ where ω_0 is the carrier frequency of the pulse. The induced frequency sweep over the pulse can be calculated from

Image removed due to copyright restrictions.

Please see:

Nakatsuka, H., D. Grischkowsky, and A. C. Balant. "Nonlinear picosecond-pulse propagation through optical fibers with positive group velocity dispersion." *Physics Review Letters* 47 (1981): 910-913.

Figure 3.13: Intensity profile, spectrum, instantaneous frequency, optimum quadratic compression and ideal compression for two cases: top row for a short fiber, i.e. high nonlinearity and low dispersion; bottom row optimum nonlinearity and dispersion.[42]

$\Delta\omega = d\Delta\phi/dt$, see Figure 3.13. Around the central part of the pulse, where most of the energy is concentrated, the phase is parabolic, leading to an approximately linear chirp in frequency. The region with linear chirp can be enlarged in the presence of positive dispersion in a Kerr medium of the same sign [42]. To compress the spectrally broadened and chirped pulse, a dispersive delay line can be used, characterized by a nearly linear group delay $T_g(\omega)$. Or if the chirp generated over the newly generated spectrum is nonlinear this chirp needs to be removed by a correspondingly nonlinear group delay $T_g(\omega)$. Figure 3.13 shows that in the case SPM and positive GDD a smoother spectrum with more linear chirp is created and therefore the final compressed pulse is of higher quality, i.e. a higher percentage of the total pulse energy is really concentrated in the short pulse and not in a large uncompressed pulse pedestal.

For a beam propagating in a homogenous medium, unfortunately the nonlinear refractive index does not only lead to a temporal phase modulation but also to a spatial phase modulation, which leads to self-focusing or defocusing and small-scale instabilities [43]. Therefore, a fundamental requirement

for pulse compression is that the Kerr effect is provided by a guiding non-linear medium so that a spatially uniform spectral broadening is obtained. In 1974 Ippen *et al.* reported the first measurement of SPM in the absence of self-trapping and self-focusing by using a guiding multimode optical fiber filled with liquid CS₂ [44]. In 1978 Stolen and Lin reported measurements of SPM in single-mode silica core fibers [45]. The important advantage of the single-mode fiber is that the phase modulation can be imposed over the entire transverse profile of the beam, thus removing the problem of unmodulated light in the wings of the beam [44]. In 1981 Nakatsuka *et al.* [42] performed the first pulse compression experiment using fibers as a Kerr medium in the positive dispersion region.

3.7.2 Spectral Broadening with Guided Modes

The electric field of a guided mode can be written as [52]:

$$E(\mathbf{r}, \omega) = A(z, \omega)F(x, y) \exp[i\beta(\omega)z] \quad (3.77)$$

where $A(z, \omega)$ is the mode-amplitude for a given frequency component, $F(x, y)$ is the mode-transverse field distribution and $\beta(\omega)$ is the mode-propagation constant. The propagation equation for the guided field splits into two equations for amplitude $A(z, \omega)$ and field pattern $F(x, y)$. In first order perturbation theory a perturbation $\Delta n = \bar{n}_2|E|^2$ of the refractive index, which is much smaller than the index step that defines the mode, does not change the modal distribution $F(x, y)$, while the mode propagation constant $\bar{\beta}(\omega)$ can be written as $\bar{\beta}(\omega) = \beta(\omega) + \Delta\beta$, where the perturbation $\Delta\beta$ is given by

$$\Delta\beta = \frac{(\omega_0/c) \int \int \Delta n |F(x, y)|^2 dx dy}{\int \int |F(x, y)|^2 dx dy}. \quad (3.78)$$

As shown by Eq.(3.78), the perturbation $\Delta\beta$, which includes the effect due to the fiber nonlinearity, is related to a spatial average on the fiber transverse section of the perturbation Δn . In this way, spatially uniform SPM is realized.

Using regular single mode fibers and prism-grating compressors, pulses as short as 6 fs at 620 nm were obtained in 1987 from 50-fs pulses generated by a colliding-pulse mode-locking dye laser [46] see Figure 3.14. More recently, 13-fs pulses from a cavity-dumped Ti:sapphire laser were compressed to 4.5

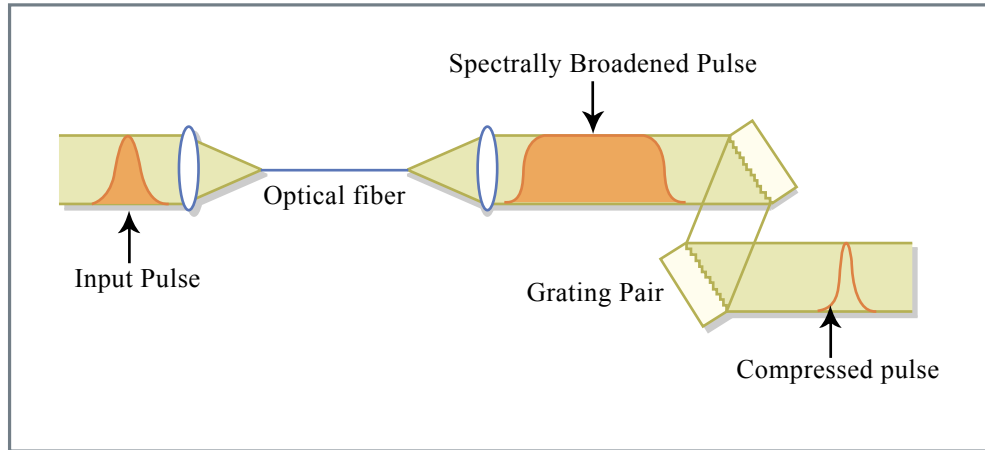


Figure 3.14: Fiber-grating pulse compressor to generate femtosecond pulses [53]

Figure by MIT OCW.

fs with the same technique using a compressor consisting of a quartz 45°-prism pair, broadband chirped mirrors and thin-film Gires-Tournois dielectric interferometers [47, 54]. The use of a single-mode optical fiber limits the pulse energy to a few nanojoule.

In 1996, using a phase modulator consisting of a hollow fiber (leaky waveguide) filled with noble gas, a powerful pulse compression technique has been introduced, which handles high-energy pulses [48]. The implementation of the hollow-fiber compression technique using 20-fs seed pulses from a Ti:sapphire system and chirped-mirrors that form a dispersive delay line has led to the generation of pulses with duration down to 4.5 fs [49] and energy up to 0.55 mJ [50]. This technique presents the advantages of a guiding element with a large-diameter mode and of a fast nonlinear medium with high damage threshold.

The possibility to take advantage of the ultrabroadband spectrum which can be generated by the phase modulation process, is strictly related to the development of dispersive delay lines capable of controlling the frequency-dependent group delay over such bandwidth.

3.7.3 Dispersion Compensation Techniques

The pulse frequency sweep (chirp) imposed by the phase modulation is approximately linear near the peak of the pulse, where most of the energy is concentrated. In the presence of dispersion in the phase modulator the chirp becomes linear over almost the whole pulse. Therefore, optimum temporal compression requires a group delay, $T_{g,comp}(\omega) = \partial\phi/\partial\omega$, characterized by a

nearly linear dependence on frequency in the dispersive delay line. Since in the case of SPM the nonlinear index n_2 is generally positive far from resonance, a negative group delay dispersion ($GDD = \partial T_g / \partial \omega$) is required in the compressor. In order to generate the shortest pulses, the pulse group delay after the phase modulator and the compressor must be nearly frequency independent. $T_g(\omega)$ can be expanded into a Taylor series around the central frequency ω_0 :

$$T_g(\omega) = \phi'(\omega_0) + \phi''(\omega_0)\Delta\omega + \frac{1}{2}\phi'''(\omega_0)\Delta\omega^2 + \frac{1}{3!}\phi''''(\omega_0)\Delta\omega^3 + \dots \quad (3.79)$$

where $\Delta\omega = \omega - \omega_0$, and $\phi''(\omega_0)$, $\phi'''(\omega_0)$, and $\phi''''(\omega_0)$ are the second-, the third-, and the fourth-order-dispersion terms, respectively. Critical values of these dispersion terms above which dispersion causes a significant change of the pulse are given by a simple scaling expression: $\phi^{(n)} = \tau_p^n$, where $\phi^{(n)}$ is the n th-order dispersion term and τ_p is the pulse duration. For example, a second order dispersion with $\phi'' = \tau_p^2$ results in a pulse broadening by more than a factor of two. Therefore dispersion-induced pulse broadening and distortion become increasingly important for decreasing pulse durations. Equation (3.79) shows that to compress a pulse to near the transform limit one should eliminate these high order dispersion terms. For instance, assuming a transform-limited input pulse to the phase modulator, the condition for third-order-dispersion-compensated compression is the following:

$$\phi''(\omega_0) = \phi''_{\text{modulator}} + \phi''_{\text{compressor}} = 0 \quad (3.80)$$

$$\phi'''(\omega_0) = \phi'''_{\text{modulator}} + \phi'''_{\text{compressor}} = 0 \quad (3.81)$$

Several compressor schemes have been developed so far that included such components as: diffraction gratings, Brewster-cut prism pairs, combination of gratings and prisms, thin prisms and chirped mirrors, and chirped mirrors only, etc. In the following we will briefly outline the main characteristics of these compressor schemes.

Grating and Prism Pairs

In 1968 Treacy demonstrated for the first time the use of a pair of diffraction gratings to achieve negative GDD [55]. In 1984 Fork et al. obtained negative GDD with pairs of Brewster-angled prisms [56]. Prism pairs have been widely used for dispersion control inside laser oscillators since they can be very low

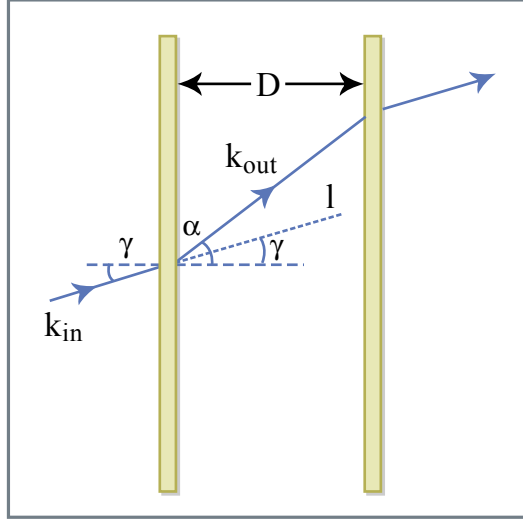


Figure 3.15: Optical path difference in a two-element dispersive delay line [107]

Figure by MIT OCW.

loss in contrast to grating pairs. In both optical systems the origin of the adjustable dispersion is the angular dispersion that arises from diffraction and refraction, respectively. The dispersion introduced by these systems can be easily calculated, by calculating the phase accumulated between the input and output reference planes [78]. To understand the main properties of these systems, we will refer to Fig. 3.15. The first element scatters the input beam with wave vector \mathbf{k}_{in} and input path vector \mathbf{l} into the direction \mathbf{k}_{out} . The beam passes between the first and the second element and is scattered back into its original direction. The phase difference by the scattered beam and the reference beam without the grating is: $\phi(\omega) = \mathbf{k}_{out}(\omega) \cdot \mathbf{l}$. Considering free-space propagation between the two elements, we have $|\mathbf{k}_{out}| = \omega/c$, and the accumulated phase can be written as

$$\phi(\omega) = \frac{\omega}{c} |\mathbf{l}| \cos[\gamma - \alpha(\omega)] = \frac{\omega}{c} \frac{D}{\cos(\gamma)} \cos[\gamma - \alpha(\omega)] \quad (3.82)$$

where: γ is the angle between the incident wave vector and the normal to the first element; α is the angle of the outgoing wave vector, which is a function of frequency; D is the spacing between the scattering elements along a direction parallel to their normal. In the case of a grating pair the frequency dependence of the diffraction angle α is governed by the grating

law, that in the case of first-order diffraction is given by:

$$\frac{2\pi c}{\omega} = d[\sin \alpha(\omega) - \sin \gamma] \quad (3.83)$$

where d is the groove spacing of the grating. Using Eq.(3.82) and Eq.(3.83), it is possible to obtain analytic expressions for the GDD and the higher-order dispersion terms (for single pass):

$$\phi''(\omega) = -\frac{4\pi^2 c D}{\omega^3 d^2 \cos^3 \alpha(\omega)} \quad (3.84)$$

$$\phi'''(\omega) = \frac{12\pi^2 c D}{\omega^4 d^2 \cos^3 \alpha(\omega)} \left(1 + \frac{2\pi c \sin \alpha(\omega)}{\omega d \cos^2 \alpha(\omega)} \right) \quad (3.85)$$

It is evident from Eq.(3.84) that grating pairs give negative dispersion. D is the distance between the gratings. A disadvantage of the grating pair is the diffraction loss. For a double-pass configuration the loss is typically 75%. Also the bandwidth for efficient diffraction is limited.

In the case of a Brewster-angled prism pair Eq.(3.82) reduces to the following expression (for single pass) [56]:

$$\phi(\omega) = \frac{\omega}{c} \ell_p \cos \beta(\omega) \quad (3.86)$$

where ℓ_p is the distance between prism apices and $\beta(\omega)$ is the angle between the refracted ray at frequency ω and the line joining the two apices. The second and third order dispersion can be expressed in terms of the optical path $P(\lambda) = \ell_p \cos \beta(\lambda)$:

$$\phi''(\omega) = \frac{\lambda^3}{2\pi c^2} \frac{d^2 P}{d\lambda^2} \quad (3.87)$$

$$\phi'''(\omega) = -\frac{\lambda^4}{4\pi^2 c^3} \left(3 \frac{d^2 P}{d\lambda^2} + \lambda \frac{d^3 P}{d\lambda^3} \right) \quad (3.88)$$

with the following derivatives of the optical path with respect to wavelength evaluated at Brewster's angle:

$$\frac{d^2 P}{d\lambda^2} = 2[n'' + (2n - n^{-3})(n')^2] \ell_p \sin \beta - 4(n')^2 \ell_p \cos \beta \quad (3.89)$$

$$\begin{aligned} \frac{d^3 P}{d\lambda^3} = & [6(n')^3(n^{-6} + n^{-4} - 2n^{-2} + 4n^2) + 12n'n''(2n - n^{-3}) \\ & + 2n'''] \ell_p \sin \beta + 12[(n^{-3} - 2n)(n')^3 - n'n''] \ell_p \cos \beta \end{aligned} \quad (3.90)$$

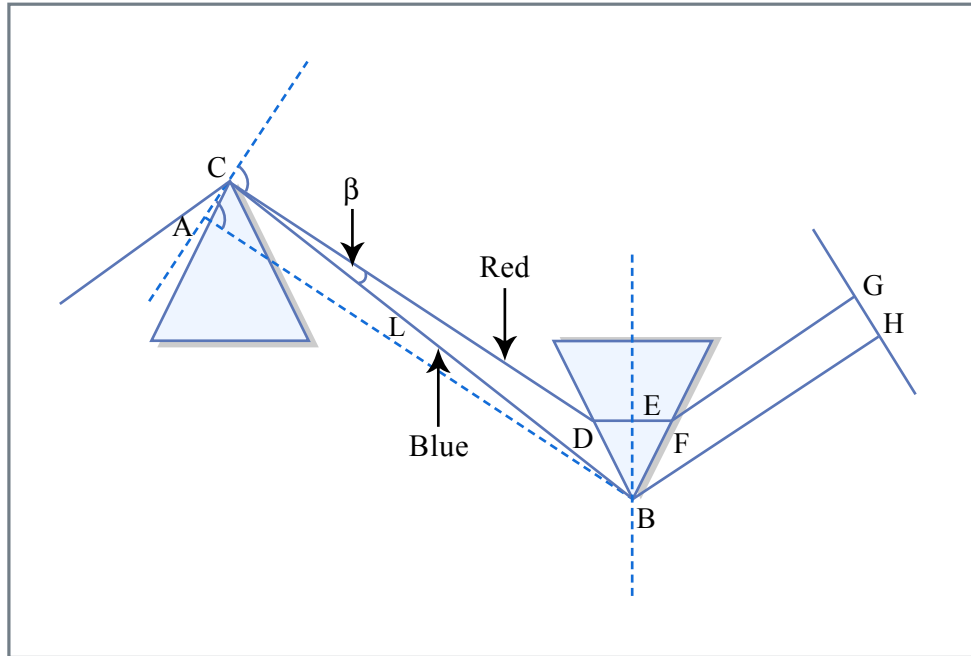


Figure 3.16: Prism pair for dispersion compensation. The blue wavelengths have less material in the light path than the red wavelengths. Therefore, blue wavelengths are less delayed than red wavelength

Figure by MIT OCW.

where n is the refractive index of the prism material; n' , n'' and n''' are respectively, the first-, second- and third-order derivatives of n , with respect to wavelength. The prism-compressor has the advantage of reduced losses. Using only fused silica prisms for dispersion compensation, sub-10-fs light pulses have been generated directly from an oscillator in 1994 [79]. In 1996, pulses with tens of microjoules energy, spectrally broadened in a gas-filled hollow fiber were compressed down to 10 fs using a prism compressor [48]. Both in the case of grating and prism pairs, negative GDD is associated with a significant amount of higher-order dispersion, which cannot be lowered or adjusted independently of the desired GDD, thus limiting the bandwidth over which correct dispersion control can be obtained. This drawback has been only partially overcome by combining prism and grating pairs with third-order dispersion of opposite sign. In this way pulses as short as 6 fs have been generated in 1987 [46], and less than 5 fs in 1997 [47], by external compression. This combination cannot be used for few-optical-cycle pulse generation either in laser oscillators, due to the high diffraction losses of the gratings, or in external compressors at high power level, due to the onset of

unwanted nonlinearities in the prisms.

3.7.4 Dispersion Compensating Mirrors

Chirped mirrors are used for the compression of high energy pulses, because they provide high dispersion with little material in the beam path, thus avoiding nonlinear effects in the compressor.

Grating and prism compressors suffer from higher order dispersion. In 1993 Robert Szipoecs and Ferenc Krausz [80] came up with a new idea, so called chirped mirrors. Laser mirrors are dielectric mirrors composed of alternating high and low index quarter wavelenth thick layers resulting in strong Bragg-reflection. In chirped mirrors the Bragg wavelength is chirped so that different wavelength penetrate different depth into the mirror upon reflection giving rise to a wavelength dependent group delay. It turns out that the generation of few-cycle pulses via external compression [95] as well as direct generation from Kerr lens mode-locked lasers [58] relies heavily on the existence of chirped mirrors [57, 83, 59] for dispersion compensation. There are two reasons to employ chirped mirrors . First the high-reflectivity bandwidth, Δf , of a standard dielectric Bragg-mirror is determined by the Fresnel reflectivity r_B of the high, n_H , and low, n_L , index materials used for the dielectric mirror

$$r_B = \frac{\Delta f}{f_c} = \frac{n_H - n_L}{n_H + n_L} \quad (3.92)$$

where f_c is again the center frequency of the mirror. Metal mirrors are in general too lossy, especially when used as intracavity laser mirrors. For material systems typically used for broadband optical coatings such as Silicon Dioxide and Titanium Dioxide with $n_{SiO_2} = 1.48$ and $n_{TiO_2} = 2.4$, (these indexes might vary depending on the deposition technique used), a fractional bandwidth $\Delta f/f_c = 0.23$ can be covered. This fractional bandwidth is only about a third of an octave spanning mirror $\Delta f/f_c = 2/3$. Furthermore, the variation in group delay of a Bragg-mirror impacts already pulses that fill half the spectral range $\Delta f = 0.23f_c$. A way out of this dilemma was found by introducing chirped mirrors [57], the equivalent of chirped fiber Bragg gratings, which at that time were already well developed components in fiber optics [60]. When the Bragg wavelength of the mirror stack is varied slowly enough and no limitation on the number of layer pairs exists, an arbitrary high reflectivity range of the mirror can be engineered. The second reason for using chirped mirrors is based on their dispersive properties due to the

wavelength dependent penetration depth of the light reflected from different positions inside the chirped multilayer structure. Mirrors are filters, and in the design of any filter, the control of group delay and group delay dispersion is difficult. This problem is further increased when the design has to operate over wavelength ranges up to an octave or more.

The matching problem Several designs for ultra broadband dispersion compensating mirrors have been developed over the last years. For dispersion compensating mirrors which do not extend the high reflectivity range far beyond what a Bragg-mirror employing the same materials can already achieve, a multi-cavity filter design can be used to approximate the desired phase and amplitude properties [61, 62]. For dispersion compensating mirrors covering a high reflectivity range of up to $\Delta f/f_c = 0.4$ the concept of double-chirped mirrors (DCMs) has been developed [83][81]. It is based on the following observations. A simple chirped mirror provides high-reflectivity over an arbitrary wavelength range and, within certain limits, a custom designable average group delay via its wavelength dependent penetration depth [73] (see Figure 3.17 (a) and (b)). However, the group delay as a function of frequency shows periodic variations due to the impedance mismatch between the ambient medium and the mirror stack, as well as within the stack (see Figure 3.17 b and Figure 3.18). A structure that mitigates these mismatches and gives better control of the group delay dispersion (GDD) is the double-chirped mirror (DCM) (Figure 3.17 c), in a way similar to that of an apodized fiber Bragg grating [64].

Figure 3.18 shows the reflectivity and group delay of several Bragg and chirped mirrors composed of 25 index steps, with $n_H = 2.5$ and $n_L = 1.5$, similar to the refractive indices of TiO_2 and SiO_2 , which result in a Fresnel reflectivity of $r_B = 0.25$. The Bragg-mirror can be decomposed in symmetric index steps [83]. The Bragg wavenumber is defined as $k_B = \pi/(n_L d_L + n_H d_H)$, where d_L and d_H are the thicknesses of the low and high index layer, respectively. The Bragg wavenumber describes the center wavenumber of a Bragg mirror composed of equal index steps. In the first case, (Figure 3.18, dash-dotted line) only the Bragg wave number is linearly chirped from $6.8\mu\text{m}^{-1} < k_B < 11\mu\text{m}^{-1}$ over the first 20 index steps and held constant over the last 5 index steps. The reflectivity of the structure is computed assuming the structure imbedded in the low index medium. The large oscillations in the group delay are caused by the different impedances of the chirped

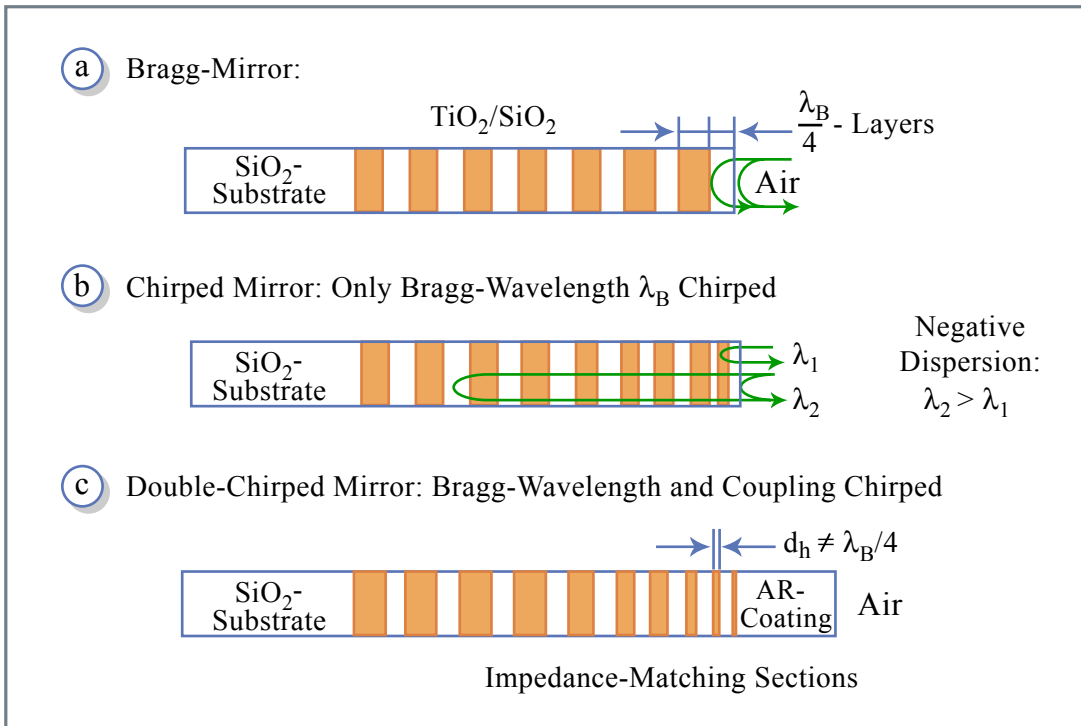


Figure 3.17: a) Standard Bragg mirror; (b) Simple chirped mirror, (c) Double-chirped mirror with matching sections to avoid residual reflections causing undesired oscillations in the GD and GDD of the mirror.

Figure by MIT OCW.

grating and the surrounding low index material causing a strong reflection at the interface of the low index material and the grating stack. By adiabatic matching of the grating impedance to the low index material this reflection can be avoided. This is demonstrated in Fig. 3.18 by the dashed and solid curves, corresponding to an additional chirping of the high index layer over the first 12 steps according to the law $d_H = (m/12)^\alpha \lambda_{B,12}/(4n_H)$ with $\alpha = 1$, and 2, for linear and quadratic adiabatic matching. The argument m denotes the m -th index step and $\lambda_{B,12} = 0.740\mu\text{m}$. The strong reduction of the oscillations in the group delay by the double-chirp technique is clearly visible. Quadratic tapering of the high index layer, and therefore, of the grating already eliminates the oscillations in the group delay completely, which can also be shown analytically by coupled mode analysis [81]. Because of the double chirp a high transmission window at the short wavelength end of the mirror opens up which is ideally suited for the pumping of Ti:sapphire lasers. So far, the double-chirped mirror is only matched to the low index material of the mirror. Ideally, the matching can be extended to any other ambient medium by a properly designed AR-coating. However, this AR-coating has to be of very high quality, i.e. very low residual reflectivity ideally a power

Image removed due to copyright restrictions.

Please see:

Kaertner, F. X., et al. "Design and fabrication of double-chirped mirrors." *Optics Letters* 15 (1990): 326-328.

Figure 3.18: Comparison of the reflectivity and group delay of chirped mirrors with 25 layer pairs and refractive indices $n_H = 2.5$, and $n_L = 1.5$. The upper portion shows the enlarged top one percent of the reflectivity. The dotted curves show the result for a simple chirped mirror. The dashed and solid curves show the result for double-chirped mirrors where in addition to the chirp in the Bragg wave number k_B the thickness of the high-index layers is also chirped over the first 12 layer pairs from zero to its maximum value for a linear chirp, i.e. $\alpha = 1$, (dashed curves) and for a quadratic chirp, i.e. $\alpha = 2$ (solid curves). [83].

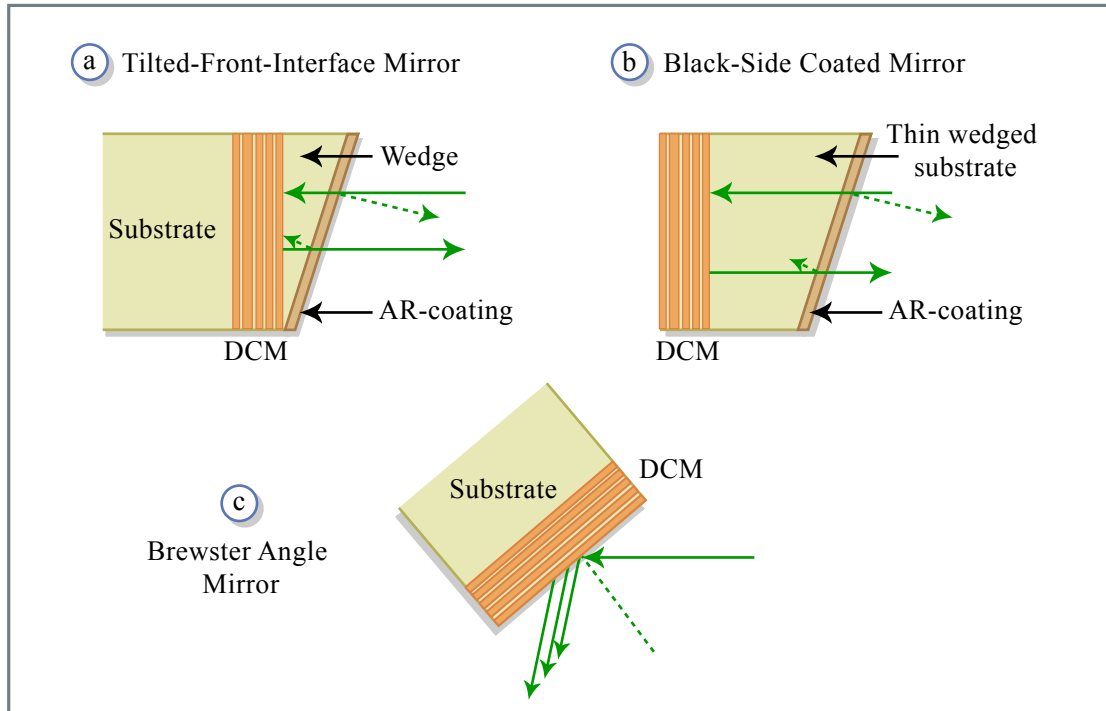


Figure 3.19: Schematic structure of proposed broadband dispersion compensating mirror system avoiding the matching to air: (a) tilted-front-interface mirror; (b) back-side coated mirror and (c) Brewster-angle mirror.

Figure by MIT OCW.

reflectivity of 10^{-4} , i.e. an amplitude reflectivity of $r = 10^{-2}$ is required. The quality of the AR-coating can be relaxed, if the residual reflection is directed out of the beam path. This is achieved in so called tilted front-side or back-side coated mirrors [65], [66], (Fig. 3.19 (a) and (b)). In the back-side coated mirror the ideal DCM structure, which is matched to the low index material of the mirror is deposited on the back of a substrate made of the same or at least very similar low index material. The AR-coating is deposited on the front of the slightly wedged substrate, so that the residual reflection is directed out of the beam and does not affect the dispersion properties. Thus the task of the AR-coating is only to reduce the Fresnel losses of the mirror at the air-substrate interface, and therefore, it is good enough for some applications, if the residual reflection at this interface is of the order of 0.5%. However, the substrate has to be very thin in order to keep the overall mirror dispersion negative, typically on the order of 200-500 μm . Laser grade quality optics are hard to make on such thin substrates and the stress induced by the coating leads to undesired deformation of the substrates. The front-side coated mirror overcomes this shortcoming

by depositing the ideal DCM-structure matched to the index of the wedge material on a regular laser grade substrate. A 100-200 μm thin wedge is bonded on top of the mirror and the AR-coating is then deposited on this wedge. This results in stable and octave spanning mirrors, which have been successfully used in external compression experiments [69]. Both structures come with limitations. First, they introduce a wedge into the beam, which leads to an undesired angular dispersion of the beam. This can partially be compensated by using these mirrors in pairs with oppositely oriented wedges. The second drawback is that it seems to be impossible to make high quality AR-coatings over one or more than one octave of bandwidth, which have less than 0.5% residual reflectivity [68], i.e. on one reflection such a mirror has at least 1% of loss, and, therefore, such mirrors cause high losses inside a laser. For external compression these losses are acceptable. A third possibility for overcoming the AR-coating problem is given by using the ideal DCM under Brewster-angle incidence, (Figure 3.19) [67]. In that case, the low index layer is automatically matched to the ambient air. However, under p-polarized incidence the index contrast or Fresnel reflectivity of a layer pair is reduced and more layer pairs are necessary to achieve high reflectivity. Also the penetration depth into the mirror increased, so that scattering and other losses in the layers become more pronounced. On the other hand, such a mirror can generate more dispersion per bounce due to the higher penetration depth. For external compression such mirrors might have advantages because they can cover bandwidths much wider than one octave. This concept is difficult to apply to the fabrication of curved mirrors. There is also a spatial chirp of the reflected beam, which may become sizeable for large penetration depth and has to be removed by back reflection or an additional bounce on another Brewster-angle mirror, that recombines the beam. For intracavity mirrors a way out of this dilemma is found by mirror pairs, which cancel the spurious reflections due to an imperfect AR-coating and matching structure in the chirped mirror [76]. Also this design has its drawbacks and limitations. It requires a high precision in fabrication and depending on the bandwidth of the mirrors it may be only possible to use them for a restricted range of angles of incidence.

Double-chirped mirror pairs

There have been several proposals to increase the bandwidth of laser mirrors by mutual compensation of GDD oscillations [70, 71, 72] using computer

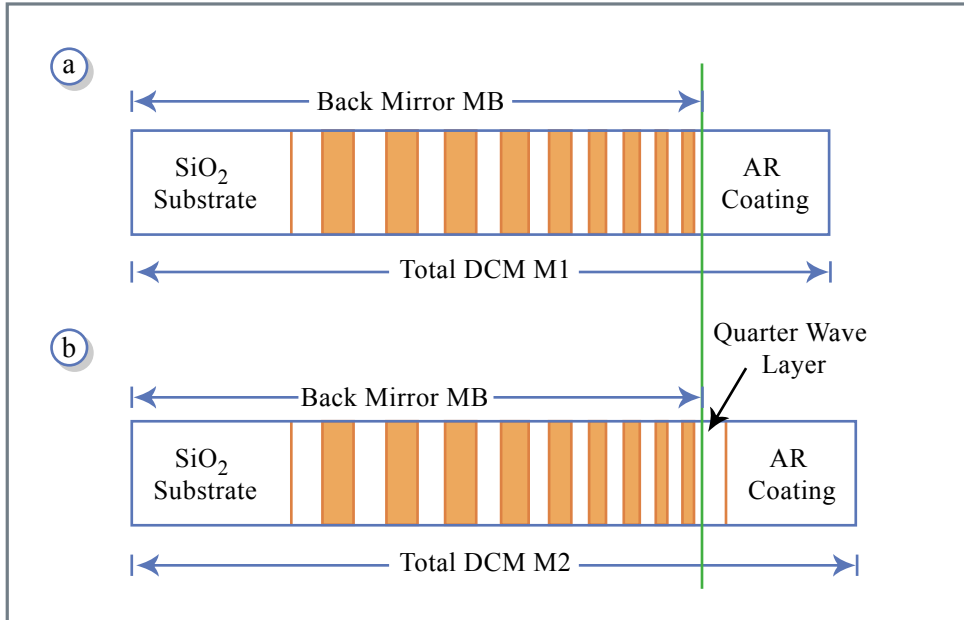


Figure 3.20: DCM-Pair M1 (a) and M2 (b). The DCM M1 can be decomposed in a double-chirped back-mirror MB matched to a medium with the index of the top most layer. In M2 a layer with a quarter wave thickness at the center frequency of the mirror and an index equivalent to the top most layer of the back-mirror MB is inserted between the back-mirror and the AR-coating. The new back-mirror comprising the quarter wave layer can be reoptimized to achieve the same phase as MB with an additional π -phase shift over the whole octave of bandwidth.

Figure by MIT OCW.

optimization. These early investigations resulted in a rather low reflectivity of less than 95% over almost half of the bandwidth considered. The ideas leading to the DCMs help us to show analytically that a design of DCM-pairs covering one octave of bandwidth, i.e. 600 nm to 1200 nm, with high reflectivity and improved dispersion characteristics is indeed possible [76]. Use of these mirror pairs in a Ti:sapphire laser system resulted in 5 fs pulses with octave spanning spectra directly from the laser [58]. Yet, the potential of these pairs is by no means fully exploited.

A DCM-Pair, see Fig. 3.20, consists of a mirror M1 and M2. Each is composed of an AR-coating and a low-index matched double-chirped back-mirror MB with given wavelength dependent penetration depth. The high reflectivity range of the back-mirror can be easily extended to one octave by simply chirping slowly enough and using a sufficient number of layer pairs.

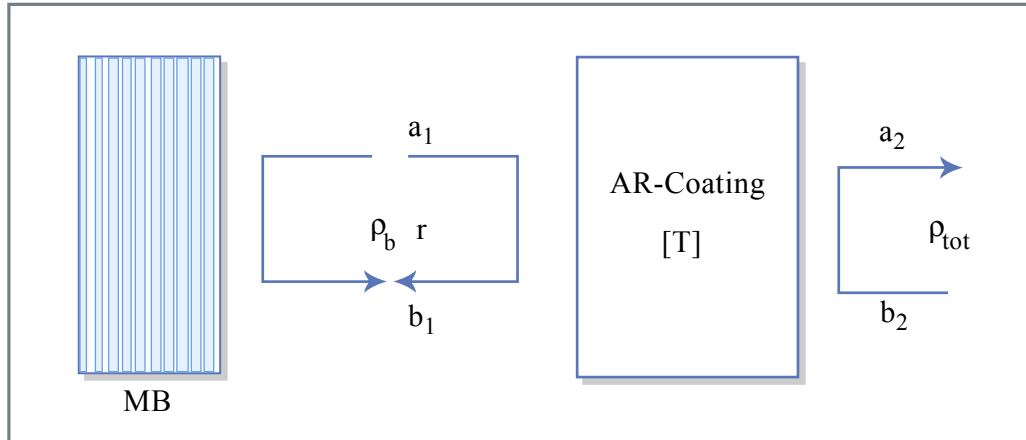


Figure 3.21: Decomposition of a DCM into a double-chirped backmirror MB and an AR-coating.

Figure by MIT OCW.

However, the smoothness of the resulting GDD strongly depends on the quality of matching provided by the AR-coating and the double-chirped section. Fig. 3.21 indicates the influence of the AR-coating on the GDD of the total DCM-structure. The AR-coating is represented as a two - port with two incoming waves a_1, b_2 and two outgoing waves a_2, b_1 . The connection between the waves at the left port and the right port is described by the transfer matrix

$$\begin{pmatrix} a_1 \\ b_1 \end{pmatrix} = T_{ar} \begin{pmatrix} a_2 \\ b_2 \end{pmatrix} \quad \text{with} \quad T_{ar} = \begin{pmatrix} \frac{1}{t} & \frac{r^*}{t^*} \\ \frac{r}{t} & \frac{1}{t^*} \end{pmatrix} \quad (3.93)$$

where we assumed that the multilayer AR-coating is lossless. Here, r and t are the complex coefficients for reflection and transmission at port 1 assuming reflection free termination of port 2. The back-mirror MB, is assumed to be perfectly matched to the first layer in the AR-coating, has full reflection over the total bandwidth under consideration. Thus its complex reflectivity in the range of interest is given by

$$\rho_b = e^{j\phi_b(\omega)} \quad (3.94)$$

The phase $\phi_b(\omega)$ is determined by the desired group delay dispersion

$$GDD_b = -d^2\phi_b(\omega)/d\omega^2 \quad (3.95)$$

up to an undetermined constant phase and group delay at the center frequency of the mirror, ω_c . All higher order derivatives of the phase are determined by the desired dispersion of the mirror. Analytic formulas for the design of DCMs, showing custom designed dispersion properties without considering the matching problem to the ambient air, can be found in [73].

The resulting total mirror reflectivity including the AR-coating follows from (3.93)

$$\rho_{tot} = \frac{t}{t^*} \rho_b \frac{1 - r^*/\rho_b}{1 - r\rho_b} \quad (3.96)$$

For the special case of a perfectly reflecting back-mirror according to Eq. (3.94) we obtain

$$\rho_{tot} = \frac{t}{t^*} e^{j\phi_b(\omega)} \frac{1 - z^*}{1 - z}, \quad \text{with } z = r e^{j\phi_b(\omega)} \quad (3.97)$$

The new reflectivity is again unity but new contributions in the phase of the resulting reflectivity appear due to the imperfect transmission properties of the AR-coating. With the transmission coefficient of the AR-coating

$$t = |t| e^{j\phi_t}, \quad (3.98)$$

The total phase of the reflection coefficient becomes

$$\phi_{tot} = 2\phi_t + \phi_b(\omega) + \phi_{GTI} \quad (3.99)$$

with

$$\phi_{GTI} = 2 \arctan \left[\frac{\text{Im}\{z\}}{1 + \text{Re}\{z\}} \right] \quad (3.100)$$

Here, ϕ_t is the phase of the transmission coefficient and ϕ_{GTI} is the phase due to the Gire-Tournois interferometer created by the non-perfect AR-coating, i.e. $r \neq 0$, and the back-mirror MB, (Figure 3.21). The phase ϕ_t of a good AR-coating, i.e. $|r| < 0.1$, is linear and, therefore, does not introduce undesired oscillations into the GD and GDD. However, the phase ϕ_{GTI} is rapidly varying since $\phi_b(\omega)$ varies over several 2π over the frequency range of interest due to the monotonic group delay of the back-mirror. The size of these oscillations scale with the quality of the AR-coating, i.e. with $|r|$. Thus, the GDD oscillations are reduced with smaller residual reflectivity of the AR-coating. Assuming, that the reflectivity r is real and smaller or equal to 0.1, the oscillations in the group delay and group delay dispersion are easily estimated by

$$T_{g,GTI} = \frac{d\phi_{GTI}}{d\omega} \approx -r T_{gb}(\omega) \cos[\phi_b(\omega)] \quad (3.101)$$

with

$$\begin{aligned} T_{gb}(\omega) &= -d\phi_b(\omega)/d\omega, \\ GDD_{GTI} &= \frac{d^2\phi_{GTI}}{d\omega^2} \\ &\approx r (T_{gb}^2(\omega) \sin[\phi_b(\omega)] - GDD_b \cos[\phi_b(\omega)]) \end{aligned} \quad (3.102)$$

The GTI-reflections add up coherently when multiple reflections on chirped mirrors occur inside the laser over one round-trip, leading to pre- and post pulses if the mode-locking mechanism is not strong enough to suppress them sufficiently. Experimental results indicate that a residual reflection in the AR-coating of $r < 0.01$ and smaller, depending on the number of reflections per round-trip, is required so that the pre- and post pulses are sufficiently suppressed. This corresponds to an AR-coating with less than 10^{-4} residual power reflectivity, which can only be achieved over a very limited range, as discussed above.

Over a limited wavelength range of 350 nm centered around 800 nm low residual power reflectivities as small as 10^{-4} have been achieved effectively after reoptimization of the AR-coating section and the double-chirped section to form a combined matching section of higher matching quality. For even larger bandwidth, approaching an octave, a residual power reflectivity of 10^{-4} is no longer possible [68]. A way out of this limitation is offered by the observation, that a coherent subtraction of the pre- and post-pulses to first order in r is possible by reflections on a mirror pair M1 and M2, see Figure 3.20 (a) and (b). A series of two reflections on a mirror with reflectivity (3.97) and on a similar mirror with an additional phase shift of π between the AR-coating and the back-mirror, having a reflectivity (3.97) where z is replaced by $-z$, leads to a coherent subtraction of the first order GTI-effects. The resulting total reflectivity of the two reflections is given by the product of the individual complex reflectivities assuming the same AR-coating

$$\rho_{tot,2} = - \left(\frac{t}{t^*} \right)^2 e^{i2\phi_b(\omega)} \frac{1 - z^{*2}}{1 - z^2} \quad (3.103)$$

Now, the GTI-effects scale like the power reflectivity of the AR-coating r^2 instead of the amplitude reflectivity r , which constitutes a tremendous improvement, since it is possible to design AR-coatings to the low index material SiO_2 of the mirror with a residual power reflectivity between 0.001 and 0.01 while covering one octave of bandwidth [68]. However, there does not exist a single physical layer which generates a phase shift of $\pi/2$ during one passage for all frequency components contained in an octave. Still, a layer with a quarter wave thickness at the center frequency is a good starting design. Then the back-mirror MB in the Mirror M2 can be reoptimized to take care of the deviation from a quarter wave thickness further away from the center frequency, because the back-mirror acts as a highly dispersive medium where the phase or group delay can be designed at will.

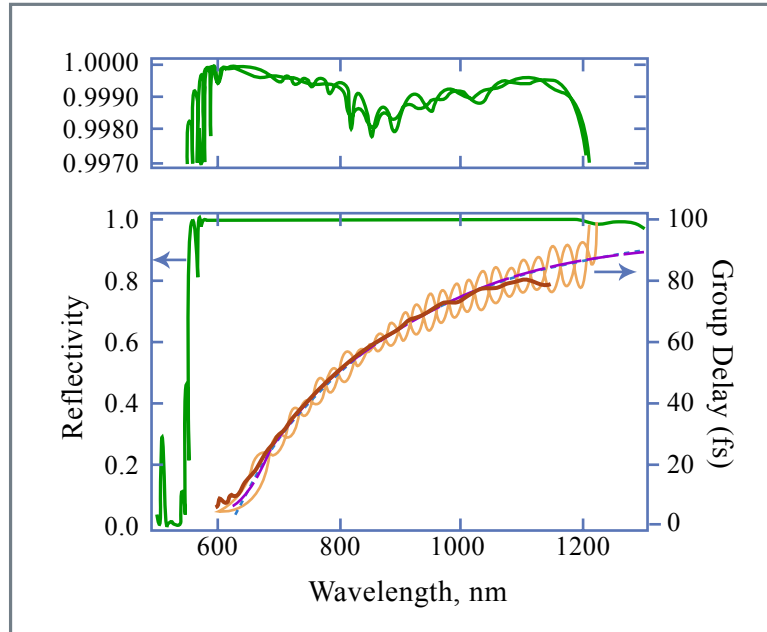


Figure 3.22: Reflectivity of the mirror with pump window shown as thick solid line with scale to the left. The group delay design goal for perfect dispersion compensation of a prismless Ti:sapphire laser is shown as thick dash-dotted line with scale to the right. The individual group delay of the designed mirrors is shown as thin line and its average as a dashed line, which is almost identical with the design goal over the wavelength range from 650-1200 nm. The measured group delay, using white light interferometry, is shown as the thick solid line from 600-1100 nm. Beyond 1100nm the sensitivity of Si-detector used prevented further measurements.

Figure by MIT OCW.

Figure 3.23 shows in the top graph the designed reflectivity of both mirrors of the pair in high resolution taking into account the absorption in the layers. The graph below shows the reflectivity of the mirror, which has in addition high transmission between 510-550 nm for pumping of the Ti:sapphire crystal. Each mirror consists of 40 layer pairs of SiO₂ and TiO₂ fabricated using ion-beam sputtering [74, 75]. Both mirror reflectivities cover more than one octave of bandwidth from 580 nm to 1200 nm or 250 to 517 THz, with an average reflectivity of about 99.9% including the absorption in the layers. In addition, the mirror dispersion corrects for the second and higher order dispersion of all intracavity elements such as the Ti:sapphire crystal and the thin, small angle, BaF₂ wedges, for fine adjustment of the dispersion from 650 nm to 1200 nm within the 12 bounces occurring in one roundtrip. The choice for the lower wavelength boundary in dispersion compensation is determined and limited by the pump window of Ti:sapphire. The dispersion measurement was performed using white light interferometry [77], up to about 1100 nm because of the silicon detector roll-off. The oscillations in the group delay of each mirror are about 10 times larger than those of high quality DCMs covering 350 nm of bandwidth [?]. However, in the average group delay of both mirrors the oscillations are ideally suppressed due to cancellation by more than a factor of ten. Therefore, the effective residual reflectivity of the mirror pair covering one octave, r^2 , is even smaller than that of conventional DCMs.

Methods for active dispersion compensation

Various schemes for active pulse compression have been developed based on the use of liquid-crystal modulators (LCM), acousto-optic modulators (AOM), and mechanically deformable mirrors.

Dispersion compensation using liquid crystal modulators A pulse shaping technique [84] based on the use of a LCM for pulse compression offers the advantage of a large bandwidth (300-1500 nm) and *in situ* adaptive phase control, see Figure 3.23. In 1997 Yelin *et al.* [85] demonstrated an adaptive method for femtosecond pulse compression based on LCM. Strongly chirped 80-fs pulses generated by an oscillator were sent in a 4-*f* pulse shaper composed of a pair of thin holographic transmission gratings. A programmable one-dimensional LCM, placed in the Fourier plane of the shaper, was used as an updatable filter for pulse spectral manipulation. Pulses as short as

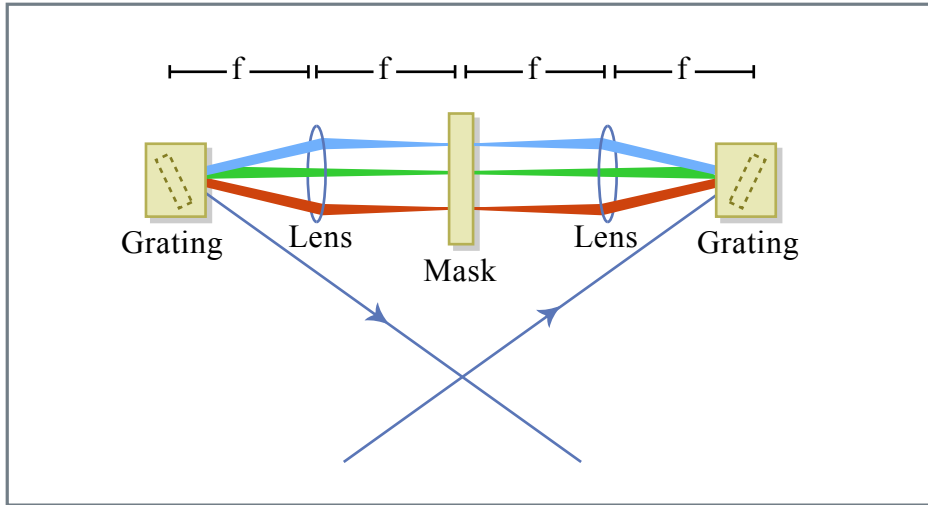


Figure 3.23: Grating Pair and LCM pulse shaper according to Weiner and Heritage [88]. To shape amplitude and phase two pulse shapers with an amplitude and phase mask each are necessary.

Figure by MIT OCW.

11 fs (transform-limited duration: 9 fs) have been obtained, employing an optimization algorithm for adaptive compression based on a search in the two-dimensional space of second- and third-order dispersion coefficients. In 2001, Karasawa *et al.* [86] demonstrated pulse compression, down to 5 fs, of broadband pulses from an argon-filled hollow fiber, using only a LCM for phase compensation. More recently [51], pulses as short as 3.8 fs have been achieved through a closed-loop combination of a liquid-crystal spatial light modulator for adaptive pulse compression and spectral-phase interferometry for direct electric-field reconstruction (SPIDER) [87] measurements as feedback signal.

One problem of the method is pixelization in the Fourier plane owing to the technology of the liquid-crystal active matrix. Diffraction on pixel edges and absorption by the black matrix introduce parasitic effects. The requirement that the actual spectral modulation should approximate a smooth function despite the fixed, finite size of the individual modulator elements, limits the temporal range over which pulse compression can be achieved [88]. Other problems are related to the optical damage of the LCM, which limits the maximum pulse energy, and to the high losses introduced by the device.

Various nonpixelated devices have been proposed: Dorrer *et al.* have reported on an optically addressed LCM (liquid crystal light valve) [89]. The light valve consists of two continuous transparent electrodes and continuous

layers of a nematic twisted liquid crystal and of photoconductive $\text{Bi}_{12}\text{SiO}_{20}$ (BSO). A local variation of illumination of the BSO layer (in the blue green spectral region) induces a change in conductivity. When a voltage is applied between the two electrodes, the variation of the BSO conductivity results in a change in the voltage drop across the liquid crystal layer. As the birefringence of the liquid crystal is voltage dependent, a local variation of the refractive index is created, which translates into a variation of the optical phase of the local spectral component. The light valve is addressed by using a display device. Pixelation effects are avoided because the light valve itself is a continuous device. The control of the light valve is more complicated than for the electrically addressed LCM. Moreover, due to its limited spatial frequency response, the spectral resolution is limited.

Dispersion compensation using acousto-optic modulators

In 1997 Tournois proposed an acousto-optic programmable dispersive filter (AOPDF), to provide large dispersion-compensation ranges[91]. The device is based on a collinear acousto-optic interaction in a birefringent uniaxial crystal, see Figure 3.24. The acoustic frequency is a variable function of time and provides control over the group delay of the diffracted optical pulse. At the same time, the spectral amplitude of the diffracted pulse is driven by the intensity of the acoustic signal. As demonstrated in Ref. [91], the optical output $E_{out}(t)$ of the AOPDF is proportional to the convolution of the optical input, $E_{in}(t)$, and the scaled acoustic signal:

$$E_{out}(t) \propto E_{in}(t) \otimes S(t/\alpha) \quad (3.104)$$

where the scaling factor $\alpha = \Delta n(V/c)$ is the ratio of the speed of sound to the speed of light times the index difference between the ordinary and the extraordinary waves. Therefore, by generating the proper function $S(t)$, it is possible to generate any arbitrary convolution with a temporal resolution given by the inverse of the filter bandwidth. Such device have been used in kilohertz chirped-pulse amplification laser chains compensating for gain narrowing and residual phase errors with the AOPDF, resulting in the generation of 17-fs transform-limited pulses [92]. The total throughput is 10-50%, depending on the bandwidth of the device. Devices approaching one octave in bandwidth are possible.

Image removed due to copyright restrictions.

Figure 3.24: Acousto-optic programmable pulse shaper. One element can shape amplitude and phase of the pulse.

Dispersion compensation using deformable mirrors

Mechanically deformable mirrors can be used for active dispersion control, as proposed by Heritage *et al.* [93]. More recently, pulse compression has been achieved using an electrostatically deformable, gold-coated, silicon nitride membrane mirror, placed in the Fourier plane of a $4f$ zero-dispersion stretcher [94]. The membrane was suspended over an array of 39 actuator electrodes. The potential applied to each actuator generates an electrostatic attraction between the membrane and the electrode, thus inducing a deformation of the mirror surface, which translates into a modulation of the phase of the spectral components of the input pulse. The total phase difference is $\phi = 2(2\pi)\Delta z/\lambda$, where Δz is the deflection of the mirror. The minimum radius of curvature of the mirror membrane is given by $R = T/P$, where T is the membrane tension and P is the maximum electrostatic pressure. This limitation of the membrane curvature restricts the possibility of the mirror correction of higher-order phases. The main advantages of this method are the following: the phase modulation is smoothly varying; reduced losses due to the high reflectivity (97%) of the mirror; relatively high actuator density. Experiments have been performed with a mode-locked Ti:sapphire laser, where the deformable mirror recompressed a 15 fs pulse, previously stretched to 90 fs by dispersion in glass, back to approximately the bandwidth limit [94].

Recently, dispersion control over a bandwidth of ~ 220 THz has been demonstrated by A. Baltuška et al. [95] using a compressor consisting of a pair of chirped mirrors and a grating dispersion line with a computer-controlled flexible mirror positioned in the focal plane. The total throughput of the pulse shaper was less than 12% because of the low diffraction efficiency of the grating. Using this compressor, the visible-near-IR pulses, generated by optical parametric amplification, were compressed to a 4-fs duration.

3.7.5 Hollow Fiber Compression Technique

Single mode fiber only allows compression of low energy pulses. In 1996 the group of DeSilvestri in Milan [48] developed a technique that enables the generation of few-cycle light pulses with energies in the millijoule range. The technique is based on propagation of laser pulses in a hollow fiber filled with noble gases (hollow fiber compression technique), see Figure 3.25. The modes of the hollow fiber are leaky modes, i.e. they experience radiation loss. However, there is one mode, the EH_{11} mode, which has considerably less loss than the higher order modes. This mode is used for pulse compression. The nonlinear index in the fiber can be controlled with the gas pressure. Typical fiber diameters are 100-500 μm and typical gas pressures are in the range of 0.1-3bar. As in the case of fiber compression it is important to consider the optimization of nonlinear interaction and dispersion. Both the medium and waveguide dispersion has to be taken into account. For more detail see ref. [107].

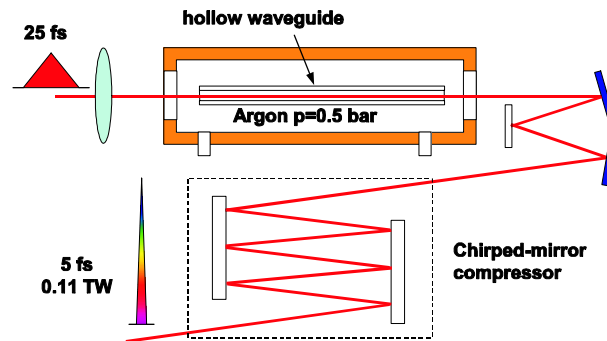


Figure 3.25: Hollow fiber compression technique [48]

For the time being, the hollow fiber compression technique is the only way to generate sub-10fs millijoule pulses. This will change soon with the advent of parametric chirped pulse amplification.

3.8 Appendix: Sech-Algebra

The hyperbolic secant is defined as

$$\operatorname{sech}(x) = \frac{1}{\operatorname{cosh}(x)} \quad (3.105)$$

See Figure 3.26

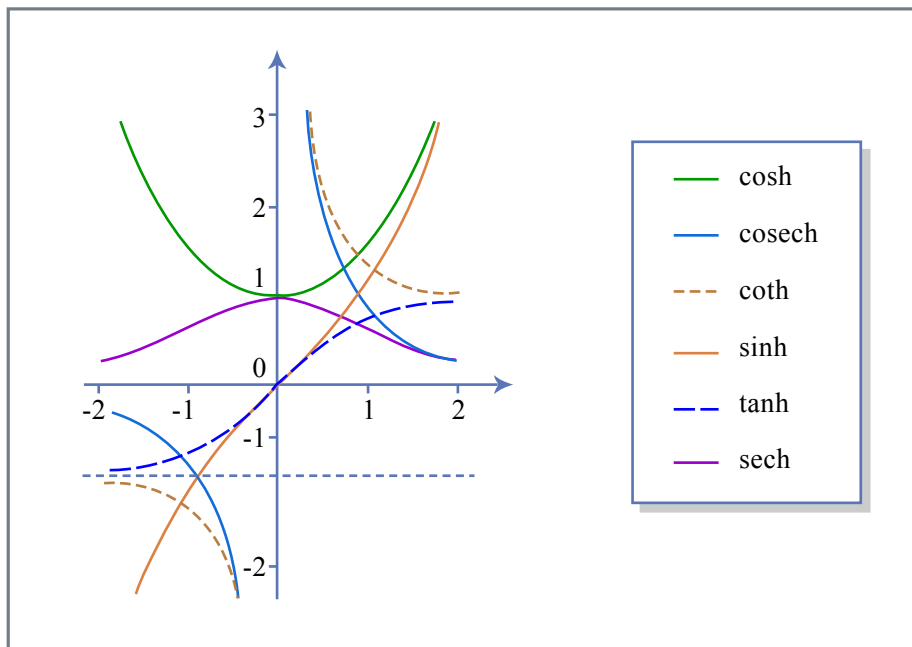


Figure 3.26: Hyperbolic functions

Figure by MIT OCW.

$$\cosh^2(x) - \sinh^2(x) = 1 \quad (3.106)$$

$$\operatorname{sech}^2(x) = 1 - \tanh^2(x) \quad (3.107)$$

$$\frac{d}{dx} \operatorname{sech}(x) = -\tanh(x) \operatorname{sech}(x) \quad (3.108)$$

$$\frac{d^2}{dx^2} \operatorname{sech}(x) = \operatorname{sech}(x) [1 - 2\operatorname{sech}^2(x)] \quad (3.109)$$

$$\int_{-\infty}^{+\infty} \operatorname{sech}(x) dx = \pi \quad (3.110)$$

$$\int_{-\infty}^{+\infty} \operatorname{sech}^2(x) dx = 2 \quad (3.111)$$

$$\int_{-\infty}^{+\infty} x^2 \operatorname{sech}^2(x) dx = \frac{\pi^2}{6} \quad (3.112)$$

function $f(t)$	Fourier-Transform $\tilde{f}(\omega) = \int f(t)e^{-j\omega t} dt$
$\operatorname{sech}(t)$	$\pi \operatorname{sech}(\frac{\pi}{2}\omega)$
$\operatorname{sech}^2(t)$	$\frac{\pi\omega}{\sinh(\frac{\pi}{2}\omega)}$
$\operatorname{sech}^3(t)$	$\frac{1}{2}(1 + \omega^2) \pi \operatorname{sech}(\frac{\pi}{2}\omega)$
$\operatorname{sech}^5(t)$	$\frac{1}{24}(\omega^4 + 10\omega^2 + 9) \pi \operatorname{sech}(\frac{\pi}{2}\omega)$
$\tanh(t)\operatorname{sech}(t)$	$-j\pi\omega \operatorname{sech}(\frac{\pi}{2}\omega)$
$\tanh^2(t)\operatorname{sech}(t)$	$\frac{1}{2}(1 - \omega^2) \pi \operatorname{sech}(\frac{\pi}{2}\omega)$
$\tanh^3(t)\operatorname{sech}(t)$	$-j\frac{\omega}{6}(5 - \omega^2) \pi \operatorname{sech}(\frac{\pi}{2}\omega)$
$\tanh(t)\operatorname{sech}^3(t)$	$-j\frac{\omega}{6}(1 + \omega^2) \pi \operatorname{sech}(\frac{\pi}{2}\omega)$
$\tanh^2(t)\operatorname{sech}^3(t)$	$\frac{1}{2}(1 + \omega^2) \pi \operatorname{sech}(\frac{\pi}{2}\omega) - \frac{1}{24}(\omega^4 + 10\omega^2 + 9) \pi \operatorname{sech}(\frac{\pi}{2}\omega)$
$t \tanh(t)\operatorname{sech}(t)$	$\pi \operatorname{sech}(\frac{\pi}{2}\omega) - \frac{\omega\pi^2}{2} \tanh(\frac{\pi}{2}\omega) \operatorname{sech}(\frac{\pi}{2}\omega)$
$t \tanh^2(t)\operatorname{sech}(t)$	$-j\omega\pi \operatorname{sech}(\frac{\pi}{2}\omega) - \frac{\pi^2}{4}(1 - \omega^2) \tanh(\frac{\pi}{2}\omega) \operatorname{sech}(\frac{\pi}{2}\omega)$
$t \tanh^3(t)\operatorname{sech}(t)$	$\frac{1}{6}(5 - 3\omega^2) \pi \operatorname{sech}(\frac{\pi}{2}\omega) - \frac{\omega\pi^2}{12}(5 - \omega^2) \tanh(\frac{\pi}{2}\omega) \operatorname{sech}(\frac{\pi}{2}\omega)$
$t \tanh(t)\operatorname{sech}^3(t)$	$\frac{1}{6}(1 + 3\omega^2) \pi \operatorname{sech}(\frac{\pi}{2}\omega) - \frac{\omega\pi^2}{12}(1 + \omega^2) \tanh(\frac{\pi}{2}\omega) \operatorname{sech}(\frac{\pi}{2}\omega)$
$t \operatorname{sech}(t)$	$-j\frac{\pi^2}{6} \tanh(\frac{\pi}{2}\omega) \operatorname{sech}(\frac{\pi}{2}\omega)$
$t \operatorname{sech}^3(t)$	$-j\omega\pi \operatorname{sech}(\frac{\pi}{2}\omega) - j\frac{\pi^2}{4}(1 + \omega^2) \tanh(\frac{\pi}{2}\omega) \operatorname{sech}(\frac{\pi}{2}\omega)$

3.9 Summary

We found, that the lowest order reversible linear effect, GVD, together with the lowest order reversible nonlinear effect in a homogeneous and isotropic medium, SPM, leads to the Nonlinear Schrödinger Equation for the envelope of the wave. This equation describes a Hamiltonian system. The equation is integrable, i.e., it does possess an infinite number of conserved quantities. The equation has soliton solutions, which show complicated but persistent oscillatory behavior. Especially, the fundamental soliton, a sech-shaped pulse, shows no dispersion which makes them ideal for long distance optical communication. Due to the universality of the NSE, this dynamics is also extremely important for modelocked lasers once the pulses become so short that the

spectra experience the dispersion and the peak powers are high enough that nonlinear effects become important. In general, this is the case for sub-picosecond pulses. Further, we found a perturbation theory, which enables us to decompose a solution of the NSE close to a fundamental soliton as a fundamental soliton and continuum radiation. We showed that periodic perturbations of the soliton may lead to side-band generation, if the nonlinear phase shift of the soliton within a period of the perturbation becomes comparable to $\pi/4$. Soliton perturbation theory will also give the frame work for studying noise in mode-locked lasers later.

A medium with positive dispersion and self-phase modulation with the same sign can be used for pulse compression. The major problem in pulse compression is to find a compressor that can that exactly inverts the group delay caused by spectral broadening. Depending on bandwidth this can be achieved by grating, prism, chirped mirrors, puls shapers, AOPDFs or a combination thereof.

Bibliography

- [1] L. Allen and J. H. Eberly: *Optical Resonance and Two-Level Atoms*, Dover (1987).
- [2] A. Yariv, "Quantum Electronics", Wiley Interscience (1975).
- [3] A. Hasegawa and F. Tapert, "Transmission of stationary nonlinear optical pulses in dispersive dielectric fibers. I. Anomalous dispersion," *Appl. Phys. Lett.* **23**, pp. 142 - 144 (1973).
- [4] V. E. Zakharov and A. B. Shabat, "Exact Theory of Two-Dimensional Self-Focusing and One-Dimensional Self-Modulation of Waves in nonlinear Media", *Zh. Eksp. Teor. Fiz.* **34**, pp. 61 - 68 (1971); [*Sov. Phys. - JETP* **34**, pp. 62 - 69 (1972).]
- [5] P. G. Drazin, and R. S. Johnson, "Solitons: An Introduction," Cambridge University Press, New York (1990).
- [6] G. B. Witham, "Linear and Nonlinear Waves," in *Pure & Applied Mathematics Series*, New York: Wiley-Interscience (1974).
- [7] G. L. Lamb, Jr., "Elements of Soliton Theory," New York: Wiley-Interscience (1980).
- [8] F. Schwabl, "Quantenmechanik," Springer, Berlin (1988).
- [9] L. F. Mollenauer and R. H. Stolen, "The soliton laser" *Opt. Lett.* **9**, pp. 13 - 15 (1984).
- [10] J. D. Moores, K. Bergman, H. A. Haus and E. P. Ippen, "Optical switching using fiber ring reflectors," *J. Opt. Soc. Am. B* **8**, pp. 594 - 601 (1990).

- [11] L. F. Mollenauer, R. H. Stolen and J. P. Gordon, "Experimental observation of picosecond pulse narrowing and solitons in optical fibers", *Phys. Rev. Lett.* **45**, pp. 1095 – 1098 (1980).
- [12] H. A. Haus and M. N. Islam, "Theory of the soliton laser," *IEEE J. Quant. Electron.* **QE-21**, pp. 1172 – 88 (1985).
- [13] N. J. Zabusky and M. D. Kruskal, "Interactions of 'solitons' in a collisionless plasma and the recurrence of initial states," *Phys. Rev. Lett.*, **15**, pp. 240 – 243 (1965).
- [14] C. S. Gardner, J. M. Greene, M. D. Kruskal and R. M. Miura, "Method for solving the Korteweg-de Vries equation," *Phys. Rev. Lett.* **19**, pp. 1095 – 1097 (1967).
- [15] M. J. Ablowitz, D. J. Kaup, A. C. Newell & H. Segur, "The inverse scattering transform - Fourier analysis for nonlinear problems," *Stud. Appl. Math.* **53**, pp. 249 – 315 (1974).
- [16] A. C. Newell, "The Inverse Scattering Transform," In *Topics in current physics. Solitons.* ed. by R. Bulloch & P. Caudrey, Berlin, Springer (1978).
- [17] V. A. Marchenko, "On the reconstruction of the potential energy from phases of the scattered waves," *Dokl. Akad. Nauk SSSR*, **104** 695 – 698 (1955).
- [18] H. A. Haus, "Optical Fiber Solitons, Their Properties and Uses," *Proc. of the IEEE* **81**, pp. 970 – 983 (1993).
- [19] R. Y. Chiao, E. Garmire, and C. H. Townes, "Self-trapping of optical beams," *Phys. Rev. Lett.* **13**, pp. 479 – 482 (1964).
- [20] A. S. Davydov, "Solitons in molecular systems", *Physica Scripta* **20**, pp. 387 – 394 (1979). London: John Murray.
- [21] Y. Kodama, and A. Hasegawa, "Nonlinear Pulse Propagation in a Monomode Dielectric Guide," *IEEE J. Quantum Electron.* **QE-23** pp. 510 – 524 (1987).
- [22] A. Hasegawa, "Optical Solitons in Fibers," Springer Verlag, Berlin (1989).

- [23] G. Placek, Marx Handbuch der Radiologie, ed. by E. Marx (Academische Verlagsgesellschaft, Leipzig, Germany, 1934), 2nd ed., Vol. VI, Part II, p. 209 – 374.
- [24] F. X. Kärtner, D. Dougherty, H. A. Haus, and E. P. Ippen, "Raman Noise and Soliton Squeezing," *J. Opt. Soc. Am. B* **11**, pp. 1267 – 1276, (1994).
- [25] V. I. Karpman, and E. M. Maslov, "Perturbation Theory for Solitons," *Sov. Phys. JETP* **46** pp. 281 – 291 (1977); J. P. Keener and D. W. McLaughlin, "Solitons under Perturbations," *Phys. Rev. A* **16**, pp. 777 – 790 (1977).
- [26] D. J. Kaup, and A. C. Newell, "Solitons as particles, oscillators, and in slowly changing media: a singular perturbation theory," *Proc. R. Soc. Lond. A.* **361**, pp. 413 – 446 (1978).
- [27] H. A. Haus and Y. Lai, "Quantum theory of soliton squeezing: a linearized approach," *Opt. Soc. Am B* **7**, 386 – 392 (1990).
- [28] D. J. Kaup, "Perturbation theory for solitons in optical fibers", *Phys. Rev. A* **42**, pp. 5689 – 5694 (1990).
- [29] J. P. Gordon and H. A. Haus, "Random walk of coherently amplified solitons in optical fiber transmission," *Opt. Lett.* **11**, 665 – 668.(1986)
- [30] S. M. J. Kelly, "Characteristic sideband instability of periodically amplified average solitons", *Electronics Letters*, **28**, pp. 806 - 807 (1992).
- [31] J. N. Elgin and S. M. J. Kelly, "Spectral modulation and the growth of resonant modes associated with periodically amplified solitons", *Opt. Lett.*, **21**, pp. 787 - 789 (1993).
- [32] J. Satsuma, and N. Yajima, "Initial Value Problems of One-Dimensional Self-Modulation of Nonlinear Waves in DIspersive Media," Supplement of the *Progress in Theoretical Physics*, **55**, pp. 284 – 306 (1974).
- [33] J. P. Gordon, "Dispersive perturbations of solitons of the nonlinear Schrödinger equation", *J. Opt. Soc. Am. B* **9**, pp. 91 – 97 (1992).

- [34] F. M. Mitschke and L. F. Mollenauer, "Discovery of the soliton self-frequency shift", *Opt. Lett.* **11**, pp. 659 – 661 (1986).
- [35] J. P. Gordon, "Theory of the soliton self-frequency shift", *Opt. Lett.* **11**, pp. 662 – 664 (1986).
- [36] A. C. Newell and J. V. Moloney, "Nonlinear Optics," Addison-Wesley Publishing Company, Redwood City, (1993).
- [37] A.M. Kowalewicz, A. T. Zare, F. X. Kärtner, J. G. Fujimoto, S. Dewald, U. Morgner, V. Scheuer, and G. Angelow, "Generation of 150-nJ pulses from a multiple-pass cavity Kerr-lens modelocked Ti:Al₂O₃ oscillator," *Opt. Lett.*, **28**, 1507-09, 2003.
- [38] F. Gires, P. Tournois, *C.R. Acad. Sci. (Paris)* **258** 6112 (1964)
- [39] J.A. Giordmaine, M.A. Duguay, J.W. Hansen: Compression of optical pulse, *IEEE J. Quantum Electron.* **4** 252-255 (1968)
- [40] R. A. Fisher, P. L. Kelly, T. K. Gustafson: Subpicosecond pulse generation using the optical Kerr effect, *Appl. Phys. Lett.* **14** 140-143 (1969)
- [41] A. Laubereau: External frequency modulation and compression of picosecond pulses, *Phys. Lett.* **29A** 539-540 (1969)
- [42] H. Nakatsuka, D. Grischkowsky, A. C. Balant: Nonlinear picosecond-pulse propagation through optical fibers with positive group velocity dispersion, *Phys. Rev. Lett.* **47** 910-913 (1981)
- [43] A.J. Campillo, S.L. Shapiro, B.R. Suydam: Periodic breakup of optical beams due to self-focusing, *Appl. Phys. Lett.* **23** 628-630 (1973)
- [44] E.P. Ippen, C.V. Shank, T.K. Gustafson: Self-phase modulation of picosecond pulses in optical fibers, *Appl. Phys. Lett.* **24** 190-192 (1974)
- [45] R.H. Stolen, C. Lin: Self-phase-modulation in silica optical fibers, *Phys. Rev. A* **17** 1448-1453 (1978)
- [46] R.L. Fork, C.H.B. Cruz, P.C. Becker, C.V. Shank: Compression of optical pulses to six femtoseconds by using cubic phase compensation, *Opt. Lett.* **12** 483-485 (1987)

- [47] A. Baltuška, Z. Wei, M.S. Pshenichnikov, D.A. Wiersma, R. Szipöcs: Optical pulse compression to 5 fs at a 1-MHz repetition rate, *Opt. Lett.* **22**, 102-104 (1997)
- [48] M. Nisoli, S. De Silvestri, O. Svelto: Generation of high energy 10 fs pulses by a new pulse compression technique, *Appl. Phys. Lett.* **68** 2793-2795 (1996)
- [49] M. Nisoli, S. De Silvestri, O. Svelto, R. Szipöcs, K. Ferencz, Ch. Spielmann, S. Sartania, F. Krausz: Compression of high-energy laser pulses below 5 fs, *Opt. Lett.* **22** 522-524 (1997)
- [50] G. Cerullo, S. De Silvestri, M. Nisoli, S. Sartania, S. Stagira, O. Svelto: Few-optical-cycle laser pulses: from high peak power to frequency tunability, *IEEE J. Sel. Topics in Quantum Electr.* **6** 948-958 (2000)
- [51] B. Schenkel, J. Biegert, U. Keller, C. Vozzi, M. Nisoli, G. Sansone, S. Stagira, S. De Silvestri, O. Svelto: Generation of 3.8-fs pulses from adaptive compression of a cascaded hollow fiber supercontinuum, *Opt. Lett.* **28** 1987-1989 (2003)
- [52] G. P. Agrawal: *Nonlinear Fiber Optics* (Academic Press, San Diego 1995)
- [53] *Ultrashort Laser Pulses*, Ed. W. Kaiser, Springer Verlag, 1988.
- [54] A. Baltuška, Z. Wei, R. Szipöcs, M. S. Pshenichnikov, D. A. Wiersma: All solid-state cavity-dumped sub-5-fs laser, *Appl. Phys. B* **65** 175-188 (1997)
- [55] E.B. Treacy: Compression of picosecond light pulses, *Phys. Lett.* **28A**, 34-35 (1968)
- [56] R.L. Fork, O.E. Martinez, J.P. Gordon: Negative dispersion using pairs of prisms, *Opt. Lett.* **9** 150-152 (1984)
- [57] R. Szipöcs, K. Ferencz, C. Spielmann, and F. Krausz, *Opt. Lett.* **19**, 201-203 (1994).
- [58] R. Ell, U. Morgner, F.X. Kärtner, J.G. Fujimoto, E.P. Ippen, V. Scheuer, G. Angelow, T. Tschudi, *Opt. Lett.* **26**, 373-375 (2001)

- [59] E.J. Mayer, J. Möbius, A. Euteneuer, W.W. Rühle, R. Szipöcs, *Opt. Lett.* **22**, 528 (1997).
- [60] K. O. Hill, F. Bilodeau, B. Malo, T. Kitagawa, S. Theriault, D. C. Johnson, J. Albert, K. Takiguch, *Opt. Lett.* **19**, 1314-1316 (1994).
- [61] A. V. Tikhonravov, M. K. Trubetskov, A. A. Tikhonravov, *OSA Topical Meeting on Optical Interference Coatings*, Tucson Arizona, February 7-12, 1998.
- [62] B. Golubovic, R. R. Austin, M. K. Steiner-Shepard, M. K. Reed, S. A. Diddams, D. J. Jones and A. G. Van Engen, *Opt. Lett.* vol. 25, pp. 175-278, 2000.
- [63] R. Szipöcs, G. DeBell, A. V. Tikhonravov, M. K. Trubetskov, *Ultrafast Optics Conference*, Ascona Switzerland, July 11-16, 1999.
- [64] M. Matsuhara, K. O. Hill, *Applied Optics* **13**, 2886-2888 (1974).
- [65] G. Tempea, V. Yakovlev, B. Bacovic, F. Krausz, and K. Ferencz, *J. Opt. Soc. Am. B* **18**, 1747-50 (2001).
- [66] N. Matuschek, L. Gallmann, D. H. Sutter, G. Steinmeyer, and U. Keller, *Appl. Phys. B* **71**, 509-522 (2000).
- [67] G. Steinmeyer, *Conference on Lasers and Electro-Optics, Cleo 2003*, Baltimore, June 2-6th, 2003.
- [68] J. A. Dobrowolski, A. V. Tikhonravov, M. K. Trubetskov, B. T. Sullivan, and P. G. Verly, *Appl. Opt.* **35**, 644-658, (1996).
- [69] A. Apolonski, A. Poppe, G. Tempea, C. Spielmann, T. Udem, R. Holzwarth, T. Hänsch, and F. Krausz, *Phys.Rev.Lett.* **85**, 740 (2000).
- [70] R. Szipöcs and A. Kohazi-Kis, *Applied Physics B* **65**, 115-135 (1997).
- [71] V. Laude and P. Tournois, paper CTuR4, *Conference on Lasers and Electrooptics*, Baltimore, USA, (1999).
- [72] R. Szipöcs, A. Köházi-Kis, S. Lakó, P. Apai, A. P. Kovács, G. DeBell, L. Mott, A. W. Louderback, A. V. Tikhonravov, M. K. Trubetskov, *Applied Physics B* **70**, S51-557 (2000).

- [73] N. Matuschek, F.X. Kärtner, U. Keller, IEEE Journal of Quantum Electronics ,JQE- **5**, 129-137 (1999).
- [74] V. Scheuer, M. Tilsch, and T. Tschudi, SPIE Conf. Proc.**2253**, 445-454,(1994).
- [75] M. Tilsch, V. Scheuer, and T. Tschudi, SPIE Conf. Proc.**2253**, 414-422 (1994).
- [76] F. X. Kärtner, U. Morgner, T. R. Schibli, E. P. Ippen J. G. Fujimoto, V. Scheuer, G. Angelow and T. Tschudi, J. of the Opt. Soc. of Am. **18**, 882-885 (2001).
- [77] K. Naganuma, K. Mogi, H. Yamada, Opt. Lett. **15**, 393 (1990).
- [78] I. Walmsley, L. Waxer, C. Dorrer: The role of dispersion in ultrafast optics, Rev. Scient. Instrum. **72** 1-29 (2001)
- [79] J. Zhou, G. Taft, C.-P. Huang, M.M. Murnane, H.C. Kapteyn, I.P. Christov: Pulse evolution in a broad-bandwidth Ti:sapphire laser, Opt. Lett. **19** 1149-1151 (1994)
- [80] R. Szipöcs, K. Ferencz, C. Spielmann, and F. Krausz: Chirped multi-layer coatings for broadband dispersion control in femtosecond lasers, Opt. Lett. **19** 201-203 (1994)
- [81] N. Matuschek, F. X. Kärtner, U. Keller: Theory of double-chirped mirrors, IEEE J. Select. Topics Quantum Electron. **4** 197-208 (1998)
- [82] G. Tempea, F. Krausz, Ch. Spielmann, K. Ferencz: Dispersion control over 150 THz with chirped dielectric mirrors, IEEE J. Select. Topics Quantum Electron. **4** 193-196 (1998)
- [83] F.X. Kärtner, N. Matuschek, T. Schibli, U. Keller, H.A. Haus, C. Heine, R. Morf, V. Scheuer, M. Tilsch, T. Tschudi: Design and fabrication of double-chirped mirrors, Opt. Lett. **22** 831-833 (1997)
- [84] A.M. Weiner, D.E. Leaird, J.S. Patel, J.R. Wullert: Programmable femtosecond pulse shaping by use of a multielement liquid-crystal phase modulator, Opt. Lett. **15** 326-328 (1990)

- [85] D. Yelin, D. Meshulach, Y. Silberberg: Adaptive femtosecond pulse compression, *Opt. Lett.* **22** 1793-1795 (1997)
- [86] N. Karasawa, L. Li, A. Suguro, H. Shigekawa, R. Morita, M. Yamashita: Optical pulse compression to 5.0 fs by use of only a spatial light modulator for phase compensation, *J. Opt. Soc. Am. B* **18** 1742-1746 (2001)
- [87] C. Iaconis, I.A. Walmsley: Self-referencing spectral interferometry for measuring ultrashort optical pulses, *IEEE J. Quantum Electron.* **35** 501-509 (1999)
- [88] A.M. Weiner: Femtosecond pulse shaping using spatial light modulators, *Rev. Scient. Instrum.* **71** 1929-1960 (2000)
- [89] C. Dorrer, F. Salin, F. Verluise, J.P. Huignard: Programmable phase control of femtosecond pulses by use of a nonpixelated spatial light modulator, *Opt. Lett.* **23** 709-711 (1998)
- [90] M.A. Dugan, J.X. Tull, W.S. Warren: High-resolution acousto-optic shaping of unamplified and amplified femtosecond laser pulses, *J. Opt. Soc. Am. B* **14** 2348-2358 (1997)
- [91] P. Tournois: Acousto-optic programmable dispersive filter for adaptive compensation of group delay time dispersion in laser systems, *Optics Comm.* **140** 245-249 (1997)
- [92] F. Verluise, V. Laude, Z. Cheng, Ch. Spielmann, P. Tournois: Amplitude and phase control of ultrashort pulses by use of an acousto-optic programmable dispersive filter: pulse compression and shaping, *Opt. Lett.* **25** 575-577 (2000)
- [93] J.P. Heritage, E.W. Chase, R.N. Thurston, M. Stern: A simple femtosecond optical third-order disperser, in *Conference on Lasers and Electro-Optics*, Vol. 10 of 1991 OSA Technical Digest Series (Optical Society of America, Washington, D.C., 1991), paper CTuB3.
- [94] E. Zeek, K. Maginnis, S. Backus, U. Russek, M.M. Murnane, G. Mourou, H. Kapteyn, G. Vdovin: Pulse compression by use of deformable mirrors, *Opt. Lett.* **24** 493-495 (2000)

- [95] A. Baltuška, T. Fuji, T. Kobayashi: Visible pulse compression to 4 fs by optical parametric amplification and programmable dispersion control, *Opt. Lett.* **27** 306-308 (2002)
- [96] E.A.J. Marcatili, R.A. Schmelzter: Hollow metallic and dielectric waveguide for long distance optical transmission and laser, *Bell Syst. Tech. J.* **43** 1783-1809 (1964)
- [97] E.-G. Neumann: *Single-Mode Fibers* (Springer-Verlag, Berlin 1988)
- [98] M. Nisoli, S. Stagira, S. De Silvestri, O. Svelto, S. Sartania, Z. Cheng, M. Lenzner, Ch. Spielmann, F. Krausz: A novel high energy pulse compression system: generation of multigigawatt sub-5-fs pulses, *Appl. Phys. B* **65** 189-196 (1997)
- [99] M. Nisoli, E. Priori, G. Sansone, S. Stagira, G. Cerullo, S. De Silvestri, C. Altucci, R. Bruzzese, C. de Lisio, P. Villoresi, L. Poletto, M. Pascolini, G. Tondello: High-Brightness High-Order Harmonic Generation by Truncated Bessel Beams in the Sub-10-fs Regime, *Phys. Rev. Lett.* **88** 33902-1-4 (2002)
- [100] T. Brabec, F. Krausz: Nonlinear Optical Pulse Propagation in the Single-Cycle Regime, *Phys. Rev. Lett.* **78** 3282-3285 (1997)
- [101] S. Stagira, E. Priori, G. Sansone, M. Nisoli, S. De Silvestri, Ch. Gadermaier: Nonlinear guided propagation of few-optical-cycle laser pulses with arbitrary polarization state, *Phys. Rev. A* (in press) (2002)
- [102] H.J. Lehmeier, W. Leupacher, A. Penzkofer: Nonresonant third order hyperpolarizability of rare gases and N₂ determined by third order harmonic generation, *Opt. Commun.* **56** 67-72 (1985)
- [103] A. Dalgarno, A. E. Kingston: The refractive indices and Verdet constants of the inert gases, *Proc. R. Soc. London Ser. A* **259** 424-429 (1966)
- [104] R. W. Boyd, *Nonlinear Optics*, Academic Press, San Diego (1992)
- [105]
- [106] G. Tempea, T. Brabec: Theory of self-focusing in a hollow waveguide, *Opt. Lett.* **23**, 762-764 (1998)

- [107] S. De Silvestri, M. Nisoli, G. Sansone, S. Stagira, and O. Svelto, "Few-Cycle Pulses by External Compression" in "Few-Cycle Pulse Generation and Its Applications, Ed. by F. X. Kaertner, Springer Verlag, 2004.
- [108] T. Brabec, F. Krausz: Intense few-cycle laser fields: frontiers of nonlinear optics, *Rev. Mod. Phys.* **72** 545-591 (2000)
- [109] D. E. Spence, P. N. Kean, W. Sibbett: 60-fsec pulse generation from a self-mode-locked Ti:sapphire laser, *Opt. Lett.* **16** 42-44 (1991)
- [110] D. Strickland, G. Mourou: Compression of amplified chirped optical pulses, *Opt. Commun.* **56** 219-221 (1985)

Chapter 4

Laser Dynamics (single-mode)

Before we start to look into the dynamics of a multi-mode laser, we should recall the technically important regimes of operation of a "single-mode" laser. The term "single-mode" is set in apostrophes, since it doesn't have to be really single-mode. There can be several modes running, for example due to spatial holeburning, but in an incoherent fashion, so that only the average power of the beam matters. For a more detailed account on single-mode laser dynamics and Q-Switching the following references are recommended [1][3][16][4][5].

4.1 Rate Equations

In section 2.5, we derived for the interaction of a two-level atom with a laser field propagating to the right the equations of motion (2.171) and (2.172), which are given here again:

$$\left(\frac{\partial}{\partial z} + \frac{1}{v_g} \frac{\partial}{\partial t} \right) A(z, t) = \frac{N\hbar}{4T_2 E_s} w(z, t) A(z, t), \quad (4.1)$$

$$\dot{w} = -\frac{w - w_0}{T_1} + \frac{|A(z, t)|^2}{E_s} w(z, t) \quad (4.2)$$

where T_1 is the energy relaxation rate, v_g the group velocity in the host material where the two level atoms are embedded, $E_s = I_s T_1$, the saturation fluence [J/cm^2], of the medium, and I_s the saturation intensity according to

Eq.(2.145)

$$I_s = \left[\frac{2T_1 T_2 Z_F}{\hbar^2} \frac{|\vec{M} \hat{E}|^2}{|\hat{E}|^2} \right]^{-1},$$

which relates the saturation intensity to the microscopic parameters of the transition like longitudinal and transversal relaxation rates as well as the dipole moment of the transition.

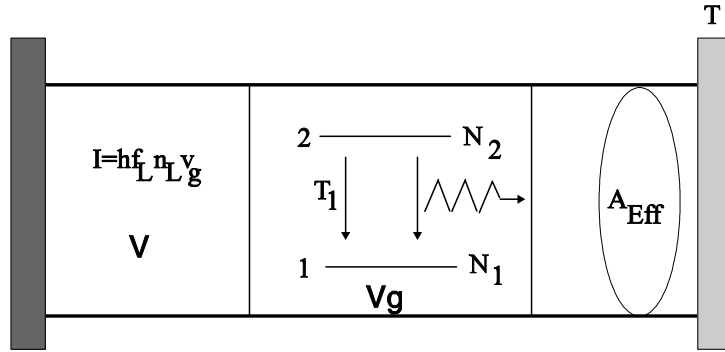


Figure 4.1: Rate equations for the two-level atom

In many cases it is more convenient to normalize (4.1) and (4.2) to the populations in level e and g or 2 and 1, respectively, N_2 and N_1 , and the density of photons, n_L , in the mode interacting with the atoms and traveling at the corresponding group velocity, v_g , see Fig. 4.1. The intensity I in a mode propagating at group velocity v_g with a mode volume V is related to the number of photons N_L stored in the mode with volume V by

$$I = hf_L \frac{N_L}{2^* V} v_g = \frac{1}{2^*} hf_L n_L v_g, \quad (4.3)$$

where hf_L is the photon energy. $2^* = 2$ for a linear laser resonator (then only half of the photons are going in one direction), and $2^* = 1$ for a ring laser. In this first treatment we consider the case of space-independent rate equations, i.e. we assume that the laser is oscillating on a single mode and pumping and mode energy densities are uniform within the laser material. With the interaction cross section σ defined as

$$\sigma = \frac{hf_L}{2^* I_s T_1}, \quad (4.4)$$

and multiplying Eq. (??) with the number of atoms in the mode, we obtain

$$\frac{d}{dt}(N_2 - N_1) = -\frac{(N_2 - N_1)}{T_1} - \sigma(N_2 - N_1)v_g n_L + R_p \quad (4.5)$$

Note, $v_g n_L$ is the photon flux, thus σ is the stimulated emission cross section between the atoms and the photons. R_p is the pumping rate into the upper laser level. A similar rate equation can be derived for the photon density

$$\frac{d}{dt}n_L = -\frac{n_L}{\tau_p} + \frac{l_g \sigma v_g}{L V_g} [N_2(n_L + 1) - N_1 n_L]. \quad (4.6)$$

Here, τ_p is the photon lifetime in the cavity or cavity decay time and the one in Eq.(4.6) accounts for spontaneous emission which is equivalent to stimulated emission by one photon occupying the mode. V_g is the volume of the active gain medium. For a laser cavity with a semi-transparent mirror with transmission T , producing a small power loss $2l = -\ln(1 - T) \approx T$ (for small T) per round-trip in the cavity, the cavity decay time is $\tau_p = 2l/T_R$, if $T_R = 2^*L/c_0$ is the roundtrip-time in linear cavity with optical length $2L$ or a ring cavity with optical length L . The optical length L is the sum of the optical length in the gain medium $n_g^{group}l_g$ and the remaining free space cavity length l_a . Internal losses can be treated in a similar way and contribute to the cavity decay time. Note, the decay rate for the inversion in the absence of a field, $1/T_1$, is not only due to spontaneous emission, but is also a result of non radiative decay processes. See for example the four level system shown in Fig. 4.2. In the limit, where the populations in the third and first level are zero, because of fast relaxation rates, i.e. $T_{32}, T_{10} \rightarrow 0$, we obtain

$$\frac{d}{dt}N_2 = -\frac{N_2}{\tau_L} - \sigma v_g N_2 n_L + R_p \quad (4.7)$$

$$\frac{d}{dt}n_L = -\frac{n_L}{\tau_p} + \frac{l_g \sigma v_g}{L V_g} N_2 (n_L + 1). \quad (4.8)$$

where $\tau_L = T_{21}$ is the lifetime of the upper laser level. Experimentally, the photon number and the inversion in a laser resonator are not

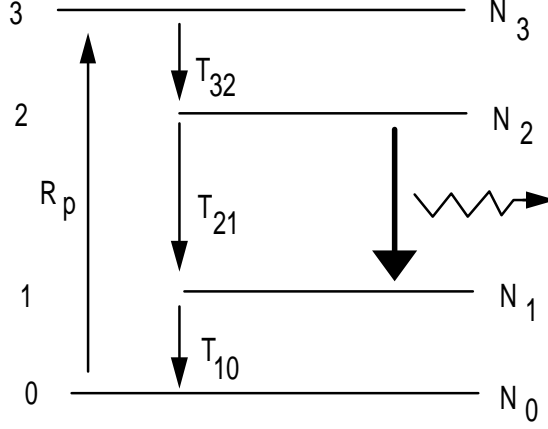


Figure 4.2: Vier-Niveau-Laser

very convenient quantities, therefore, we normalize both equations to the round-trip amplitude gain $g = \frac{l_g \sigma v_g}{L 2V_g} N_2 T_R$ experienced by the light and the circulating intracavity power $P = I \cdot A_{eff}$

$$\frac{d}{dt}g = -\frac{g - g_0}{\tau_L} - \frac{gP}{E_{sat}} \quad (4.9)$$

$$\frac{d}{dt}P = -\frac{1}{\tau_p}P + \frac{2g}{T_R}(P + P_{vac}), \quad (4.10)$$

with

$$E_s = I_s A_{eff} \tau_L = \frac{hf_L}{2\sigma} \quad (4.11)$$

$$P_{sat} = E_{sat}/\tau_L \quad (4.12)$$

$$P_{vac} = hf_L v_g / 2L = hf_L / T_R \quad (4.13)$$

$$g_0 = \frac{2^* v_g R_p}{2A_{eff} c_0} \sigma \tau_L, \quad (4.14)$$

the small signal round-trip gain of the laser. Note, the factor of two in front of gain and loss is due to the fact, the g and l are gain and loss with respect to amplitude. Eq.(4.14) elucidates that the figure of merit that characterizes the small signal gain achievable with a certain laser material is the $\sigma\tau_L$ -product.

Laser Medium	Wave-length λ_0 (nm)	Cross Section σ (cm ²)	Upper-St. Lifetime τ_L (μ s)	Linewidth $\Delta f_{FWHM} = \frac{2}{T_2}$ (THz)	Typ	Refr. index n
Nd ³⁺ :YAG	1,064	$4.1 \cdot 10^{-19}$	1,200	0.210	H	1.82
Nd ³⁺ :LSB	1,062	$1.3 \cdot 10^{-19}$	87	1.2	H	1.47 (ne)
Nd ³⁺ :YLF	1,047	$1.8 \cdot 10^{-19}$	450	0.390	H	1.82 (ne)
Nd ³⁺ :YVO ₄	1,064	$2.5 \cdot 10^{-19}$	50	0.300	H	2.19 (ne)
Nd ³⁺ :glass	1,054	$4 \cdot 10^{-20}$	350	3	H/I	1.5
Er ³⁺ :glass	1,55	$6 \cdot 10^{-21}$	10,000	4	H/I	1.46
Ruby	694.3	$2 \cdot 10^{-20}$	1,000	0.06	H	1.76
Ti ³⁺ :Al ₂ O ₃	660-1180	$3 \cdot 10^{-19}$	3	100	H	1.76
Cr ³⁺ :LiSAF	760-960	$4.8 \cdot 10^{-20}$	67	80	H	1.4
Cr ³⁺ :LiCAF	710-840	$1.3 \cdot 10^{-20}$	170	65	H	1.4
Cr ³⁺ :LiSGAF	740-930	$3.3 \cdot 10^{-20}$	88	80	H	1.4
He-Ne	632.8	$1 \cdot 10^{-13}$	0.7	0.0015	I	~1
Ar ⁺	515	$3 \cdot 10^{-12}$	0.07	0.0035	I	~1
CO ₂	10,600	$3 \cdot 10^{-18}$	2,900,000	0.000060	H	~1
Rhodamin-6G	560-640	$3 \cdot 10^{-16}$	0.0033	5	H	1.33
semiconductors	450-30,000	$\sim 10^{-14}$	~ 0.002	25	H/I	3 - 4

Table 4.1: Wavelength range, cross-section for stimulated emission, upper-state lifetime, linewidth, typ of lineshape (H=homogeneously broadened, I=inhomogeneously broadened) and index for some often used solid-state laser materials, and in comparison with semiconductor and dye lasers.

The larger this product the larger is the small signal gain g_0 achievable with a certain laser material. Table 4.1

From Eq.(2.145) and (4.4) we find the following relationship between the interaction cross section of a transition and its microscopic parameters like linewidth, dipole moment and energy relaxation rate

$$\sigma = \frac{hf_L}{I_{sat}T_1} = \frac{2T_2}{\hbar^2 Z_F} \frac{|\vec{M}\hat{E}|^2}{|\hat{E}|^2}.$$

This equation tells us that broadband laser materials naturally do show smaller gain cross sections, if the dipole moment is the same.

4.2 Built-up of Laser Oscillation and Continuous Wave Operation

If $P_{vac} \ll P \ll P_{sat} = E_{sat}/\tau_L$, than $g = g_0$ and we obtain from Eq.(4.10), neglecting P_{vac}

$$\frac{dP}{P} = 2(g_0 - l) \frac{dt}{T_R} \quad (4.15)$$

or

$$P(t) = P(0)e^{2(g_0-l)\frac{t}{T_R}}. \quad (4.16)$$

The laser power builds up from vacuum fluctuations until it reaches the saturation power, when saturation of the gain sets in within the built-up time

$$T_B = \frac{T_R}{2(g_0 - l)} \ln \frac{P_{sat}}{P_{vac}} = \frac{T_R}{2(g_0 - l)} \ln \frac{A_{eff}T_R}{\sigma\tau_L}. \quad (4.17)$$

Some time after the built-up phase the laser reaches steady state, with the saturated gain and steady state power resulting from Eqs.(4.9-4.10), neglecting in the following the spontaneous emission, and for $\frac{d}{dt} = 0$:

$$g_s = \frac{g_0}{1 + \frac{P_s}{P_{sat}}} = l \quad (4.18)$$

$$P_s = P_{sat} \left(\frac{g_0}{l} - 1 \right), \quad (4.19)$$

Image removed due to copyright restrictions.

Please see:

Keller, U., Ultrafast Laser Physics, Institute of Quantum Electronics, Swiss Federal Institute of Technology, ETH Hönggerberg—HPT, CH-8093 Zurich, Switzerland.

Figure 4.3: Built-up of laser power from spontaneous emission noise.

4.3 Stability and Relaxation Oscillations

How does the laser reach steady state, once a perturbation has occurred?

$$g = g_s + \Delta g \quad (4.20)$$

$$P = P_s + \Delta P \quad (4.21)$$

Substitution into Eqs.(4.9-4.10) and linearization leads to

$$\frac{d\Delta P}{dt} = +2\frac{P_s}{T_R}\Delta g \quad (4.22)$$

$$\frac{d\Delta g}{dt} = -\frac{g_s}{E_{sat}}\Delta P - \frac{1}{\tau_{stim}}\Delta g \quad (4.23)$$

where $\frac{1}{\tau_{stim}} = \frac{1}{\tau_L} \left(1 + \frac{P_s}{P_{sat}}\right)$ is the stimulated lifetime. The perturbations decay or grow like

$$\begin{pmatrix} \Delta P \\ \Delta g \end{pmatrix} = \begin{pmatrix} \Delta P_0 \\ \Delta g_0 \end{pmatrix} e^{st}. \quad (4.24)$$

which leads to the system of equations (using $g_s = l$)

$$A \begin{pmatrix} \Delta P_0 \\ \Delta g_0 \end{pmatrix} = \begin{pmatrix} -s & 2\frac{P_s}{T_R} \\ -\frac{T_R}{E_{sat}2\tau_p} & -\frac{1}{\tau_{stim}} - s \end{pmatrix} \begin{pmatrix} \Delta P_0 \\ \Delta g_0 \end{pmatrix} = 0. \quad (4.25)$$

There is only a solution, if the determinante of the coefficient matrix vanishes, i.e.

$$s \left(\frac{1}{\tau_{stim}} + s \right) + \frac{P_s}{E_{sat}\tau_p} = 0, \quad (4.26)$$

which determines the relaxation rates or eigen frequencies of the linearized system

$$s_{1/2} = -\frac{1}{2\tau_{stim}} \pm \sqrt{\left(\frac{1}{2\tau_{stim}}\right)^2 - \frac{P_s}{E_{sat}\tau_p}}. \quad (4.27)$$

Introducing the pump parameter $r = 1 + \frac{P_s}{P_{sat}}$, which tells us how often we pump the laser over threshold, the eigen frequencies can be rewritten as

$$s_{1/2} = -\frac{1}{2\tau_{stim}} \left(1 \pm j \sqrt{\frac{4(r-1)\tau_{stim}}{r\tau_p} - 1} \right), \quad (4.28)$$

$$= -\frac{r}{2\tau_L} \pm j \sqrt{\frac{(r-1)}{\tau_L\tau_p} - \left(\frac{r}{2\tau_L}\right)^2} \quad (4.29)$$

There are several conclusions to draw:

- (i): The stationary state $(0, g_0)$ for $g_0 < l$ and (P_s, g_s) for $g_0 > l$ are always stable, i.e. $\text{Re}\{s_i\} < 0$.
- (ii): For lasers pumped above threshold, $r > 1$, the relaxation rate becomes complex, i.e. there are relaxation oscillations

$$s_{1/2} = -\frac{1}{2\tau_{stim}} \pm j \sqrt{\frac{1}{\tau_{stim}\tau_p}}. \quad (4.30)$$

with frequency ω_R equal to the geometric mean of inverse stimulated lifetime and photon life time

$$\omega_R = \sqrt{\frac{1}{\tau_{stim}\tau_p}}. \quad (4.31)$$

There is definitely a parameter range of pump powers for laser with long upper state lifetimes, i.e. $\frac{r}{4\tau_L} < \frac{1}{\tau_p}$

- If the laser can be pumped strong enough, i.e. r can be made large enough so that the stimulated lifetime becomes as short as the cavity decay time, relaxation oscillations vanish.

The physical reason for relaxation oscillations and later instabilities is, that the gain reacts to slow on the light field, i.e. the stimulated lifetime is long in comparison with the cavity decay time.

Example: diode-pumped Nd:YAG-Laser

$$\begin{aligned}\lambda_0 &= 1064 \text{ nm}, \sigma = 4 \cdot 10^{-20} \text{ cm}^2, A_{eff} = \pi (100 \mu\text{m} \times 150 \mu\text{m}), r = 50 \\ \tau_L &= 1.2 \text{ ms}, l = 1\%, T_R = 10 \text{ ns}\end{aligned}$$

From Eq.(4.4) we obtain:

$$\begin{aligned}I_{sat} &= \frac{hf_L}{\sigma\tau_L} = 3.9 \frac{\text{kW}}{\text{cm}^2}, P_{sat} = I_{sat}A_{eff} = 1.8 \text{ W}, P_s = 91.5 \text{ W} \\ \tau_{stim} &= \frac{\tau_L}{r} = 24 \mu\text{s}, \tau_p = 1 \mu\text{s}, \omega_R = \sqrt{\frac{1}{\tau_{stim}\tau_p}} = 2 \cdot 10^5 \text{ s}^{-1}.\end{aligned}$$

Figure 4.4 shows the typically observed fluctuations of the output of a solid-state laser with long upperstate life time of several $100 \mu\text{s}$ in the time and frequency domain.

One can also define a quality factor for the relaxation oscillations by the ratio of imaginary to real part of the complex eigen frequencies 4.29

$$Q = \sqrt{\frac{4\tau_L (r - 1)}{\tau_p r^2}},$$

which can be as large a several thousand for solid-state lasers with long upper-state lifetimes in the millisecond range.

Image removed due to copyright restrictions.

Please see:

Keller, U., Ultrafast Laser Physics, Institute of Quantum Electronics, Swiss Federal Institute of Technology, ETH Honggerberg—HPT, CH-8093 Zurich, Switzerland.

Figure 4.4: Typically observed relaxation oscillations in time and frequency domain.

4.4 Q-Switching

The energy stored in the laser medium can be released suddenly by increasing the Q-value of the cavity so that the laser reaches threshold. This can be done actively, for example by quickly moving one of the resonator mirrors in place or passively by placing a saturable absorber in the resonator [1, 16]. Hellwarth was first to suggest this method only one year after the invention of

Image removed due to copyright restrictions.

Please see:

Keller, U., *Ultrafast Laser Physics*, Institute of Quantum Electronics, Swiss Federal Institute of Technology, ETH Hönggerberg—HPT, CH-8093 Zurich, Switzerland.

Figure 4.5: Gain and loss dynamics of an actively Q-switched laser.

the laser. As a rough orientation for a solid-state laser, the following relation for the relevant time scales is generally valid

$$\tau_L \gg T_R \gg \tau_p. \quad (4.32)$$

4.4.1 Active Q-Switching

Fig. 4.5 shows the principle dynamics of an actively Q-switched laser. The laser is pumped by a pump pulse with a length on the order of the upper-state lifetime, while the intracavity losses are kept high enough, so that the laser can not reach threshold. Therefore, the laser medium acts as an energy storage. The energy only relaxes by spontaneous and nonradiative transitions. Then suddenly the intracavity loss is reduced, for example by a rotating cavity mirror. The laser is pumped way above threshold and the light field builds up exponentially with the net gain until the pulse energy comes close to the saturation energy of the gain medium. The gain saturates and is extracted, so that the laser is shut off by the pulse itself.

A typical actively Q-switched pulse is asymmetric: The rise time is proportional to the net gain after the Q-value of the cavity is actively switched to a high value. The light intensity grows proportional to $2g_0/T_R$. When the gain is depleted, the fall time mostly depends on the cavity decay time τ_p . For short Q-switched pulses a short cavity length, high gain and a large change in the cavity Q is necessary. If the Q-switch is not fast, the pulse width may be limited by the speed of the switch. Typical electro-optical and acousto-optical switches are 10 ns and 50 ns, respectively

Image removed due to copyright restrictions.

Please see:

Keller, U., Ultrafast Laser Physics, Institute of Quantum Electronics, Swiss Federal Institute of Technology, ETH Hönggerberg—HPT, CH-8093 Zurich, Switzerland.

Figure 4.6: Asymmetric actively Q-switched pulse.

For example, with a diode-pumped Nd:YAG microchip laser [6] using an electro-optical switch based on $LiTaO_3$ Q-switched pulses as short as 270 ps at repetition rates of 5 kHz, peak powers of 25 kW at an average power of 34 mW, and pulse energy of $6.8 \mu\text{J}$ have been generated (Figure 4.7).

Image removed due to copyright restrictions.

Please see:

Kafka, J. D., and T. Baer. "Mode-locked erbium-doped fiber laser with soliton pulse shaping." *Optics Letters* 14 (1989): 1269-1271.

Figure 4.7: Q-switched microchip laser using an electro-optic switch. The pulse is measured with a sampling scope [8]

Similar results were achieved with Nd:YLF [7] and the corresponding setup is shown in Fig. 4.8.

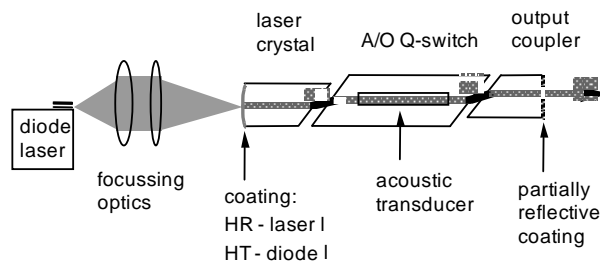


Figure 4.8: Set-up of an actively Q-switched laser.

4.4.2 Single-Frequency Q-Switched Pulses

Q-switched lasers only deliver stable output if they oscillate single frequency. Usually this is not automatically achieved. One method to achieve this is by seeding with a single-frequency laser during Q-switched operation, so that there is already a population in one of the longitudinal modes before the pulse is building up. This mode will extract all the energy before the other modes can do, see Figure 4.9

Image removed due to copyright restrictions.

Please see:

Keller, U., Ultrafast Laser Physics, Institute of Quantum Electronics, Swiss Federal Institute of Technology, ETH Hönggerberg—HPT, CH-8093 Zurich, Switzerland.

Figure 4.9: Output intensity of a Q-switched laser without a) and with seeding b).

Another possibility to achieve single-mode output is either using an etalon in the cavity or making the cavity so short, that only one longitudinal mode is within the gain bandwidth (Figure 4.10). This is usually only the case if the cavity length is on the order of a few millimeters or below. The microchip laser [6][11][10] can be combined with an electro-optic modulator to achieve

very compact high peak power lasers with sub-nanosecond pulsewidth (Figure 4.7).

Image removed due to copyright restrictions.

Please see:

Keller, U., Ultrafast Laser Physics, Institute of Quantum Electronics, Swiss Federal Institute of Technology, ETH Hönggerberg—HPT, CH-8093 Zurich, Switzerland.

Figure 4.10: In a microchip laser the resonator can be so short, that there is only one longitudinal mode within the gain bandwidth.

4.4.3 Theory of Active Q-Switching

We want to get some insight into the pulse built-up and decay of the actively Q-switched pulse. We consider the ideal situation, where the loss of the laser cavity can be instantaneously switched from a high value to a low value, i.e. the quality factor is switched from a low value to a high value, respectively (Figure: 4.11)

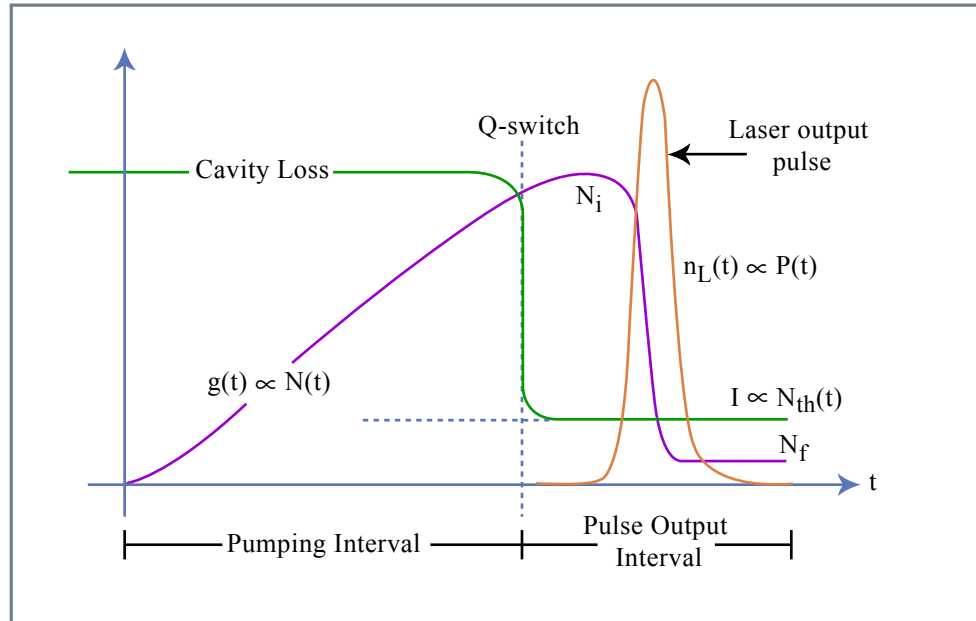


Figure 4.11: Active Q-Switching dynamics assuming an instantaneous switching [16].

Figure by MIT OCW.

Pumping Interval:

During pumping with a constant pump rate R_p , proportional to the small signal gain g_0 , the inversion is built up. Since there is no field present, the gain follows the simple equation:

$$\frac{d}{dt}g = -\frac{g - g_0}{\tau_L}, \quad (4.33)$$

or

$$g(t) = g_0(1 - e^{-t/\tau_L}), \quad (4.34)$$

Pulse Built-up-Phase:

Assuming an instantaneous switching of the cavity losses we look for an approximate solution to the rate equations starting of with the initial gain or inversion $g_i = hf_L N_{2i}/(2E_{sat}) = hf_L N_i/(2E_{sat})$, we can safely leave the index away since there is only an upper state population. We further assume that during pulse built-up the stimulated emission rate is the dominate term changing the inversion. Then the rate equations simplify to

$$\frac{d}{dt}g = -\frac{gP}{E_{sat p}} \quad (4.35)$$

$$\frac{d}{dt}P = \frac{2(g-l)}{T_R}P, \quad (4.36)$$

resulting in

$$\frac{dP}{dg} = \frac{2E_{sat}}{T_R} \left(\frac{l}{g} - 1 \right). \quad (4.37)$$

We use the following initial conditions for the intracavity power $P(t=0) = 0$ and initial gain $g(t=0) = g_i = r \cdot l$. Note, r means how many times the laser is pumped above threshold after the Q-switch is operated and the intracavity losses have been reduced to l . Then 4.37 can be directly solved and we obtain

$$P(t) = \frac{2E_{sat}}{T_R} \left(g_i - g(t) + l \ln \frac{g(t)}{g_i} \right). \quad (4.38)$$

From this equation we can deduce the maximum power of the pulse, since the growth of the intracavity power will stop when the gain is reduced to the losses, $g(t)=l$, (Figure 4.11)

$$P_{\max} = \frac{2lE_{sat}}{T_R} (r - 1 - \ln r) \quad (4.39)$$

$$= \frac{E_{sat}}{\tau_p} (r - 1 - \ln r). \quad (4.40)$$

This is the first important quantity of the generated pulse and is shown normalized in Figure 4.12.

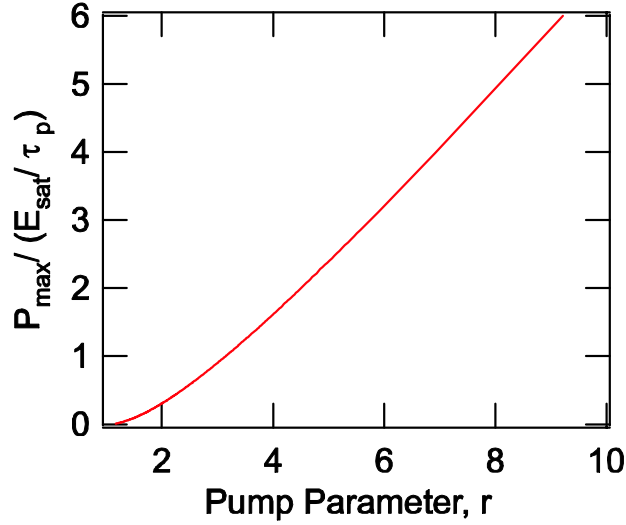


Figure 4.12: Peak power of emitted pulse as function of pump parameter.

Next, we can find the final gain g_f , that is reached once the pulse emission is completed, i.e. that is when the right side of (4.38) vanishes

$$\left(g_i - g_f + l \ln \left(\frac{g_f}{g_i} \right) \right) = 0 \quad (4.41)$$

Using the pump parameter $r = g_i/l$, this gives as an expression for the ratio between final and initial gain or between final and initial inversion

$$1 - \frac{g_f}{g_i} + \frac{1}{r} \ln \left(\frac{g_f}{g_i} \right) = 0, \quad (4.42)$$

$$1 - \frac{N_f}{N_i} + \frac{1}{r} \ln \left(\frac{N_f}{N_i} \right) = 0, \quad (4.43)$$

which depends only on the pump parameter. Assuming further, that there are no internal losses, then we can estimate the pulse energy generated by

$$E_P = (N_i - N_f) h f_L. \quad (4.44)$$

This is also equal to the output coupled pulse energy since no internal losses are assumed. Thus, if the final inversion gets small all the energy stored in

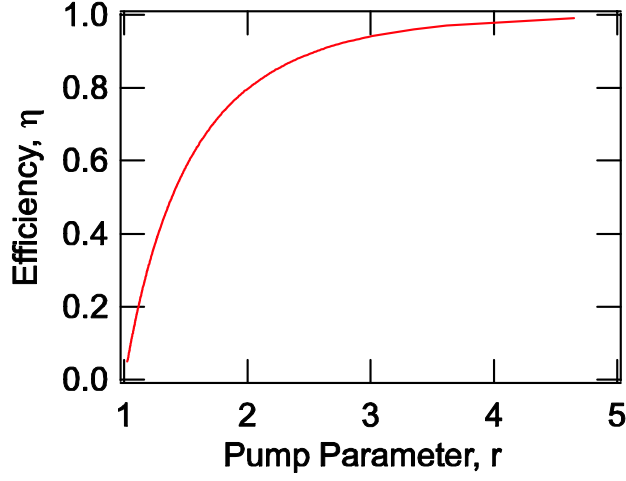


Figure 4.13: Energy extraction efficiency as a function of pump power.

the gain medium can be extracted. We define the energy extraction efficiency η

$$\eta = \frac{N_i - N_f}{N_i}, \quad (4.45)$$

that tells us how much of the initially stored energy can be extracted using eq.(4.43)

$$\eta + \frac{1}{r} \ln(1 - \eta) = 0. \quad (4.46)$$

This efficiency is plotted in Figure 4.13.

Note, the energy extraction efficiency only depends on the pump parameter r . Now, the emitted pulse energy can be written as

$$E_P = \eta(r) N_i h f_L. \quad (4.47)$$

and we can estimate the pulse width of the emitted pulse by the ratio between pulse energy and peak power using (4.40) and (4.47)

$$\begin{aligned} \tau_{Pulse} &= \frac{E_P}{2lP_{peak}} = \tau_p \frac{\eta(r)}{(r-1-\ln r)} \frac{N_i h f_L}{2lE_{sat}} \\ &= \tau_p \frac{\eta(r)}{(r-1-\ln r)} \frac{g_i}{l} \\ &= \tau_p \frac{\eta(r) \cdot r}{(r-1-\ln r)}. \end{aligned} \quad (4.48)$$

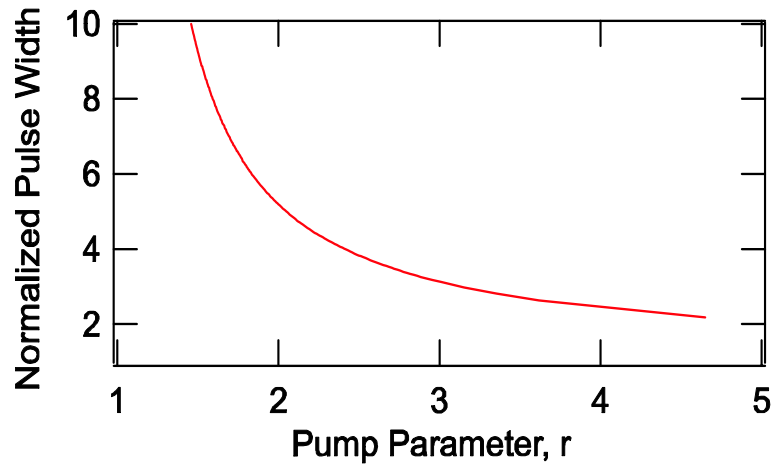


Figure 4.14: Normalized pulse width as a function of pump parameter.

The pulse width normalized to the cavity decay time τ_p is shown in Figure 4.14.

4.4.4 Passive Q-Switching

In the case of passive Q-switching the intracavity loss modulation is performed by a saturable absorber, which introduces large losses for low intensities of light and small losses for high intensity.

Relaxation oscillations are due to a periodic exchange of energy stored in the laser medium by the inversion and the light field. Without the saturable absorber these oscillations are damped. If for some reason there is too much gain in the system, the light field can build up quickly. Especially for a low gain cross section the backaction of the growing laser field on the inversion is weak and it can grow further. This growth is favored in the presence of loss that saturates with the intensity of the light. The laser becomes unstable, the field intensity grows as long as the gain does not saturate below the net loss, see Fig.4.15.

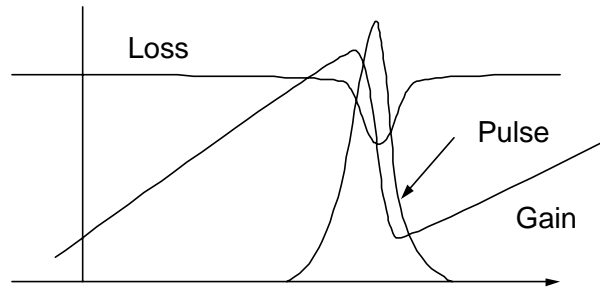


Figure 4.15: Gain and loss dynamics of a passively Q-switched laser

Now, we want to show that the saturable absorber leads to a destabilization of the relaxation oscillations resulting in the giant pulse laser.

We extend our laser model by a saturable absorber as shown in Fig. 4.16

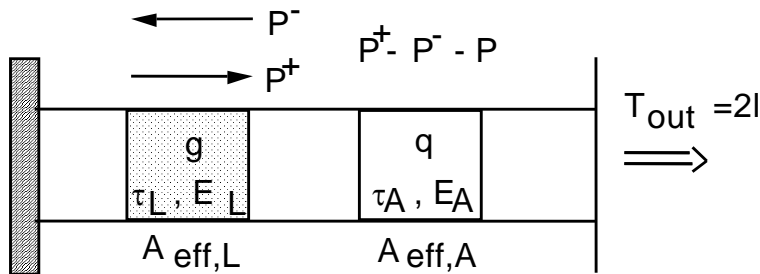


Figure 4.16: Simple laser model described by rate equations. We assume small output coupling so that the laser power within one roundtrip can be considered position independent. Neglecting standing wave effects in the cavity, the field density is related to twice the circulating power P^+ or P^- .

Rate equations for a passively Q-switched laser

We make the following assumptions: First, the transverse relaxation times of the equivalent two level models for the laser gain medium and for the saturable absorber are much faster than any other dynamics in our system, so that we can use rate equations to describe the laser dynamics. Second, we assume that the changes in the laser intensity, gain and saturable absorption

are small on a time scale on the order of the round-trip time T_R in the cavity, (i.e. less than 20%). Then, we can use the rate equations of the laser as derived above plus a corresponding equation for the saturable loss q similar to the equation for the gain.

$$T_R \frac{dP}{dt} = 2(g - l - q)P \quad (4.49)$$

$$T_R \frac{dg}{dt} = -\frac{g - g_0}{T_L} - \frac{gT_R P}{E_L} \quad (4.50)$$

$$T_R \frac{dq}{dt} = -\frac{q - q_0}{T_A} - \frac{qT_R P}{E_A} \quad (4.51)$$

where P denotes the laser power, g the amplitude gain per roundtrip, l the linear amplitude losses per roundtrip, g_0 the small signal gain per roundtrip and q_0 the unsaturated but saturable losses per roundtrip. The quantities $T_L = \tau_L/T_R$ and $T_A = \tau_A/T_R$ are the normalized upper-state lifetime of the gain medium and the absorber recovery time, normalized to the round-trip time of the cavity. The energies $E_L = h\nu A_{eff,L}/2^*\sigma_L$ and $E_A = h\nu A_{eff,A}/2^*\sigma_A$ are the saturation energies of the gain and the absorber, respectively. .

For solid state lasers with gain relaxation times on the order of $\tau_L \approx 100 \mu s$ or more, and cavity round-trip times $T_R \approx 10$ ns, we obtain $T_L \approx 10^4$. Furthermore, we assume absorbers with recovery times much shorter than the round-trip time of the cavity, i.e. $\tau_A \approx 1 - 100$ ps, so that typically $T_A \approx 10^{-4}$ to 10^{-2} . This is achievable in semiconductors and can be engineered at will by low temperature growth of the semiconductor material [20, 30]. As long as the laser is running cw and single mode, the absorber will follow the instantaneous laser power. Then, the saturable absorption can be adiabatically eliminated, by using eq.(4.51)

$$q = \frac{q_0}{1 + P/P_A} \quad \text{with} \quad P_A = \frac{E_A}{\tau_A}, \quad (4.52)$$

and back substitution into eq.(4.49). Here, P_A is the saturation power of the absorber. At a certain amount of saturable absorption, the relaxation oscillations become unstable and Q-switching occurs. To find the stability criterion, we linearize the system

$$T_R \frac{dP}{dt} = (g - l - q(P))P \quad (4.53)$$

$$T_R \frac{dg}{dt} = -\frac{g - g_0}{T_L} - \frac{gT_R P}{E_L}. \quad (4.54)$$

Stationary solution

As in the case for the cw-running laser the stationary operation point of the laser is determined by the point of zero net gain

$$\frac{g_0}{1 + P_s/P_L} = l + \frac{q_0}{1 + P_s/P_A}. \quad (4.55)$$

The graphical solution of this equation is shown in Fig. 4.17

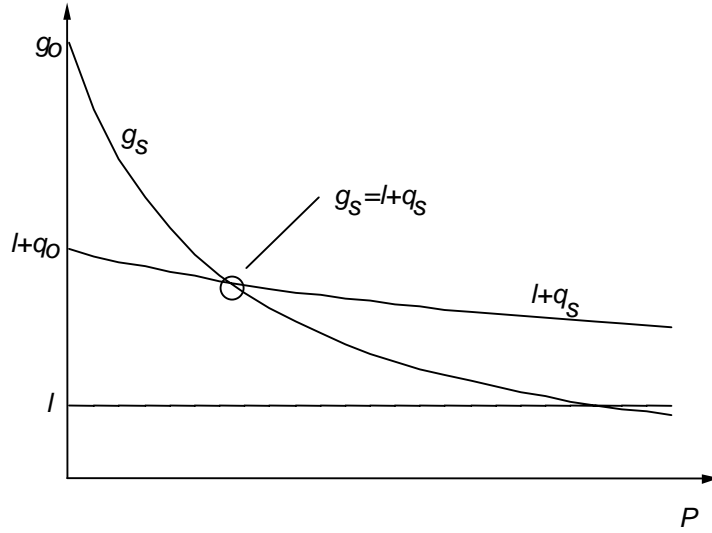


Figure 4.17: Graphical solution of the stationary operating point.

Stability of stationary operating point or the condition for Q-switching

For the linearized system, the coefficient matrix corresponding to Eq.(4.25) changes only by the saturable absorber [23]:

$$T_R \frac{d}{dt} \begin{pmatrix} \Delta P_0 \\ \Delta g_0 \end{pmatrix} = A \begin{pmatrix} \Delta P_0 \\ \Delta g_0 \end{pmatrix}, \quad \text{with } A = \begin{pmatrix} -2 \frac{dq}{dP} \Big|_{cw} P_s & 2P_s \\ -\frac{g_s T_R}{E_L} & -\frac{T_R}{\tau_{stim}} \end{pmatrix} \quad (4.56)$$

The coefficient matrix A does have eigenvalues with negative real part, if and only if its trace is negative and the determinate is positive which results in

two conditions

$$-2P \frac{dq}{dP} \Big|_{cw} < \frac{r}{T_L} \quad \text{with} \quad r = 1 + \frac{P_A}{P_L} \quad \text{and} \quad P_L = \frac{E_L}{\tau_L}, \quad (4.57)$$

and

$$\frac{dq}{dP} \Big|_{cw} \frac{r}{T_L} + 2g_s \frac{r-1}{T_L} > 0. \quad (4.58)$$

After cancelation of T_L we end up with

$$\left| \frac{dq}{dP} \Big|_{cw} \right| < \left| \frac{dg_s}{dP} \Big|_{cw} \right|. \quad (4.59)$$

For a laser which starts oscillating on its own, relation 4.59 is automatically fulfilled since the small signal gain is larger than the total losses, see Fig. 4.17. Inequality (4.57) has a simple physical explanation. The right hand side of (4.57) is the relaxation time of the gain towards equilibrium, at a given pump power and constant laser power. The left hand side is the decay time of a power fluctuation of the laser at fixed gain. If the gain can not react fast enough to fluctuations of the laser power, relaxation oscillations grow and result in passive Q-switching of the laser.

As can be seen from Eq.(4.55) and Eq.(4.57), we obtain

$$-2T_L P \frac{dq}{dP} \Big|_{cw} = 2T_L q_0 \frac{\frac{P}{\chi P_L}}{\left(1 + \frac{P}{\chi P_L}\right)^2} \Big|_{cw} < r_s \quad \text{with} \quad \chi = \frac{P_A}{P_L}, \quad (4.60)$$

where χ is an effective "stiffness" of the absorber against cw saturation. The stability relation (4.60) is visualized in Fig. 4.18.

Image removed due to copyright restrictions.

Please see:

Kaertner, Franz, et al. "Control of solid state laser dynamics by semiconductor devices." *Optical Engineering* 34, no. 7 (July 1995): 2024-2036.

Figure 4.18: Graphical representation of cw-Q-switching stability relation for different products $2q_0T_L$. The cw-stiffness used for the the plots is $\chi = 100$.

The tendency for a laser to Q-switch increases with the product q_0T_L and decreases if the saturable absorber is hard to saturate, i.e. $\chi \gg 1$. As can be inferred from Fig. 4.18 and eq.(4.60), the laser can never Q-switch, i.e. the left side of eq.(4.60) is always smaller than the right side, if the quantity

$$MDF = \frac{2q_0T_L}{\chi} < 1 \quad (4.61)$$

is less than 1. The abbreviation MDF stands for mode locking driving force, despite the fact that the expression (4.61) governs the Q-switching instability. We will see, in the next section, the connection of this parameter with mode locking. For solid-state lasers with long upper state life times, already very small amounts of saturable absorption, even a fraction of a percent, may lead to a large enough mode locking driving force to drive the laser into Q-switching. Figure 4.19 shows the regions in the $\chi - P/P_L$ - plane where Q-switching can occur for fixed MDF according to relation (4.60). The area above the corresponding MDF-value is the Q-switching region. For $MDF < 1$, cw-Q-switching can not occur. Thus, if a cw-Q-switched laser has to be designed, one has to choose an absorber with a $MDF > 1$. The further the operation point is located in the cw-Q-switching domain the more pronounced the cw-Q-switching will be. To understand the nature of the instability we look at the eigen solution and eigenvalues of the linearized equations of mo-

Image removed due to copyright restrictions.

Please see:

Kaertner, Franz, et al. "Control of solid state laser dynamics by semiconductor devices." *Optical Engineering* 34, no. 7 (July 1995): 2024-2036.

Figure 4.19: For a given value of the MDF, cw-Q-switching occurs in the area above the corresponding curve. For a MDF-value less than 1 cw-Q-switching can not occur.

tion 4.56

$$\frac{d}{dt} \begin{pmatrix} \Delta P_0(t) \\ \Delta g_0(t) \end{pmatrix} = s \begin{pmatrix} \Delta P_0(t) \\ \Delta g_0(t) \end{pmatrix} \quad (4.62)$$

which results in the eigenvalues

$$sT_R = \frac{A_{11} + A_{22}}{2} \pm j \sqrt{A_{11}A_{22} - A_{12}A_{21} - \left(\frac{A_{11} + A_{22}}{2}\right)^2}. \quad (4.63)$$

With the matrix elements according to eq.(4.56) we get

$$s = \frac{-\frac{2}{T_R} \frac{dq}{dP}|_{cw} P_s - \frac{1}{\tau_{stim}}}{2} \pm j\omega_Q \quad (4.64)$$

$$\omega_Q = \sqrt{-\frac{2}{T_R} \frac{dq}{dP}|_{cw} P_s \frac{r}{\tau_L} + \frac{r-1}{\tau_p \tau_L} - \left(\frac{-\frac{2}{T_R} \frac{dq}{dP}|_{cw} P_s - \frac{1}{\tau_{stim}}}{2}\right)^2} \quad (4.65)$$

where the pump parameter is now defined as the ratio between small signal gain the total losses in steady state, i.e. $r = g_0/(l + q_s)$. This somewhat lengthy expression clearly shows, that when the system becomes unstable,

$-2 \frac{dq}{dP}|_{cw} P_s > \frac{T_R}{\tau_{stim}}$, with $\tau_L \gg \tau_p$, there is a growing oscillation with frequency

$$\omega_Q \approx \sqrt{\frac{r-1}{\tau_p \tau_L}} \approx \sqrt{\frac{1}{\tau_p \tau_{stim}}}. \quad (4.66)$$

That is, passive Q-switching can be understood as a destabilization of the relaxation oscillations of the laser. If the system is only slightly in the instable regime, the frequency of the Q-switching oscillation is close to the relaxation oscillation frequency. If we define the growth rate γ_Q , introduced by the saturable absorber as a parameter, the eigen values can be written as

$$s = \frac{1}{2} \left(\gamma_Q - \frac{1}{\tau_{stim}} \right) \pm j \sqrt{\gamma_Q \frac{r}{\tau_L} + \frac{r-1}{\tau_p \tau_L} - \left(\frac{\gamma_Q - \frac{1}{\tau_{stim}}}{2} \right)^2}. \quad (4.67)$$

Figure 4.20 shows the root locus plot for a system with and without a saturable absorber. The saturable absorber destabilizes the relaxation oscillations. The type of bifurcation is called a Hopf bifurcation and results in an oscillation.

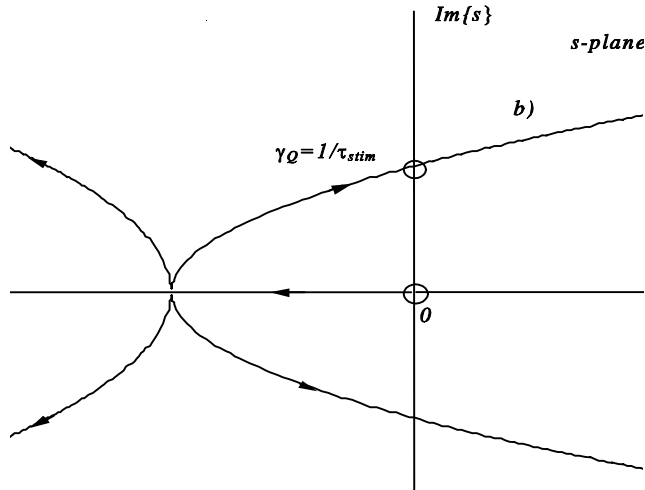


Figure 4.20: Root locus plot for the linearized rate equations. a) Without saturable absorber as a function of the pump parameter r ; b) With saturable absorber as a function of γ_Q .

As an example, we consider a laser with the following parameters: $\tau_L = 250\mu s$, $T_R = 4ns$, $2l_0 = 0.1$, $2q_0 = 0.005$, $2g_0 = 2$, $P_L/P_A = 100$. The rate equations are solved numerically and shown in Figures 4.21 and 4.22.

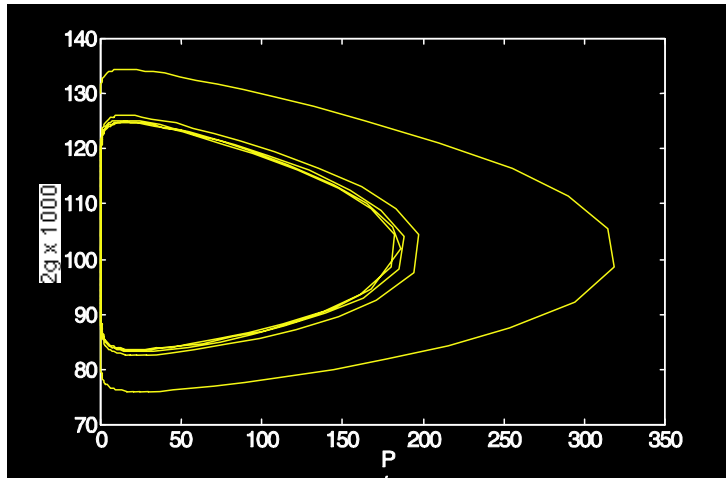


Figure 4.21: Phase space plot of the rate equations. It takes several oscillations, until the steady state limit cycle is reached.

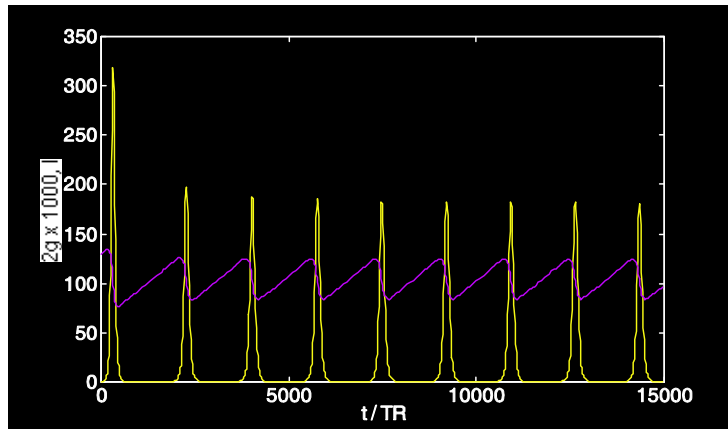


Figure 4.22: Solution for gain and output power as a function of time.

4.5 Example: Single Mode CW-Q-Switched Microchip Lasers

Q-switched microchip lasers are compact and simple solid-state lasers, which can provide a high peak power with a diffraction limited output beam. Due to the extremely short cavity length, typically less than 1 mm, single-frequency Q-switched operation with pulse widths well below a ns can be achieved. Pulse durations of 337 ps and 218 ps have been demonstrated with a passively Q-switched microchip laser consisting of a Nd:YAG crystal bonded to a thin piece of Cr⁴⁺:YAG [8, 9]. Semiconductor saturable absorbers were used to passively Q-switch a monolithic Nd:YAG laser producing 100 ns pulses [38].

4.5.1 Set-up of the Passively Q-Switched Microchip Laser

Figure 4.23(a) shows the experimental set-up of the passively Q-switched microchip laser and Fig. 4.23(b) the structure of the semiconductor saturable absorber [12, 13]. The saturable absorber structure is a so called anti-resonant Fabry-Perot saturable absorber (A-FPSA), because in a microchip laser the beam size is fixed by the thermal lens that builds up in the laser crystal, when pumped with the diode laser. Thus, one can use the top reflector of the A-FPSA to scale the effective saturation intensity of the absorber with respect to the intracavity power. The 200 or 220 μm thick Nd:YVO₄ or Nd:LaSc₃(BO₃)₄, (Nd:LSB) laser crystal [39] is sandwiched between a 10% output coupler and the A-FPSA. The latter is coated for high reflection at the pump wavelength of 808 nm and a predesigned reflectivity at the laser wavelength of 1.062 μm , respectively. The laser crystals are pumped by a semiconductor diode laser at 808 nm through a dichroic beam-splitter, that transmits the pump light and reflects the output beam at 1.064 μm for the Nd:YVO₄ or 1.062 μm for the Nd:LSB laser. To obtain short Q-switched pulses, the cavity has to be as short as possible. The highly doped laser crystals with a short absorption length of only about 100 μm lead to a short but still efficient microchip laser [13]. The saturable absorber consists of a dielectric top mirror and 18 pairs of GaAs/InGaAs MQW's grown on a GaAs/AlAs Bragg-mirror. The total optical thickness of the absorber is on the order of 1 μm . Therefore, the increase of the cavity length due to the

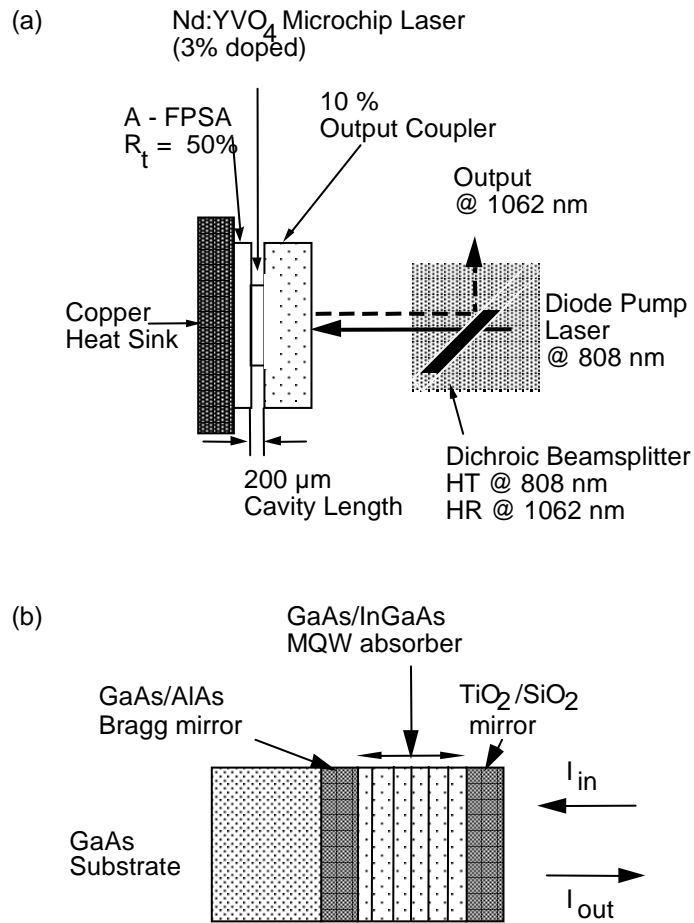


Figure 4.23: (a) Experimental set-up of the cw-passively Q-switched Nd:YVO₄ microchip-laser. (b) Structure of the anti-resonant Fabry-Perot semiconductor saturable absorber [37].

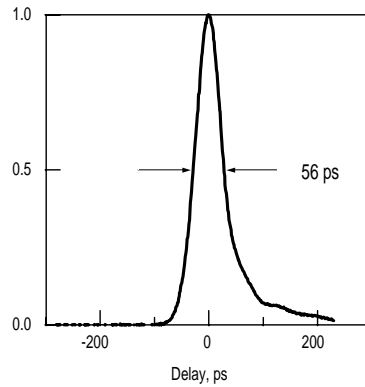


Figure 4.24: Single-Mode Q-switched pulse achieved with Nd:YVO₄ microchip laser.

absorber is negligible. For more details see [12, 13]. Pulses as short as 56 ps, Fig. (4.24), have been achieved with Nd:LSB-crystals.

4.5.2 Dynamics of a Q-Switched Microchip Laser

The passively Q-switched microchip laser, shown in Fig. 4.23(a), is perfectly modelled by the rate equations (4.49) to (4.51). To understand the basic dependence of the cw-Q-switching dynamics on the absorber parameters, we performed numerical simulations of the Nd:LSB microchip laser, as shown in Fig. 4.23. The parameter set used, is given in Table 4.2. For these parameters, we obtain according to eq.(4.55) a mode locking driving force of $MDF = 685$. This laser operates clearly in the cw-Q-switching regime as soon as the laser is pumped above threshold. Note, the Q-switching condition (4.61) has only limited validity for the microchip laser considered here, because, the cavity length is much shorter than the absorber recovery time. Thus the adiabatic elimination of the absorber dynamics is actually not any longer justified. Figures 4.25 and 4.26 show the numerical solution of the set of rate equations (4.49) to (4.51) on a microsecond timescale and a picosecond timescale close to one of the pulse emission events.

No analytic solution to the set of rate equations is known. Therefore, optimization of Q-switched lasers has a long history [4, 5], which in general results in complex design criteria [5], if the most general solution to the rate

parameter	value
$2 g_0$	0.7
$2 q_0$	0.03
$2 l$	0.14
T_R	2.7 ps
τ_L	87 μ s
τ_A	24 ps
E_L	20 μ J
E_A	7.7 nJ

Table 4.2: Parameter set used for the simulation of the dynamics of the Q-switched microchip laser.

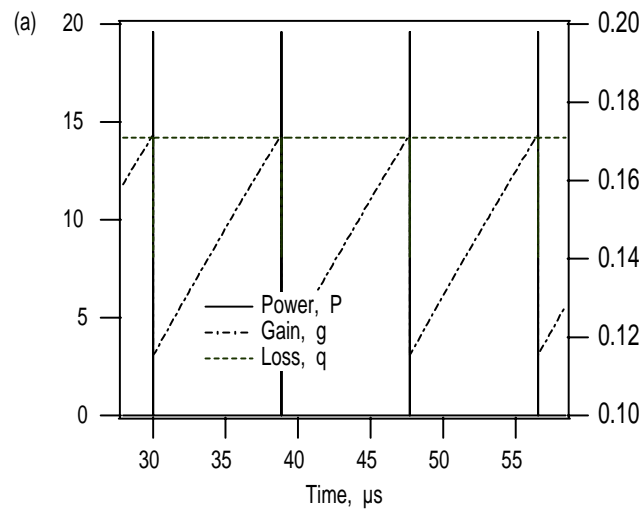


Figure 4.25: Dynamics of the Q-switched microchip laser by numerical solution of the rate equations on a microsecond timescale.

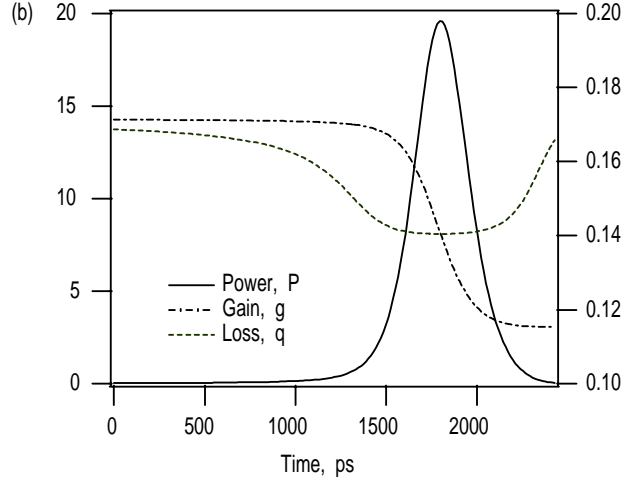


Figure 4.26: Dynamics of the Q-switched microchip laser by numerical solution of the rate equations on a picosecond timescale.

equations is considered. However, a careful look at the simulation results leads to a set of very simple design criteria, as we show in the following. As seen from Fig. 4.25, the pulse repetition time T_{rep} is many orders of magnitude longer than the width of a Q-switched pulse. Thus, between two pulse emissions, the gain increases due to pumping until the laser reaches threshold. This is described by eq.(4.50), where the stimulated emission term can be neglected. Therefore, the pulse repetition rate is determined by the relation that the gain has to be pumped to threshold again $g_{th} = l + q_0$, if it is saturated to the value g_f after pulse emission. In good approximation, $g_f = l - q_0$, as long as it is a positive quantity. If $T_{rep} < \tau_L$, one can linearize the exponential and we obtain

$$g_{th} - g_f = g_0 \frac{T_{rep}}{\tau_L} \quad (4.68)$$

$$T_{rep} = \tau_L \frac{g_{th} - g_f}{g_0} = \tau_L \frac{2q_0}{g_0}. \quad (4.69)$$

Figure 4.26 shows, that the power increases, because, the absorber saturates faster than the gain. To obtain a fast raise of the pulse, we assume an absorber which saturates much easier than the gain, i.e. $E_A \ll E_L$, and the

recovery times of gain and absorption shall be much longer than the pulse width τ_{pulse} , $\tau_A \gg \tau_{pulse}$. Since, we assume a slow gain and a slow absorber, we can neglect the relaxation terms in eqs.(4.50) and (4.51) during growth and decay of the pulse. Then the equations for gain and loss as a function of the unknown Q-switched pulse shape $f_Q(t)$

$$P(t) = E_P f_Q(t) \quad (4.70)$$

can be solved. The pulse shape $f_Q(t)$ is again normalized, such that its integral over time is one and E_P is, therefore, the pulse energy. Analogous to the derivation for the Q-switched mode locking threshold in eqs.(4.84) and (4.85), we obtain

$$q(t) = q_0 \exp \left[-\frac{E_P}{E_A} \int_{-\infty}^t f_Q(t') dt' \right], \quad (4.71)$$

$$g(t) = g_{th} \exp \left[-\frac{E_P}{E_L} \int_{-\infty}^t f_Q(t') dt' \right]. \quad (4.72)$$

Substitution of these expressions into the eq.(4.49) for the laser power, and integration over the pulse width, determines the extracted pulse energy. The result is a balance between the total losses and the gain.

$$l + q_P(E_P) = g_P(E_P) \quad (4.73)$$

with

$$q_P(E_P) = q_0 \frac{1 - \exp \left[-\frac{E_P}{E_A} \right]}{\frac{E_P}{E_A}}, \quad (4.74)$$

$$g_P(E_P) = g_{th} \frac{1 - \exp \left[-\frac{E_P}{E_L} \right]}{\frac{E_P}{E_L}}. \quad (4.75)$$

Because, we assumed that the absorber is completely saturated, we can set $q_P(E_P) \approx 0$. Figure 4.27 shows the solution of eq.(4.73), which is the pulse energy as a function of the ratio between saturable and nonsaturable losses $s = q_0/l$. Also approximate solutions for small and large s are shown as the dashed curves. Thus, the larger the ratio between saturable and nonsaturable losses is, the larger is the intracavity pulse energy, which is not

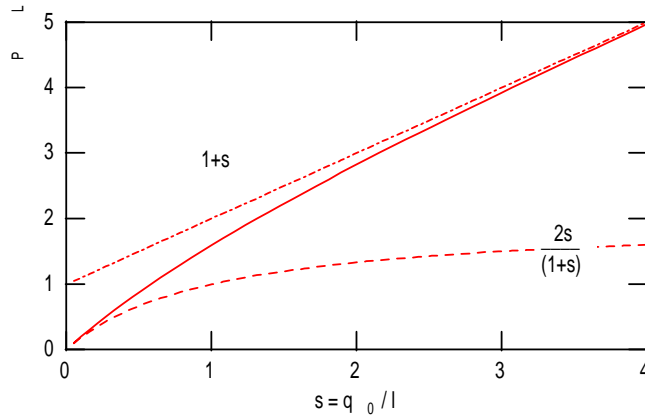


Figure 4.27: (—) Intracavity pulse energy as a function of the ratio between saturable and nonsaturable losses s . (---) Approximations for small and large values for s .

surprising. Note, the extracted pulse energy is proportional to the output coupling, which is $2l$ if no other losses are present. If we assume, $s \ll 1$, then, we can use approximately the low energy approximation

$$E_P = 2E_L \frac{q_0}{l + q_0}. \quad (4.76)$$

The externally emitted pulse energy is then given by

$$E_P^{ex} = 2lE_P = E_L \frac{4lq_0}{l + q_0}. \quad (4.77)$$

Thus, the total extracted pulse energy is completely symmetric in the saturable and non saturable losses. For a given amount of saturable absorption, the extracted pulse energy is maximum for an output coupling as large as possible. Of course threshold must still be reached, i.e. $l + q_0 < g_0$. Thus, in the following, we assume $l > q_0$ as in Fig. 4.26. The absorber is immediately bleached, after the laser reaches threshold. The light field growth and extracts some energy stored in the gain medium, until the gain is saturated to the low loss value l . Then the light field decays again, because the gain is below the loss. During decay the field can saturate the gain by a similar amount as during build-up, as long as the saturable losses are smaller than

the constant output coupler losses l , which we shall assume in the following. Then the pulse shape is almost symmetric as can be seen from Fig. 4.26(b) and is well approximated by a secant hyperbolicus square for reasons that will become obvious in a moment. Thus, we assume

$$f_Q(t) = \frac{1}{2\tau_P} \operatorname{sech}^2\left(\frac{t}{\tau_P}\right). \quad (4.78)$$

With the assumption of an explicit pulse form, we can compute the pulse width by substitution of this ansatz into eq.(4.49) and using (4.71), (4.72)

$$-\frac{2T_R}{\tau_P} \tanh\left(\frac{t}{\tau_P}\right) = g_{th} \exp\left[-\frac{E_P}{2E_L} \left(1 + \tanh\left(\frac{t}{\tau_P}\right)\right)\right] - l. \quad (4.79)$$

Again, we neglect the saturated absorption. If we expand this equation up to first order in E_P/E_L and compare coefficients, we find from the constant term the energy (4.77), and from the tanh-term we obtain the following simple expression for the pulse width

$$\tau_P = 2\frac{T_R}{q_0}. \quad (4.80)$$

For the FWHM pulse width of the resulting sech^2 -pulse we obtain

$$\tau_{P,FWHM} = 3.5\frac{T_R}{q_0}. \quad (4.81)$$

Thus, for optimum operation of a Q-switched microchip laser, with respect to minimum pulse width and maximum extracted energy in the limits considered here, we obtain a very simple design criterium. If we have a maximum small signal round-trip gain g_0 , we should design an absorber with q_0 somewhat smaller than $g_0/2$ and an output coupler with $q_0 < l < g_0 - q_0$, so that the laser still fulfills the cw-Q-switching condition. It is this simple optimization, that allowed us to reach the shortest pulses ever generated from a cw-Q-switched solid-state laser. Note, for a maximum saturable absorption of $2 q_0 = 13\%$, a cavity roundtrip time of $T_R = 2.6$ ps for the Nd:YVO₄ laser, one expects from (4.81) a pulse width of about $\tau_P = 70$ ps, which is close to what we observed in the experiment above. We achieved pulses between 56 and 90 ps [13]. The typical extracted pulse energies were on the order of $E_P = 0.1 - 0.2$ μ J for pulses of about 60 ps [13]. Using a saturation energy of

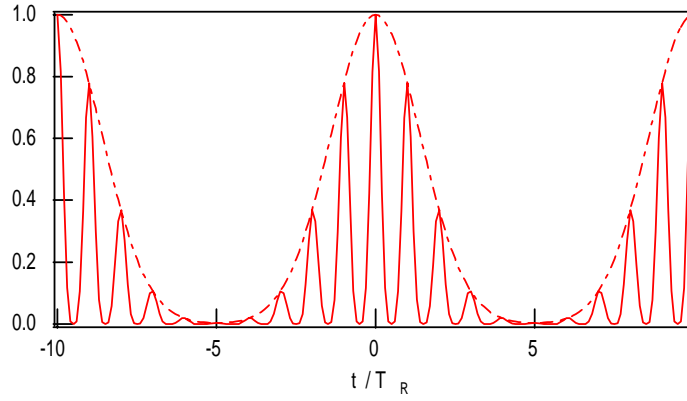


Figure 4.28: Laser output power as a function of time, when operating in the Q-switched mode-locked regime.

about $E_L = 30 \mu\text{J}$ and an output coupler loss of $2l = 0.1$, we expect, according to (4.77), a maximum extracted pulse energy of $E_P^{ex} = 2 \mu\text{J}$. Thus, we have a deviation of one order of magnitude, which clearly indicates that the absorber still introduces too much of nonsaturable intracavity losses. Lowering of these losses should lead to $\mu\text{J} - 50 \text{ ps}$ pulses from this type of a very simple and cheap laser, when compared with any other pulse generation technique.

4.6 Q-Switched Mode Locking

To understand the regime of Q-switched mode locking, we reconsider the rate equations (4.49) to (4.51). Fig. 4.28 shows, that we can describe the laser power on two time scales. One is on the order of the Q-switching envelope and occurs on multiple round-trips in the laser cavity, $T = mT_R$. Therefore, it is on the order of microseconds. The other time scale t is a short time scale on the order of the pulse width, i.e. picoseconds. Assuming a normalized pulse shape $f_n(t)$ for the n -th pulse such that

$$\int_{-T_R/2}^{T_R/2} f_n(t - nT_R) dt = 1, \quad (4.82)$$

we can make the following ansatz for the laser power

$$P(T, t) = E_P(T) \sum_{n=-\infty}^{\infty} f_n(t - nT_R). \quad (4.83)$$

Here, $E_P(T = mT_R)$ is the pulse energy of the m -th pulse, which only changes appreciably over many round-trips in the cavity. The shape of the m -th pulse, $f_m(t)$, is not yet of further interest. For simplicity, we assume that the mode-locked pulses are much shorter than the recovery time of the absorber. In this case, the relaxation term of the absorber in Eq.(4.52) can be neglected during the duration of the mode-locked pulses. Since the absorber recovery time is assumed to be much shorter than the cavity round-trip time, the absorber is unsaturated before the arrival of a pulse. Thus, for the saturation of the absorber during one pulse, we obtain

$$q(T = mT_R, t) = q_0 \exp \left[-\frac{E_P(T)}{E_A} \int_{-T_R/2}^t f_m(t') dt' \right]. \quad (4.84)$$

Then, the loss in pulse energy per roundtrip can be written as

$$q_P(T) = \int_{-T_R/2}^{T_R/2} f_m(t) q(T = mT_R, t) dt = q_0 \frac{1 - \exp \left[-\frac{E_P(T)}{E_A} \right]}{\frac{E_P(T)}{E_A}}. \quad (4.85)$$

Eq. (4.85) shows that the saturable absorber saturates with the pulse energy and not with the average intensity of the laser, as in the case of cw-Q-switching (4.52). Therefore, the absorber is much more strongly bleached at the same average power. After averaging Eqs.(4.49) and (4.50) over one round-trip, we obtain the following two equations for the dynamics of the pulse energy and the gain on a coarse grained time scale T :

$$T_R \frac{dE_P}{dT} = 2(g - l - q_P(E_P))E_P, \quad (4.86)$$

$$T_R \frac{dg}{dT} = -\frac{g - g_0}{T_L} - \frac{gE_P}{E_L}. \quad (4.87)$$

This averaging is allowed, because the saturation of the gain medium within one pulse is negligible, due to the small interaction cross section of the solid-state laser material. Comparing Eqs.(4.49), (4.50) and (4.52) with (4.84), (4.86) and (4.87), it becomes obvious that the stability criterion (4.53)

also applies to Q-switched mode locking if we replace the formula for cw-saturation of the absorber (4.52) by the formula for pulsed saturation (4.85). Then, stability against Q-switched mode locking requires

$$-2E_P \left. \frac{dq_P}{dE_P} \right|_{cw-mod} < \left. \frac{r}{T_L} \right|_{cw-mod}, \quad (4.88)$$

with

$$-2E_P \left. \frac{dq_P}{dE_P} \right|_{cw-mod} = 2q_0 \frac{1 - \exp\left[-\frac{E_P}{E_A}\right] \left(1 + \frac{E_P}{E_A}\right)}{\frac{E_P}{E_A}}. \quad (4.89)$$

When expressed in terms of the average power $P = E_P/T_R$, similar to Eq.(4.60), we obtain

$$-2T_L E_P \left. \frac{dq_P}{dE_P} \right|_{cw-mod} = 2T_L q_0 \frac{1 - \exp\left[-\frac{P}{\chi_P P_L}\right] \left(1 + \frac{P}{\chi_P P_L}\right)}{\frac{P}{\chi_P P_L}}, \quad (4.90)$$

where $\chi_P = \chi T_A$ describes an effective stiffness of the absorber compared with the gain when the laser is cw-mode-locked at the same average power as the cw laser. Thus, similar to the case of cw-Q-switching and mode locking it is useful to introduce the driving force for Q-switched mode locking

$$QMDF = \frac{2q_0 T_L}{\chi_P}. \quad (4.91)$$

Figure 4.29 shows the relation (4.88) for different absorber strength. In going from Fig. 4.18 to Fig. 4.29, we used $T_A = 0.1$. We see, that the short normalized recovery time essentially leads to a scaling of the abscissa, when going from Fig. 4.18 to Fig. 4.29 while keeping all other parameters constant. Comparing Eqs.(4.61) with (4.91), it follows that, in the case of cw-mode locking, the absorber is more strongly saturated by a factor of $1/T_A$, which can easily be as large as 1000. Therefore, the Q-switched mode locking driving force is much larger than the mode locking driving force, MDF, Accordingly, the tendency for Q-switched mode locking is significantly higher than for cw Q-switching. However, now, it is much easier to saturate the absorber with an average power well below the damage threshold of the absorber (Fig. 4.29). Therefore, one is able to leave the regime of Q-switched mode locking at a large enough intracavity power.

Image removed due to copyright restrictions.

Please see:

Kaertner, Franz, et al. "Control of solid state laser dynamics by semiconductor devices." *Optical Engineering* 34, no. 7 (July 1995): 2024-2036.

Figure 4.29: Visualization of the stability relations for Q-switched mode locking for different products $2q_0T_L$. The assumed stiffness for pulsed operation is $\chi_P = 10$, which corresponds to $T_A = 0.1$. The functional form of the relations for cw Q-switching and Q-switched mode locking is very similar. The change in the stiffness, when going from cw to pulsed saturation, thus essentially rescales the x-axis. For low-temperature grown absorbers, T_A can be as small as 10^{-6}

Image removed due to copyright restrictions.

Please see:

Kaertner, Franz, et al. "Control of solid state laser dynamics by semiconductor devices." *Optical Engineering* 34, no. 7 (July 1995): 2024-2036.

Figure 4.30: Self-Starting of mode locking and stability against Q-switched mode locking

We summarize our results for Q-switched mode locking in Fig. 4.30. It shows the stability boundary for Q-switched mode locking according to eq.(4.88), for different strengths of the saturable absorber, i.e. different values $2q_0T_L$. One may also derive minimum critical mode locking driving force for self-starting modelocking of the laser MDF_c due to various processes in the laser [24][25][27][28]. Or, with the definition of the pulsed stiffness, we obtain

$$\chi_{p,c} \leq \frac{2q_0T_L}{MDF_c} T_A. \quad (4.92)$$

Thus, for a self-starting laser which shows pure cw-mode locking, we have to design the absorber such that its MDF is greater than this critical value. Or expressed differently, the pulsed stiffness has to be smaller than the critical value $\chi_{p,c}$, at a fixed value for the absorber strength q_0 . There is always a trade-off: On one hand, the mode locking driving force has to be large enough for self-starting. On the other hand the saturable absorption has to be small enough, so that the laser can be operated in a parameter regime where it is stable against Q-switching mode locking, see Fig. (4.30).

4.7 Summary

Starting from a simple two level laser and absorber model, we characterized the dynamics of solid-state lasers mode-locked and Q-switched by a saturable absorber. The unique properties of solid-state laser materials, i.e. their long upper-state life time and their small cross sections for stimulated emission, allow for a separation of the laser dynamics on at least two time scales. One process is the energy build-up and decay, which occurs typically on a time scale of the upper state lifetime or cavity decay time of the laser. The other process is the pulse shaping, which occurs within several roundtrips in the cavity. Separating these processes, we can distinguish between the different laser dynamics called cw-Q-switching, Q-switched mode locking and cw-mode locking. We found the stability boundaries of the different regimes, which give us guidelines for the design of absorbers for a given solid state laser to favour one of these regimes. Semiconductor absorbers are a good choice for saturable absorbers to modelock lasers, since the carrier lifetime can be engineered by low temperature growth [20]. When the pulses become short enough, the laser pulse saturates the absorber much more efficiently, which stabilizes the laser against undesired Q-switched mode locking. It has

been demonstrated experimentally, that this technique can control the laser dynamics of a large variety of solid-state lasers, such as Nd:YAG, Nd:YLF, Nd:YV0₄, [18] in the picosecond regime.

With semiconductor devices and soliton formation due to negative GVD and SPM, we can use similar semiconductor absorbers to modelock the lasers in the femtosecond regime [35]. The stability criteria derived here can be applied to both picosecond and femtosecond lasers. However, the characteristics of the absorber dynamics may change drastically when going from picosecond to femtosecond pulses [36]. Especially, the saturation energy may depend not only on excitation wavelength, but also on the pulsewidth. In addition there may be additional loss mechanisms for the pulse, for example due to soliton formation there are additional filter losses of the pulse which couple to the energy of the pulse via the area theorem. This has to be taken into account, before applying the theory to fs-laser systems, which will be discussed in more detail later.

Bibliography

- [1] R. W. Hellwarth, Eds., *Advances in Quantum Electronics*, Columbia Press, New York (1961).
- [2] A. E. Siegman, "Lasers," University Science Books, Mill Valley, California (1986).
- [3] O. Svelto, "Principles of Lasers," Plenum Press, NY 1998.
- [4] W. G. Wagner and B. A. Lengyel "Evolution of the Giant Pulse in a Laser," *J. Appl. Opt.* **34**, 2040 – 2046 (1963).
- [5] J. J. Degnan, "Theory of the Optimally Coupled Q-switched Laser," *IEEE J. Quantum Electron.* **QE-25**, 214 – 220 (1989). and "Optimization of Passively Q-switched Lasers," *IEEE J. Quantum Electron.* **QE-31**, 1890 – 1901 (1995).
- [6] J. J. Zayhowski, C. D. III, *Optics Lett.* **17**, 1201 (1992)
- [7] S. H. Plaessmann, K. S. Yamada, C. E. Rich, W. M. Grossman, *Applied Optics* **32**, 6618 (1993)
- [8] J. J. Zayhowski, C. Dill, "Diode-pumped passively Q-switched picosecond microchip lasers," *Opt. Lett.* **19**, pp. 1427 – 1429 (1994).
- [9] J. J. Zayhowski, J. Ochoa, C. Dill, "UV generation with passively Q-switched picosecond microchip lasers," *Conference on Lasers and Electro Optics*, (Baltimore, USA) 1995, paper CTuM2 p. 139.
- [10] P. Wang, S.-H. Zhou, K. K. Lee, Y. C. Chen, "Picosecond laser pulse generation in a monolithic self-Q-switched solid-state laser," *Opt. Com* **114**, pp. 439 – 441 (1995).

- [11] J. J. Zayhowski, "Limits imposed by spatial hole burning on the single-mode operation of standing-wave laser cavities," *Opt. Lett.* **15**, 431 – 433 (1990).
- [12] B. Braun, F. X. Kärtner, U. Keller, J.-P. Meyn and G. Huber, "Passively Q-switched 180 ps Nd:LaSc₃(BO₃)₄ microchip laser," *Opt. Lett.* **21**, pp. 405 – 407 (1996).
- [13] B. Braun, F. X. Kärtner, G. Zhang, M. Moser and U. Keller, "56 ps Passively Q-switched diode-pumped microchip laser," *Opt. Lett.* **22**, 381-383, 1997.
- [14] O. Forster, "Analysis I, Differential- und Integralrechnung einer Veränderlichen," Vieweg, Braunschweig (1983).
- [15] E. P. Ippen, "Principles of passive mode locking," *Appl. Phys.* **B 58**, pp. 159 – 170 (1994).
- [16] A. Penzkofer, "Passive Q-switching and mode-locking for the generation of nanosecond to femtosecond Pulses," *Appl. Phys.* **B 46**, pp. 43 – 60 (1988).
- [17] U. Keller, D. A. B. Miller, G. D. Boyd, T. H. Chiu, J. F. Ferguson, M. T. Asom, "Solid-state low-loss intracavity saturable absorber for Nd:YLF lasers: an antiresonant semiconductor Fabry-Perot saturable absorber," *Opt. Lett.* **17**, pp. 505 – 507 (1992).
- [18] U. Keller, "Ultrafast all-solid-state laser technology," *Appl. Phys.* **B 58**, pp. 347-363 (1994).
- [19] J. P. Meyn, "Neodym-Lanthan-Scandium-Borat: Ein neues Material für miniaturisierte Festkörperlaser," PhD Thesis, Universität Hamburg.
- [20] G. L. Witt, R. Calawa, U. Mishra, E. Weber, Eds., "Low Temperature (LT) GaAs and Related Materials," **241** Pittsburgh, (1992).
- [21] H. Haken, "Synergetics: An Introduction," Springer Verlag, Berlin (1983).
- [22] A. Yariv, "Quantum Electronics", Wiley Interscience (1975).

- [23] H. A. Haus, "Parameter ranges for cw passive modelocking," *IEEE J. Quantum Electron.*, **QE-12**, pp. 169 – 176 (1976).
- [24] E. P. Ippen, L. Y. Liu, H. A. Haus, "Self-starting condition for additive-pulse modelocked lasers," *Opt. Lett.* **15**, pp. 183 – 18 (1990).
- [25] F. Krausz, T. Brabec, C. Spielmann, "Self-starting passive modelocking," *Opt. Lett.* **16**, pp. 235 – 237 (1991).
- [26] H. A. Haus, E. P. Ippen, "Self-starting of passively mode-locked lasers," *Opt. Lett.* **16**, pp. 1331 – 1333 (1991).
- [27] J. Herrmann, "Starting dynamic, self-starting condition and mode-locking threshold in passive, coupled-cavity or Kerr-lens mode-locked solid-state lasers," *Opt. Com.* **98**, pp. 111 – 116 (1993).
- [28] C. J. Chen, P. K. A. Wai and C. R. Menyuk, "Self-starting of passively modelocked lasers with fast saturable absorbers," *Opt. Lett.* **20**, pp. 350 – 352 (1995).
- [29] R. W. Boyd, "Nonlinear Optics," Academic Press, New York, (1992).
- [30] L. R. Brovelli, U. Keller, T. H. Chiu, "Design and Operation of Antiresonant Fabry-Perot Saturable Semiconductor Absorbers for Mode-Locked Solid-State Lasers," *J. Opt. Soc. of Am. B* **12**, pp. 311 – 322 (1995).
- [31] K. Smith, E. J. Greer, R. Wyatt, P. Wheatley, N. J. Doran, "Totally integrated erbium fiber soliton laser pumped by laser diode," *Electr. Lett.* **27**, pp. 244 – 245 (1990).
- [32] U. Keller, T. K. Woodward, D. L. Sivco, A. Y. Cho, "Coupled-Cavity Resonant Passive Modelocked Nd:Yttrium Lithium Fluoride Laser," *Opt. Lett.* **16** pp. 390 – 392 (1991).
- [33] U. Keller, T. H. Chiu, "Resonant passive modelocked Nd:YLF laser," *IEEE J. Quantum Electron.* **QE-28**, pp. 1710 – 1721 (1992).
- [34] G. P. Agrawal, N. A. Olsson, "Self-Phase Modulation and Spectral Broadening of Optical Pulses in Semiconductor Laser Amplifiers," *IEEE J. Quantum Electron.* **25**, pp. 2297 - 2306 (1989).

- [35] D. Kopf, K. J. Weingarten, L. Brovelli, M. Kamp, U. Keller, "Diode-pumped 100-fs passively mode-locked Cr:LiSAF using an A-FPSA," *Opt. Lett.* **19**, pp. (1994).
- [36] W. H. Knox, D. S. Chemla G. Livescu, J. E. Cunningham, and J. E. Henry, "Femtosecond Carrier Thermalization in Dense Fermi Seas," *Phys. Rev. Lett.* **61**, 1290 – 1293 (1988).
- [37] B. Braun, U. Keller, "Single frequency Q-switched ring laser with an antiresonant Fabry-Perot saturable absorber," *Opt. Lett.* **20**, pp. 1020 – 1022 (1995).
- [38] S. A. Kutovoi, V. V. Laptev, S. Y. Matsnev, "Lanthanum scandoborate as a new highly efficient active medium of solid state lasers," *Sov. J. Quantum Electr.* **21**, pp. 131 – 132 (1991).
- [39] B. Beier, J.-P. Meyn, R. Knappe, K.-J. Boller, G. Huber, R. Wallenstein, *Appl. Phys. B* **58**, 381 – (1994).

Chapter 5

Active Mode Locking

For simplicity, we assume, that the laser operates in the transverse fundamental modes and, therefore, we only have to treat the longitudinal modes of the laser similar to a simple plane parallel Fabry-Perot resonator (Figure: 5.1). We consider one polarization of the field only, however, as we will say later for some mode-locked laser polarization dynamics will become important.

The task of mode-locking is to get as many of the longitudinal modes lasing in a phase synchronous fashion, such that the superposition of all modes represents a pulse with a spatial extent much shorter than the cavity. The pulse will then propagate at the group velocity corresponding to the center frequency of the pulse.

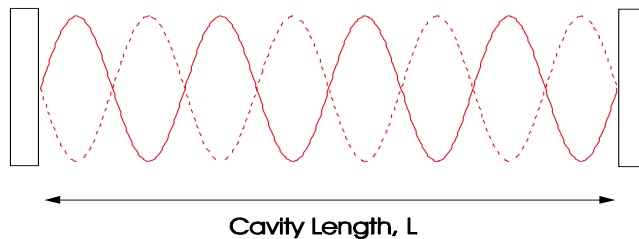


Figure 5.1: Fabry-Perot resonator

5.1 The Master Equation of Mode Locking

Lets consider for the moment the cold cavity (i.e. there is only a simple linear medium in the cavity no lasing). The most general solution for the intracavity field is a superpositon of left- and rightward running waves

$$E^{(left)}(z, t) = Re \left\{ \sum_{n=0}^{\infty} \hat{E}_n e^{j(\Omega_n t + K_n z)} \right\}, \quad (5.1)$$

and

$$E^{(right)}(z, t) = Re \left\{ \sum_{n=0}^{\infty} \hat{E}_n e^{j(\Omega_n t - K_n z)} \right\}. \quad (5.2)$$

The possible values for the wavenumbers are $K_n = n\pi/L$, resulting from the boundary conditions on metallic mirrors or periodicity after one roundtrip in the cavity. If the mirrors are perfectly reflecting, the leftward and rightward moving waves Eqs.(5.1) and (5.2) contain the same information and it is sufficient to treat only one of them. Usually one of the cavity mirrors is not perfectly reflecting in order to couple out light, however, this can be considered a perturbation to the ideal mode structure.

We consider the modes in Eq.(5.2) as a continuum and replace the sum by an integral

$$E^{(right)}(z, t) = \frac{1}{2\pi} Re \left\{ \int_{K=0}^{\infty} \hat{E}(K) e^{j(\Omega(K)t - Kz)} dK \right\} \quad (5.3)$$

with

$$\hat{E}(K_m) = \hat{E}_m 2L. \quad (5.4)$$

Eq.(5.3) is similar to the pulse propagation discussed in chapter 2 and describes the pulse propagation in the resonator. However, here it is rather an initial value problem, rather than a boundary value problem. Note, the wavenumbers of the modes are fixed, not the frequencies. To emphasize this even more, we introduce a new time variable $T = t$ and a local time frame $t' = t - z/v_{g,0}$, instead of the propagation distance z , where $v_{g,0}$ is the group velocity at the central wave number K_{n_0} of the pulse

$$v_{g,0} = \left. \frac{\partial \omega}{\partial k} \right|_{k=0} = \left. \left(\frac{\partial k}{\partial \omega} \right)^{-1} \right|_{\omega=0}. \quad (5.5)$$

For introduction of a slowly varying envelope, we shift the frequency and wavenumber by the center frequency $\omega_0 = \Omega_{n_0}$ and center wave number $k_0 = K_{n_0}$

$$k = K - K_{n_0}, \quad (5.6)$$

$$\omega(k) = \Omega(K_{n_0} + k) - \Omega_{n_0}, \quad (5.7)$$

$$\hat{E}(k) = \hat{E}(K_{n_0} + k), \quad (5.8)$$

The temporal evolution of the pulse is than determined by

$$E^{(right)}(z, t) = \frac{1}{2\pi} \text{Re} \left\{ \int_{-K_{n_0} \rightarrow -\infty}^{\infty} \hat{E}(k) e^{j(\omega(k)t - kz)} dk \right\} e^{j(\omega_0 t - k_0 z)}. \quad (5.9)$$

Analogous to chapter 2, we define a slowly varying field envelope, that is already normalized to the total power flow in the beam

$$A(z, t) = \sqrt{\frac{A_{eff}}{2Z_0}} \frac{1}{2\pi} \int_{-\infty}^{\infty} \hat{E}(k) e^{j(\omega(k)t - kz)} dk. \quad (5.10)$$

With the retarded time t' and time T , we obtain analogous to Eq. (2.184).

$$A(T, t') = \sqrt{\frac{A_{eff}}{2Z_0}} \frac{1}{2\pi} \int_{-\infty}^{\infty} \hat{E}(k) e^{j((\omega(k) - v_{g,0}k)T + kv_{g,0}t')} dk. \quad (5.11)$$

which can be written as

$$T_R \frac{\partial A(T, t')}{\partial T} \Big|_{(GDD)} = j \sum_{n=2}^{\infty} D_n \left(-j \frac{\partial^n}{\partial t'^n} \right)^n A(T, t'), \quad (5.12)$$

with the dispersion coefficients per resonator round-trip $T_R = \frac{2L}{v_{g,0}}$

$$D_n = \frac{2L}{n! v_{g,0}^{n+1}} \frac{\partial^{n-1} v_g(k)}{\partial k^{n-1}} \Big|_{k=0}. \quad (5.13)$$

The dispersion coefficients (5.13) look somewhat suspicious, however, it is not difficult to show, that they are equivalent to derivatives of the roundtrip phase $\phi_R(\Omega) = \frac{\Omega}{c} n(\Omega) 2L$ in the resonator at the center frequency

$$D_n = -\frac{1}{n!} \frac{\partial^n \phi_R^{(n)}(\Omega)}{\partial \Omega^n} \Big|_{\Omega=\omega_0}, \quad (5.14)$$

Sofar, only the lossless resonator is treated. The gain and loss can be modelled by adding a term like

$$T_R \frac{\partial A(T, t')}{\partial T} \Big|_{(loss)} = -lA(T, t') \quad (5.15)$$

where l is the amplitude loss per round-trip. In an analogous manner we can write for the gain

$$T_R \frac{\partial A(T, t')}{\partial T} \Big|_{(gain)} = \left(g(T) + D_g \frac{\partial^2}{\partial t'^2} \right) A(T, t'), \quad (5.16)$$

where $g(T)$ is the gain and D_g is the curvature of the gain at the maximum of the Lorentzian lineshape.

$$D_g = \frac{g(T)}{\Omega_g^2} \quad (5.17)$$

D_g is the gain dispersion. $g(T)$ is an average gain, which can be computed from the rate equation valid for each unit cell in the resonator. The distributed gain obeys the equation

$$\frac{\partial g(z, t)}{\partial t} = -\frac{g - g_0}{\tau_L} - g \frac{|A(z, t)|^2}{E_L}, \quad (5.18)$$

where E_L is the saturation energy $E_L = \frac{h\nu_L}{2^* \sigma_L} A_{eff}$, τ_L the upper state lifetime and σ_L the gain cross section. For typical solid-state lasers, the intracavity pulse energy is much smaller than the saturation energy. Therefore, the gain changes within one roundtrip are small. Furthermore, we assume that the gain saturates spatially homogeneous, $g(z, t') = g(t')$. Then, the equation for the average gain $g(T)$ can be found by averaging (5.18) over one round-trip and we obtain

$$\frac{\partial g(T)}{\partial T} = -\frac{g - g_0}{\tau_L} - g \frac{W(T)}{E_L T_R}, \quad (5.19)$$

where $W(T)$ is the intracavity pulse energy at time $t = T$

$$W(T) = \int_{t'=-T_R/2}^{T_R/2} |A(T, t')|^2 dt' \approx \int_{-\infty}^{\infty} |A(T, t')|^2 dt'. \quad (5.20)$$

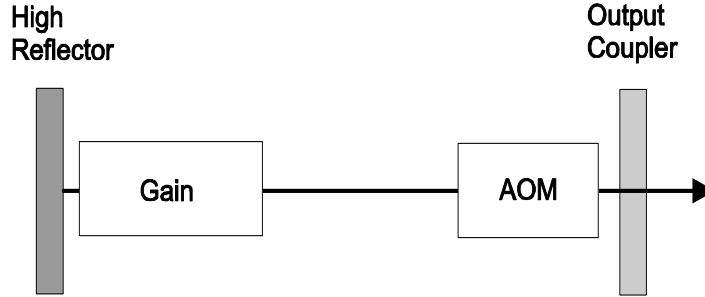


Figure 5.2: Actively modelocked laser with an amplitude modulator (Acousto-Optic-Modulator).

Taking all effects into account, the linear ones: loss, dispersion, gain and gain dispersion, as well as the nonlinear ones like saturable absorption and self-phase modulation, we end up with the master equation of modelocking

$$\begin{aligned}
 T_R \frac{\partial A(T, t')}{\partial T} &= -lA(T, t') + j \sum_{n=2}^{\infty} D_n \left(j \frac{\partial^n}{\partial t'^n} \right) A(T, t') \\
 &+ g(T) \left(1 + \frac{1}{\Omega_g^2} \frac{\partial^2}{\partial t'^2} \right) A(T, t') \\
 &- q(T, t') A(T, t') - j\delta |A(T, t')|^2 A(T, t').
 \end{aligned} \tag{5.21}$$

To keep notation simple, we replace t' by t again. This equation was first derived by Haus [4] under the assumption of small changes in pulse shape per round-trip and per element passed within one round-trip.

5.2 Active Mode Locking by Loss Modulation

Active mode locking was first investigated in 1970 by Kuizenga and Siegman using a gaussian pulse analyses, which we want to delegate to the exercises [3]. Later in 1975 Haus [4] introduced the master equation approach (5.21). We follow the approach of Haus, because it also shows the stability of the solution.

We introduce a loss modulator into the cavity, for example an acousto-optic modulator, which periodically varies the intracavity loss according to

Image removed due to copyright restrictions.

Please see:

Keller, U., Ultrafast Laser Physics, Institute of Quantum Electronics, Swiss Federal Institute of Technology, ETH Hönggerberg—HPT, CH-8093 Zurich, Switzerland.

Figure 5.3: Schematic representation of the master equation for an actively mode-locked laser.

$q(t) = M(1 - \cos(\omega_M t))$. The modulation frequency has to be very precisely tuned to the resonator round-trip time, $\omega_M = 2\pi/T_R$, see Fig.5.2. The modelocking process is then described by the master equation

$$T_R \frac{\partial A}{\partial T} = \left[g(T) + D_g \frac{\partial^2}{\partial t^2} - l - M(1 - \cos(\omega_M t)) \right] A. \quad (5.22)$$

neglecting GDD and SPM. The equation can be interpreted as the total pulse shaping due to gain, loss and modulator, see Fig.5.3.

If we fix the gain in Eq. (5.22) at its stationary value, what ever it might be, Eq.(5.22) is a linear p.d.e, which can be solved by separation of variables. The pulses, we expect, will have a width much shorter than the round-trip time T_R . They will be located in the minimum of the loss modulation where the cosine-function can be approximated by a parabola and we obtain

$$T_R \frac{\partial A}{\partial T} = \left[g - l + D_g \frac{\partial^2}{\partial t^2} - M_s t^2 \right] A. \quad (5.23)$$

M_s is the modulation strength, and corresponds to the curvature of the loss modulation in the time domain at the minimum loss point

$$D_g = \frac{g}{\Omega_g^2}, \quad (5.24)$$

$$M_s = \frac{M\omega_M^2}{2}. \quad (5.25)$$

The differential operator on the right side of (5.23) corresponds to the Schrödinger-Operator of the harmonic oscillator problem. Therefore, the eigen functions of this operator are the Hermite-Gaussians

$$A_n(T, t) = A_n(t)e^{\lambda_n T/T_R}, \quad (5.26)$$

$$A_n(t) = \sqrt{\frac{W_n}{2^n \sqrt{\pi} n! \tau_a}} H_n(t/\tau_a) e^{-\frac{t^2}{2\tau_a^2}}, \quad (5.27)$$

where τ_a defines the width of the Gaussian. The width is given by the fourth root of the ratio between gain dispersion and modulator strength

$$\tau_a = \sqrt[4]{D_g/M_s}. \quad (5.28)$$

Note, from Eq. (5.26) we can follow, that the gain per round-trip of each eigenmode is given by λ_n (or in general the real part of λ_n), which are given by

$$\lambda_n = g_n - l - 2M_s\tau_a^2(n + \frac{1}{2}). \quad (5.29)$$

The corresponding saturated gain for each eigen solution is given by

$$g_n = \frac{1}{1 + \frac{W_n}{P_L T_R}}, \quad (5.30)$$

where W_n is the energy of the corresponding solution and $P_L = E_L/\tau_L$ the saturation power of the gain. Eq. (5.29) shows that for given g the eigen solution with $n = 0$, the ground mode, has the largest gain per roundtrip. Thus, if there is initially a field distribution which is a superposition of all eigen solutions, the ground mode will grow fastest and will saturate the gain to a value

$$g_s = l + M_s\tau_a^2. \quad (5.31)$$

such that $\lambda_0 = 0$ and consequently all other modes will decay since $\lambda_n < 0$ for $n \geq 1$. This also proves the stability of the ground mode solution [4]. Thus active modelocking without detuning between resonator round-trip time and modulator period leads to Gaussian steady state pulses with a FWHM pulse width

$$\Delta t_{FWHM} = 2 \ln 2 \tau_a = 1.66 \tau_a. \quad (5.32)$$

The spectrum of the Gaussian pulse is given by

$$\tilde{A}_0(\omega) = \int_{-\infty}^{\infty} A_0(t)e^{i\omega t} dt \quad (5.33)$$

$$= \sqrt{\sqrt{\pi}W_n\tau_a} e^{-\frac{(\omega\tau_a)^2}{2}}, \quad (5.34)$$

and its FWHM is

$$\Delta f_{FWHM} = \frac{1.66}{2\pi\tau_a}. \quad (5.35)$$

Therefore, the time-bandwidth product of the Gaussian is

$$\Delta t_{FWHM} \cdot \Delta f_{FWHM} = 0.44. \quad (5.36)$$

The stationary pulse shape of the modelocked laser is due to the parabolic loss modulation (pulse shortening) in the time domain and the parabolic filtering (pulse stretching) due to the gain in the frequency domain, see Figs. 5.4 and 5.5. The stationary pulse is achieved when both effects balance. Since external modulation is limited to electronic speed and the pulse width does only scale with the inverse square root of the gain bandwidth actively modelocking typically only results in pulse width in the range of 10-100ps.

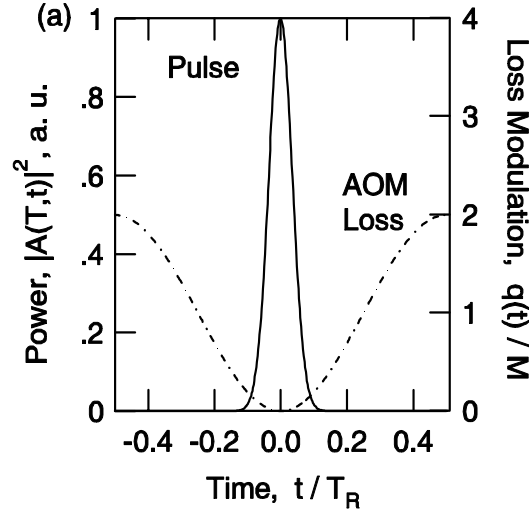


Figure 5.4: (a) Loss modulation gives pulse shortening in each roundtrip

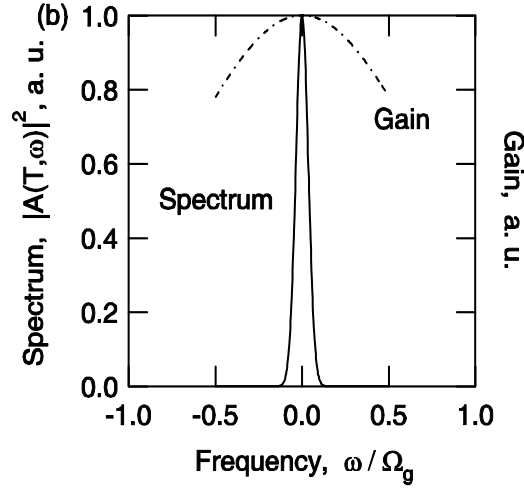


Figure 5.5: (b) the finite gain bandwidth gives pulse broadening in each roundtrip. For a certain pulse width there is balance between the two processes.

For example: Nd:YAG; $2l = 2g = 10\%$, $\Omega_g = \pi\Delta f_{FWHM} = 0.65$ THz, $M = 0.2$, $f_m = 100$ MHz, $D_g = 0.24$ ps², $M_s = 4 \cdot 10^{16} s^{-1}$, $\tau_p \approx 99$ ps.

With the pulse width (5.28), Eq.(5.31) can be rewritten in several ways

$$g_s = l + M_s\tau_a^2 = l + \frac{D_g}{\tau_a^2} = l + \frac{1}{2}M_s\tau_a^2 + \frac{1}{2}\frac{D_g}{\tau_a^2}, \quad (5.37)$$

which means that in steady state the saturated gain is lifted above the loss level l , so that many modes in the laser are maintained above threshold. There is additional gain necessary to overcome the loss of the modulator due to the finite temporal width of the pulse and the gain filter due to the finite bandwidth of the pulse. Usually

$$\frac{g_s - l}{l} = \frac{M_s\tau_a^2}{l} \ll 1, \quad (5.38)$$

since the pulses are much shorter than the round-trip time and the stationary pulse energy can therefore be computed from

$$g_s = \frac{1}{1 + \frac{W_s}{P_L T_R}} = l. \quad (5.39)$$

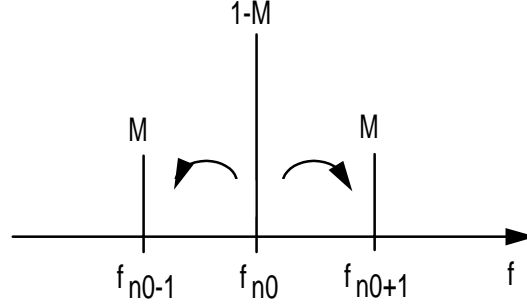


Figure 5.6: Modelocking in the frequency domain: The modulator transverses energy from each mode to its neighboring mode, thereby redistributing energy from the center to the wings of the spectrum. This process seeds and injection locks neighboring modes.

The name modelocking originates from studying this pulse formation process in the frequency domain. Note, the term

$$-M [1 - \cos(\omega_M t)] A$$

does generate sidebands on each cavity mode present according to

$$\begin{aligned} & -M [1 - \cos(\omega_M t)] \exp(j\omega_{n_0} t) \\ = & -M \left[\exp(j\omega_{n_0} t) - \frac{1}{2} \exp(j(\omega_{n_0} t - \omega_M t)) - \frac{1}{2} \exp(j(\omega_{n_0} t + \omega_M t)) \right] \\ = & M \left[-\exp(j\omega_{n_0} t) + \frac{1}{2} \exp(j\omega_{n_0-1} t) + \frac{1}{2} \exp(j\omega_{n_0+1} t) \right] \end{aligned}$$

if the modulation frequency is the same as the cavity round-trip frequency. The sidebands generated from each running mode is injected into the neighboring modes which leads to synchronisation and locking of neighboring modes, i.e. mode-locking, see Fig.5.6

5.3 Active Mode-Locking by Phase Modulation

Side bands can also be generated by a phase modulator instead of an amplitude modulator. However, the generated sidebands are out of phase with

the carrier, which leads to a chirp on the steady state pulse. We can again use the master equation to study this type of modelocking. All that changes is that the modulation becomes imaginary, i.e. we have to replace M by jM in Eq.(5.22)

$$T_R \frac{\partial A}{\partial T} = \left[g(T) + D_g \frac{\partial^2}{\partial t^2} - l - jM (1 - \cos(\omega_M t)) \right] A. \quad (5.40)$$

The imaginary unit can be pulled through much of the calculation and we arrive at the same Hermite Gaussian eigen solutions (5.26,5.27), however, the parameter τ_a becomes τ'_a and is now complex and not quite the pulse width

$$\tau'_a = \sqrt[4]{-j} \sqrt[4]{D_g/M_s}. \quad (5.41)$$

The ground mode or stationary solution is given by

$$A_0(t) = \sqrt{\frac{W_s}{2^n \sqrt{\pi} n! \tau'_a}} e^{-\frac{t^2}{2\tau_a^2} \frac{1}{\sqrt{2}}(1+j)}, \quad (5.42)$$

with $\tau_a = \sqrt[4]{D_g/M_s}$ as before. We end up with chirped pulses. How does the pulse shortening actually work, because the modulator just puts a chirp on the pulse, it does actually not shorten it? One can easily show, that if a Gaussian pulse with chirp parameter β

$$A_0(t) \sim e^{-\frac{t^2}{2\tau_a^2} \frac{1}{\sqrt{2}}(1+j\beta)}, \quad (5.43)$$

has a chirp $\beta > 1$, subsequent filtering is actually shortening the pulse.

5.4 Active Mode Locking with Additional SPM

Due to the strong focussing of the pulse in the gain medium also additional self-phase modulation can become important. Lets consider the case of an actively mode-locked laser with additional SPM, see Fig. 5.7. One can write down the corresponding master equation

$$T_R \frac{\partial A}{\partial T} = \left[g(T) + D_g \frac{\partial^2}{\partial t^2} - l - M_s t^2 - j\delta |A|^2 \right] A. \quad (5.44)$$

Unfortunately, there is no analytic solution to this equation. But it is not difficult to guess what will happen in this case. As long as the SPM is not

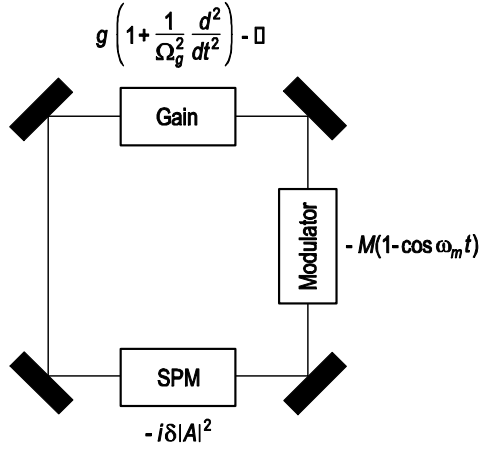


Figure 5.7: Active mode-locking with SPM

excessive, the pulses will experience additional self-phase modulation, which creates a chirp on the pulse. Thus one can make an ansatz with a chirped Gaussian similar to (5.43) for the steady state solution of the master equation (5.44)

$$A_0(t) = A e^{-\frac{t^2}{2\tau_a^2}(1+j\beta)+j\Psi T/T_R} \quad (5.45)$$

Note, we allow for an additional phase shift per roundtrip Ψ , because the added SPM does not leave the phase invariant after one round-trip. This is still a steady state solution for the intensity envelope. Substitution into the master equation using the intermediate result

$$\frac{\partial^2}{\partial t^2} A_0(t) = \left\{ \frac{t^2}{\tau_a^4} (1+j\beta)^2 - \frac{1}{\tau_a^2} (1+j\beta) \right\} A_0(t). \quad (5.46)$$

leads to

$$j\Psi A_0(t) = \left\{ g - l + D_g \left[\frac{t^2}{\tau_a^4} (1+j\beta)^2 - \frac{1}{\tau_a^2} (1+j\beta) \right] - M_s t^2 - j\delta |A|^2 e^{-\frac{t^2}{\tau_a^2}} \right\} A_0(t). \quad (5.47)$$

To find an approximate solution we expand the Gaussian in the bracket, which is a consequence of the SPM to first order in the exponent.

$$j\Psi = g - l + D_g \left[\frac{t^2}{\tau_a^4} (1 + j\beta)^2 - \frac{1}{\tau_a^2} (1 + j\beta) \right] - M_s t^2 - j\delta |A|^2 \left(1 - \frac{t^2}{\tau_a^2} \right). \quad (5.48)$$

This has to be fulfilled for all times, so we can compare coefficients in front of the constant terms and the quadratic terms, which leads to two complex conditions. This leads to four equations for the unknown pulsewidth τ_a , chirp β , round-trip phase Ψ and the necessary excess gain $g - l$. With the nonlinear peak phase shift due to SPM, $\phi_0 = \delta |A|^2$. Real and Imaginary parts of the quadratic terms lead to

$$0 = \frac{D_g}{\tau_a^4} (1 - \beta^2) - M_s, \quad (5.49)$$

$$0 = 2\beta \frac{D_g}{\tau_a^4} + \frac{\phi_0}{\tau_a^2}, \quad (5.50)$$

and the constant terms give the excess gain and the additional round-trip phase.

$$g - l = \frac{D_g}{\tau_a^2}, \quad (5.51)$$

$$\Psi = D_g \left[-\frac{1}{\tau_a^2} \beta \right] - \phi_0. \quad (5.52)$$

The first two equations directly give the chirp and pulse width.

$$\beta = -\frac{\phi_0 \tau_a^2}{2D_g} \quad (5.53)$$

$$\tau_a^4 = \frac{D_g}{M_s + \frac{\phi_0^2}{4D_g}}. \quad (5.54)$$

However, one has to note, that this simple analysis does not give any hint on the stability of these approximate solution. Indeed computer simulations show, that after an additional pulse shorting of about a factor of 2 by SPM beyond the pulse width already achieved by pure active mode-locking on its own, the SPM drives the pulses unstable [5]. This is one of the reasons, why very broadband laser media, like Ti:sapphire, can not simply generate

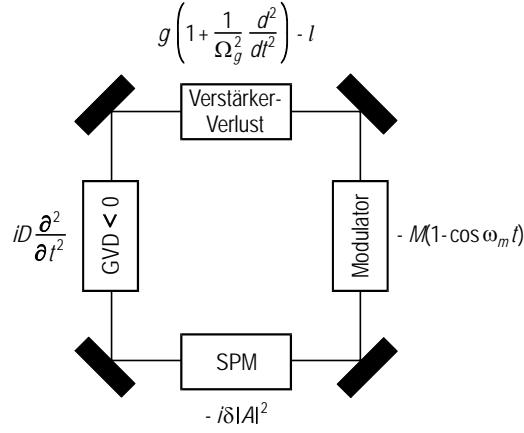


Figure 5.8: Active mode-locking with additional soliton formation

femtosecond pulses via active modelocking. The SPM occurring in the gain medium for very short pulses drives the modelocking unstable. Additional stabilization measures have to be adopted. For example the addition of negative group delay dispersion might lead to stable soliton formation in the presence of the active modelocker.

5.5 Active Mode Locking with Soliton Formation

Experimental results with fiber lasers [8, 9, 11] and solid state lasers [10] indicated that soliton shaping in the negative GDD regime leads to pulse stabilization and considerable pulse shortening. With sufficient negative dispersion and self-phase modulation in the system and picosecond or even femtosecond pulses, it is possible that the pulse shaping due to GDD and SPM is much stronger than due to modulation and gain filtering, see Fig. 5.8. The resulting master equation for this case is

$$T_R \frac{\partial A}{\partial T} = \left[g + (D_g - j |D|) \frac{\partial^2}{\partial t^2} - l - M (1 - \cos(\omega_M t)) - j \delta |A|^2 \right] A. \quad (5.55)$$

For the case, that soliton formation takes over, the steady state solution a soliton plus a continuum contribution

$$A(T, t) = (a(x)e^{jpt} + a_c(T, t)) e^{-j\theta} \quad (5.56)$$

with

$$a(x) = A \operatorname{sech}(x), \quad \text{and} \quad x = \frac{1}{\tau}(t + 2D \int_0^T p(T') dT' - t_0) \quad (5.57)$$

where a_c is the continuum contribution. The phase is determined by

$$\theta(T) = \theta_0(T) - \frac{D}{T_R} \int_0^T \left(\frac{1}{\tau(T')^2} - p(T')^2 \right) dT', \quad (5.58)$$

whereby we always assume that the relation between the soliton energy and soliton width is maintained (3.9)

$$\frac{|D|}{\tau(T)^2} = \frac{\delta A(T)^2}{2}. \quad (5.59)$$

We also allow for a continuous change in the soliton amplitude A or energy $W = 2A^2\tau$ and the soliton variables phase θ_0 , carrier frequency p and timing t_0 . ϕ_0 is the soliton phase shift per roundtrip

$$\phi_0 = \frac{|D|}{\tau^2}. \quad (5.60)$$

However, we assume that the changes in carrier frequency, timing and phase stay small. Introducing (5.56) into (5.55) we obtain according to the soliton perturbation theory developed in chapter 3.5

$$\begin{aligned} & T_R \left[\frac{\partial a_c}{\partial T} + \frac{\partial W}{\partial T} \mathbf{f}_w + \frac{\partial \Delta \theta}{\partial T} \mathbf{f}_\theta + \frac{\partial \Delta p}{\partial T} \mathbf{f}_p + \frac{\partial \Delta t}{\partial T} \mathbf{f}_t \right] \\ &= \phi_0 \mathbf{L} (\mathbf{a}_c + \Delta p \mathbf{f}_p) + \mathbf{R} (\mathbf{a} + \Delta p \mathbf{f}_p + \mathbf{a}_c) \\ & \quad - M \omega_M \sin(\omega_M \tau x) \Delta t \mathbf{a}(x) \end{aligned} \quad (5.61)$$

The last term arises because the active modelocker breaks the time invariance of the system and leads to a restoring force pushing the soliton back to its equilibrium position. \mathbf{L} , \mathbf{R} are the operators of the linearized NSE and of the active mode locking scheme, respectively

$$\mathbf{R} = g \left(1 + \frac{1}{\Omega_g^2 \tau^2} \frac{\partial^2}{\partial x^2} \right) - l - M (1 - \cos(\omega_M \tau x)), \quad (5.62)$$

The vectors \mathbf{f}_w , \mathbf{f}_θ , \mathbf{f}_p and \mathbf{f}_t describe the change in the soliton when the soliton energy, phase, carrier frequency and timing varies.

5.5.1 Stability Condition

We want to show, that a stable soliton can exist in the presence of the modelocker and gain dispersion if the ratio between the negative GDD and gain dispersion is sufficiently large. From (5.61) we obtain the equations of motion for the soliton parameters and the continuum by carrying out the scalar product with the corresponding adjoint functions. Specifically, for the soliton energy we get

$$T_R \frac{\partial W}{\partial T} = 2 \left(g - l - \frac{g}{3\Omega_g^2 \tau^2} - \frac{\pi^2}{24} M \omega_M^2 \tau^2 \right) W + \langle \mathbf{f}_w^{(+)} | \mathbf{R} \mathbf{a}_c \rangle . \quad (5.63)$$

We see that gain saturation does not lead to a coupling between the soliton and the continuum to first order in the perturbation, because they are orthogonal to each other in the sense of the scalar product (3.36). This also means that to first order the total field energy is contained in the soliton.

Thus to zero order the stationary soliton energy $W_0 = 2A_0^2 \tau$ is determined by the condition that the saturated gain is equal to the total loss due to the linear loss l , gain filtering and modulator loss

$$g - l = \frac{\pi^2}{24} M \omega_M^2 \tau^2 + \frac{g}{3\Omega_g^2 \tau^2} \quad (5.64)$$

with the saturated gain

$$g = \frac{g_0}{1 + W_0/E_L} . \quad (5.65)$$

Linearization around this stationary value gives for the soliton perturbations

$$\begin{aligned}
 T_R \frac{\partial \Delta W}{\partial T} &= 2 \left(- \frac{g}{(1 + W_0/E_L)} \left(\frac{W_0}{E_L} + \frac{1}{3\Omega_g^2 \tau^2} \right) \right. \\
 &\quad \left. + \frac{\pi^2}{12} M \omega_M^2 \tau^2 \right) \Delta W + \langle \mathbf{f}_w^{(+)} | \mathbf{R} \mathbf{a}_c \rangle
 \end{aligned} \tag{5.66}$$

$$T_R \frac{\partial \Delta \theta}{\partial T} = \langle \mathbf{f}_\theta^{(+)} | \mathbf{R} \mathbf{a}_c \rangle \tag{5.67}$$

$$T_R \frac{\partial \Delta p}{\partial T} = - \frac{4g}{3\Omega_g^2 \tau^2} \Delta p + \langle \mathbf{f}_p^{(+)} | \mathbf{R} \mathbf{a}_c \rangle \tag{5.68}$$

$$\begin{aligned}
 T_R \frac{\partial \Delta t}{\partial T} &= - \frac{\pi^2}{6} M \omega_M^2 \tau^2 \Delta t + 2|D| \Delta p \\
 &\quad + \langle \mathbf{f}_t^{(+)} | \mathbf{R} \mathbf{a}_c \rangle
 \end{aligned} \tag{5.69}$$

and for the continuum we obtain

$$\begin{aligned}
 T_R \frac{\partial g(k)}{\partial T} &= j\Phi_0(k^2 + 1)g(k) + \langle \mathbf{f}_k^{(+)} | \mathbf{R} \mathbf{a}_c \rangle \\
 &\quad + \langle \mathbf{f}_k^{(+)} | \mathbf{R} (\mathbf{a}_0(x) + \Delta w \mathbf{f}_w + \Delta p \mathbf{f}_p) \rangle \\
 &\quad - \langle \mathbf{f}_k^{(+)} | M \omega_M \sin(\omega_M \tau x) \mathbf{a}_0(x) \rangle . \Delta t
 \end{aligned} \tag{5.70}$$

Thus the action of the active modelocker and gain dispersion has several effects. First, the modelocker leads to a restoring force in the timing of the soliton (5.69). Second, the gain dispersion and the active modelocker lead to coupling between the perturbed soliton and the continuum which results in a steady excitation of the continuum.

However, as we will see later, the pulse width of the soliton, which can be stabilized by the modelocker, is not too far from the Gaussian pulse width by only active mode locking. Then relation

$$\omega_M \tau \ll 1 \ll \Omega_g \tau \tag{5.71}$$

is fulfilled. The weak gain dispersion and the weak active modelocker only couples the soliton to the continuum, but to first order the continuum does not couple back to the soliton. Neglecting higher order terms in the matrix elements of eq.(5.70) [6] results in a decoupling of the soliton perturbations from the continuum in (5.66) to (5.70). For a laser far above threshold, i.e.

$W_0/E_L \gg 1$, gain saturation always stabilizes the amplitude perturbation and eqs.(5.67) to (5.69) indicate for phase, frequency and timing fluctuations. This is in contrast to the situation in a soliton storage ring where the laser amplifier compensating for the loss in the ring is below threshold [14].

By inverse Fourier transformation of (5.70) and weak coupling, we obtain for the associated function of the continuum

$$\begin{aligned} T_R \frac{\partial G}{\partial T} = & \left[g - l + j\Phi_0 + \frac{g}{\Omega_g^2} (1 - jD_n) \frac{\partial^2}{\partial t^2} \right. \\ & \left. - M(1 - \cos(\omega_M t)) \right] G + \mathcal{F}^{-1} \left\{ \langle \mathbf{f}_k^{(+)} | \mathbf{R} \mathbf{a}_0(x) \rangle \right. \\ & \left. - \langle \mathbf{f}_k^{(+)} | M \omega_M \sin(\omega_M \tau x) \mathbf{a}_0(x) \rangle \Delta t \right\} \end{aligned} \quad (5.72)$$

where D_n is the dispersion normalized to the gain dispersion

$$D_n = |D| \Omega_g^2 / g. \quad (5.73)$$

Note, that the homogeneous part of the equation of motion for the continuum, which governs the decay of the continuum, is the same as the homogeneous part of the equation for the noise in a soliton storage ring at the position where no soliton or bit is present [14]. Thus the decay of the continuum is not affected by the nonlinearity, but there is a continuous excitation of the continuum by the soliton when the perturbing elements are passed by the soliton. Thus under the above approximations the question of stability of the soliton solution is completely governed by the stability of the continuum (5.72). As we can see from (5.72) the evolution of the continuum obeys the active mode locking equation with GVD but with a value for the gain determined by (5.64). In the parabolic approximation of the cosine, we obtain again the Hermite Gaussians as the eigensolutions for the evolution operator but the width of these eigensolutions is now given by

$$\tau_c = \tau_a \sqrt[4]{(1 - jD_n)} \quad (5.74)$$

and the associated eigenvalues are

$$\lambda_m = j\Phi_0 + g - l - M \omega_M^2 \tau_a^2 \sqrt{(1 - jD_n)} \left(m + \frac{1}{2}\right). \quad (5.75)$$

The gain is clamped to the steady state value given by condition (5.64) and we obtain

$$\lambda_m = +j\Phi_0 + \frac{1}{3}\sqrt{D_g M_s} \left[\left(\frac{\tau_a}{\tau}\right)^2 + \frac{\pi^2}{4} \left(\frac{\tau_a}{\tau}\right)^{-2} - 6\sqrt{(1-jD_n)}\left(m + \frac{1}{2}\right) \right]. \quad (5.76)$$

Stability is achieved when all continuum modes see a net loss per roundtrip, $Re\{\lambda_m\} < 0$ for $m \geq 0$, i.e. we get from (5.76)

$$\left(\frac{\tau_a}{\tau}\right)^2 + \frac{\pi^2}{4} \left(\frac{\tau}{\tau_a}\right)^2 < 3Re\{\sqrt{(1-jD_n)}\}. \quad (5.77)$$

Relation (5.77) establishes a quadratic inequality for the pulse width reduction ratio $\xi = (\tau_a/\tau)^2$, which is a measure for the pulse width reduction due to soliton formation

$$\xi^2 - 3Re\{\sqrt{(1-jD_n)}\}\xi + \frac{\pi^2}{4} < 0. \quad (5.78)$$

As has to be expected, this inequality can only be satisfied if we have a minimum amount of negative normalized dispersion so that a soliton can be formed at all

$$D_{n,crit} = 0.652. \quad (5.79)$$

Therefore our perturbation ansatz gives only meaningful results beyond this critical amount of negative dispersion. Since ξ compares the width of a Gaussian with that of a secant hyperbolic it is more relevant to compare the full width half maximum of the intensity profiles [?] of the corresponding pulses which is given by

$$R = \frac{1.66}{1.76} \sqrt{\xi}. \quad (5.80)$$

Image removed due to copyright restrictions.

Please see:

Kaertner, F., D. Kopf, and U. Keller. "Solitary-pulse stabilization and shortening in actively mode-locked lasers." *Journal of the Optical Society of America B* 12, no. 3 (March 1995): 486.

Figure 5.9: Pulselwidth reduction as a function of normalized dispersion. Below $D_{n,crit} = 0.652$ no stable soliton can be formed.

Figure 5.9 shows the maximum pulse width reduction R allowed by the stability criterion (5.78) as a function of the normalized dispersion. The critical value for the pulse width reduction is $R_{crit} \approx 1.2$. For large normalized dispersion Fig. 1 shows that the soliton can be kept stable at a pulse width reduced by up to a factor of 5 when the normalized dispersion can reach a value of 200. Even at a moderate negative dispersion of $D_n = 5$, we can achieve a pulselwidth reduction by a factor of 2. For large normalized dispersion the stability criterion (5.78) approaches asymptotically the behavior

$$\xi < \sqrt{\frac{9D_n}{2}} \quad \text{or} \quad R < \frac{1.66}{1.76} \sqrt[4]{\frac{9D_n}{2}}. \quad (5.81)$$

Thus, the possible pulse-width reduction scales with the fourth root of the normalized dispersion indicating the need of an excessive amount of dispersion necessary to maintain a stable soliton while suppressing the continuum. The physical reason for this is that gain filtering and the active modelocker continuously shed energy from the soliton into the continuum. For the soliton the action of GVD and SPM is always in balance and maintains the pulse shape. However, as can be seen from (5.72), the continuum, which can be viewed as a weak background pulse, does not experience SPM once it is generated and therefore gets spread by GVD. This is also the reason why the eigenstates of the continuum consist of long chirped pulses that scale

also with the fourth root of the dispersion (5.74). Then, the long continuum pulses suffer a much higher loss in the active modulator in contrast to the short soliton which suffers reduced gain when passing the gain medium due to its broader spectrum. The soliton is stable as long as the continuum sees less roundtrip gain than the soliton.

In principle by introducing a large amount of negative dispersion the theory would predict arbitrarily short pulses. However, the master equation (5.55) only describes the laser system properly when the nonlinear changes of the pulse per pass are small. This gives an upper limit to the nonlinear phase shift Φ_0 that the soliton can undergo during one roundtrip. A conservative estimation of this upper limit is given with $\Phi_0 = 0.1$. Then the action of the individual operators in (5.55) can still be considered as continuous. Even if one considers larger values for the maximum phase shift allowed, since in fiber lasers the action of GVD and SPM occurs simultaneously and therefore eq.(5.55) may describe the laser properly even for large nonlinear phase shifts per roundtrip, one will run into intrinsic soliton and sideband instabilities for Φ_0 approaching 2π [30, 31]. Under the condition of a limited phase shift per roundtrip we obtain

$$\tau^2 = \frac{|D|}{\Phi_0}. \quad (5.82)$$

Thus from (5.32), the definition of ξ , (5.81) and (5.82) we obtain for the maximum possible reduction in pulsewidth

$$R_{max} = \frac{1.66}{1.76} \sqrt[12]{\frac{(9\Phi_0/2)^2}{D_g M_s}} \quad (5.83)$$

and therefore for the minimum pulsewidth

$$\tau_{min} = \sqrt[6]{\frac{2D_g^2}{9\Phi_0 M_s}}. \quad (5.84)$$

The necessary amount of normalized negative GVD is then given by

$$D_n = \frac{2}{9} \sqrt[3]{\frac{(9\Phi_0/2)^2}{D_g M_s}}. \quad (5.85)$$

Eqs.(5.83) to (5.85) constitute the main results of this paper, because they allow us to compute the possible pulse width reduction and the necessary

Image removed due to copyright restrictions.

Please see:

Kaertner, F., D. Kopf, and U. Keller. "Solitary-pulse stabilization and shortening in actively mode-locked lasers." *Journal of the Optical Society of America B* 12, no. 3 (March 1995): 486.

Table 5.1: Maximum pulsewidth reduction and necessary normalized GVD for different laser systems. In all cases we used for the saturated gain $g = 0.1$ and the soliton phase shift per roundtrip $\Phi_0 = 0.1$. For the broadband gain materials the last column indicates rather long transient times which calls for regenerative mode locking.

negative GVD for a given laser system. Table (5.1) shows the evaluation of these formulas for several gain media and typical laser parameters.

Table 5.1 shows that soliton formation in actively mode-locked lasers may lead to considerable pulse shortening, up to a factor of 10 in Ti:sapphire. Due to the 12th root in (5.83) the shortening depends mostly on the bandwidth of the gain material which can change by several orders of magnitude for the different laser materials. The amount of negative dispersion for achieving this additional pulse shortening is in a range which can be achieved by gratings, Gires-Tournois interferometers, or prisms.

Of course, in the experiment one has to stay away from these limits to suppress the continuum sufficiently. However, as numerical simulations show, the transition from stable to instable behaviour is remarkably sharp. The reason for this can be understood from the structure of the eigenvalues for the continuum (5.76). The time scale for the decay of transients is given by the inverse of the real part of the fundamental continuum mode which diverges at the transition to instability. Nevertheless, a good estimate for this transient time is given by the leading term of the real part of (5.76)

$$\frac{\tau_{trans}}{T_R} = \frac{1}{Re\{\lambda_0\}} \approx \frac{3}{\sqrt{D_g M_s R^2}} \quad (5.86)$$

This transient time is also shown in Table (5.1) for different laser systems. Thus these transients decay, if not too close to the instability border, on time scales from approximately 1,000 up to some 100,000 roundtrips, depending strongly on the gain bandwidth and modulation strength. Consequently, to first order the eigenvalues of the continuum modes, which are excited by the right hand side of (5.72), are purely imaginary and independent of the mode number, i.e. $\lambda_n \approx j\Phi_0$. Therefore, as long as the continuum is stable, the solution to (5.72) is given by

$$G(x) = \frac{-j}{\Phi_0} \mathcal{F}^{-1} \left\{ \begin{array}{l} \langle \mathbf{f}_k^{(+)} | \mathbf{R}\mathbf{a}_0(x) \rangle \\ - M_s \tau^2 \langle \mathbf{f}_k^{(+)} | x \mathbf{a}_0(x) \rangle \frac{\Delta t}{\tau} \end{array} \right\}. \quad (5.87)$$

Thus, in steady state the continuum is on the order of

$$|G(x)| \approx \frac{A_0 D_g}{\Phi_0 \tau^2} = \frac{A_0}{D_n}. \quad (5.88)$$

which demonstrates again the spreading of the continuum by the dispersion. Equation (5.88) shows that the nonlinear phase shift of the solitary pulse per round trip has to be chosen as large as possible. This also maximizes the normalized dispersion, so that the radiation shed from the soliton into the continuum changes the phase rapidly enough such that the continuum in steady state stays small. Note that the size of the generated continuum according to (5.88) is rather independent of the real part of the lowest eigenvalue of the continuum mode. Therefore, the border to instability is very sharply defined. However, the time scale of the transients at the transition to instability can become arbitrarily long. Therefore, numerical simulations are only trustworthy if the time scales for transients in the system are known from theoretical considerations as those derived above in (5.86). The simulation time for a given laser should be at least of the order of 10 times τ_{trans} or even longer, if operated close to the instability point, as we will see in the next section.

5.5.2 Numerical simulations

Table 5.1 shows that soliton formation in actively mode-locked lasers may lead to considerable pulse shortening, up to a factor of 10 in Ti:sapphire. We want to illustrate that at the example of a Nd:YAG laser, which is chosen due to its moderate gain bandwidth, and therefore, its large gain dispersion. This will limit the pulsewidth reduction possible to about 3, but the decay time of the continuum (5.86) (see also Table 5.1) is then in a range of 700 roundtrips so that the steady state of the mode-locked laser can be reached with moderate computer time, while the approximations involved are still satisfied. The system parameters used for the simulation are shown in table 5.2. For the simulation of eq.(5.55) we use the standard split-step Fourier transform method. Here the discrete action of SPM and GDD per roundtrip is included by choosing the integration step size for the T integration to be the roundtrip time T_R . We used a discretisation of 1024 points over the bandwidth of $1THz$, which corresponds to a resolution in the time domain of $1ps$. The following figures, show only one tenth of the simulated window in time and frequency.

Figure 5.10 shows the result of the simulation starting with a 68-ps-long Gaussian pulse with a pulse energy of $W = 40$ nJ for $D_n = 24$, i.e. $D = -17$ ps². For the given SPM coefficient this should lead to stable pulse shortening by a factor of $R = 2.8$. Thus after at least a few thousand roundtrips the

parameter	value
l	0.1
g_0	1
P_L	1W
Ω_g	$2\pi \cdot 60GHz$
ω_M	$2\pi \cdot 0.25GHz$
T_R	4ns
M	0.2
δ	$1.4 \cdot 10^{-4}W^{-1}$
D	$-17ps^2 / -10ps^2$

Table 5.2: Parameters used for numerical simulations

Image removed due to copyright restrictions.

Please see:

Kaertner, F., D. Kopf, and U. Keller. "Solitary-pulse stabilization and shortening in actively mode-locked lasers." *Journal of the Optical Society of America B* 12, no. 3 (March 1995): 486.

Figure 5.10: Time evolution of the pulse intensity in a Nd:YAG laser for the parameters in Table 5.2, $D = -17ps^2$, for the first 1,000 roundtrips in the laser cavity, starting with a 68ps long Gaussian pulse.

laser should be in steady state again with a FWHM pulsewidth of 24 ps. Fig. 5.10 shows the pulse evolution over the first thousand round-trips, i.e. $4\mu\text{s}$ real time. The long Gaussian pulse at the start contains an appreciable amount of continuum. The continuum part of the solution does not experience the nonlinear phase shift due to SPM in contrast to the soliton. Thus the soliton interferes with the continuum periodically with the soliton period of $T_{\text{soliton}}/T_R = 2\pi/\phi_0 = 20\pi$. This is the reason for the oscillations of the pulse amplitude seen in Fig. 5.10 which vanish with the decay of the continuum. Note also that the solitary pulse is rapidly formed, due to the large nonlinear phase shift per roundtrip. Figure 5.11 shows the simulation in time and frequency domain over 10,000 roundtrips. The laser reaches steady state after about 4,000 roundtrips which corresponds to $6 \times \tau_{\text{trans}}$ and the final pulsewidth is 24 ps in exact agreement with the predictions of the analytic formulas derived above.

Lower normalized dispersion of $D_n = 15$ or $D = -10 \text{ ps}^2$ only allows for a reduction in pulsewidth by $R = 2.68$. However, using the same amount of SPM as before we leave the range of stable soliton generation.

Image removed due to copyright restrictions.

Please see:

Kaertner, F., D. Kopf, and U. Keller. "Solitary-pulse stabilization and shortening in actively mode-locked lasers." *Journal of the Optical Society of America B* 12, no. 3 (March 1995): 486.

Figure 5.11: Time evolution of the intensity (a) and spectrum (b) for the same parameters as Fig. 2 over 10,000 roundtrips. The laser reaches steady state after about 4,000 roundtrips.

Image removed due to copyright restrictions.

Please see:

Kaertner, F., D. Kopf, and U. Keller. "Solitary-pulse stabilization and shortening in actively mode-locked lasers." *Journal of the Optical Society of America B* 12, no. 3 (March 1995): 486.

Figure 5.12: (a) Time evolution of the intensity in a Nd:YAG laser for the parameters in Table 5.2 over the first 1,000 round-trips. The amount of negative dispersion is reduced to $D = -10ps^2$, starting again from a 68ps long pulse. The continuum in this case does not decay as in Fig. 5.2 and 5.3 due to the insufficient dispersion. (b) Same simulation over 50,000 round-trips.

Figure 5.12(a) shows similar to Fig. 5.10 the first 1,000 roundtrips in that case. Again the solitary pulse is rapidly formed out of the long Gaussian initial pulse. But in contrast to the situation in Fig. 5.10, the continuum does not any longer decay on this time scale. The dispersion is too low to spread the continuum rapidly enough. The continuum then accumulates over many roundtrips as can be seen from Fig. 5.12(b). After about 10,000 roundtrips the continuum has grown so much that it extracts an appreciable amount of energy from the soliton. But surprisingly the continuum modes stop growing after about 30,000 roundtrips and a new quasi stationary state is reached.

5.5.3 Experimental Verification

The theory above explains very well the ps Ti:sapphire experiments [10] in the regime where the pulses are stabilized by the active modelocker alone. Gires-Tournois interferometers were used to obtain large amounts of negative GDD to operate the laser in the stable soliton regime derived above. Here we want to discuss in more detail the experimental results obtained recently with a regeneratively, actively mode-locked Nd:glass laser [7], resulting in 310 fs. If SPM and GVD could be neglected, the weak modelocker would produce Gaussian pulses with a FWHM of $\tau_{a,FWHM} = 10$ ps. However, the strong SPM prevents stable pulse formation. The negative dispersion available in the experiment is too low to achieve stable soliton formation, because the pulse width of the soliton at this power level is given by $\tau = 4|D|/(\delta W) = 464$ fs, for the example discussed. The normalized dispersion is not large enough to allow for such a large pulse width reduction. Providing enough negative dispersion results in a 310 fs perfectly sech-shaped soliton-like pulse as shown in Fig. 5.13. A numerical simulation of this case would need millions of roundtrips through the cavity until a stationary state is reached. That means milliseconds of real time, but would necessitate days of computer time. Also the transition to instable behaviour has been observed, which is the characteristic occurrence of a short solitary fs-pulse together with a long ps-pulse due to the instable continuum as we have found in the numerical simulation for the case of a Nd:YAG laser (see Fig. 5.12(b)). Figure 5.14 shows the signal of a fast detector diode on the sampling oscilloscope. The detector has an overall bandwidth of $25GHz$ and therefore can not resolve the fs-pulse, but can resolve the width of the following roughly $100ps$ long pulse.

Image removed due to copyright restrictions.

Please see:

Kaertner, F., D. Kopf, and U. Keller. "Solitary-pulse stabilization and shortening in actively mode-locked lasers." *Journal of the Optical Society of America B* 12, no. 3 (March 1995): 486.

Figure 5.13: Autocorrelation of the actively mode-locked pulse (solid line) and corresponding $sech^2$ fit (dashed line) with additional soliton formation.

Image removed due to copyright restrictions.

Please see:

Kaertner, F., D. Kopf, and U. Keller. "Solitary-pulse stabilization and shortening in actively mode-locked lasers." *Journal of the Optical Society of America B* 12, no. 3 (March 1995): 486.

Figure 5.14: Sampling signal of fast detector when the mode-locked laser operates at the transition to instability. The short fs pulse can not be resolved by the detector and therefore results in a sharp spike corresponding to the detector response time. In advance of the fs-pulse travels a roughly 100ps long pulse.

5.6 Summary

The main result of this section is, that pure active mode-locking with an amplitude modulator leads to Gaussian pulses. The width is inverse proportional to the square root of the gain bandwidth. A phase modulator leads to chirped Gaussian pulses. A soliton much shorter than the Gaussian pulse due to pure active mode locking can be stabilized by an active modelocker. This finding also has an important consequence for passive mode locking. It implies that a slow saturable absorber, i.e. an absorber with a recovery time much longer than the width of the soliton, is enough to stabilize the pulse, i.e. to modelock the laser.

Bibliography

- [1] H. A. Haus, "Short Pulse Generation", in Compact Sources of Ultrashort Pulses, ed. by I. N. Duling III, Cambridge University Press (1995).
- [2] D. J. Kuizenga and A. E. Siegman, "FM and AM Mode Locking of the Homogeneous Laser - Part I: Theory," IEEE J. of Quantum Electron. **QE-6**, pp. 694 – 708 (1970).
- [3] D. J. Kuizenga and A. E. Siegman, "FM and AM modelocking of the homogeneous laser - part I: theory," IEEE J. Qunat. Electron. **6**, pp. 694 – 701 (1970).
- [4] H. A. Haus, "A Theory of Forced Mode Locking", IEEE Journal of Quantum Electronics **QE-11**, pp. 323 - 330 (1975).
- [5] H. A. Haus and Y. Silberberg, "Laser modelocking with addition of nonlinear index", IEEE Journal of Quantum Electronics **QE-22**, pp. 325 - 331 (1986).
- [6] F. X. Kärtner, D. Kopf, U. Keller, "Solitary pulse stabilization and shortening in actively mode-locked lasers," J. Opt. Soc. of Am. **B12**, pp. 486 – 496 (1995).
- [7] D. Kopf, F. X. Kärtner, K. J. Weingarten, U. Keller, "Pulse shortening in a Nd:glass laser by gain reshaping and soliton formation, Opt. Lett. **19**, 2146 – 2248 (1994).
- [8] J.D. Kafka and T. Baer, "Mode-locked erbium-doped fiber laser with soliton pulse shaping", Opt. Lett. **14**, pp. 1269 – 1271 (1989).
- [9] K. Smith, R. P. Davey, B. P. Nelson and E.J. Greer, "Fiber and Solid-State Lasers", (Digest No. 120), London, UK, 19 May 1992, P.1/1-4.

- [10] J.D. Kafka, M. L. Watts and J.W.J. Pieterse, "Picosecond and femtosecond pulse generation in a regeneratively mode-locked Ti:Sapphire laser", IEEE J. Quantum Electron. **QE-28**, pp. 2151 – 2162 (1992).
- [11] F. Fontana, N. Ridi, M. Romagnoli, P. Franco, "Fully integrated 30 ps modelocked fiber laser electronically tunable over 1530 - 1560 nm", Opt. Comm. **107**, pp. 240 – 244 (1994).
- [12] D. J. Jones, H. A. Haus and E. P. Ippen, "Solitons in an Actively Mod-locked Fiber Laser," to appear in Opt. Lett.
- [13] U. Keller, T. H. Chiu and J. F. Ferguson, "Self-starting femtosecond mode-locked Nd:glass laser using intracavity saturable absorber," - Opt. Lett. **18**, pp. 1077 - 1079 (1993).
- [14] H. A. Haus and A. Mecozzi, "Long-term storage of a bit stream of solitons", Opt. Lett. **21**, 1500 – 1502 (1992).

5.7 Active Modelocking with Detuning

So far, we only considered the case of perfect synchronism between the round-trip of the pulse in the cavity and the external modulator. Technically, such perfect synchronism is not easy to achieve. One way would be to do regenerative mode locking, i.e. a part of the output signal of the modelocked laser is detected, the beatnote at the round-trip frequency is filtered out from the detector, and sent to an amplifier, which drives the modulator. This procedure enforces synchronism if the cavity length undergoes fluctuations due to acoustic vibrations and thermal expansion.

Nevertheless, it is interesting to know how sensitive the system is against detuning between the modulator and the resonator. It turns out that this is a physically and mathematically rich situation, which applies to many other phenomena occurring in externally driven systems, such as the transition from laminar to turbulent flow in hydrodynamics. This transition has puzzled physicists for more than a hundred years [1]. During the last 5 to 10 years, a scenario for the transition to turbulence has been put forward by Trefethen and others [2]. This model gives not only a quantitative description of the kind of instability that leads to a transition from laminar, i.e. highly ordered dynamics, to turbulent flow, i.e. chaotic motion, but also an intuitive physical picture why turbulence is occurring. Such a picture is the basis for many laser instabilities especially in synchronized laser systems. According to this theory, turbulence is due to strong transient growth of deviations from a stable stationary point of the system together with a nonlinear feedback mechanism. The nonlinear feedback mechanism couples part of the amplified perturbation back into the initial perturbation. Therefore, the perturbation experiences strong growth repeatedly. Once the transient growth is large enough, a slight perturbation from the stable stationary point renders the system into turbulence. Small perturbations are always present in real systems in the form of system intrinsic noise or environmental noise and, in computer simulations, due to the finite precision. The predictions of the linearized stability analysis become meaningless in such cases. The detuned actively modelocked laser is an excellent example of such a system, which in addition can be studied analytically. The detuned case has been only studied experimentally [3][4] or numerically [5] so far. Here, we consider an analytical approach. Note, that this type of instability can not be detected by a linear stability analysis which is widely used in laser theories and which we use in this course very often to prove stable pulse formation.

One has to be aware that such situations may arise, where the results of a linearized stability analysis have only very limited validity.

The equation of motion for the pulse envelope in an actively modelocked laser with detuning can be written as

$$T_M \frac{\partial A(T, t)}{\partial T} = \left[g(T) - l + D_f \frac{\partial^2}{\partial t^2} - M(1 - \cos(\omega_M t)) + T_d \frac{\partial}{\partial t} \right] A(T, t). \quad (5.89)$$

Here, $A(T, t)$ is the pulse envelope as before. There is the time T which is coarse grained on the time scale of the resonator round-trip time T_R and the time t , which resolves the resulting pulse shape. The saturated gain is denoted by $g(T)$ and left dynamical, because we no longer assume that the gain and field dynamics reaches a steady state eventually. The curvature of the intracavity losses in the frequency domain, which limit the bandwidth of the laser, is given by D_f and left fixed for simplicity. M is the depth of the loss modulation introduced by the modulator with angular frequency $\omega_M = 2\pi/T_M$, where T_M is the modulator period. Note that Eq.(5.89) describes the change in the pulse between one period of modulation. The detuning between resonator round-trip time and the modulator period is $T_d = T_M - T_R$. This detuning means that the pulse hits the modulator with some temporal off-set after one round-trip, which can be described by adding the term $T_d \frac{\partial}{\partial t} A$ in the master equation. The saturated gain g obeys a separate ordinary differential equation

$$\frac{\partial g(T)}{\partial T} = -\frac{g(T) - g_0}{\tau_L} - g \frac{W(T)}{P_L}. \quad (5.90)$$

As before, g_0 is the small signal gain due to the pumping, P_L the saturation power of the gain medium, τ_L the gain relaxation time and $W(T) = \int |A(T, t)|^2 dt$ the total field energy stored in the cavity at time T .

As before, we expect pulses with a pulse width much shorter than the round-trip time in the cavity and we assume that they still will be placed in time near the position where the modulator introduces low loss (Figure 5.15), so that we can still approximate the cosine by a parabola

$$T_M \frac{\partial A}{\partial T} = \left[g - l + D_f \frac{\partial^2}{\partial t^2} - M_s t^2 + T_d \frac{\partial}{\partial t} \right] A. \quad (5.91)$$

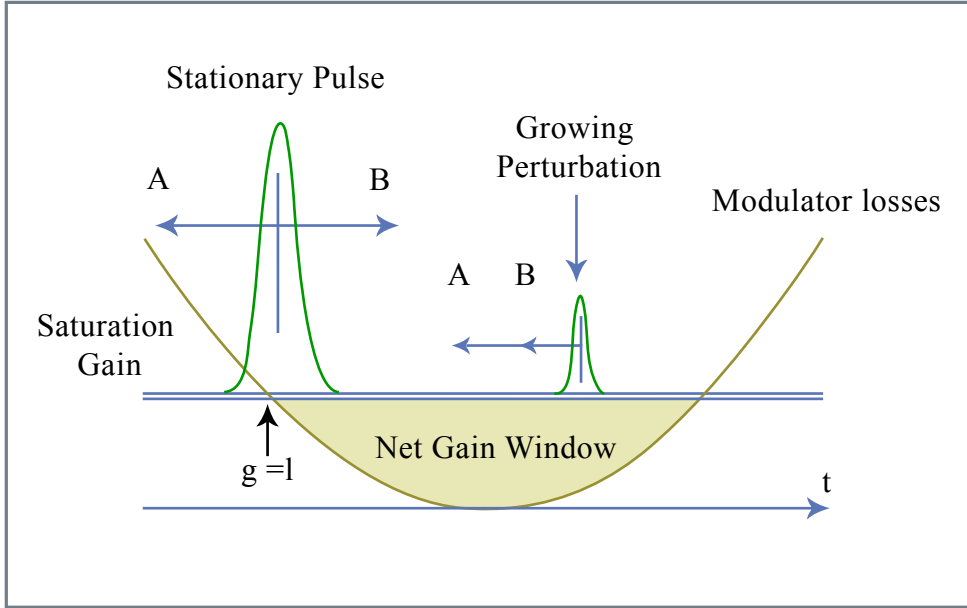


Figure 5.15: Drifting pulse dynamics in a detuned actively modelocked laser for the situation, where the modulator period is larger than the cavity round-trip time. The displacement A is caused by the mismatch between the cavity round-trip time and the modulator period. The displacement B is due to unequal losses experienced by the front and the back of the pulse in the modulator. The gain saturates to a level where a possible stationary pulse experiences no net gain or loss, which opens up a net gain window following the pulse. Perturbations within that window get amplified while drifting towards the stationary pulse.

Figure by MIT OCW.

Here, $M_s = M\omega_M^2/2$ is the curvature of the loss modulation at the point of minimum loss as before. The time t is now allowed to range from $-\infty$ to $+\infty$, since the modulator losses make sure that only during the physically allowed range $-T_R/2 \ll t \ll T_R/2$ radiation can build up.

In the case of vanishing detuning, i.e. $T_d = 0$, the differential operator on the right side of (5.91), which generates the dynamics and is usually called a evolution operator \hat{L} , corresponds to the Schrödinger operator of the harmonic oscillator. Therefore, it is useful to introduce the creation and annihilation operators

$$\hat{a} = \frac{1}{\sqrt{2}} \left(\frac{\tau_a \partial}{\partial t} + \frac{t}{\tau_a} \right), \quad \hat{a}^\dagger = \frac{1}{\sqrt{2}} \left(-\frac{\tau_a \partial}{\partial t} + \frac{t}{\tau_a} \right), \quad (5.92)$$

with $\tau_a = \sqrt[4]{D_f/M_s}$. The evolution operator \hat{L} is then given by

$$\hat{L} = g - l - 2\sqrt{D_f M_s} \left(\hat{a}^\dagger \hat{a} + \frac{1}{2} \right) \quad (5.93)$$

and the evolution equation (5.91) can be written as

$$T_M \frac{\partial A}{\partial T} = \hat{L} A. \quad (5.94)$$

Consequently, the eigensolutions of this evolution operator are the Hermite-Gaussians, which we used already before

$$A_n(T, t) = u_n(t) e^{\lambda_n T/T_M} \quad (5.95)$$

$$u_n(t) = \sqrt{\frac{W_n}{2^n \sqrt{\pi} n! \tau_a}} H_n(t/\tau_a) e^{-\frac{t^2}{2\tau_a^2}} \quad (5.96)$$

and τ_a is the pulsewidth of the Gaussian. (see Figure 5.16a)

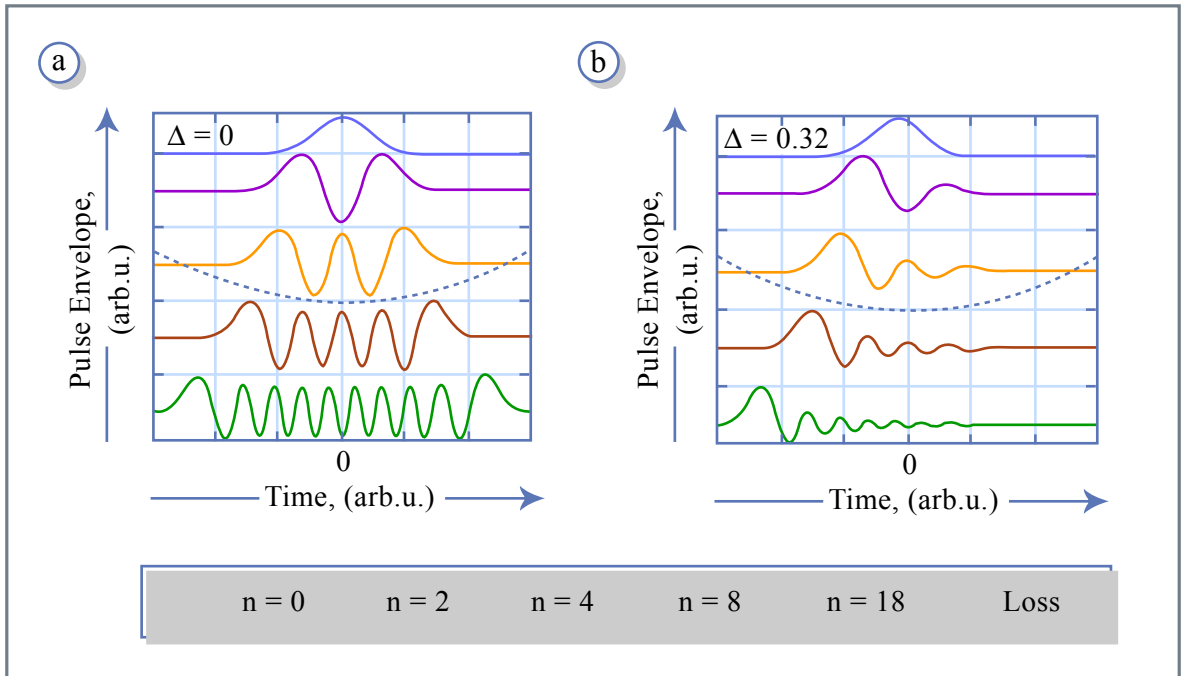


Figure 5.16: Lower order eigenmodes of the linearized system for zero detuning, $\Delta = 0$, (a) and for a detuning, $\Delta = 0.32$, in (b).

Figure by MIT OCW.

The eigenmodes are orthogonal to each other because the evolution operator is hermitian in this case.

The round-trip gain of the eigenmode $u_n(t)$ is given by its eigenvalue (or in general by the real part of the eigenvalue) which is given by $\lambda_n = g_n - l - 2\sqrt{D_f M_s}(n + 0.5)$ where $g_n = g_0 \left(1 + \frac{W_n}{P_L T_R}\right)^{-1}$, with $W_n = \int |u_n(t)|^2 dt$.

The eigenvalues prove that, for a given pulse energy, the mode with $n = 0$, which we call the ground mode, experiences the largest gain. Consequently, the ground mode will saturate the gain to a value such that $\lambda_0 = 0$ in steady state and all other modes experience net loss, $\lambda_n < 0$ for $n > 0$, as discussed before. This is a stable situation as can be shown rigorously by a linearized stability analysis [6]. Thus active modelocking with perfect synchronization produces Gaussian pulses with a $1/e$ -half width of the intensity profile given by τ_a .

In the case of non zero detuning T_d , the situation becomes more complex. The evolution operator, (5.93), changes to

$$\hat{L}_D = g - l - 2\sqrt{D_f M_s} \left[(\hat{a}^\dagger - \Delta) (\hat{a} + \Delta) + \left(\frac{1}{2} + \Delta^2\right) \right] \quad (5.97)$$

with the normalized detuning

$$\Delta = \frac{1}{2\sqrt{2D_f M_s} \tau_a} T_d. \quad (5.98)$$

Introducing the shifted creation and annihilation operators, $\hat{b}^\dagger = \hat{a}^\dagger + \Delta$ and $\hat{b} = \hat{a} + \Delta$, respectively, we obtain

$$\hat{L}_D = \Delta g - 2\sqrt{D_f M_s} (\hat{b}^\dagger \hat{b} - 2\Delta \hat{b}) \quad (5.99)$$

with the excess gain

$$\Delta g = g - l - 2\sqrt{D_f M_s} \left(\frac{1}{2} + \Delta^2\right) \quad (5.100)$$

due to the detuning. Note, that the resulting evolution operator is not any longer hermitian and even not normal, i.e. $[A, A^\dagger] \neq 0$, which causes the eigenmodes to become nonnormal [8]. Nevertheless, it is an easy exercise to compute the eigenvectors and eigenvalues of the new evolution operator in terms of the eigenstates of $\hat{b}^\dagger \hat{b}$, $|l\rangle$, which are the Hermite Gaussians centered around Δ . The eigenvectors $|\varphi_n\rangle$ to \hat{L}_D are found by the ansatz

$$|\varphi_n\rangle = \sum_{l=0}^n c_l^n |l\rangle, \quad \text{with } c_{l+1}^n = \frac{n-l}{2\Delta\sqrt{l+1}} c_l^n. \quad (5.101)$$

The new eigenvalues are $\lambda_n = g_n - l - 2\sqrt{D_f M_s}(\Delta^2 + n + 0.5)$. By inspection, it is again easy to see, that the new eigenstates form a complete basis in

$L_2(\mathbb{R})$. However, the eigenvectors are no longer orthogonal to each other. The eigensolutions as a function of time are given as a product of a Hermite Polynomial and a shifted Gaussian $u_n(t) = \langle t | \varphi_n \rangle \sim H_n(t/\tau_a) \exp \left[-\frac{(t-\sqrt{2}\Delta\tau_a)^2}{2\tau_a^2} \right]$. Again, a linearized stability analysis shows that the ground mode, i.e. $|\varphi_0\rangle$, a Gaussian, is a stable stationary solution. Surprisingly, the linearized analysis predicts stability of the ground mode for all values of the detuning in the parabolic modulation and gain approximation. This result is even independent from the dynamics of the gain, i.e. the upper state lifetime of the active medium, as long as there is enough gain to support the pulse. Only the position of the maximum of the ground mode, $\sqrt{2}\Delta \cdot \tau_a$, depends on the normalized detuning.

Figure 5.15 summarizes the results obtained so far. In the case of detuning, the center of the stationary Gaussian pulse is shifted away from the position of minimum loss of the modulator. Since the net gain and loss within one round-trip in the laser cavity has to be zero for a stationary pulse, there is a long net gain window following the pulse in the case of detuning due to the necessary excess gain. Figure 2 shows a few of the resulting lowest order eigenfunctions for the case of a normalized detuning $\Delta = 0$ in (a) and $\Delta = 0.32$ in (b). These eigenfunctions are not orthogonal as a result of the nonnormal evolution operator

5.7.1 Dynamics of the Detuned Actively Mode-locked Laser

To get insight into the dynamics of the system, we look at computer simulations for a Nd:YLF Laser with the parameters shown in Table 5.3 Figures

$$\begin{array}{ll}
 E_L = 366 \mu J & g_0 = 0.79 \\
 \tau_L = 450 \mu s & M_s = 2.467 \cdot 10^{17} s^{-2} \\
 \Omega_g = 1.12 THz & D_g = 2 \cdot 10^{-26} s^2 \\
 T_R = 4 ns & \tau_a = 17 ps \\
 l = 0.025 & \lambda_0 = 1.047 \mu m \\
 M = 0.2 &
 \end{array}$$

Table 5.3: Data used in the simulations of a Nd:YLF laser.

5.17 show the temporal evolution of the coefficient c_n , when the master equa-

tion is decomposed into Hermite Gaussians centered at $t=0$ according to Eq.(5.96).

$$A(T, t) = \sum_{n=0}^{\infty} c_n(T) u_n(t)$$

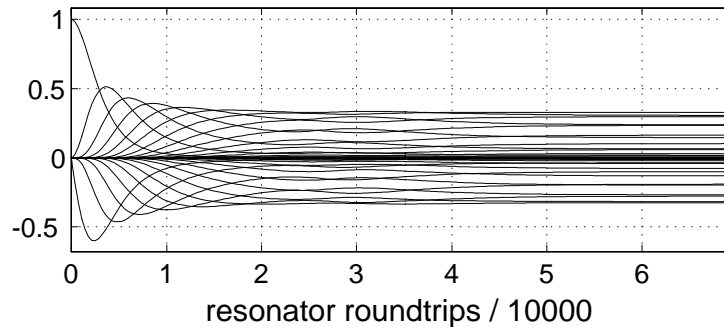


Figure 5.17: Coefficients of the envelope in a Hermite-Gaussian-Basis, as a function of resonator round-trips. The normalized detuning is $\Delta = 3.5$. The simulation starts from the steady state without detuning. The curve starting at 1 is the ground mode. To describe a shifted pulse, many modes are necessary.

Figure 5.18 and 5.19 shows the deviation from the steady state gain and the pulse envelope in the time domain for a normalized detuning of $\Delta = 3.5$.

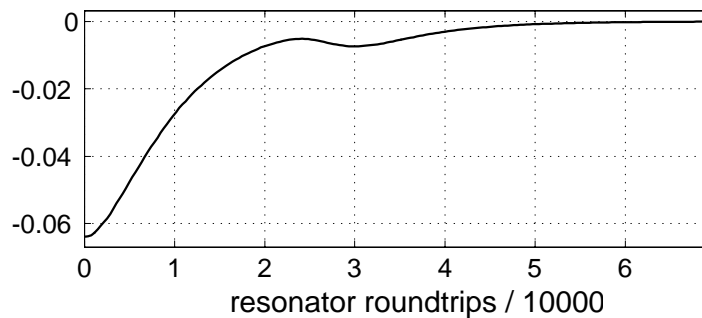


Figure 5.18: Gain as a function of the number of roundtrips. It changes to a higher level.

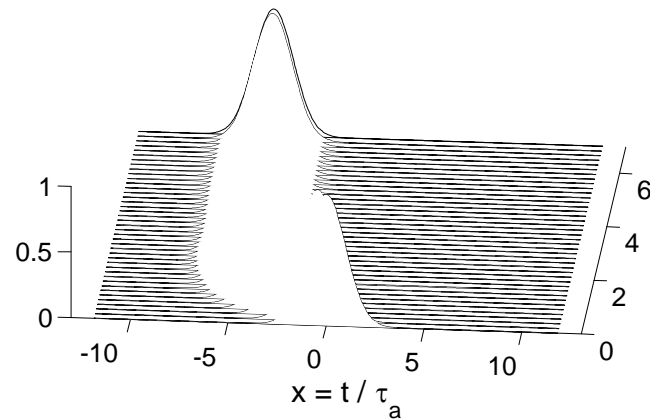


Figure 5.19: Temporal evolution of the pulse envelope. The pulse shifts slowly into the new equilibrium position at $\sqrt{2} \Delta = 4.9$ in agreement with the simulation.

Figures 5.20 to 5.22 show the same quantities for a slightly higher normalized detuning of $\Delta = 4$.

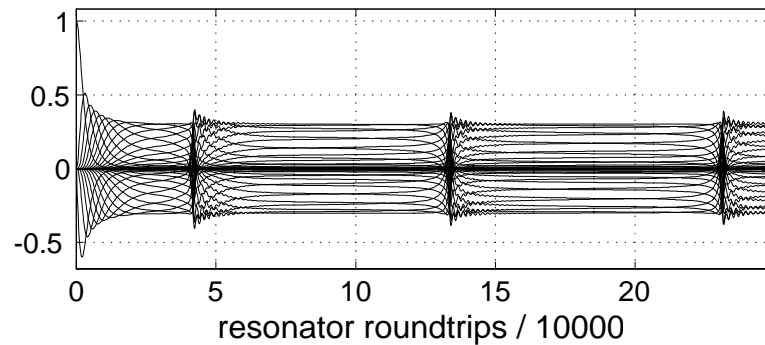


Figure 5.20: Temporal evolution of the coefficients in a Hermite-Gaussian Basis at a normalized detuning of $\Delta = 4$. Almost periodically short interrupting events of the otherwise regular motion can be easily recognized (Intermittent Behavior). Over an extended period time between such events the laser approaches almost a steady state.

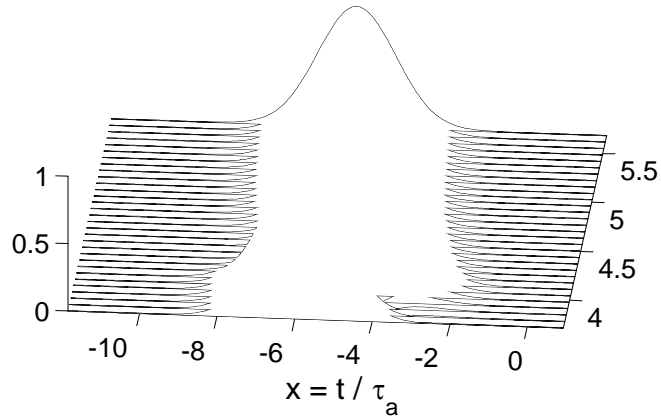


Figure 5.22: Time evolution of pulse envelope.

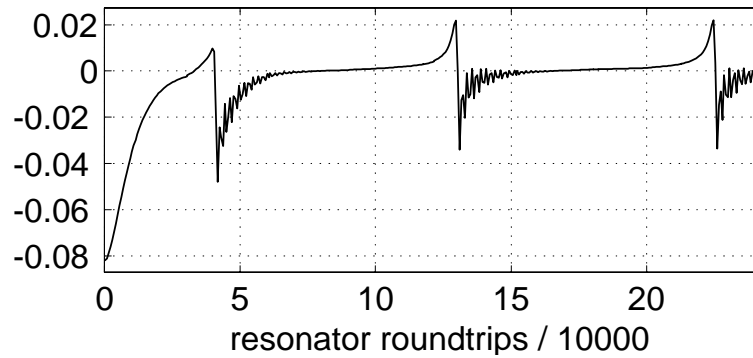


Figure 5.21: Temporal evolution of deviation from quasi steady state gain.

The pictures clearly show that the system does not approach a steady state anymore, but rather stays turbulent, i.e. the dynamics is chaotic.

5.7.2 Nonnormal Systems and Transient Gain

To get insight into the dynamics of a nonnormal time evolution, we consider the following two-dimensional nonnormal system

$$\frac{du}{dt} = Au, \quad u(0) = u_0, \quad u(t) = e^{At}u_0 \quad (5.102)$$

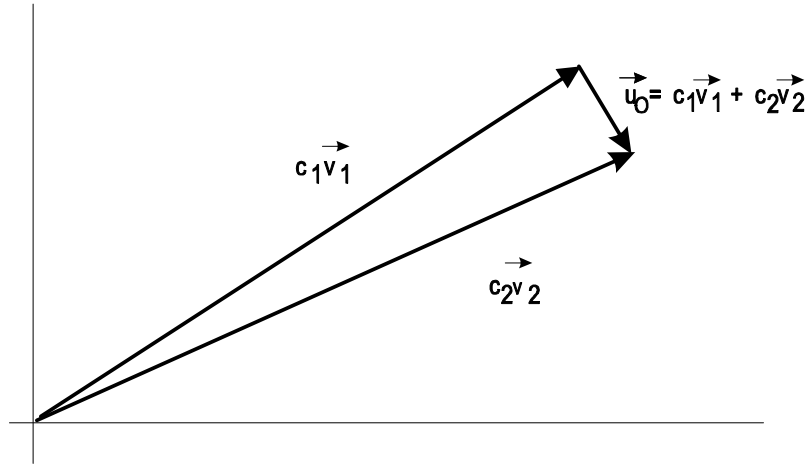


Figure 5.23: Decomposition of an initial perturbation in the eigen basis.

with

$$A = \begin{pmatrix} -\frac{1}{2} & \frac{a}{2} \\ 0 & -1 \end{pmatrix} \Rightarrow A^\dagger = \begin{pmatrix} -\frac{1}{2} & 0 \\ \frac{a}{2} & -1 \end{pmatrix}, \quad [A, A^\dagger] = \frac{a}{4} \begin{pmatrix} a & 1 \\ 1 & a \end{pmatrix} \neq 0. \quad (5.103)$$

The parameter a scales the strength of the nonnormality, similar to the detuning Δ in the case of a modelocked laser or the Reynolds number in hydrodynamics, where the linearized Navier-Stokes Equations constitute a nonnormal system.

The eigenvalues and vectors of the linear system are

$$\lambda_1 = -\frac{1}{2}, \quad v_1 = \begin{pmatrix} 1 \\ 0 \end{pmatrix}, \quad \lambda_2 = -1, \quad v_2 = \frac{1}{\sqrt{1+a^2}} \begin{pmatrix} a \\ -1 \end{pmatrix} \quad (5.104)$$

The eigenvectors build a complete system and every initial vector can be decomposed in this basis. However, for large a , the two eigenvectors become more and more parallel, so that a decomposition of a small initial vector almost orthogonal to the basis vectors needs large components (Figure 5.23)

The solution is

$$u(t) = e^{At} u_0 = c_1 e^{-t/2} \vec{v}_1 + c_2 e^{-t} \vec{v}_2.$$

Since the eigenvalues are negative, both contributions decay, and the system is stable. However, one eigen component decays twice as fast than

the other one. Of importance to us is the transient gain that the system is showing due to the fact of near parallel eigen vectors. Both coefficients c_1 and c_2 are large. When one of the components decays, the other one is still there and the resulting vector

$$u(t \rightarrow 2) \approx c_1 e^{-1} \vec{v}_1.$$

can be much larger than the initial perturbation during this transient phase. This is transient gain. It can become arbitrarily large for large a .

5.7.3 The Nonnormal Behavior of the Detuned Laser

The nonnormality of the operator, $[\hat{L}_D, \hat{L}_D^\dagger] \sim \Delta$, increases with detuning. Figure 5.24 shows the normalized scalar products between the eigenmodes for different values of the detuning

$$C(m, n) = \left| \frac{\langle \varphi_m | \varphi_n \rangle}{\sqrt{\langle \varphi_m | \varphi_m \rangle \langle \varphi_n | \varphi_n \rangle}} \right|. \quad (5.105)$$

The eigenmodes are orthogonal for zero detuning. The orthogonality vanishes with increased detuning. The recursion relation (5.101) tells us that the overlap of the new eigenmodes with the ground mode increases for increasing detuning. This corresponds to the parallelization of the eigenmodes of the linearized problem which leads to large transient gain, $\|e^{\hat{L}_D t}\|$, in a nonnormal situation [2]. Figure 5.24d shows the transient gain for an initial perturbation from the stationary ground mode calculated by numerical simulations of the linearized system using an expansion of the linearized system in terms of Fock states to the operator \hat{b} . A normalized detuning of $\Delta = 3$ already leads to transient gains for perturbations of the order of 10^6 within 20,000 round-trips which lead to an enormous sensitivity of the system against perturbations. An analytical solution of the linearized system neglecting the gain saturation shows that the transient gain scales with the detuning according to $\exp(2\Delta^2)$. This strong super exponential growth with increasing detuning determines the dynamics completely.

Image removed due to copyright restrictions.

Please see:

Kaertner, F. X., et al. "Turbulence in Mode-locked Lasers". *Physical Review Letters* 82, no. 22 (May 1999): 4428-4431.

Figure 5.24: Scalar products of eigenvectors as a function of the eigenvector index for the cases $\Delta = 0$ shown in (a), $\Delta = 1$ in (b) and $\Delta = 3$ in (c). (d) shows the transient gain as a function of time for these detunings computed and for $\Delta = 2$, from the linearized system dynamics.

Image removed due to copyright restrictions.

Please see:

Kaertner, F. X., et al. "Turbulence in Mode-locked Lasers". *Physical Review Letters* 82, no. 22 (May 1999): 4428-4431.

Figure 5.25: Critical detuning obtained from numerical simulations as a function of the normalized pumping rate and cavity decay time divided by the upper-state lifetime. The critical detuning is almost independent of all laser parameters shown. The mean critical detuning is $\Delta \approx 3.65$.

Figure 5.25 shows the surface of the transition to turbulence in the parameter space of a Nd:YLF laser, i.e. critical detuning Δ , the pumping rate $r = g_0/l$ and the ratio between the cavity decay time $T_{cav} = T_R/l$ and the upper state lifetime τ_L . In this model, we did not include the spontaneous emission.

The transition to turbulence always occurs at a normalized detuning of about $\Delta \approx 3.7$ which gives a transient gain $\exp(2\Delta^2) = 10^{12}$. This means that already uncertainties of the numerical integration algorithm are amplified to a perturbation as large as the stationary state itself. To prove that the system dynamics becomes really chaotic, one has to compute the Liapunov coefficient [9]. The Liapunov coefficient describes how fast the phase space trajectories separate from each other, if they start in close proximity. It is formally defined in the following way. Two trajectories $y(t)$ and $z(t)$ start in close vicinity at $t = t_0$

$$\|y(t_0) - z(t_0)\| = \varepsilon = 10^{-4}. \quad (5.106)$$

Then, the system is run for a certain time Δt and the logarithmic growth rate, i.e. Liapunov coefficient, of the distance between both trajectories is evaluated using

$$\lambda_0 = \ln \left(\frac{\|y(t_0 + \Delta t) - z(t_0 + \Delta t)\|}{\varepsilon} \right) \quad (5.107)$$

For the next iteration the trajectory $z(t)$ is rescaled along the distance between $y(t_0 + \Delta t)$ and $z(t_0 + \Delta t)$ according to

$$z(t_1) = y(t_0 + \Delta t) + \varepsilon \frac{y(t_0 + \Delta t) - z(t_0 + \Delta t)}{\|y(t_0 + \Delta t) - z(t_0 + \Delta t)\|}. \quad (5.108)$$

The new points of the trajectories $z(t_1 + \Delta t)$ and $y(t_1 + \Delta t) = y(t_0 + 2\Delta t)$ are calculated and a new estimate for the Liapunov coefficient λ_1 is calculated using Eq.(5.107) with new indices. This procedure is continued and the Liapunov coefficient is defined as the average of all the approximations over a long enough iteration, so that its changes are below a certain error bound from iteration to iteration.

$$\lambda = \frac{1}{N} \sum_{n=0}^N \lambda_n \quad (5.109)$$

Figure 5.26 shows the Liapunov coefficient of the Nd:YLF laser discussed above, as a function of the normalized detuning. When the Liapunov coefficient becomes positive, i.e. the system becomes exponentially sensitive to

small changes in the initial conditions, the system is called chaotic. The graph clearly indicates that the dynamics is chaotic above a critical detuning of about $\Delta_c \approx 3.7$.

Image removed due to copyright restrictions.

Please see:

Kaertner, F. X., et al. "Turbulence in Mode-locked Lasers". *Physical Review Letters* 82, no. 22 (May 1999): 4428-4431.

Figure 5.26: Liapunov coefficient over normalized detuning.

In the turbulent regime, the system does not reach a steady state, because it is nonperiodically interrupted by a new pulse created out of the net gain window, see Figure 5.15, following the pulse for positive detuning. This pulse saturates the gain and the nearly formed steady state pulse is destroyed and finally replaced by a new one. The gain saturation provides the nonlinear feedback mechanism, which strongly perturbs the system again, once a strong perturbation grows up due to the transient linear amplification mechanism.

The critical detuning becomes smaller if additional noise sources, such as the spontaneous emission noise of the laser amplifier and technical noise sources are taken into account. However, due to the super exponential growth, the critical detuning will not depend strongly on the strength of the noise sources. If the spontaneous emission noise is included in the simulation, we obtain the same shape for the critical detuning as in Fig. 5.25, however the critical detuning is lowered to about $\Delta_c \approx 2$. Note that this critical detuning is very insensitive to any other changes in the parameters of the system. Therefore, one can expect that actively mode-locked lasers without regenerative feedback run unstable at a real detuning, see (5.98) given by

$$T_d = 4\sqrt{2D_f M_s \tau_a} \quad (5.110)$$

For the above Nd:YLF laser, using the values in Table 5.3 results in a relative precision of the modulation frequency of

$$\frac{T_d}{T_R} = 1.7 \cdot 10^{-6}.$$

The derived value for the frequency stability can easily be achieved and maintained with modern microwave synthesizers. However, this requires that the cavity length of Nd:YLF laser is also stable to this limit. Note that the thermal expansion coefficient for steel is $1.6 \cdot 10^{-5}/K$.

Bibliography

- [1] Lord Kelvin, *Philos. Mag.* **24**, 188 (1887); A. Sommerfeld, *Int. Mathem. Kongr. Rom 1908*, Vol. III, S. 116; W. M. F. Orr, *Proc. Irish Acad.* **27**, (1907).
- [2] L. Trefethen, A. Trefethen, S. C. Reddy u. T. Driscoll, *Science* **261**, 578 (1993); S. C. Reddy, D. Henningson, *J. Fluid Mech.* **252**, 209 (1993); *Phys. Fluids* **6**, 1396 (1994); S. Reddy et al., *SIAM J. Appl. Math.* **53**, 15 (1993); T. Gebhardt and S. Grossmann, *Phys. Rev. E* **50**, 3705 (1994).
- [3] H. J. Eichler, *Opt. Comm.* **56**, 351 (1986). H. J. Eichler, I. G. Koltchanov and B. Liu, *Appl. Phys. B* **61**, 81 (1995).
- [4] U. Morgner and F. Mitschke, *Phys. Rev. A* **54**, 3149 (1997).
- [5] H. J. Eichler, I. G. Koltchanov and B. Liu, *Appl. Phys. B* **61**, 81 - 88 (1995).
- [6] H. A. Haus, *IEEE JQE* **11**, 323 (1975).
- [7] H. A. Haus, D. J. Jones, E. P. Ippen and W. S. Wong, *Journal of Light-wave Technology*, 14, 622 (1996).
- [8] G. Bachman and L. Narici, "Functional Analysis", New York, Academic Press (1966).
- [9] A. Wolf, J. B. Swift, H. L. Swinney and J. A. Vastano, *Physica D* **16**, 285 (1985).

Chapter 6

Passive Modelocking

As we have seen in chapter 5 the pulse width in an actively modelocked laser is inverse proportional to the fourth root of the curvature in the loss modulation. In active modelocking one is limited to the speed of electronic signal generators. Therefore, this curvature can never be very strong. However, if the pulse can modulate the absorption on its own, the curvature of the absorption modulation can become large, or in other words the net gain window generated by the pulse can be as short as the pulse itself. In this case, the net gain window shortens with the pulse. Therefore, passively modelocked lasers can generate much shorter pulses than actively modelocked lasers.

However, a suitable saturable absorber is required for passive modelocking. Depending on the ratio between saturable absorber recovery time and final pulse width, one may distinguish between the regimes of operation shown in Figure 6.1, which depicts the final steady state pulse formation process. In a solid state laser with intracavity pulse energies much lower than the saturation energy of the gain medium, gain saturation can be neglected. Then a fast saturable absorber must be present that opens and closes the net gain window generated by the pulse immediately before and after the pulse. This modelocking principle is called fast saturable absorber modelocking, see Figure 6.1 a).

In semiconductor and dye lasers usually the intracavity pulse energy exceeds the saturation energy of the gain medium and so the the gain medium undergoes saturation. A short net gain window can still be created, almost independent of the recovery time of the gain, if a similar but unpumped medium is introduced into the cavity acting as an absorber with a somewhat lower saturation energy then the gain medium. For example, this can be

Image removed due to copyright restrictions.

Please see:

Kartner, F. X., and U. Keller. "Stabilization of soliton-like pulses with a slow saturable absorber." *Optics Letters* 20 (1990): 16-19.

Figure 6.1: Pulse-shaping and stabilization mechanisms owing to gain and loss dynamics in passively mode-locked lasers: (a) using only a fast saturable absorber; (b) using a combination of gain and loss saturation; (c) using a saturable absorber with a finite relaxation time and soliton formation.

arranged for by stronger focusing in the absorber medium than in the gain medium. Then the absorber bleaches first and opens a net gain window, that is closed by the pulse itself by bleaching the gain somewhat later, see Figure 6.1 b). This principle of modelocking is called slow-saturable absorber modelocking.

When modelocking of picosecond and femtosecond lasers with semiconductor saturable absorbers has been developed it became obvious that even with rather slow absorbers, showing recovery times of a few picoseconds, one was able to generate sub-picosecond pulses resulting in a significant net gain window after the pulse, see Figure 6.1 c). From our investigation of active modelocking in the presence of soliton formation, we can expect that such a situation may still be stable up to a certain limit in the presence of strong soliton formation. This is the case and this modelocking regime is called soliton modelocking, since solitary pulse formation due to SPM and GDD shapes the pulse to a stable sech-shape despite the open net gain window following the pulse.

6.1 Slow Saturable Absorber Mode Locking

Due to the small cross section for stimulated emission in solid state lasers, typical intracavity pulse energies are much smaller than the saturation energy of the gain. Therefore, we neglected the effect of gain saturation due to one pulse so far, the gain only saturates with the average power. However, there are gain media which have large gain cross sections like semiconductors and dyes, see Table 4.1, and typical intracavity pulse energies may become large enough to saturate the gain considerably in a single pass. In fact, it is this effect, which made the mode-locked dye laser so successful. The model for the slow saturable absorber mode locking has to take into account the change of gain in the passage of one pulse [1, 2]. In the following, we consider a modelocked laser, that experiences in one round-trip a saturable gain and a slow saturable absorber. In the dye laser, both media are dyes with different saturation intensities or with different focusing into the dye jets so that gain and loss may show different saturation energies. The relaxation equation of the gain, in the limit of a pulse short compared with its relaxation time, can be approximated by

$$\frac{dg}{dt} = -g \frac{|A(t)|^2}{E_L} \quad (6.1)$$

The coefficient E_L is the saturation energy of the gain. Integration of the equation shows, that the gain saturates with the pulse energy $E(t)$

$$E(t) = \int_{-T_{R/2}}^t dt |A(t)|^2 \quad (6.2)$$

when passing the gain

$$g(t) = g_i \exp[-E(t)/E_L] \quad (6.3)$$

where g_i is the initial small signal gain just before the arrival of the pulse. A similar equation holds for the loss of the saturable absorber whose response (loss) is represented by $q(t)$

$$q(t) = q_0 \exp[-E(t)/E_A] \quad (6.4)$$

where E_A is the saturation energy of the saturable absorber. If the background loss is denoted by l , the master equation of mode-locking becomes

$$\begin{aligned} \frac{1}{T_R} \frac{\partial}{\partial T} A &= [g_i (\exp(-E(t)/E_L)) A - lA - \\ & q_0 \exp(-E(t)/E_A)] A + \frac{1}{\Omega_f^2} \frac{\partial^2}{\partial t^2} A \end{aligned} \quad (6.5)$$

Here, we have replaced the filtering action of the gain $D_g = \frac{1}{\Omega_f^2}$ as produced by a separate fixed filter. An analytic solution to this integro-differential equation can be obtained with one approximation: the exponentials are expanded to second order. This is legitimate if the population depletions of the gain and saturable absorber media are not excessive. Consider one of these expansions:

$$q_0 \exp(-E(t)/E_A) \approx q_0 \left[1 - (E(t)/E_A) + \frac{1}{2} (E(t)/E_A)^2 \right]. \quad (6.6)$$

We only consider the saturable gain and loss and the finite gain bandwidth. Then the master equation is given by

$$T_R \frac{\partial A(T, t)}{\partial T} = \left[g(t) - q(t) - l + D_f \frac{\partial^2}{\partial t^2} \right] A(T, t). \quad (6.7)$$

The filter dispersion, $D_f = 1/\Omega_f^2$, effectively models the finite bandwidth of the laser, that might not be only due to the finite gain bandwidth, but includes all bandwidth limiting effects in a parabolic approximation. Suppose the pulse is a symmetric function of time. Then the first power of the integral gives an antisymmetric function of time, its square is symmetric. An antisymmetric function acting on the pulse $A(t)$ causes a displacement. Hence, the steady state solution does not yield zero for the change per pass, the derivative $\frac{1}{T_R} \frac{\partial A}{\partial T}$ must be equated to a time shift Δt of the pulse. When this is done one can confirm easily that $A(t) = A_o \operatorname{sech}(t/\tau)$ is a solution of (6.6) with constraints on its coefficients. Thus we, are looking for a "steady state" solution $A(t, T) = A_o \operatorname{sech}(\frac{t}{\tau} + \alpha \frac{T}{T_R})$. Note, that α is the fraction of the pulsewidth, the pulse is shifted in each round-trip due to the shaping by loss and gain. The constraints on its coefficients can be easily found using

the following relations for the sech-pulse

$$E(t) = \int_{-T_R/2}^t dt |A(t)|^2 = \frac{W}{2} \left(1 + \tanh\left(\frac{t}{\tau} + \alpha \frac{T}{T_R}\right) \right) \quad (6.8)$$

$$E(t)^2 = \left(\frac{W}{2}\right)^2 \left(2 + 2\tanh\left(\frac{t}{\tau} + \alpha \frac{T}{T_R}\right) - \operatorname{sech}^2\left(\frac{t}{\tau} + \alpha \frac{T}{T_R}\right) \right) \quad (6.9)$$

$$T_R \frac{\partial}{\partial T} A(t, T) = -\alpha \tanh\left(\frac{t}{\tau} + \alpha \frac{T}{T_R}\right) A(t, T) \quad (6.10)$$

$$\frac{1}{\Omega_f^2} \frac{\partial^2}{\partial t^2} A(t, T) = \frac{1}{\Omega_f^2 \tau^2} \left(1 - 2\operatorname{sech}^2\left(\frac{t}{\tau} + \alpha \frac{T}{T_R}\right) \right) A(t, T), \quad (6.11)$$

substituting them into the master equation (6.5) and collecting the coefficients in front of the different temporal functions. The constant term gives the necessary small signal gain

$$g_i \left[1 - \frac{W}{2E_L} + \left(\frac{W}{2E_L}\right)^2 \right] = l + q_0 \left[1 - \frac{W}{2E_A} + \left(\frac{W}{2E_A}\right)^2 \right] - \frac{1}{\Omega_f^2 \tau^2}. \quad (6.12)$$

The constant in front of the odd tanh –function delivers the timing shift per round-trip

$$\alpha = \frac{\Delta t}{\tau} = g_i \left[\frac{W}{2E_L} - \left(\frac{W}{2E_L}\right)^2 \right] - q_0 \left[\frac{W}{2E_A} - \left(\frac{W}{2E_A}\right)^2 \right]. \quad (6.13)$$

And finally the constant in front of the sech²-function determines the pulsewidth

$$\frac{1}{\tau^2} = \frac{\Omega_f^2 W^2}{8} \left(\frac{q_0}{E_A^2} - \frac{g_i}{E_L^2} \right) \quad (6.14)$$

These equations have important implications. Consider first the equation for the inverse pulsewidth, (6.14). In order to get a real solution, the right hand side has to be positive. This implies that $q_0/E_A^2 > g_i/E_L^2$. The saturable absorber must saturate more easily, and, therefore more strongly, than the gain medium in order to open a net window of gain (Figure 6.2).

This was accomplished in a dye laser system by stronger focusing into the saturable absorber-dye jet (Reducing the saturation energy for the saturable absorber) than into the gain-dye jet (which was inverted, i.e. optically

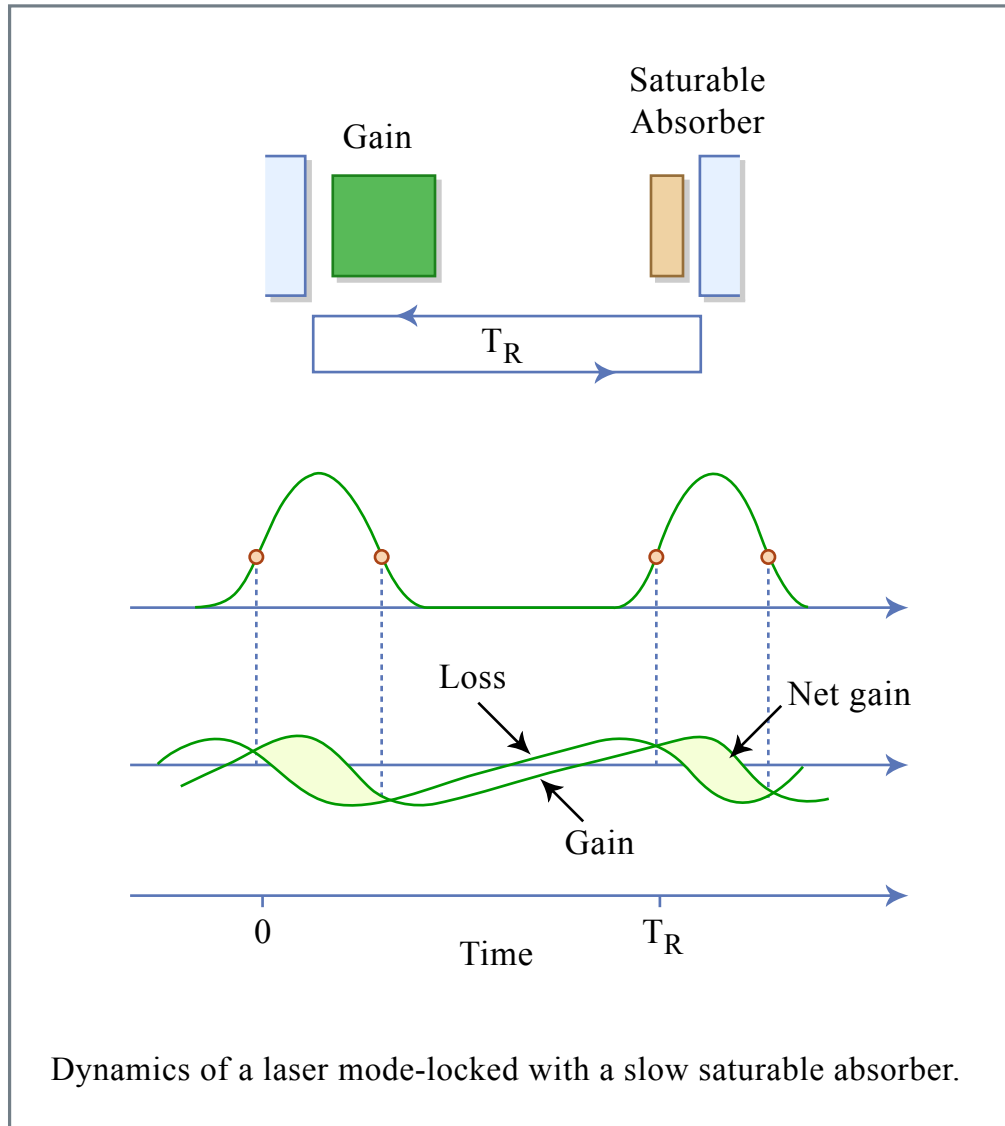


Figure 6.2: Dynamics of a laser mode-locked with a slow saturable absorber.

Figure by MIT OCW.

pumped). Equation (6.12) makes a statement about the net gain before passage of the pulse. The net gain before passage of the pulse is

$$g_i - q_0 - l = -\frac{1}{\Omega_f^2 \tau^2} + g_i \left[\frac{W}{2E_L} - \left(\frac{W}{2E_L} \right)^2 \right] - q_0 \left[\frac{W}{2E_A} - \left(\frac{W}{2E_A} \right)^2 \right]. \quad (6.15)$$

Using condition (6.14) this can be expressed as

$$g_i - q_0 - l = g_i \left[\frac{W}{2E_L} \right] - q_0 \left[\frac{W}{2E_A} \right] + \frac{1}{\Omega_f^2 \tau^2}. \quad (6.16)$$

This gain is negative since the effect of the saturable absorber is larger than that of the gain. Since the pulse has the same exponential tail after passage as before, one concludes that the net gain after passage of the pulse is the same as before passage and thus also negative. The pulse is stable against noise build-up both in its front and its back. This principle works if the ratio between the saturation energies for the saturable absorber and gain $\chi_P = E_A/E_P$ is very small. Then the shortest pulsewidth achievable with a given system is

$$\tau = \frac{4}{\sqrt{q_0} \Omega_f} \frac{E_A}{W} > \frac{2}{\sqrt{q_0} \Omega_f}. \quad (6.17)$$

The greater sign comes from the fact that our theory is based on the expansion of the exponentials, which is only true for $\frac{W}{2E_A} < 1$. If the filter dispersion $1/\Omega_f^2$ that determines the bandwidth of the system is again replaced by an average gain dispersion g/Ω_g^2 and assuming $g = q_0$. Note that the modelocking principle of the dye laser is a very fascinating one due to the fact that actually non of the elements in the system is fast. It is the interplay between two media that opens a short window in time on the scale of femtoseconds. The media themselves just have to be fast enough to recover completely between one round trip, i.e. on a nanosecond timescale.

Over the last fifteen years, the dye laser has been largely replaced by solid state lasers, which offer even more bandwidth than dyes and are on top of that much easier to handle because they do not show degradation over time. With it came the need for a different mode locking principle, since the saturation energy of these broadband solid-state laser media are much higher

than the typical intracavity pulse energies. The absorber has to open and close the net gain window.

6.2 Fast Saturable Absorber Mode Locking

The dynamics of a laser modelocked with a fast saturable absorber is again covered by the master equation (5.21) [3]. Now, the losses q react instantly on the intensity or power $P(t) = |A(t)|^2$ of the field

$$q(A) = \frac{q_0}{1 + \frac{|A|^2}{P_A}}, \quad (6.18)$$

where P_A is the saturation power of the absorber. There is no analytic solution of the master equation (5.21) with the absorber response (6.18). Therefore, we make expansions on the absorber response to get analytic insight. If the absorber is not saturated, we can expand the response (6.18) for small intensities

$$q(A) = q_0 - \gamma|A|^2, \quad (6.19)$$

with the saturable absorber modulation coefficient $\gamma = q_0/P_A$. The constant nonsaturated loss q_0 can be absorbed in the losses $l_0 = l + q_0$. The resulting master equation is, see also Fig. 6.3

$$T_R \frac{\partial A(T, t)}{\partial T} = \left[g - l_0 + D_f \frac{\partial^2}{\partial t^2} + \gamma|A|^2 + jD_2 \frac{\partial^2}{\partial t^2} - j\delta|A|^2 \right] A(T, t). \quad (6.20)$$

Image removed due to copyright restrictions.

Please see:

Keller, U., Ultrafast Laser Physics, Institute of Quantum Electronics, Swiss Federal Institute of Technology, ETH Hönggerberg—HPT, CH-8093 Zurich, Switzerland.

Figure 6.3: Schematic representation of the master equation for a passively modelocked laser with a fast saturable absorber.

Eq. (6.20) is a generalized Ginzburg-Landau equation well known from superconductivity with a rather complex solution manifold.

6.2.1 Without GDD and SPM

We consider first the situation without SPM and GDD, i.e. $D_2 = \delta = 0$

$$T_R \frac{\partial A(T, t)}{\partial T} = \left[g - l_0 + D_f \frac{\partial^2}{\partial t^2} + \gamma |A|^2 \right] A(T, t). \quad (6.21)$$

Up to the imaginary unit, this equation is still very similar to the NSE. To find the final pulse shape and width, we look for the stationary solution

$$T_R \frac{\partial A_s(T, t)}{\partial T} = 0.$$

Since the equation is similar to the NSE, we try the following ansatz

$$A_s(T, t) = A_s(t) = A_0 \operatorname{sech} \left(\frac{t}{\tau} \right). \quad (6.22)$$

Note, there is

$$\frac{d}{dx} \operatorname{sech} x = -\tanh x \operatorname{sech} x, \quad (6.23)$$

$$\begin{aligned} \frac{d^2}{dx^2} \operatorname{sech} x &= \tanh^2 x \operatorname{sech} x - \operatorname{sech}^3 x, \\ &= (\operatorname{sech} x - 2 \operatorname{sech}^3 x). \end{aligned} \quad (6.24)$$

Substitution of ansatz (6.22) into the master equation (6.21), assuming steady state, results in

$$\begin{aligned} 0 &= \left[(g - l_0) + \frac{D_f}{\tau^2} \left[1 - 2 \operatorname{sech}^2 \left(\frac{t}{\tau} \right) \right] \right. \\ &\quad \left. + \gamma |A_0|^2 \operatorname{sech}^2 \left(\frac{t}{\tau} \right) \right] \cdot A_0 \operatorname{sech} \left(\frac{t}{\tau} \right). \end{aligned} \quad (6.25)$$

Comparison of the coefficients with the sech - and sech^3 -expressions results in the conditions for the pulse peak intensity and pulse width τ and for the saturated gain

$$\frac{D_f}{\tau^2} = \frac{1}{2} \gamma |A_0|^2, \quad (6.26)$$

$$g = l_0 - \frac{D_f}{\tau^2}. \quad (6.27)$$

From Eq.(6.26) and with the pulse energy of a sech pulse, see Eq.(3.8), $W = 2|A_0|^2\tau$,

$$\tau = \frac{4D_f}{\gamma W}. \quad (6.28)$$

Eq. (6.28) is rather similar to the soliton width with the exception that the conservative pulse shaping effects GDD and SPM are replaced by gain dispersion and saturable absorption. The soliton phase shift per roundtrip is replaced by the difference between the saturated gain and loss in Eq.(6.28). It is interesting to have a closer look on how the difference between gain and loss $\frac{D_f}{\tau^2}$ per round-trip comes about. From the master equation (6.21) we can derive an equation of motion for the pulse energy according to

$$T_R \frac{\partial W(T)}{\partial T} = T_R \frac{\partial}{\partial T} \int_{-\infty}^{\infty} |A(T, t)|^2 dt \quad (6.29)$$

$$= T_R \int_{-\infty}^{\infty} \left[A(T, t)^* \frac{\partial}{\partial T} A(T, t) + c.c. \right] dt \quad (6.30)$$

$$= 2G(g_s, W)W, \quad (6.31)$$

where G is the net energy gain per roundtrip, which vanishes when steady state is reached [3]. Substitution of the master equation into (6.30) with

$$\int_{-\infty}^{\infty} (\operatorname{sech}^2 x) dx = 2, \quad (6.32)$$

$$\int_{-\infty}^{\infty} (\operatorname{sech}^4 x) dx = \frac{4}{3}, \quad (6.33)$$

$$-\int_{-\infty}^{\infty} \operatorname{sech} x \frac{d^2}{dx^2} (\operatorname{sech} x) dx = \int_{-\infty}^{\infty} \left(\frac{d}{dx} \operatorname{sech} x \right)^2 dx = \frac{2}{3}. \quad (6.34)$$

results in

$$G(g_s, W) = g_s - l_0 - \frac{D_f}{3\tau^2} + \frac{2}{3}\gamma|A_0|^2 \quad (6.35)$$

$$= g_s - l_0 + \frac{1}{2}\gamma|A_0|^2 = g_s - l_0 + \frac{D_f}{\tau^2} = 0 \quad (6.36)$$

with the saturated gain

$$g_s(W) = \frac{g_0}{1 + \frac{W}{P_L T_R}} \quad (6.37)$$

Equation (6.36) together with (6.28) determines the pulse energy

$$\begin{aligned} g_s(W) &= \frac{g_0}{1 + \frac{W}{P_L T_R}} = l_0 - \frac{D_f}{\tau^2} \\ &= l_0 - \frac{(\gamma W)^2}{16D_g} \end{aligned} \quad (6.38)$$

Figure 6.4 shows the time dependent variation of gain and loss in a laser modelocked with a fast saturable absorber on a normalized time scale Here, we assumed that the absorber saturates linearly with intensity up to a maximum value $q_0 = \gamma A_0^2$. If this maximum saturable absorption is completely exploited see Figure 6.5. The minimum pulse width achievable with a given saturable absorption q_0 results from Eq.(6.26)

$$\frac{D_f}{\tau^2} = \frac{q_0}{2}, \quad (6.39)$$

to be

$$\tau = \sqrt{\frac{2}{q_0} \frac{1}{\Omega_f}}. \quad (6.40)$$

Image removed due to copyright restrictions.

Please see:

Kartner, F. X., and U. Keller. "Stabilization of soliton-like pulses with a slow saturable absorber." *Optics Letters* 20 (1990): 16-19.

Figure 6.4: Gain and loss in a passively modelocked laser using a fast saturable absorber on a normalized time scale $x = t/\tau$. The absorber is assumed to saturate linearly with intensity according to $q(A) = q_0 \left(1 - \frac{|A|^2}{A_0^2}\right)$.

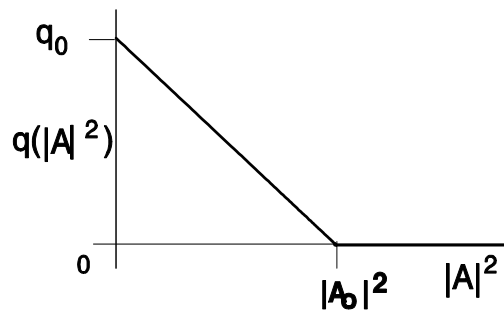


Figure 6.5: Saturation characteristic of an ideal saturable absorber

Note that in contrast to active modelocking, now the achievable pulse width is scaling with the inverse gain bandwidth, which gives much shorter pulses. Figure 6.4 can be interpreted as follows: In steady state, the saturated gain is below loss, by about one half of the exploited saturable loss before and after the pulse. This means, that there is net loss outside the pulse, which keeps the pulse stable against growth of instabilities at the leading and trailing edge of the pulse. If there is stable mode-locked operation, there must be always net loss far away from the pulse, otherwise, a continuous wave signal running at the peak of the gain would experience more gain than the pulse and would break through. From Eq.(6.35) follows, that one third of the exploited saturable loss is used up during saturation of the absorber and actually only one sixth is used to overcome the filter losses due to the finite gain bandwidth. Note, there is a limit to the minimum pulse width, which comes about, because the saturated gain (6.27) is $g_s = l + \frac{1}{2}q_0$ and, therefore, from Eq.(6.40), if we assume that the finite bandwidth of the laser is set by the gain, i.e. $D_f = D_g = \frac{g}{\Omega_g^2}$ we obtain for $q_0 \gg l$

$$\tau_{\min} = \frac{1}{\Omega_g} \quad (6.41)$$

for the linearly saturating absorber model. This corresponds to mode locking over the full bandwidth of the gain medium, since for a sech-shaped pulse, the time-bandwidth product is 0.315, and therefore,

$$\Delta f_{FWHM} = \frac{0.315}{1.76 \cdot \tau_{\min}} = \frac{\Omega_g}{1.76 \cdot \pi}. \quad (6.42)$$

As an example, for Ti:sapphire this corresponds to $\Omega_g = 270$ THz, $\tau_{\min} = 3.7$ fs, $\tau_{FWHM} = 6.5$ fs.

6.2.2 With GDD and SPM

After understanding what happens without GDD and SPM, we look at the solutions of the full master equation (6.20) with GDD and SPM. It turns out, that there exist steady state solutions, which are chirped hyperbolic secant functions [4]

$$A_s(T, t) = A_0 \left(\operatorname{sech} \left(\frac{t}{\tau} \right) \right)^{(1+j\beta)} e^{j\psi T/T_R}, \quad (6.43)$$

$$= A_0 \operatorname{sech} \left(\frac{t}{\tau} \right) \exp \left[j\beta \ln \operatorname{sech} \left(\frac{t}{\tau} \right) + j\psi T/T_R \right]. \quad (6.44)$$

Where ψ is the round-trip phase shift of the pulse, which we have to allow for. Only the intensity of the pulse becomes stationary. There is still a phase-shift per round-trip due to the difference between the group and phase velocity (these effects have been already transformed away) and the nonlinear effects. As in the last section, we can substitute this ansatz into the master equation and compare coefficients. Using the following relations

$$\frac{d}{dx} (f(x)^b) = b f(x)^{b-1} \frac{d}{dx} f(x) \quad (6.45)$$

$$\frac{d}{dx} (\operatorname{sech} x)^{(1+j\beta)} = -(1+j\beta) \tanh x (\operatorname{sech} x)^{(1+j\beta)}, \quad (6.46)$$

$$\frac{d^2}{dx^2} (\operatorname{sech} x)^{(1+j\beta)} = ((1+j\beta)^2 - (2+3j\beta - \beta^2) \operatorname{sech}^2 x) \quad (6.47)$$

$$(\operatorname{sech} x)^{(1+j\beta)}. \quad (6.48)$$

in the master equation and comparing the coefficients to the same functions leads to two complex equations

$$\frac{1}{\tau^2} (D_f + jD_2) (2 + 3j\beta - \beta^2) = (\gamma - j\delta) |A_0|^2, \quad (6.49)$$

$$l_0 - \frac{(1+j\beta)^2}{\tau^2} (D_f + jD_2) = g - j\psi. \quad (6.50)$$

These equations are extensions to Eqs.(6.26) and (6.27) and are equivalent to four real equations for the phase-shift per round-trip ψ , the pulse width τ , the chirp β and the peak power $|A_0|^2$ or pulse energy. The imaginary part of Eq.(6.50) determines the phase-shift only, which is most often not of importance. The real part of Eq.(6.50) gives the saturated gain

$$g = l_0 - \frac{1 - \beta^2}{\tau^2} D_f + \frac{2\beta D_2}{\tau^2}. \quad (6.51)$$

The real part and imaginary part of Eq.(6.49) give

$$\frac{1}{\tau^2} [D_f (2 - \beta^2) - 3\beta D_2] = \gamma |A_0|^2, \quad (6.52)$$

$$\frac{1}{\tau^2} [D_2 (2 - \beta^2) + 3\beta D_f] = -\delta |A_0|^2. \quad (6.53)$$

We introduce the normalized dispersion, $D_n = D_2/D_f$, and the pulse width of the system without GDD and SPM, i.e. the width of the purely saturable

absorber modelocked system, $\tau_0 = 4D_f/(\gamma W)$. Deviding Eq.(6.53) by (6.52) and introducing the normalized nonlinearity $\delta_n = \delta/\gamma$, we obtain a quadratic equation for the chirp,

$$\frac{D_n (2 - \beta^2) + 3\beta}{(2 - \beta^2) - 3\beta D_n} = -\delta_n,$$

or after some reodering

$$\frac{3\beta}{2 - \beta^2} = \frac{\delta_n + D_n}{-1 + \delta_n D_n} \equiv \frac{1}{\chi}. \quad (6.54)$$

Note that χ depends only on the system parameters. Therefore, the chirp is given by

$$\beta = -\frac{3}{2}\chi \pm \sqrt{\left(\frac{3}{2}\chi\right)^2 + 2}. \quad (6.55)$$

Knowing the chirp, we obtain from Eq.(6.52) the pulsewidth

$$\tau = \frac{\tau_0}{2} (2 - \beta^2 - 3\beta D_n), \quad (6.56)$$

which, with Eq.(6.54), can also be written as

$$\tau = \frac{3\tau_0}{2}\beta (\chi - D_n) \quad (6.57)$$

In order to be physically meaning full the pulse width has to be a positive number, i.e. the product $\beta (\chi - D_n)$ has always to be greater than 0, which determines the root in Eq.(6.55)

$$\beta = \begin{cases} -\frac{3}{2}\chi + \sqrt{\left(\frac{3}{2}\chi\right)^2 + 2}, & \text{for } \chi > D_n \\ -\frac{3}{2}\chi - \sqrt{\left(\frac{3}{2}\chi\right)^2 + 2}, & \text{for } \chi < D_n \end{cases}. \quad (6.58)$$

Figure 6.6(a,b and d) shows the resulting chirp, pulse width and nonlinear round-trip phase shift with regard to the system parameters [4][5]. A necessary but not sufficient criterion for the stability of the pulses is, that there must be net loss leading and following the pulse. From Eq.(6.51), we obtain

$$g_s - l_0 = -\frac{1 - \beta^2}{\tau^2} D_f + \frac{2\beta D_2}{\tau^2} < 0. \quad (6.59)$$

If we define the stability parameter S

$$S = 1 - \beta^2 - 2\beta D_n > 0, \quad (6.60)$$

S has to be greater than zero, as shown in Figure 6.6 (d).

Image removed due to copyright restrictions.

Please see:

Haus, H. A., J. G. Fujimoto, E. P. Ippen. "Structure for additive pulse modelocking." *Journal of Optical Society of Americas B* 8 (1991): 208.

Figure 6.6: (a) Pulsethickness, (b) Chirp parameter, (c) Net gain following the pulse, which is related to stability. (d) Phase shift per pass. [4]

Figure 6.6 (a-d) indicate that there are essentially three operating regimes. First, without GDD and SPM, the pulses are always stable. Second, if there is strong soliton-like pulse shaping, i.e. $\delta_n \gg 1$ and $-D_n \gg 1$ the chirp is always much smaller than for positive dispersion and the pulses are soliton-like. At last, the pulses are even chirp free, if the condition $\delta_n = -D_n$ is fulfilled. Then the solution is

$$A_s(T, t) = A_0 \left(\operatorname{sech} \left(\frac{t}{\tau} \right) \right) e^{j\psi T/T_R}, \text{ for } \delta_n = -D_n. \quad (6.61)$$

Note, for this discussion we always assumed a positive SPM-coefficient. In this regime we also obtain the shortest pulses directly from the system, which can be a factor 2-3 shorter than by pure saturable absorber modelocking. Note that Figure 6.6 indicates even arbitrarily shorter pulses if the nonlinear index, i.e. δ_n is further increased. However, this is only an artifact of the linear approximation of the saturable absorber, which can now become arbitrarily large, compare (6.18) and (6.19). As we have found from the analysis of the fast saturable absorber model, Figure 6.4, only one sixth of the saturable absorption is used for overcoming the gain filtering. This is so, because the saturable absorber has to shape and stabilize the pulse against breakthrough of cw-radiation. With SPM and GDD this is relaxed. The pulse shaping can be done by SPM and GDD alone, i.e. soliton formation and the absorber only has to stabilize the pulse. But then all of the saturable absorption can be used up for stability, i.e. six times as much, which allows for additional pulse shortening by a factor of about $\sqrt{6} = 2.5$ in a parabolic filter situation. Note, that for an experimentalist a factor of three is a large number. This tells us that the 6.5 fs limit for Ti:sapphire derived above from the saturable absorber model can be reduced to 2.6 fs including GDD and SPM, which is about one optical cycle of 2.7 fs at a center wavelength of 800nm. At that point all approximations, we have made so far break down. If the amount of negative dispersion is reduced too much, i.e. the pulses become too short, the absorber cannot keep them stable anymore.

If there is strong positive dispersion, the pulses again become stable and long, but highly chirped. The pulse can then be compressed externally, however not completely to their transform limit, because these are nonlinearly chirped pulses, see Eq.(6.43).

In the case of strong solitonlike pulse shaping, the absorber doesn't have to be really fast, because the pulse is shaped by GDD and SPM and the absorber has only to stabilize the soliton against the continuum. This regime has been called Soliton mode locking.

6.3 Soliton Mode Locking

If strong soliton formation is present in the system, the saturable absorber doesn't have to be fast [6][7][8], see Figure 6.7. The master equation describing

the mode locking process is given by

$$T_R \frac{\partial A(T, t)}{\partial T} = \left[g - l + (D_f + jD) \frac{\partial^2}{\partial t^2} - j\delta |A(T, t)|^2 - q(T, t) \right] A(T, t). \quad (6.62)$$

The saturable absorber obeys a separate differential equation that describes the absorber response to the pulse in each round trip

$$\frac{\partial q(T, t)}{\partial t} = -\frac{q - q_0}{\tau_A} - \frac{|A(T, t)|^2}{E_A}. \quad (6.63)$$

Where τ_A is the absorber recovery time and E_A the saturation energy. If the soliton shaping effects are much larger than the pulse

Image removed due to copyright restrictions.

Please see:

Kartner, F. X., and U. Keller. "Stabilization of soliton-like pulses with a slow saturable absorber." *Optics Letters* 20 (1990): 16-19.

Figure 6.7: Response of a slow saturable absorber to a soliton-like pulse. The pulse experiences loss during saturation of the absorber and filter losses. The saturated gain is equal to these losses. The loss experienced by the continuum, l_c must be higher than the losses of the soliton to keep the soliton stable.

Image removed due to copyright restrictions.

Please see:

Kartner, F. X., and U. Keller. "Stabilization of soliton-like pulses with a slow saturable absorber." *Optics Letters* 20 (1990): 16-19.

Figure 6.8: The continuum, that might grow in the open net gain window following the pulse is spread by dispersion into the regions of high absorption.

shaping due to the filter and the saturable absorber, the steady state pulse will be a soliton and continuum contribution similar to the case of active mode locking with strong soliton formation as discussed in section 5.5

$$A(T, t) = \left(A \operatorname{sech}\left(\frac{t}{\tau}\right) + a_c(T, t) \right) e^{-j\phi_0 \frac{T}{T_R}} \quad (6.64)$$

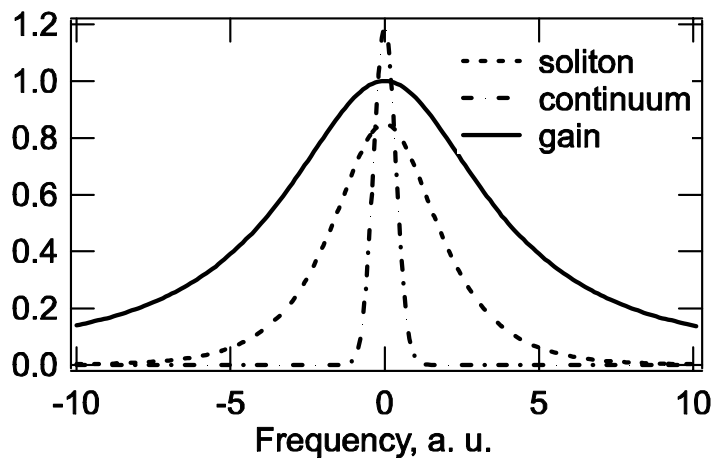


Figure 6.9: Normalized gain, soliton and continuum. The continuum is a long pulse exploiting the peak of the gain

The continuum can be viewed as a long pulse competing with the soliton for the available gain. In the frequency domain, see Figure 6.9, the soliton has a broad spectrum compared to the continuum. Therefore, the continuum experiences the peak of the gain, whereas the soliton spectrum on average experiences less gain. This advantage in gain of the continuum has to be compensated for in the time domain by the saturable absorber response, see Figure 6.8. Whereas for the soliton, there is a balance of the nonlinearity and the dispersion, this is not so for the continuum. Therefore, the continuum is spread by the dispersion into the regions of high absorption. This mechanism has to clean up the gain window following the soliton and caused by the slow recovery of the absorber. As in the case of active modelocking, once the soliton is too short, i.e. a too long net-gain window arises, the loss of the continuum may be lower than the loss of the soliton, see Figure 6.7 and the continuum may break through and destroy the single pulse soliton solution. As a rule of thumb the absorber recovery time can be about 10 times longer than the soliton width. This modelocking principle is especially important for modelocking of lasers with semiconductor saturable absorbers, which show typical absorber recovery times that may range from 100fs-100 ps. Pulses as short as 13fs have been generated with semiconductor saturable absorbers [11]. Figure 6.10 shows the measured spectra from a Ti:sapphire laser modelocked with a saturable absorber for different values for the intracavity dispersion. Lowering the dispersion, increases the bandwidth of the soliton and therefore its loss, while lowering at the same time the loss for the continuum. At some value of the dispersion the laser has to become unstable by break through of the continuum. In the example shown, this occurs at a dispersion value of about $D = -500fs^2$. The continuum break-through is clearly visible by the additional spectral components showing up at the center of the spectrum. Reducing the dispersion even further might lead again to more stable but complicated spectra related to the formation of higher order solitons. Note the spectra shown are time averaged spectra.

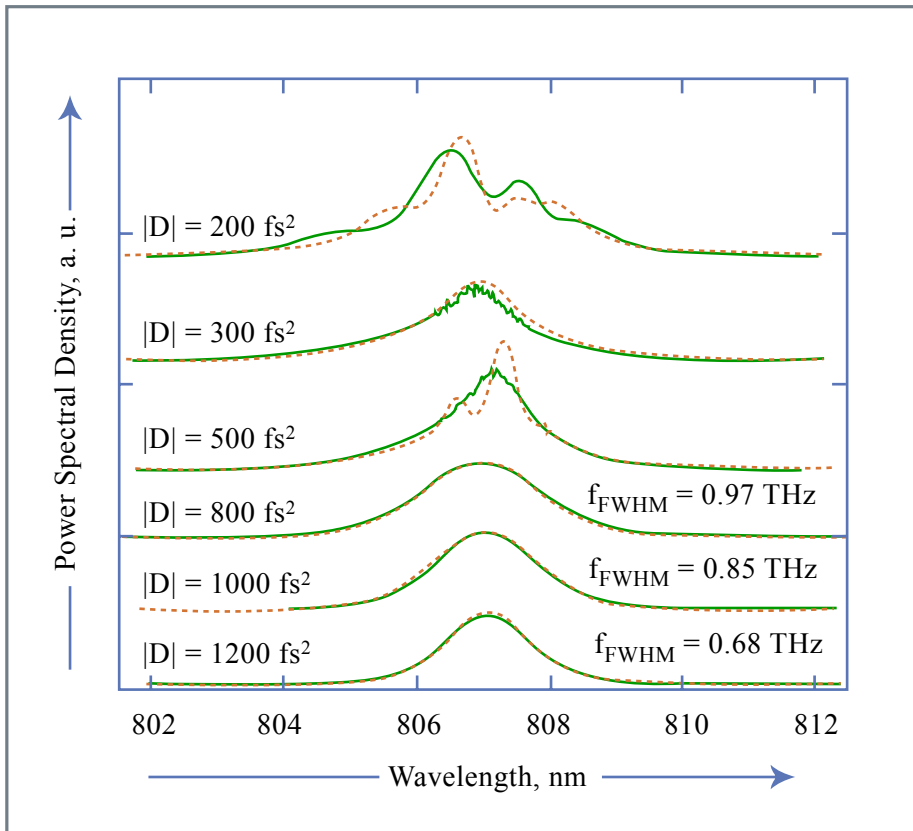


Figure 6.10: Measured (—) and simulated (- - -) spectra from a semiconductor saturable absorber modelocked Ti:sapphire laser for various values of the net intracavity dispersion.

Figure by MIT OCW.

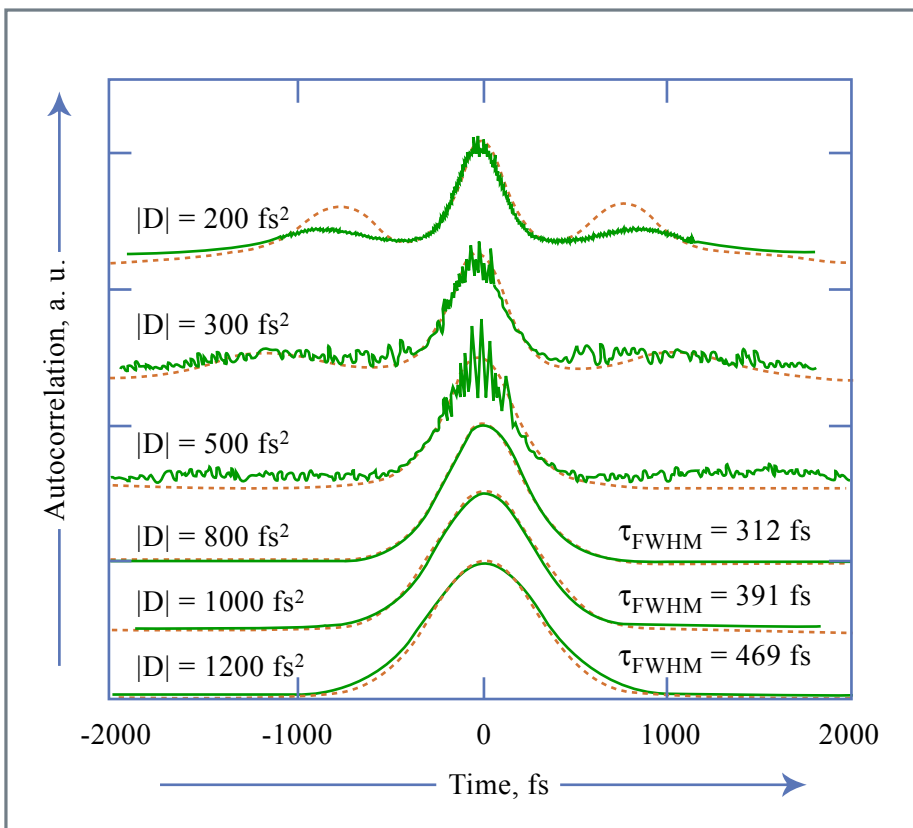


Figure 6.11: Measured (—) and simulated (- - -) autocorrelations corresponding to the spectra shown in Figure 6.10.

Figure by MIT OCW.

The continuum leads to a background pedestal in the intensity autocorrelation of the emitted pulse, see Figure 6.11. The details of the spectra and autocorrelation may strongly depend on the detailed absorber response.

6.4 Dispersion Managed Soliton Formation

The nonlinear Schrödinger equation describes pulse propagation in a medium with continuously distributed dispersion and self-phase-modulation. For lasers generating pulses as short as 10 fs and below, it was first pointed out by Spielmann et al. that large changes in the pulse occur within one roundtrip and that the ordering of the pulse-shaping elements within the cavity has a major effect on the pulse formation [9]. The discrete action of linear dispersion in the arms of the laser resonator and the discrete, but simultaneous, action of positive SPM and positive GDD in the laser crystal cannot any longer be neglected. The importance of strong dispersion variations for the laser dynamics was first discovered in a fiber laser and called stretched pulse modelocking [11]. The positive dispersion in the Er-doped fiber section of a fiber ring laser was balanced by a negative dispersive passive fiber. The pulse circulating in the ring was stretched and compressed by as much as a factor of 20 in one roundtrip. One consequence of this behavior was a dramatic decrease of the nonlinearity and thus increased stability against the SPM induced instabilities. The sidebands, due to periodic perturbations of the soliton, as discussed in section 3.6, are no longer observed (see Fig. 6.12).

Image removed due to copyright restrictions.

Please see:

Tamura, K., E. P. Ippen, H. A. Haus, and L. E. Nelson. "77-fs pulse generation from a stretched-pulse mode-locked all-fiber ring laser." *Optics Letters* 18 (1993): 1080-1082.

Figure 6.12: Spectra of mode-locked Er-doped fiber lasers operating in the conventional soliton regime, i.e. net negative dispersion and in the stretched pulse mode of operation at almost zero average dispersion [11].

The energy of the output pulses could be increased 100 fold. The minimum pulsewidth was 63 fs, with a bandwidth much broader than the erbium gain bandwidth [12]. Figure 6.12 also shows the spectral enhancement of the fiber laser in the dispersion managed regime. The generation of ultrashort pulses from solid state lasers like Ti:sapphire has progressed over the past decade and led to the generation of pulses as short as 5 fs directly from the laser. At such short pulse lengths the pulse is stretched up to a factor of ten when propagating through the laser crystal creating a dispersion managed soliton [10]. The spectra generated with these lasers are not of simple shape for many reasons. Here, we want to consider the impact on the spectral shape and laser dynamics due to dispersion managed soliton formation.

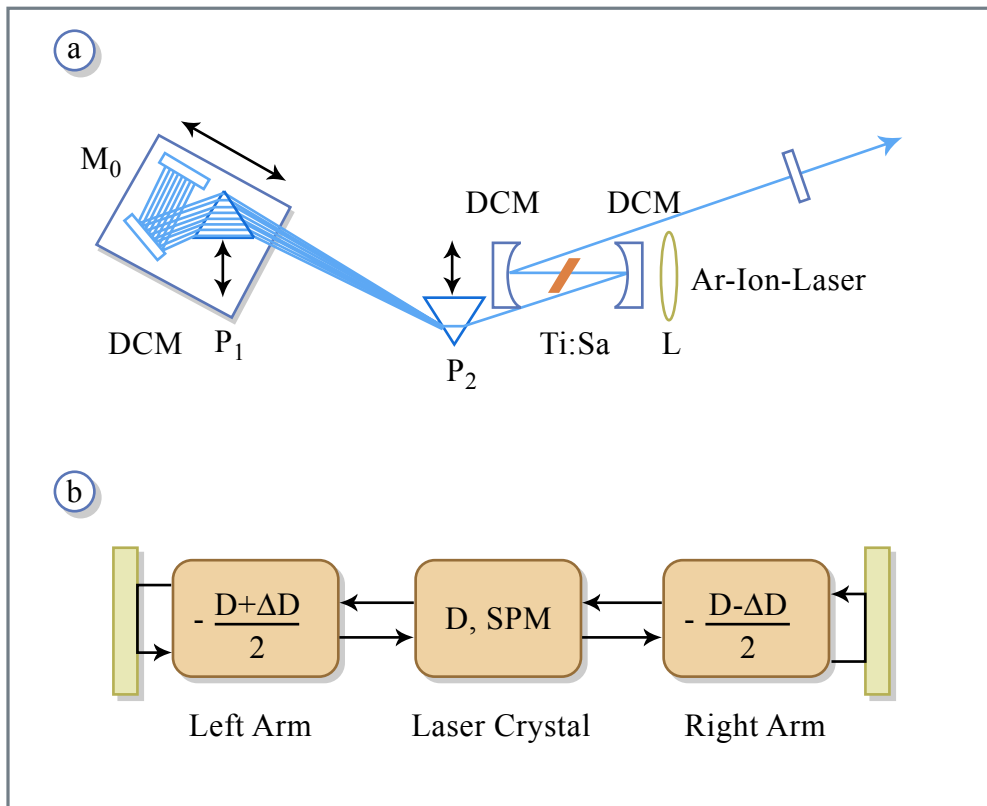


Figure 6.13: (a) Schematic of a Kerr-lens mode-locked Ti:sapphire laser: P's, prisms; L, lens; DCM's, double-chirped mirror; Ti:Sa, Ti:sapphire. (b) Correspondence with dispersion-managed fiber transmission.

Figure by MIT OCW.

A mode-locked laser producing ultrashort pulses consists at least of a gain

medium (Ti:sapphire crystal) and dispersion balancing components (mirrors, prism pairs), see Fig. 6.13 a. The system can be decomposed into the resonator arms and the crystal, see Fig. 6.13 b. To achieve ultrashort pulses, the dispersion-balancing components should produce near-zero net dispersion while the dispersion element(s) individually produce significant group delay over the broad bandwidth of the laser pulse. This fact suggests an analogy with dispersion-managed pulse propagation along a dispersion-managed fiber transmission link [14]. A system with sufficient variation of dispersion can support solitary waves. One can show that the Kerr nonlinearity produces a self-consistent nonlinear scattering potential that permits formation of a periodic solution with a simple phase factor in a system with zero net dispersion. The pulses are analogous to solitons in that they are self-consistent solutions of the Hamiltonian (lossless) problem as the conventional solitons discussed above. But they are not secant hyperbolic in shape. Figure 6.14 shows a numerical simulation of a self-consistent solution of the Hamiltonian pulse-propagation problem in a linear medium of negative dispersion and subsequent propagation in a nonlinear medium of positive dispersion and positive self-phase modulation, following the equation

$$\frac{\partial}{\partial z}A(z, t) = jD(z)\frac{\partial^2}{\partial t^2}A(z, t) - j\delta(z)|A|^2A(z, t) \quad (6.65)$$

In Fig. 6.15 the steady state intensity profiles are shown at the center of the negative dispersion segment over 1000 roundtrips. It is clear that the solution repeats itself from period to period, i.e. there is a new solitary wave that solves the piecewise nonlinear Schroedinger equation 6.65, dispersion managed soliton. In contrast to the conventional soliton the dispersion managed soliton of equation 6.65 (with no SAM and no filtering) resemble Gaussian pulses down to about -10 dB from the peak, but then show rather complicated structure, see Fig. 6.15. The dispersion map $D(z)$ used is shown as an inset in Figure 6.14. One can additionally include saturable gain, Lorentzian gain filtering, and a fast saturable absorber. Figure 6.14 shows the behavior in one period (one round trip through the resonator) including these effects. The response of the absorber is $q(A) = q_o/(1 + |A|^2/P_A)$, with $q_o = 0.01/\text{mm}$ and $P_A = 1$ MW. The bandwidth-limited gain is modeled by the Lorentzian profile with gain bandwidth $2\pi \times 43$ THz. The filtering and saturable absorption reduce the spectral and temporal side lobes of the Hamiltonian problem. As can be inferred from Fig. 6.14, the steady state pulse formation can be understood in the following way. By symmetry the pulses are chirp free in

Image removed due to copyright restrictions.

Please see:

Chen, Y., et al. "Dispersion managed mode-locking." *Journal of Optical Society of Americas B* 16 (1999): 1999-2004.

Figure 6.14: Pulse shaping in one round trip. The negative segment has no nonlinearity.

the middle of the dispersion cells. A chirp free pulse starting in the center of the gain crystal, i.e. nonlinear segment is spectrally broadened by the SPM and disperses in time due to the GVD, which generates a rather linear chirp over the pulse. After the pulse is leaving the crystal it experiences negative GVD during propagation through the left or right resonator arm, which is compressing the positively chirped pulse to its transform limit at the end of the arm, where an output coupler can be placed. Back propagation towards the crystal imposes a negative chirp, generating the time reversed solution of the nonlinear Schrödinger equation (6.65). Therefore, subsequent propagation in the nonlinear crystal is compressing the pulse spectrally and temporally to its initial shape in the center of the crystal. The spectrum is narrower in the crystal than in the negative-dispersion sections, because it is negatively prechirped before it enters the SPM section and spectral spreading occurs again only after the pulse has been compressed. This result further explains that in a laser with a linear cavity, for which the negative dispersion is located in only one arm of the laser resonator (i.e. in the prism pair and no use of chirped mirrors) the spectrum is widest in the arm that contains the negative dispersion. In a laser with a linear cavity, for which the negative dispersion is equally distributed in both arms of the cavity, the pulse runs

through the dispersion map twice per roundtrip. The pulse is short at each end of the cavity and, most importantly, the pulses are identical in each pass through the crystal, which exploits the saturable absorber action (Kerr-Lens Modelocking in this case, as will be discussed in the next chapter) twice per roundtrip, in contrast to an asymmetric dispersion distribution in the resonator arms. Thus a symmetric dispersion distribution leads to an effective saturable absorption that is twice as strong as an asymmetric dispersion distribution resulting in substantially shorter pulses. Furthermore, the dispersion swing between the negative and positive dispersion sections is only half, which allows for shorter dispersion-managed solitons operating at the same average power level.

Image removed due to copyright restrictions.

Please see:

Chen, Y., et al. "Dispersion managed mode-locking." *Journal of Optical Society of Americas B* 16 (1999): 1999-2004.

Figure 6.15: Simulation of the Hamiltonian problem. Intensity profiles at the center of the negatively dispersive segment are shown for successive roundtrips. The total extent in 1000 roundtrips. $D = D^{(\pm)} = \pm 60 \text{ fs}^2/\text{mm}$, segment of crystal length $L = 2 \text{ mm}$, $\tau_{\text{FWHM}} = 5.5 \text{ fs}$, $\delta = 0$ for $D < 0$, $\delta = 1$ $(\text{MW mm})^{-1}$ for $D > 0$. [10]

To further illustrate the efficiency of the dispersion managed soliton formation, we present a series of simulations that start with a linear segment of negative dispersion and a nonlinear segment of positive dispersion of the same magnitude, saturable absorber action, and filtering.

Image removed due to copyright restrictions.

Please see:

Chen, Y., et al. "Dispersion managed mode-locking." *Journal of Optical Society of Americas B* 16 (1999): 1999-2004.

Figure 6.16: Sequence of pulse profiles in the center of the negatively dispersive segment for three magnitudes of SPM. $t_o = 3$ fs, with solid curves (5.5 fs) for $\delta = 1$ (MW mm)⁻¹, dashed-dotted curve (7 fs) for $\delta = 0.5$ (MW mm)⁻¹, and dashed curves for no SPM of $\delta = 0$. The dispersion map is of Fig. 6.14. The output coupler loss is 3%. [10]

The dashed curve in Figure 6.16 shows the pulse shape for gain, loss, saturable absorption and gain filtering only. We obtained the other traces by increasing the SPM while keeping the energy fixed through adjustment of the gain. As one can see, increasing the SPM permits shorter pulses. The shortest pulse can be approximately three times shorter than the pulse without SPM. The parameters chosen for the simulations are listed in the figure caption. In this respect, the behavior is similar to the fast saturable absorber case with conventional soliton formation as discussed in the last section.

A major difference in the dispersion managed soliton case is illustrated in Fig. 6.17. The figure shows the parameter ranges for a dispersion-managed soliton system (no gain, no loss, no filtering) that is unbalanced such as to result in the net dispersion that serves as the abscissa of the figure. Each curve gives the locus of energy versus net cavity dispersion for a stretching

ratio $S = LD/\tau_{\text{FWHM}}^2$ (or pulse width with fixed crystal length L). One can see that for pulse width longer than 8 fs with crystal length $L = 2$ mm, no solution of finite energy exists in the dispersion managed system for zero or positive net dispersion. Pulses of durations longer than 8 fs require net negative dispersion. Hence one can reach the ultrashort dispersion managed soliton operation at zero net dispersion only by first providing the system with negative dispersion. At the same energy, one can form a shorter pulse by reducing the net dispersion, provided that the 8 fs threshold has been passed. For a fixed dispersion swing $\pm D$, the stretching increases quadratically with the spectral width or the inverse pulse width. Long pulses with no stretching have a sech shape. For stretching ratios of 3-10 the pulses are Gaussian shaped. For even larger stretching ratios the pulse spectra become increasingly more flat topped, as shown in Fig. 6.16.

Image removed due to copyright restrictions.

Please see:

Chen, Y., et al. "Dispersion managed mode-locking." *Journal of Optical Society of Americas B* 16 (1999): 1999-2004.

Figure 6.17: Energy of the pulse in the lossless dispersion-managed system with stretching $S = LD/\tau_{\text{FWHM}}^2$ or for a fixed crystal length L and pulsewidth as parameters; $D = 60$ fs²/mm for Ti:sapphire at 800 nm [10].

To gain insight into the laser dynamics and later on in their noise and tuning behavior, it is advantageous to formulate also a master equation approach for the dispersion managed soliton case [16]. Care has to be taken of the fact that the Kerr-phase shift is produced by a pulse of varying amplitude and width as it circulates around the ring. The Kerr-phase shift for a pulse

of constant width, $\delta|a|^2$ had to be replaced by a phase profile that mimics the average shape of the pulse, weighted by its intensity. Therefore, the SPM action is replaced by

$$\delta|A|^2 = \delta_o|A_o|^2 \left(1 - \mu \frac{t^2}{\tau^2}\right) \quad (6.66)$$

where A_o is the pulse amplitude at the position of minimum width. The Kerr-phase profile is expanded to second order in t . The coefficient δ_o and μ are evaluated variationally. The saturable absorber action is similarly expanded. Finally, the net intracavity dispersion acting on average on the pulse is replaced by the effective dispersion D_{net} in the resonator within one roundtrip. The master equation becomes

$$\begin{aligned} T_R \frac{\partial}{\partial T} A &= (g - l)A + \left(\frac{1}{\Omega_f^2} + jD_{\text{net}} \right) \frac{\partial^2}{\partial t^2} A \\ &+ (\gamma_o - j\delta_o)|A_o|^2 \left(1 - \mu \frac{t^2}{\tau^2}\right) A \end{aligned} \quad (6.67)$$

This equation has Gaussian-pulse solutions. The master equation (6.67) is a patchwork, it is not an ordinary differential equation. The coefficients in the equation depend on the pulse solution and eventually have to be found iteratively. Nevertheless, the equation accounts for the pulse shaping in the system in an analytic fashion. It will allow us to extend the conventional soliton perturbation theory to the case of dispersion managed solitons.

There is one more interesting property of the stretched pulse operation that needs to be emphasized. Dispersion managed solitons may form even when the net dispersion as seen by a linearly propagating pulse is zero or slightly positive. This is a surprising result which was discovered in the study of dispersion managed soliton propagation [14]. It turns out that the stretched pulse changes its spectrum during propagation through the two segments of fiber with opposite dispersion or in the case of a Ti:Sapphire laser in the nonlinear crystal. The spectrum in the segment with normal (positive) dispersion is narrower, than in the segment of anomalous (negative) dispersion, see Figure 6.14. The pulse sees an effective net negative dispersion, provided that the positive D_{net} is not too large. In (6.67) the D_{net} is to be replaced by D_{eff} which can be computed variationally. Thus,

dispersion managed soliton-like solutions can exist even when D_{net} is zero. However, they exist only if the stretching factor is large, see Figure 6.17.

A remarkable property of the dispersion managed solitons is that they do not radiate (generate continuum) even though they propagate in a medium with abrupt dispersion changes. This can be understood by the fact, that the dispersion managed soliton is a solution of the underlying dynamics incorporating already the periodic dispersion variations including the Kerr-effect. This is in contrast to the soliton in a continuously distributed dispersive environment, where periodic variations in dispersion and nonlinearity leads to radiation.

Bibliography

- [1] G.H.C. New: "Pulse evolution in mode-locked quasicontinuous lasers," IEEE J. Quantum Electron. **10**, 115-124 (1974)
- [2] H. A. Haus, "Theory of Mode Locking with a Slow Saturable Absorber," IEEE J. Quantum Electron. **11**, pp. 736 – 746 (1975).
- [3] H. A. Haus, "Theory of modelocking with a fast saturable absorber," J. Appl. Phys. **46**, pp. 3049 – 3058 (1975).
- [4] H. A. Haus, J. G. Fujimoto, E. P. Ippen, "Structures for additive pulse modelocking," J. Opt. Soc. of Am. **B 8**, pp. 2068 – 2076 (1991).
- [5] E. P. Ippen, "Principles of passive mode locking," Appl. Phys. **B 58**, pp. 159 – 170 (1994).
- [6] F. X. Kärtner and U. Keller, "Stabilization of soliton-like pulses with a slow saturable absorber," Opt. Lett. **20**, 16 – 19 (1995).
- [7] F.X. Kärtner, I.D. Jung, U. Keller: TITLE, "Soliton Modelocking with Saturable Absorbers," Special Issue on Ultrafast Electronics, Photonics and Optoelectronics, IEEE J. Sel. Top. Quantum Electron. **2**, 540-556 (1996)
- [8] I. D. Jung, F. X. Kärtner, L. R. Brovelli, M. Kamp, U. Keller, "Experimental verification of soliton modelocking using only a slow saturable absorber," Opt. Lett. **20**, pp. 1892 – 1894 (1995).
- [9] C. Spielmann, P.F. Curley, T. Brabec, F. Krausz: Ultrabroad-band femtosecond lasers, IEEE J. Quantum Electron. **30**, 1100-1114 (1994).

- [10] Y. Chen, F. X. Kärtner, U. Morgner, S. H. Cho, H. A. Haus, J. G. Fujimoto, and E. P. Ippen, "Dispersion managed mode-locking," *J. Opt. Soc. Am. B* **16**, 1999-2004, 1999.
- [11] K. Tamura, E.P. Ippen, H.A. Haus, L.E. Nelson: 77-fs pulse generation from a stretched-pulse mode-locked all-fiber ring laser, *Opt. Lett.* **18**, 1080-1082 (1993)
- [12] K. Tamura, E.P. Ippen, H.A. Haus: Pulse dynamics in stretched-pulse lasers, *Appl. Phys. Lett.* **67**, 158-160 (1995)
- [13] F.X. Kärtner, J. A. d. Au, U. Keller, "Mode-Locking with Slow and Fast Saturable Absorbers-What's the Difference,". *Sel. Top. Quantum Electron.* **4**, 159 (1998)
- [14] J.H.B. Nijhof, N.J. Doran, W. Forysiak, F.M. Knox: Stable soliton-like propagation in dispersion-managed system with net anomalous, zero, and normal dispersion, *Electron. Lett.* **33**, 1726-1727 (1997)
- [15] Y. Chen, H.A. Haus: Dispersion-managed solitons in the net positive dispersion regime, *J. Opt. Soc. Am. B* **16**, 24-30 (1999)
- [16] H.A. Haus, K. Tamura, L.E. Nelson, E.P. Ippen, "Stretched-pulse additive pulse modelocking in fiber ring lasers: theory and experiment," *IEEE J. Quantum Electron.* **31**, 591-598 (1995)
- [17] I. D. Jung, F. X. Kärtner, N. Matuschek, D. H. Sutter, F. Morier-Genoud, Z. Shi, V. Scheuer, M. Tilsch, T. Tschudi, U. Keller, "Semiconductor saturable absorber mirrors supporting sub-10 fs pulses," *Appl. Phys. B* **65**, pp. 137-150 (1997).

Chapter 7

Kerr-Lens and Additive Pulse Mode Locking

There are many ways to generate saturable absorber action. One can use real saturable absorbers, such as semiconductors or dyes and solid-state laser media. One can also exploit artificial saturable absorbers. The two most prominent artificial saturable absorber modelocking techniques are called Kerr-Lens Mode Locking (KLM) and Additive Pulse Mode Locking (APM). APM is sometimes also called Coupled-Cavity Mode Locking (CCM). KLM was invented in the early 90's [1][2][3][4][5][6][7], but was already predicted to occur much earlier [8][9][10].

7.1 Kerr-Lens Mode Locking (KLM)

The general principle behind Kerr-Lens Mode Locking is sketched in Fig. 7.1. A pulse that builds up in a laser cavity containing a gain medium and a Kerr medium experiences not only self-phase modulation but also self focussing, that is nonlinear lensing of the laser beam, due to the nonlinear refractive index of the Kerr medium. A spatio-temporal laser pulse propagating through the Kerr medium has a time dependent mode size as higher intensities acquire stronger focussing. If a hard aperture is placed at the right position in the cavity, it strips of the wings of the pulse, leading to a shortening of the pulse. Such combined mechanism has the same effect as a saturable absorber. If the electronic Kerr effect with response time of a few femtoseconds or less is used, a fast saturable absorber has been created. Instead of a sep-

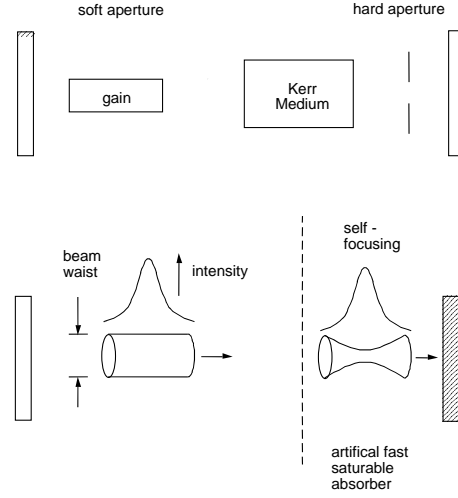


Figure 7.1: Principle mechanism of KLM. The hard aperture can be also replaced by the soft aperture due to the spatial variation of the gain in the laser crystal.

arate Kerr medium and a hard aperture, the gain medium can act both as a Kerr medium and as a soft aperture (i.e. increased gain instead of saturable absorption). The sensitivity of the laser mode size on additional nonlinear lensing is drastically enhanced if the cavity is operated close to the stability boundary of the cavity. Therefore, it is of prime importance to understand the stability ranges of laser resonators. Laser resonators are best understood in terms of paraxial optics [11][12][14][13][15].

7.1.1 Review of Paraxial Optics and Laser Resonator Design

The solutions to the paraxial wave equation, which keep their form during propagation, are the Hermite-Gaussian beams. Since we consider only the fundamental transverse modes, we are dealing with the Gaussian beam

$$U(r, z) = \frac{U_o}{q(z)} \exp \left[-jk \frac{r^2}{2q(z)} \right], \quad (7.1)$$

with the complex q-parameter $q = a + jb$ or its inverse

$$\frac{1}{q(z)} = \frac{1}{R(z)} - j \frac{\lambda}{\pi w^2(z)}. \quad (7.2)$$

The Gaussian beam intensity $I(z, r) = |U(r, z)|^2$ expressed in terms of the power P carried by the beam is given by

$$I(r, z) = \frac{2P}{\pi w^2(z)} \exp \left[-\frac{2r^2}{w^2(z)} \right]. \quad (7.3)$$

The use of the q-parameter simplifies the description of Gaussian beam propagation. In free space propagation from z_1 to z_2 , the variation of the beam parameter q is simply governed by

$$q_2 = q_1 + z_2 - z_1, \quad (7.4)$$

where q_2 and q_1 are the beam parameters at z_1 and z_2 . If the beam waist, at which the beam has a minimum spot size w_0 and a planar wavefront ($R = \infty$), is located at $z = 0$, the variations of the beam spot size and the radius of curvature are explicitly expressed as

$$w(z) = w_0 \left[1 + \left(\frac{\lambda z}{\pi w_0^2} \right)^2 \right]^{1/2}, \quad (7.5)$$

and

$$R(z) = z \left[1 + \left(\frac{\pi w_0^2}{\lambda z} \right)^2 \right]. \quad (7.6)$$

The angular divergence of the beam is inversely proportional to the beam waist. In the far field, the half angle divergence is given by,

$$\theta = \frac{\lambda}{\pi w_0}, \quad (7.7)$$

as illustrated in Figure 7.2.

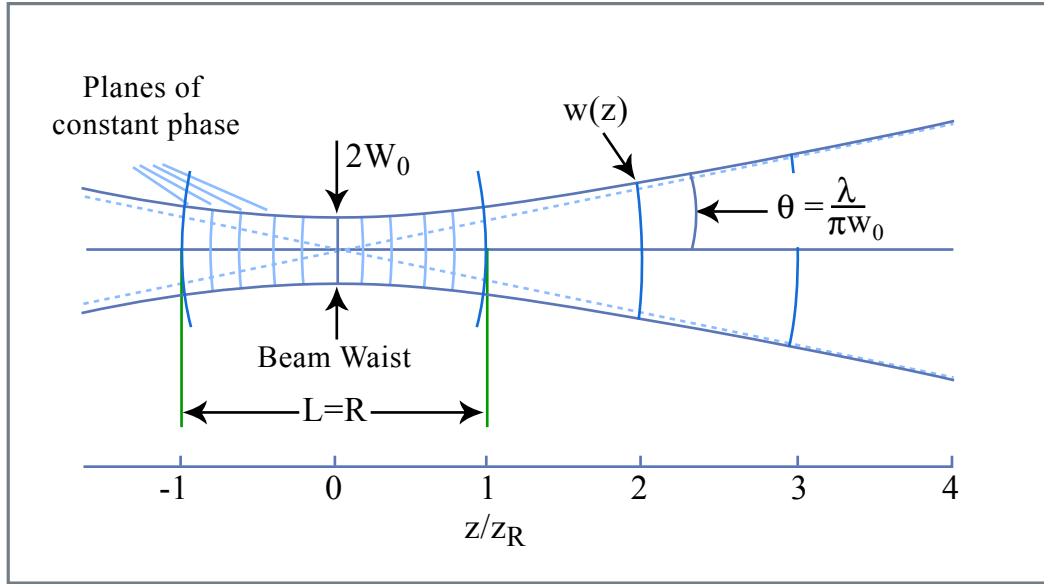


Figure 7.2: Gaussian beam and its characteristics.

Figure by MIT OCW.

Due to diffraction, the smaller the spot size at the beam waist, the larger the divergence. The Rayleigh range is defined as the distance from the waist over which the beam area doubles and can be expressed as

$$z_R = \frac{\pi w_0^2}{\lambda}. \quad (7.8)$$

The confocal parameter of the Gaussian beam is defined as twice the Rayleigh range

$$b = 2z_R = \frac{2\pi w_0^2}{\lambda}, \quad (7.9)$$

and corresponds to the length over which the beam is focused. The propagation of Hermite-Gaussian beams through paraxial optical systems can be efficiently evaluated using the ABCD-law [11]

$$q_2 = \frac{Aq_1 + B}{Cq_1 + D} \quad (7.10)$$

where q_1 and q_2 are the beam parameters at the input and the output planes of the optical system or component. The ABCD matrices of some optical elements are summarized in Table 7.1. If a Gaussian beam with a waist w_{01} is focused by a thin lens a distance z_1 away from the waist, there will be a

new focus at a distance

$$z_2 = f + \frac{(z_1 - f)f^2}{(z_1 - f)^2 + \left(\frac{\pi w_{01}^2}{\lambda}\right)^2}, \quad (7.11)$$

and a waist w_{02}

$$\frac{1}{w_{02}^2} = \frac{1}{w_{01}^2} \left(1 - \frac{z_1}{f}\right)^2 + \frac{1}{f^2} \left(\frac{\pi w_{01}}{\lambda}\right)^2 \quad (7.12)$$

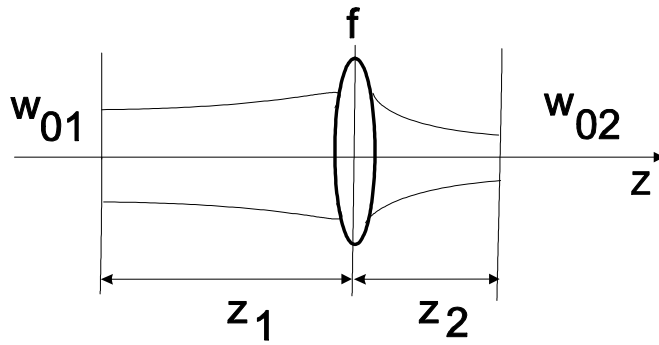


Figure 7.3: Focusing of a Gaussian beam by a lens.

7.1.2 Two-Mirror Resonators

We consider the two mirror resonator shown in Figure 7.4.

Optical Element	ABCD-Matrix
Free Space Distance L	$\begin{pmatrix} 1 & L \\ 0 & 1 \end{pmatrix}$
Thin Lens with focal length f	$\begin{pmatrix} 1 & 0 \\ -1/f & 1 \end{pmatrix}$
Mirror under Angle θ to Axis and Radius R Sagittal Plane	$\begin{pmatrix} 1 & 0 \\ \frac{-2 \cos \theta}{R} & 1 \end{pmatrix}$
Mirror under Angle θ to Axis and Radius R Tangential Plane	$\begin{pmatrix} 1 & 0 \\ \frac{-2}{R \cos \theta} & 1 \end{pmatrix}$
Brewster Plate under Angle θ to Axis and Thickness d , Sagittal Plane	$\begin{pmatrix} 1 & \frac{d}{n} \\ 0 & 1 \end{pmatrix}$
Brewster Plate under Angle θ to Axis and Thickness d , Tangential Plane	$\begin{pmatrix} 1 & \frac{d}{n^3} \\ 0 & 1 \end{pmatrix}$

Table 7.1: ABCD matrices for commonly used optical elements.

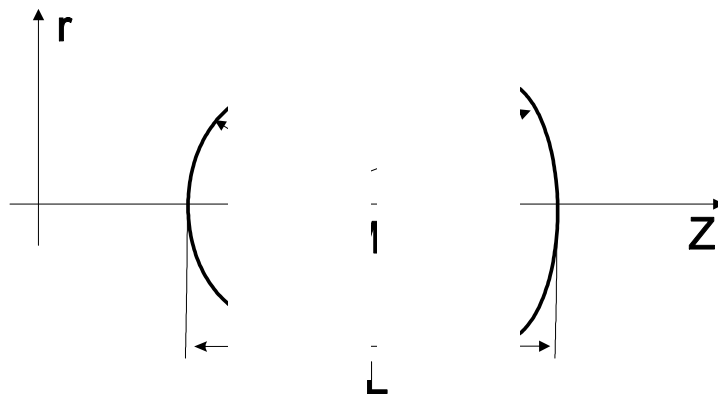


Figure 7.4: Two-Mirror Resonator with curved mirrors with radii of curvature R_1 and R_2 .

The resonator can be unfolded for an ABCD-matrix analysis, see Figure 7.5.

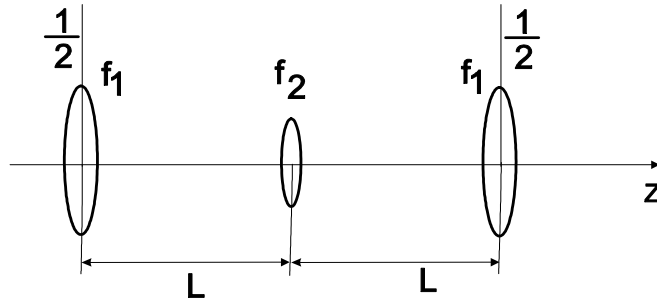


Figure 7.5: Two-mirror resonator unfolded. Note, only one half of the focusing strength of mirror 1 belongs to a fundamental period describing one resonator roundtrip.

The product of ABCD matrices describing one roundtrip according to Figure 7.5 are then given by

$$M = \begin{pmatrix} 1 & 0 \\ \frac{-1}{2f_1} & 1 \end{pmatrix} \begin{pmatrix} 1 & L \\ 0 & 1 \end{pmatrix} \begin{pmatrix} 1 & 0 \\ \frac{-1}{f_2} & 1 \end{pmatrix} \begin{pmatrix} 1 & L \\ 0 & 1 \end{pmatrix} \begin{pmatrix} 1 & 0 \\ \frac{-1}{2f_1} & 1 \end{pmatrix} \quad (7.13)$$

where $f_1 = R_1/2$, and $f_2 = R_2/2$. To carry out this product and to formulate the cavity stability criteria, it is convenient to use the cavity parameters $g_i = 1 - L/R_i$, $i = 1, 2$. The resulting cavity roundtrip ABCD-matrix can be written in the form

$$M = \begin{pmatrix} (2g_1g_2 - 1) & 2g_2L \\ 2g_1(g_1g_2 - 1)/L & (2g_1g_2 - 1) \end{pmatrix} = \begin{pmatrix} A & B \\ C & D \end{pmatrix}. \quad (7.14)$$

Resonator Stability

The ABCD matrices describe the dynamics of rays propagating inside the resonator. An optical ray is characterized by the vector $\mathbf{r} = \begin{pmatrix} r \\ r' \end{pmatrix}$, where r is the distance from the optical axis and r' the slope of the ray to the optical axis. The resonator is stable if no ray escapes after many round-trips, which is the case when the eigenvalues of the matrix M are less than one. Since we have a lossless resonator, i.e. $\det|M| = 1$, the product of the eigenvalues has to be 1 and, therefore, the stable resonator corresponds to the case of a complex conjugate pair of eigenvalues with a magnitude of 1. The eigenvalue

equation to M is given by

$$\det |M - \lambda \cdot 1| = \det \begin{pmatrix} (2g_1g_2 - 1) - \lambda & 2g_2L \\ 2g_1(g_1g_2 - 1)/L & (2g_1g_2 - 1) - \lambda \end{pmatrix} = 0, \quad (7.15)$$

$$\lambda^2 - 2(2g_1g_2 - 1)\lambda + 1 = 0. \quad (7.16)$$

The eigenvalues are

$$\lambda_{1/2} = (2g_1g_2 - 1) \pm \sqrt{(2g_1g_2 - 1)^2 - 1}, \quad (7.17)$$

$$= \begin{cases} \exp(\pm\theta), \cosh \theta = 2g_1g_2 - 1, & \text{for } |2g_1g_2 - 1| > 1 \\ \exp(\pm j\psi), \cos \psi = 2g_1g_2 - 1, & \text{for } |2g_1g_2 - 1| \leq 1 \end{cases}. \quad (7.18)$$

The case of a complex conjugate pair with a unit magnitude corresponds to a stable resonator. Therefore, the stability criterion for a stable two mirror resonator is

$$|2g_1g_2 - 1| \leq 1. \quad (7.19)$$

The stable and unstable parameter ranges are given by

$$\text{stable} : 0 \leq g_1 \cdot g_2 = S \leq 1 \quad (7.20)$$

$$\text{unstable} : g_1g_2 \leq 0; \text{ or } g_1g_2 \geq 1. \quad (7.21)$$

where $S = g_1 \cdot g_2$, is the stability parameter of the cavity. The stability criterion can be easily interpreted geometrically. Of importance are the distances between the mirror mid-points M_i and cavity end points, i.e. $g_i = (R_i - L)/R_i = -S_i/R_i$, as shown in Figure 7.6.

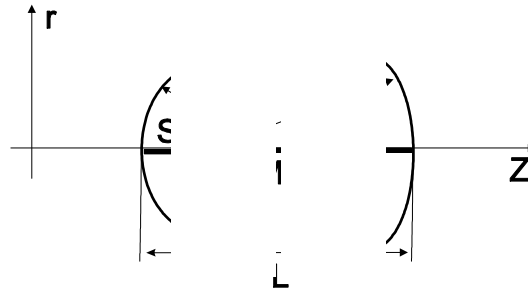


Figure 7.6: The stability criterion involves distances between the mirror mid-points M_i and cavity end points. i.e. $g_i = (R_i - L)/R_i = -S_i/R_i$.

The following rules for a stable resonator can be derived from Figure 7.6 using the stability criterion expressed in terms of the distances S_i . Note, that the distances and radii can be positive and negative

$$\text{stable : } 0 \leq \frac{S_1 S_2}{R_1 R_2} \leq 1. \quad (7.22)$$

The rules are:

- A resonator is stable, if the mirror radii, laid out along the optical axis, overlap.
- A resonator is unstable, if the radii do not overlap or one lies within the other.

Figure 7.7 shows stable and unstable resonator configurations.

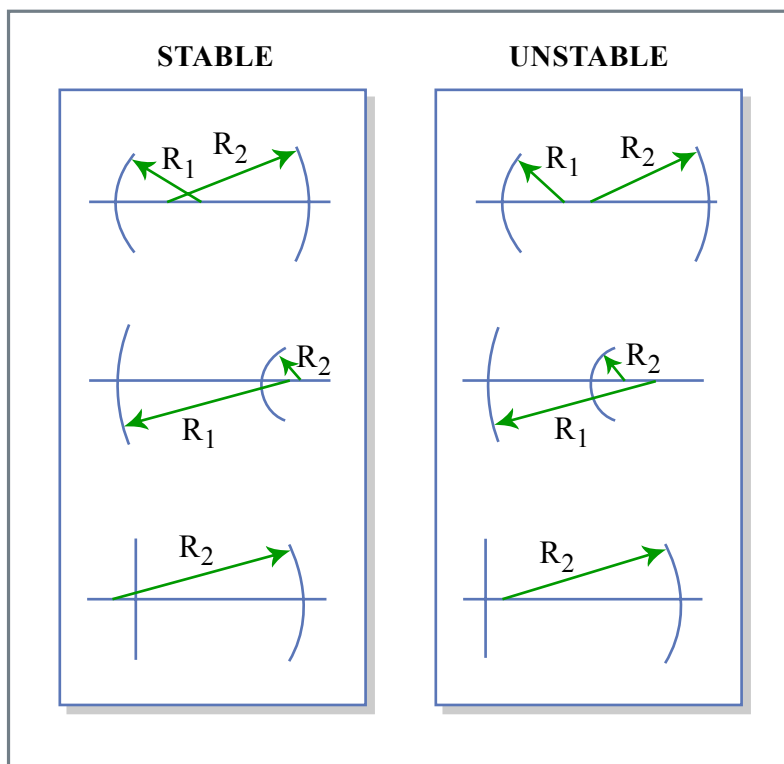


Figure 7.7: Illustration of stable and unstable resonator configurations.

Figure by MIT OCW.

For a two-mirror resonator with concave mirrors and $R_1 \leq R_2$, we obtain the general stability diagram as shown in Figure 7.8. There are two ranges for the mirror distance L , within which the cavity is stable, $0 \leq L \leq R_1$ and

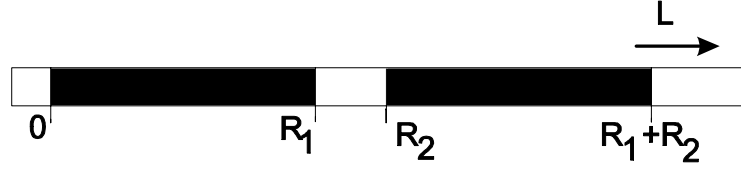


Figure 7.8: Stable regions (black) for the two-mirror resonator.

$R_2 \leq L \leq R_1 + R_2$. It is interesting to investigate the spot size at the mirrors and the minimum spot size in the cavity as a function of the mirror distance L .

Resonator Mode Characteristics

The stable modes of the resonator reproduce themselves after one round-trip, i.e. from Eq.(7.10) we find

$$q_1 = \frac{Aq_1 + B}{Cq_1 + D} \quad (7.23)$$

The inverse q-parameter, which is directly related to the phase front curvature and the spot size of the beam, is determined by

$$\left(\frac{1}{q}\right)^2 + \frac{A-D}{B} \left(\frac{1}{q}\right) + \frac{1-AD}{B^2} = 0. \quad (7.24)$$

The solution is

$$\left(\frac{1}{q}\right)_{1/2} = -\frac{A-D}{2B} \pm \frac{j}{2|B|} \sqrt{(A+D)^2 - 1} \quad (7.25)$$

If we apply this formula to (7.15), we find the spot size on mirror 1

$$\left(\frac{1}{q}\right)_{1/2} = -\frac{j}{2|B|} \sqrt{(A+D)^2 - 1} = -j \frac{\lambda}{\pi w_1^2}. \quad (7.26)$$

or

$$w_1^4 = \left(\frac{2\lambda L}{\pi}\right)^2 \frac{g_2}{g_1} \frac{1}{1 - g_1 g_2} \quad (7.27)$$

$$= \left(\frac{\lambda R_1}{\pi}\right)^2 \frac{R_2 - L}{R_1 - L} \left(\frac{L}{R_1 + R_2 - L}\right). \quad (7.28)$$

By symmetry, we find the spot size on mirror 3 via switching index 1 and 2:

$$w_2^4 = \left(\frac{2\lambda L}{\pi} \right)^2 \frac{g_1}{g_2} \frac{1}{1 - g_1 g_2} \quad (7.29)$$

$$= \left(\frac{\lambda R_2}{\pi} \right)^2 \frac{R_1 - L}{R_2 - L} \left(\frac{L}{R_1 + R_2 - L} \right). \quad (7.30)$$

The intracavity focus can be found by transforming the focused Gaussian beam with the propagation matrix

$$\begin{aligned} M &= \begin{pmatrix} 1 & z_1 \\ 0 & 1 \end{pmatrix} \begin{pmatrix} 1 & 0 \\ \frac{-1}{2f_1} & 1 \end{pmatrix} \\ &= \begin{pmatrix} 1 - \frac{z_1}{2f_1} & z_1 \\ \frac{-1}{2f_1} & 1 \end{pmatrix}, \end{aligned} \quad (7.31)$$

to its new focus by properly choosing z_1 , see Figure 7.9.

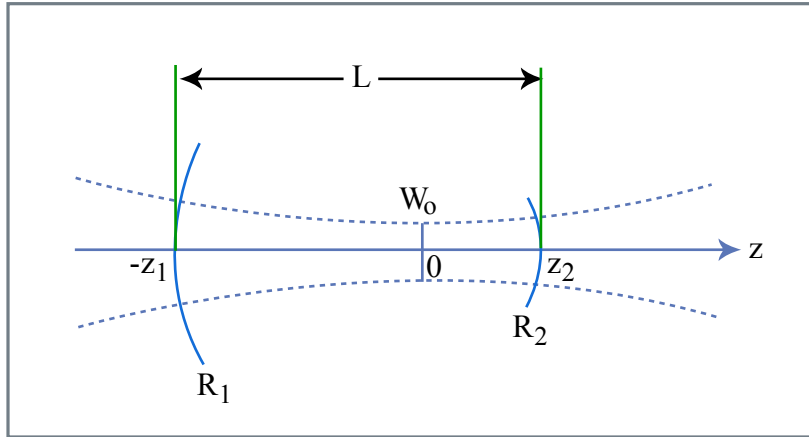


Figure 7.9: Two-mirror resonator

Figure by MIT OCW.

A short calculation results in

$$z_1 = L \frac{g_2 (g_1 - 1)}{2g_1 g_2 - g_1 - g_2} \quad (7.32)$$

$$= \frac{L(L - R_2)}{2L - R_1 - R_2}, \quad (7.33)$$

and, again, by symmetry

$$z_2 = L \frac{g_1 (g_2 - 1)}{2g_1 g_2 - g_1 - g_2} \quad (7.34)$$

$$= \frac{L(L - R_1)}{2L - R_1 - R_2} = L - z_1. \quad (7.35)$$

The spot size in the intracavity focus is

$$w_o^4 = \left(\frac{\lambda L}{\pi}\right)^2 \frac{g_1 g_2 (1 - g_1 g_2)}{(2g_1 g_2 - g_1 - g_2)^2} \quad (7.36)$$

$$= \left(\frac{\lambda}{\pi}\right)^2 \frac{L(R_1 - L)(R_2 - L)(R_1 + R_2 - L)}{(R_1 + R_2 - 2L)^2}. \quad (7.37)$$

All these quantities for the two-mirror resonator are shown in Figure 7.11. Note, that all resonators and the Gaussian beam are related to the confocal resonator as shown in Figure 7.10.

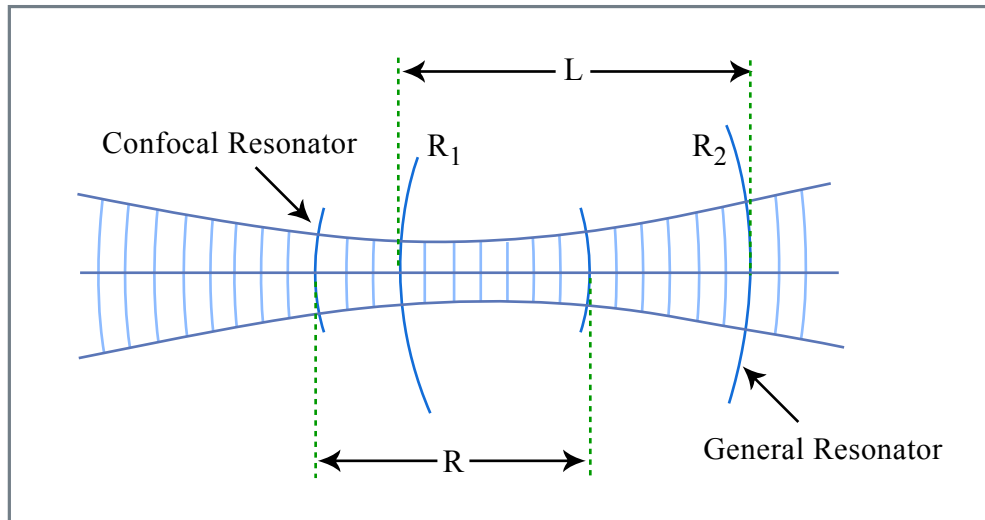


Figure 7.10: Two-mirror resonator and its relationship with the confocal resonator.

Figure by MIT OCW.

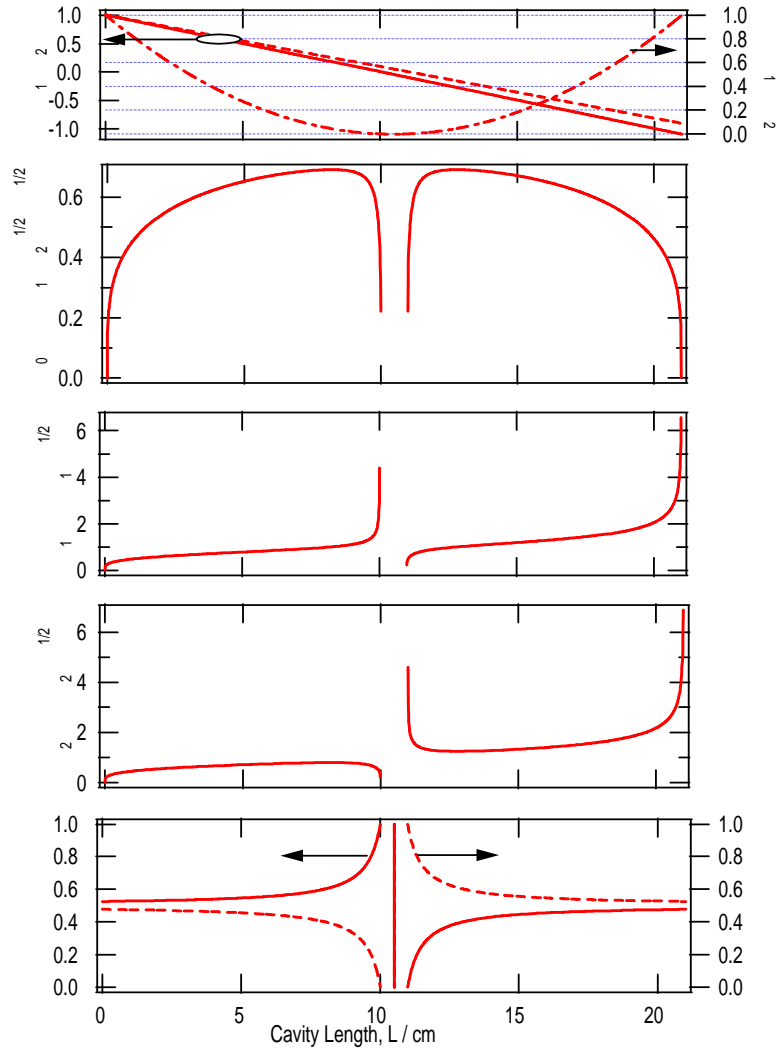


Figure 7.11: From top to bottom: Cavity parameters, g_1 , g_2 , S , w_0 , w_1 , w_2 , z_1 and z_2 for the two-mirror resonator with $R_1 = 10$ cm and $R_2 = 11$ cm.

7.1.3 Four-Mirror Resonators

More complex resonators, like the four-mirror resonator depicted in Figure 7.12 a) can be transformed to an equivalent two-mirror resonator as shown in Figure 7.4 b) and c)

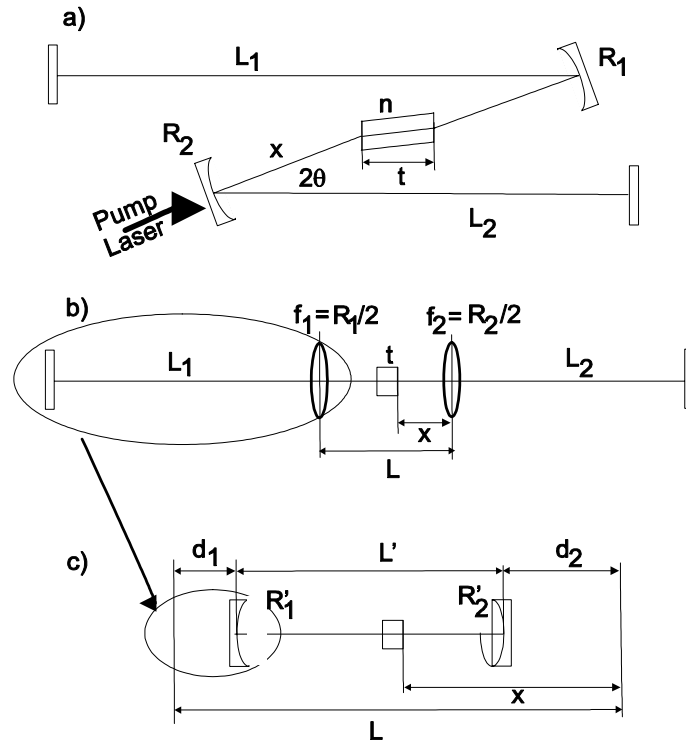


Figure 7.12: a) Four-mirror resonator with gain medium of refractive index n , and thickness t . Folding angles have to be adjusted for astigmatism compensation. b) Equivalent lens cavity. Note that the new focal lengths do not yet account for the different equivalent radii of curvature due to nonnormal incidence on the mirrors. c) Equivalent two-mirror cavity with imaged end mirrors.

Each of the resonator arms (end mirror, L_1 , R_1) or (end mirror, L_2 , R_2) is equivalent to a new mirror with a new radius of curvature $R'_{1/2}$ positioned a distance $d_{1/2}$ away from the old reference plane [12]. This follows simply from the fact that each symmetric optical system is equivalent to a lens positioned

at a distance d from the old reference plane

$$\begin{aligned} M &= \begin{pmatrix} A & B \\ C & A \end{pmatrix} = \begin{pmatrix} 1 & d \\ 0 & 1 \end{pmatrix} \begin{pmatrix} 1 & 0 \\ \frac{-1}{f} & 1 \end{pmatrix} \begin{pmatrix} 1 & d \\ 0 & 1 \end{pmatrix} \\ &= \begin{pmatrix} 1 - \frac{d}{f} & d\left(2 - \frac{d}{f}\right) \\ \frac{-1}{f} & 1 - \frac{d}{f} \end{pmatrix} \end{aligned} \quad (7.38)$$

with

$$\begin{aligned} d &= \frac{A-1}{C} \\ \frac{-1}{f} &= C \end{aligned} \quad (7.39)$$

The matrix of the resonator arm 1 is given by

$$M = \begin{pmatrix} 1 & 0 \\ \frac{-2}{R_1} & 1 \end{pmatrix} \begin{pmatrix} 1 & 2L_1 \\ 0 & 1 \end{pmatrix} \begin{pmatrix} 1 & 0 \\ \frac{-2}{R_1} & 1 \end{pmatrix} = \begin{pmatrix} 1 - \frac{4L_1}{R_1} & 2L_1 \\ \frac{-4}{R_1} \left(1 - \frac{2L_1}{R_1}\right) & 1 - \frac{4L_1}{R_1} \end{pmatrix} \quad (7.40)$$

from which we obtain

$$d_1 = -\frac{R_1}{2} \frac{1}{1 - R_1/(2L_1)}, \quad (7.41)$$

$$R'_1 = -\left(\frac{R_1}{2}\right)^2 \frac{1}{L_1 [1 - R_1/(2L_1)]}. \quad (7.42)$$

For arm lengths $L_{1/2}$ much larger than the radius of curvature, the new radius of curvature is roughly by a factor of $\frac{R_1}{4L_1}$ smaller. Typical values are $R_1 = 10$ cm and $L_1 = 50$ cm. Then the new radius of curvature is $R'_1 = 5$ mm. The analogous equations apply to the other resonator arm

$$d_2 = -\frac{R_2}{2} \frac{1}{1 - R_2/(2L_2)}, \quad (7.43)$$

$$R'_2 = -\left(\frac{R_2}{2}\right)^2 \frac{1}{L_2 [1 - R_2/(2L_2)]}. \quad (7.44)$$

Note that the new mirror radii are negative for $R_i/L_i < 1$. The new distance L' between the equivalent mirrors is then also negative over the region where the resonator is stable, see Fig.7.8. We obtain

$$L' = L + d_1 + d_2 = L - \frac{R_1 + R_2}{2} - \delta \quad (7.45)$$

$$\delta = \frac{R_1}{2} \left[\frac{1}{1 - R_1/(2L_1)} - 1 \right] + \frac{R_2}{2} \left[\frac{1}{1 - R_2/(2L_2)} - 1 \right] \quad (7.46)$$

$$= -(R'_1 + R'_2) \quad (7.47)$$

or

$$L = \frac{R_1 + R_2}{2} - (R'_1 + R'_2) + L' \quad (7.48)$$

From the discussion in section 7.1.2, we see that the stability ranges cover at most a distance δ . Figure 7.13 shows the resonator characteristics as a function of the cavity length L for the following parameters $R_1 = R_2 = 10$ cm and $L_1 = 100$ cm and $L_2 = 75$ cm, which lead to

$$\begin{aligned} d_1 &= -5.26 \text{ cm} \\ R'_1 &= -0.26 \text{ cm} \end{aligned} \quad (7.49)$$

$$\begin{aligned} d_2 &= -5.36 \text{ cm} \\ R'_2 &= -0.36 \text{ cm} \end{aligned} \quad (7.50)$$

$$L' = L - 10.62 \text{ cm} \quad (7.51)$$

Note, that the formulas (7.27) to (7.37) can be used with all quantities replaced by the corresponding primed quantities in Eq.(7.49) - (7.51). The result is shown in Fig. 7.13. The transformation from L to L' transforms the stability ranges according to Fig. 7.14. The confocal parameter of the laser mode is approximately equal to the stability range.

Astigmatism Compensation

So far, we have considered the curved mirrors under normal incidence. In a real cavity this is not the case and one has to analyze the cavity performance for the tangential and sagittal beam separately. The gain medium, usually a thin plate with a refractive index n and a thickness t , generates astigmatism. Astigmatism means that the beam foci for sagittal and tangential plane are not at the same position. Also, the stability regions of the cavity are different for the different planes and the output beam is elliptical. This is so, because a beam entering a plate under an angle refracts differently in both planes, as described by different ABCD matrices for tangential and sagittal plane, see Table 7.1. Fortunately, one can balance the astigmatism of the beam due to

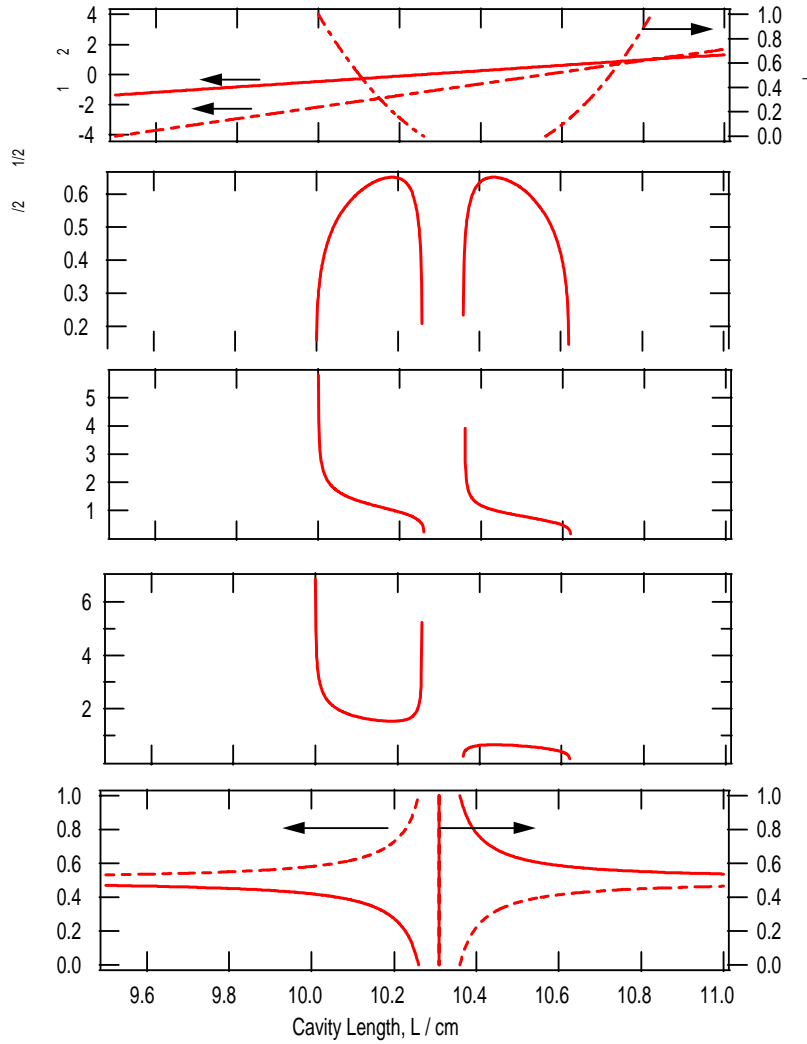


Figure 7.13: From top to bottom: Cavity parameters, g_1 , g_2 , S , w_0 , w_1 , w_2 , z_1 and z_2 for the four-mirror resonator with $R_1 = R_2 = 10$ cm, $L_1 = 100$ cm and $L_2 = 75$ cm.



Figure 7.14: Transformed stability range for the four mirror resonator with $R = (R_1 + R_2)/2$.

the plate by the astigmatism introduced by the curved mirrors at a specific incidence angle θ on the mirrors [12]. The focal length of the curved mirrors under an angle are given by

$$\begin{aligned} f_s &= f / \cos \theta \\ f_t &= f \cdot \cos \theta \end{aligned} \quad (7.52)$$

The propagation distance in a plate with thickness t under Brewster's angle is given by $t\sqrt{n^2 + 1}/n$. Thus, the equivalent traversing distances in the sagittal and the tangential planes are (Table 7.1),

$$\begin{aligned} d_s &= t\sqrt{n^2 + 1}/n^2 \\ d_f &= t\sqrt{n^2 + 1}/n^4 \end{aligned} \quad (7.53)$$

The different distances have to compensate for the different focal lengths in the sagittal and tangential planes. Assuming two identical mirrors $R = R_1 = R_2$, leads to the condition

$$d_s - 2f_s = d_t - 2f_t. \quad (7.54)$$

With $f = R/2$ we find

$$R \sin \theta \tan \theta = Nt, \quad \text{where } N = \sqrt{n^2 + 1} \frac{n^2 - 1}{n^4} \quad (7.55)$$

Note, that t is the thickness of the plate as opposed to the path length of the beam in the plate. The equation gives a quadratic equation for $\cos \theta$

$$\cos^2 \theta + \frac{Nt}{R} \cos \theta - 1 = 0 \quad (7.56)$$

$$\cos \theta_{1/2} = -\frac{Nt}{2R} \pm \sqrt{1 + \left(\frac{Nt}{2R}\right)^2} \quad (7.57)$$

Since the angle is positive, the only solution is

$$\theta = \arccos \left[\sqrt{1 + \left(\frac{Nt}{2R}\right)^2} - \frac{Nt}{2R} \right]. \quad (7.58)$$

This concludes the design and analysis of the linear resonator.

7.1.4 The Kerr Lensing Effects

At high intensities, the refractive index in the gain medium becomes intensity dependent

$$n = n_0 + n_2 I. \quad (7.59)$$

The Gaussian intensity profile of the beam creates an intensity dependent index profile

$$I(r) = \frac{2P}{\pi w^2} \exp \left[-2\left(\frac{r}{w}\right)^2 \right]. \quad (7.60)$$

In the center of the beam the index can be approximated by a parabola

$$n(r) = n'_0 \left(1 - \frac{1}{2} \gamma^2 r^2 \right), \text{ where} \quad (7.61)$$

$$n'_0 = n_0 + n_2 \frac{2P}{\pi w^2}, \quad \gamma = \frac{1}{w^2} \sqrt{\frac{8n_2 P}{n'_0 \pi}}. \quad (7.62)$$

A thin slice of a parabolic index medium is equivalent to a thin lens. If the parabolic index medium has a thickness t , then the ABCD matrix describing the ray propagation through the medium at normal incidence is [16]

$$M_K = \begin{pmatrix} \cos \gamma t & \frac{1}{n'_0 \gamma} \sin \gamma t \\ -n'_0 \gamma \sin \gamma t & \cos \gamma t \end{pmatrix}. \quad (7.63)$$

Note that, for small t , we recover the thin lens formula ($t \rightarrow 0$, but $n'_0 \gamma^2 t = 1/f = \text{const.}$). If the Kerr medium is placed under Brewster's angle, we again have to differentiate between the sagittal and tangential planes. For the

sagittal plane, the beam size entering the medium remains the same, but for the tangential plane, it opens up by a factor n'_0

$$\begin{aligned} w_s &= w \\ w_t &= w \cdot n'_0 \end{aligned} \quad (7.64)$$

The spotsizes proportional to w^2 has to be replaced by $w^2 = w_s w_t$. Therefore, under Brewster angle incidence, the two planes start to interact during propagation as the gamma parameters are coupled together by

$$\gamma_s = \frac{1}{w_s w_t} \sqrt{\frac{8n_2 P}{n'_0 \pi}} \quad (7.65)$$

$$\gamma_t = \frac{1}{w_s w_t} \sqrt{\frac{8n_2 P}{n'_0 \pi}} \quad (7.66)$$

Without proof (see [12]), we obtain the matrices listed in Table 7.2. For low

Optical Element	ABCD-Matrix
Kerr Medium Normal Incidence	$M_K = \begin{pmatrix} \cos \gamma t & \frac{1}{n'_0 \gamma} \sin \gamma t \\ -n'_0 \gamma \sin \gamma t & \cos \gamma t \end{pmatrix}$
Kerr Medium Sagittal Plane	$M_{Ks} = \begin{pmatrix} \cos \gamma_s t & \frac{1}{n'_0 \gamma_s} \sin \gamma_s t \\ -n'_0 \gamma_s \sin \gamma_s t & \cos \gamma_s t \end{pmatrix}$
Kerr Medium Tangential Plane	$M_{Kt} = \begin{pmatrix} \cos \gamma_t t & \frac{1}{n'_0 \gamma_t} \sin \gamma_t t \\ -n'_0 \gamma_t \sin \gamma_t t & \cos \gamma_t t \end{pmatrix}$

Table 7.2: ABCD matrices for Kerr media, modelled with a parabolic index profile $n(r) = n'_0 \left(1 - \frac{1}{2} \gamma^2 r^2\right)$.

peak power P , the Kerr lensing effect can be neglected and the matrices in Table 7.2 converge towards those for linear propagation. When the laser is mode-locked, the peak power P rises by many orders of magnitude, roughly the ratio of cavity round-trip time to the final pulse width, assuming a constant pulse energy. For a 100 MHz, 10 fs laser, this is a factor of 10^6 . With the help of the matrix formulation of the Kerr effect, one can iteratively find the steady state beam waists in the laser. Starting with the values for the linear cavity, one can obtain a new resonator mode, which gives improved

values for the beam waists by calculating a new cavity round-trip propagation matrix based on a given peak power P . This scheme can be iterated until there is only a negligible change from iteration to iteration. Using such a simulation, one can find the change in beam waist at a certain position in the resonator between cw-operation and mode-locked operation, which can be expressed in terms of the delta parameter

$$\delta_{s,t} = \frac{1}{p} \frac{w_{s,t}(P, z) - w_{s,t}(P = 0, z)}{w_{s,t}(P = 0, z)} \quad (7.67)$$

where p is the ratio between the peak power and the critical power for self-focusing

$$p = P/P_{crit}, \text{ with } P_{crit} = \lambda_L^2 / (2\pi n_2 n_0^2). \quad (7.68)$$

To gain insight into the sensitivity of a certain cavity configuration for KLM, it is interesting to compute the normalized beam size variations $\delta_{s,t}$ as a function of the most critical cavity parameters. For the four-mirror cavity, the natural parameters to choose are the distance between the crystal and the pump mirror position, x , and the mirror distance L , see Figure 7.12. Figure 7.15 shows such a plot for the following cavity parameters $R_1 = R_2 = 10$ cm, $L_1 = 104$ cm, $L_2 = 86$ cm, $t = 2$ mm, $n = 1.76$ and $P = 200$ kW.

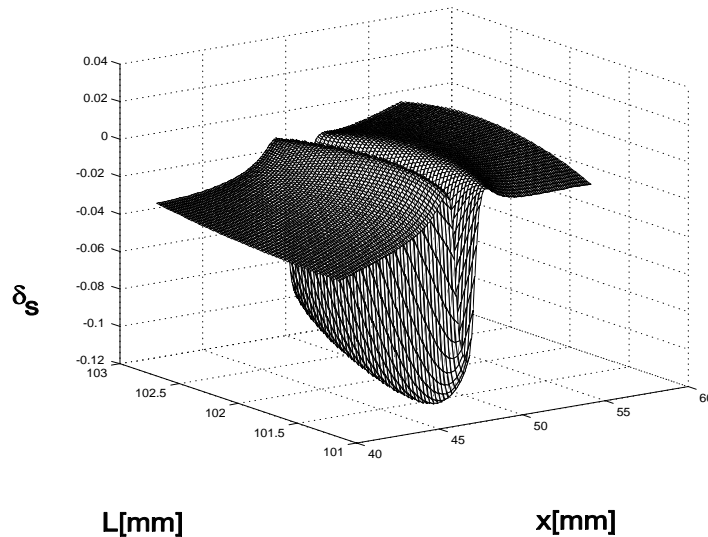


Figure 7.15: Beam narrowing ratio δ_s , for cavity parameters $R_1 = R_2 = 10$ cm, $L_1 = 104$ cm, $L_2 = 86$ cm, $t = 2$ mm, $n = 1.76$ and $P = 200$ kW

Courtesy of Onur Kuzucu. Used with permission.

The Kerr lensing effect can be exploited in different ways to achieve mode locking.

Soft-Aperture KLM

In the case of soft-aperture KLM, the cavity is tuned in such a way that the Kerr lensing effect leads to a shrinkage of the laser mode when mode-locked. The non-saturated gain in a laser depends on the overlap of the pump mode and the laser mode. From the rate equations for the radial photon distribution $N(r)$ and the inversion $N_P(r)$ of a laser, which are proportional to the intensities of the pump beam and the laser beam, we obtain a gain, that is proportional to the product of $N(r)$ and $N_P(r)$. If we assume that the focus of the laser mode and the pump mode are at the same position and neglect the variation of both beams as a function of distance, we obtain

$$\begin{aligned} g &\sim \int_0^\infty N(r) * N_P(r) r dr \\ &\sim \int_0^\infty \frac{2P_P}{\pi w_P^2} \exp\left[-\frac{2r^2}{w_P^2}\right] \frac{2}{\pi w_L^2} \exp\left[-\frac{2r^2}{w_L^2}\right] r dr \end{aligned}$$

With the beam cross sections of the pump and the laser beam in the gain medium, $A_P = \pi w_P^2$ and $A_L = \pi w_L^2$, we obtain

$$g \sim \frac{1}{A_P + A_L}.$$

If the pump beam is much stronger focused in the gain medium than the laser beam, a shrinkage of the laser mode cross section in the gain medium leads to an increased gain. When the laser operates in steady state, the change in saturated gain would have to be used for the investigation. However, the general argument carries through even for this case. Figure 7.16 shows the variation of the laser mode size in and close to the crystal in a soft-aperture KLM laser due to self-focusing.

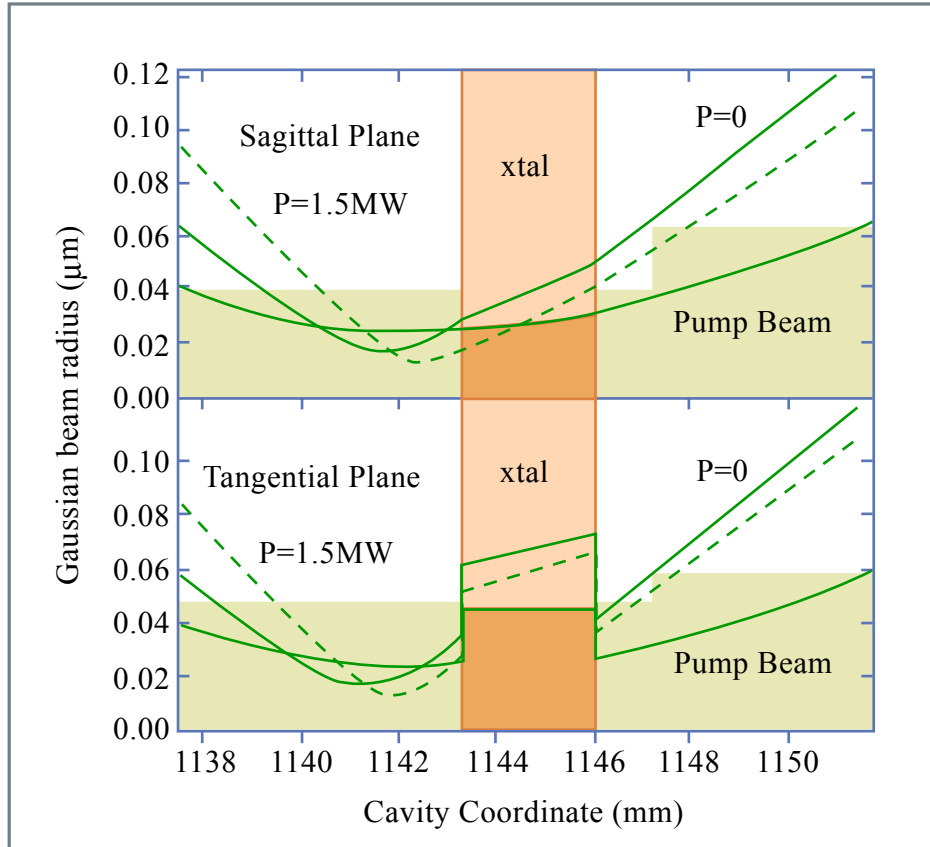


Figure 7.16: Variation of laser mode size in and close to the crystal in a soft aperture KLM laser due to self-focussing.

Figure by MIT OCW.

Hard-Aperture KLM

In a hard-aperture KLM-Laser, one of the resonator arms contains (usually close to the end mirrors) an aperture such that it cuts the beam slightly. When Kerr lensing occurs and leads to a shrinkage of the beam at this position, the losses of the beam are reduced. Note, that depending on whether the aperture is positioned in the long or short arm of the resonator, the operating point of the cavity at which Kerr lensing favours or opposes mode-locking may be quite different (see Figure 7.13).

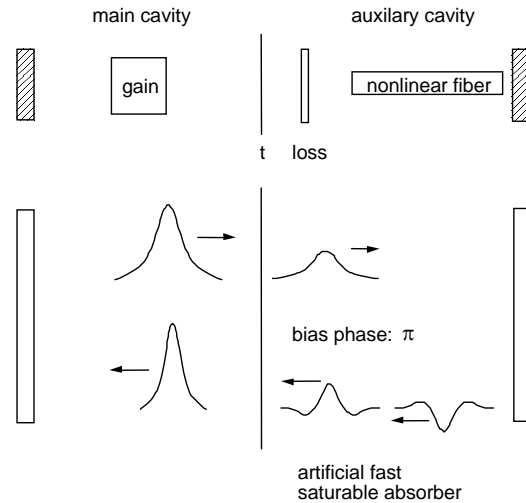


Figure 7.17: Principle mechanism of APM.

7.2 Additive Pulse Mode Locking

Like Kerr-Lens Mode Locking also Additive Pulse Mode Locking (APM) is an artificial saturable absorber effect [17][18][19][20][21][22]. Figure 7.17 shows the general principle at work. A small fraction of the light emitted from the main laser cavity is injected externally into a nonlinear fiber. In the fiber strong SPM occurs and introduces a significant phase shift between the peak and the wings of the pulse. In the case shown the phase shift is π

A part of the modified and heavily distorted pulse is reinjected into the cavity in an interferometrically stable way, such that the injected pulse interferes constructively with the next cavity pulse in the center and destructively in the wings. This superposition leads to a shorter intracavity pulse and the pulse shaping generated by this process is identical to the one obtained from a fast saturable absorber. Again, an artificial saturable absorber action is generated.

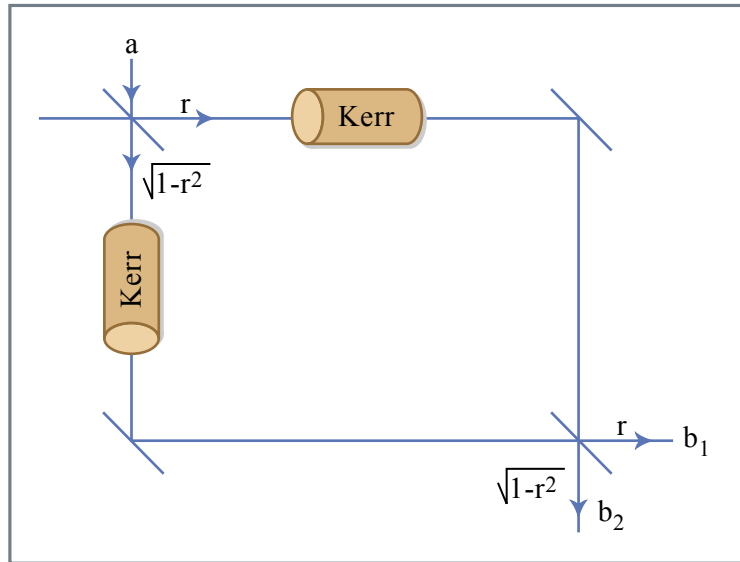


Figure 7.18: Schematic of nonlinear Mach-Zehnder interferometer.

Figure by MIT OCW.

Figure 7.18 shows a simple nonlinear interferometer. In practice, such an interferometer can be realized in a self-stabilized way by the use of both polarizations in an isotropic Kerr medium with polarizer and analyzer as shown in Figure 7.19.

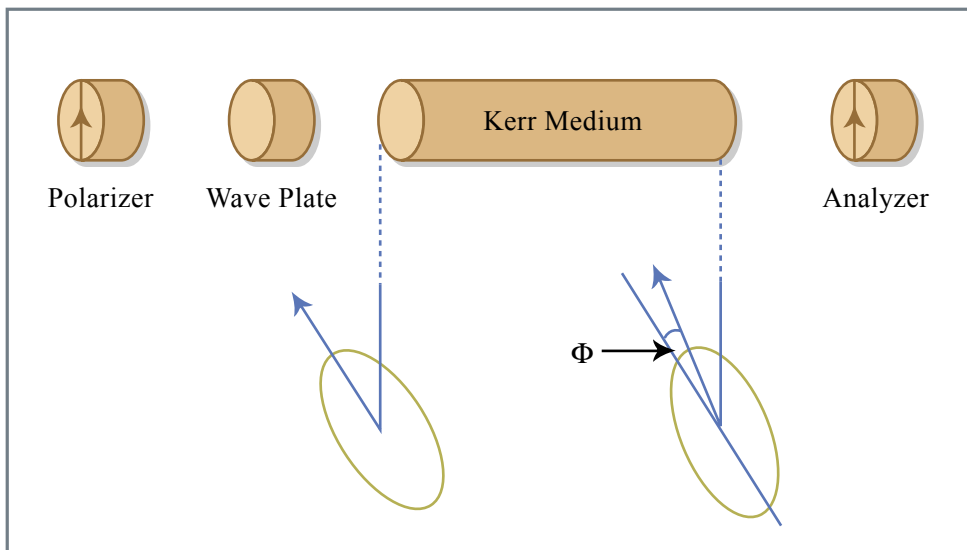


Figure 7.19: Nonlinear Mach-Zehnder interferometer using nonlinear polarization rotation in a fiber [25].

Figure by MIT OCW.

The Kerr effect rotates the polarization ellipse and thus transforms phase modulation into amplitude modulation. The operation is in one-to-one correspondence with that of the nonlinear Mach-Zehnder interferometer of Fig.

7.18. The system of Figure 7.18 can be analyzed rather simply and thus it is worthwhile to look at the derivation and the implicit assumptions. The couplers are described by the scattering matrices

$$S = \begin{bmatrix} r & \sqrt{1-r^2} \\ \sqrt{1-r^2} & -r \end{bmatrix}. \quad (7.69)$$

The outputs of the interferometer are then

$$b_1 = [r^2 e^{-j\phi_1} + (1-r^2)e^{-j\phi_2}] a, \quad (7.70)$$

$$b_2 = 2r\sqrt{1-r^2} \exp\left[-j\frac{\phi_1 + \phi_2}{2}\right] \sin\left[\frac{\phi_2 - \phi_1}{2}\right] a, \quad (7.71)$$

ϕ_1 and ϕ_2 are the phase shifts in the two arms composed of both linear "bias" contributions ϕ_{bi} and the Kerr phase shifts ϕ_{Ki}

$$\phi_i = \phi_{bi} + \phi_{Ki}, \quad (i = 1, 2), \quad (7.72)$$

$$\phi_{Ki} = \kappa_i |a|^2, \quad (i = 1, 2). \quad (7.73)$$

The power in output port two is related to the linear and nonlinear losses

$$\begin{aligned} |b_2|^2 &= 2r^2 (1-r^2) (1 - \cos[\phi_2 - \phi_1]) |a|^2 \\ &= 2r^2 (1-r^2) \{(1 - \cos[\phi_{b2} - \phi_{b1}]) + \\ &\quad + \sin[\phi_{b2} - \phi_{b1}] (\phi_{K2} - \phi_{K1})\} |a|^2 \end{aligned} \quad (7.74)$$

Depending on the bias phase $\phi_b = \phi_{b2} - \phi_{b1}$, the amplitude loss is

$$l = r^2 (1-r^2) (1 - \cos \phi_b) |a|^2, \quad (7.75)$$

and the γ -parameter of the equivalent fast saturable absorber is

$$\gamma = (\kappa_1 - \kappa_2) r^2 (1-r^2) \sin \phi_b. \quad (7.76)$$

If the interferometer forms part of a resonant system, the frequency of the system is affected by the phase shift of the interferometer and in turn affects the phase.

When the resonant frequencies of the linear system ($\gamma = \delta = 0$) without the interferometer should remain the resonant frequencies with the interferometer, the net phase shift of the interferometer has to be chosen to be zero. Since a small loss has been assumed and hence $r^2 \gg 1-r^2$

$$\text{Im} [r^2 e^{-j\phi_{b1}} + (1-r^2) e^{-j\phi_{b2}}] = \text{Im} [r^2(1-j\phi_{b1}) + (1-r^2) e^{-j\phi_{b2}}] = 0 \quad (7.77)$$

or

$$\phi_{b1} = \frac{-(1-r^2)}{r^2} \sin \phi_{b2}. \quad (7.78)$$

and $\cos \phi_{b1} = 1$. With this adjustment, the response of the interferometer becomes

$$\begin{aligned} b_1 \approx & a + \Delta a = a - (1-r^2)(1-\cos \phi) a \\ & -(1-r^2)(\phi_{K2} - \phi_{K1}) \sin \phi a \\ & -jr^2\phi_{K1} - j(1-r^2)\phi_{K2} \cos \phi a, \end{aligned} \quad (7.79)$$

where we have set $\phi = \phi_{b2}$. This gives for the parameters of the master equation l , γ and δ

$$l = (1-r^2)(1-\cos \phi), \quad (7.80)$$

$$\gamma = (\kappa_1 - \kappa_2)(1-r^2) \sin \phi, \quad (7.81)$$

$$\delta = \kappa_1 r^2 + \kappa_2(1-r^2) \cos \phi. \quad (7.82)$$

Due to the special choice of the bias phase there is no contribution of the nonlinear interferometer to the linear phase. This agrees with expressions (7.75) and (7.76). The Kerr coefficients are

$$\kappa_1 = r^2 \left(\frac{2\pi}{\lambda} \right) \frac{n_2}{A_{eff}} L_{Kerr}, \quad (7.83)$$

$$\kappa_2 = (1-r^2) \left(\frac{2\pi}{\lambda} \right) \frac{n_2}{A_{eff}} L_{Kerr}. \quad (7.84)$$

Here, λ is the free space wavelength of the optical field, A_{eff} is the effective area of the mode, n_2 the intensity dependent refractive index, and L_{Kerr} is the length of the Kerr medium. Figure 7.20 is the saturable absorber coefficient γ normalized to the loss and Kerr effect (note that γ goes to zero when the loss goes to zero) as a function of r^2 .

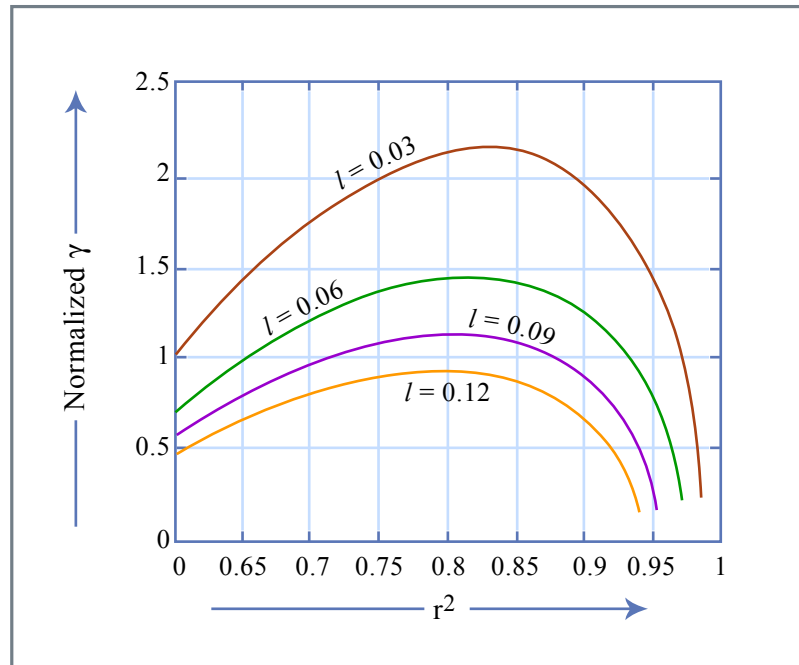


Figure 7.20: Normalized saturable absorber coefficient $\gamma / \left[\left(\frac{2\pi}{\lambda} \right) \frac{n_2}{A_{eff}} L_{Kerr} l \right]$ as a function of r^2 with loss l as parameter [25].

Figure by MIT OCW.

Large saturable absorber coefficients can be achieved at moderate loss values.

Bibliography

- [1] D. E. Spence, P. N. Kean, W. Sibbett, "60-fsec pulse generation from a self-mode-locked Ti:Sapphire laser", *Opt. Lett.* **16**, pp. 42 – 44 (1991)
- [2] U. Keller, G. W 'tHooft, W. H. Knox, J. E. Cunningham, "Femtosecond Pulses from a Continuously Self-Starting Passively Mode-Locked Ti:Sapphire Laser," *Opt. Lett.* **16**, pp.1022 – 1024 (1991).
- [3] D. K. Negus, L. Spinelli, N. Goldblatt, G. Feugnet, "Sub-100 femtosecond pulse generation by Kerr lens modelocking in Ti:Sapphire," in *Advanced Solid-State Lasers*, G. Dube, L. Chase, Eds. (Optical Society of America, Washington, D.C., 1991), **10**, pp.120 – 124.
- [4] F. Salin, J. Squier and M. Piche, "Mode locking of Ti:Al₂O₃ lasers and self-focusing: a Gaussian approximation," *Opt. Lett.* **16**, pp. 1674 – 1676 (1991).
- [5] M. Piche, F. Salin, "Self-mode locking of solid-state lasers without apertures", *Opt. Lett.* **18**, pp. 1041 – 1043 (1993).
- [6] G. Cerullo, S. De Silvestri, V. Magni, L. Pallaro, "Resonators for Kerr-lens mode-locked femtosecond Ti:sapphire lasers", *Opt. Lett.* **19**, pp. 807 – 809 (1994).
- [7] G. Cerullo, S. De Silvestri, V. Magni, "Self-starting Kerr Lens Mode-Locking of a Ti:Sapphire Laser", *Opt. Lett.* **19**, pp. 1040 – 1042 (1994).
- [8] L. Dahlström, "Passive modelocking and Q-switching of high power lasers by means of the optical Kerr effect," *Opt. Comm.* **5**, pp. 157 – 162 (1972).

- [9] E. G. Lariontsev and V. N. Serkin, "Possibility of using self-focusing for increasing contrast and narrowing of ultrashort light pulses," *Sov. J. Quant. Electron.* **5**, pp. 769 – 800 (1975).
- [10] K. Sala, M. C. Richardson, N. R. Isenor, "Passive modelocking of Lasers with the optical Kerr effect modulator," *IEEE J. Quant. Electron.* **QE-13**, pp. 915 – 924 (1977).
- [11] H. Kogelnik and T. Li, "Laser Beams and Resonators," *Appl. Opt.* **5**, pp. 1550 – 1566 (1966).
- [12] H. Kogelnik, E. P. Ippen, A. Dienes and C. V. Shank, "Astigmatically Compensated Cavities for CW Dye Lasers," *IEEE J. Quantum Electron.* **QE-8**, pp. 373 – 379 (1972).
- [13] O. Svelto, "Principles of Lasers," 3rd Edition, Plenum Press, New York and London, (1989).
- [14] H. A. Haus, "Fields and Waves in Optoelectronics", Prentice Hall 1984.
- [15] F. K. Kneubühl and M. W. Sigrist, "Laser," 3rd Edition, Teubner Verlag, Stuttgart (1991).
- [16] A. E. Siegman, "Lasers," University Science Books, Mill Valley, California (1986).
- [17] K. J. Blow and D. Wood, "Modelocked lasers with nonlinear external cavities," *J. Opt. Soc. Am. B* **5**, pp. 629 – 632 (1988).
- [18] K. J. Blow and B. P. Nelson, "Improved mode locking of an F-center laser with a nonlinear nonsoliton external cavity," *Opt. Lett.* **13**, pp. 1026 – 1028 (1988).
- [19] P. N. Kean, X. Zhu, D. W. Crust, R. S. Grant, N. Langford and W. Sibbett, "Enhanced mode locking of color-center lasers," *Opt. Lett.* **14**, pp. 39 – 41 (1989).
- [20] J. Mark, L. Y. Liu, K. L. Hall, H. A. Haus and E. P. Ippen, "Femtosecond pulse generation in a laser with a nonlinear external resonator," *Opt. Lett.* **14**, pp. 48 – 50 (1989).

- [21] E. P. Ippen, H. A. Haus and L. Y. Liu, "Additive pulse mode locking," *J. Opt. Soc. Am. B* **6**, pp. 1736 – 1745 (1989).
- [22] J. Goodberlet, J. Jacobson and J. G. Fujimoto, P. A. Schultz and T. Y. Fan, "Self-starting additive-pulse mode-locked diode-pumped Nd:YAG laser", *Opt. Lett.* **15**, pp. 504 –506 (1990).
- [23] F. X. Kärtner, L. R. Brovelli, D. Kopf, M. Kamp, I. Calasso and U. Keller: "Control of Solid-State Laser Dynamics by Semiconductor Devices, *Optical Engineering*, **34**, pp. 2024 – 2036, (1995).
- [24] K. Tamura, "Additive-pulse limiting", *Opt. Lett.* **19**, pp. 31 – 33 (1994).
- [25] H. A. Haus, J. G. Fujimoto and E. P. Ippen, "Analytic Theory of Additive Pulse and Kerr Lens Mode Locking," *IEEE J. Quantum Electron.* **28**, pp. 2086 – 2095 (1992).
- [26] H. A. Haus, J. G. Fujimoto and E. P. Ippen, "Structures of Additive Pulse Mode Locking," *J. Opt. Soc. Am.* **8**, pp. 2068 – 2076 (1991).

Chapter 8

Semiconductor Saturable Absorbers

Sofar we only considered artificial saturable absorbers, but there is of course the possibility to use real absorbers for modelocking. A prominent candidate for a saturable absorber is semiconductor material, which was pioneered by Islam, Knox and Keller [1][2][3]. The great advantage of using semiconductor materials is that the wavelength range over which these absorbers operate can be chosen by material composition and bandstructure engineering, if semiconductor heterostructures are used (see Figure 8.1). Even though, the basic physics of carrier dynamics in these structures is to a large extent well understood [4], the actual development of semiconductor saturable absorbers for mode locking is still very much ongoing.

Image removed due to copyright restrictions.

Please see:

Keller, U., Ultrafast Laser Physics, Institute of Quantum Electronics, Swiss Federal Institute of Technology, ETH Hönggerberg—HPT, CH-8093 Zurich, Switzerland. Used with permission.

Figure 8.1: Energy Gap, corresponding wavelength and lattice constant for various compound semiconductors. The dashed lines indicate indirect transitions.

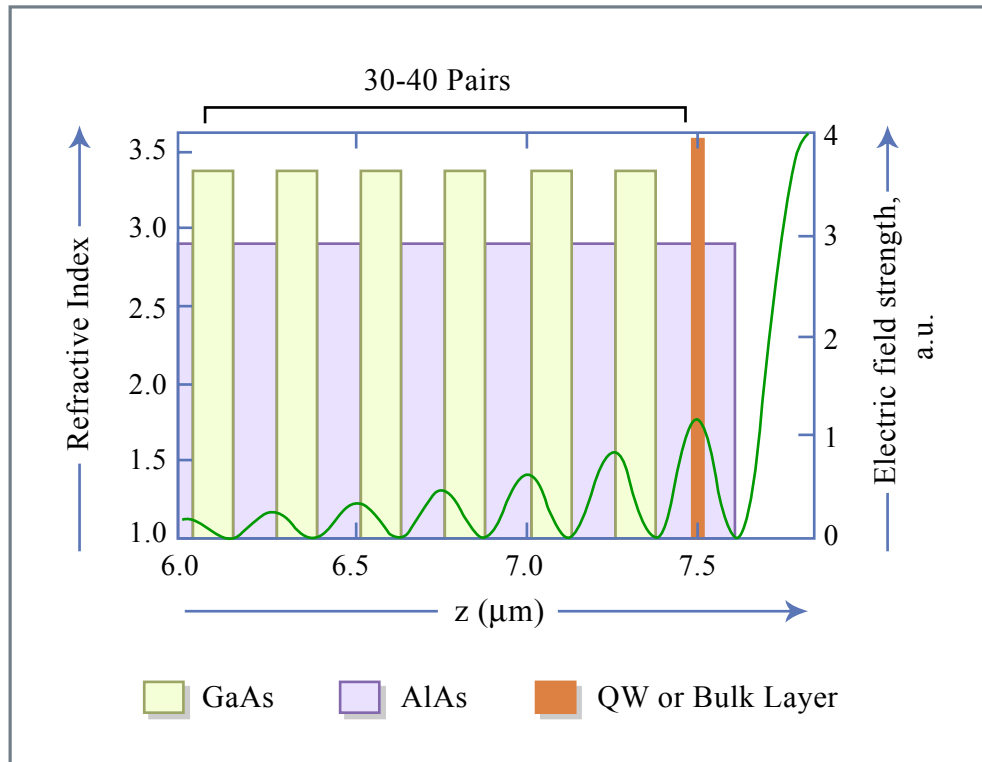


Figure 8.2: Typical semiconductor saturable absorber structure. A semiconductor heterostructure (here AlAs/GaAs) is grown on a GaAs-Wafer (20-40 pairs). The layer thicknesses are chosen to be quarter wave at the center wavelength at which the laser operates. This structure acts as a quarter-wave Bragg mirror. On top of the Bragg mirror a half-wave thick layer of the low index material (here AlAs) is grown, which has a field maximum in its center. At the field maximum either a bulk layer of GaAlAs or a single- or multiple Quantum Well (MQW) structure is embedded, which acts as a saturable absorber for the operating wavelength of the laser.

Figure by MIT OCW.

A typical semiconductor saturable absorber structure is shown in Figure 8.2. A semiconductor heterostructure (here AlAs/GaAs) is grown on a GaAs-Wafer (20-40 pairs). The layer thicknesses are chosen to be quarter wave at the center wavelength at which the laser operates. These structures act as quarter-wave Bragg mirror. On top of the Bragg mirror, a half-wave thick layer of the low index material (here AlAs) is grown, which has a field-maximum in its center. At the field maximum, either a bulk layer of a compound semiconductor or a single-or multiple Quantum Well (MQW) structure is embedded, which acts as a saturable absorber for the operating wavelength of the laser. The absorber mirror serves as one of the endmirrors in the laser (see Figure 8.3).

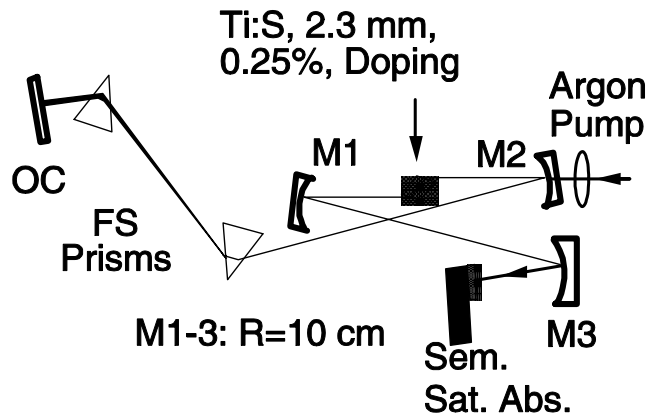


Figure 8.3: The semiconductor saturable absorber, mounted on a heat sink, is used as one of the cavity end mirrors. A curved mirror determines the spot-size of the laser beam on the saturable absorber and, therefore, scales the energy fluence on the absorber at a given intracavity energy.

8.1 Carrier Dynamics and Saturation Properties

There is a rich ultrafast carrier dynamics in these materials, which can be favorably exploited for saturable absorber design. The carrier dynamics in bulk semiconductors occurs on three major time scales (see Figure 8.4 [5]). When electron-hole pairs are generated, this excitation can be considered

as an equivalent two-level system if the interaction between the carriers is neglected, which is a very rough assumption.

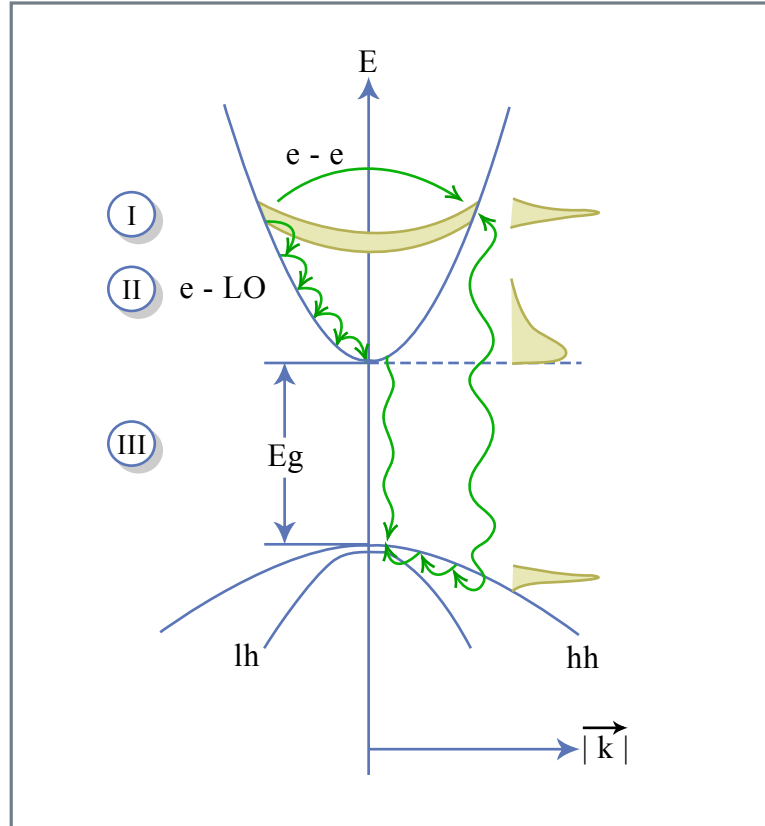


Figure 8.4: Carrier dynamics in a bulk semiconductor material. Three time scales can be distinguished. I. Coherent carrier dynamics, which at room temperature may last between 10-50 fs depending on excitation density. II. Thermalization between the carriers due to carrier-carrier scattering and cooling to the lattice temperature by LO-Phonon emission. III. Carrier-trapping or recombination [5].

Figure by MIT OCW.

There is a coherent regime (I) with a duration of 10-50 fs depending on conditions and material. Then in phase (II), carrier-carrier scattering sets in and leads to destruction of coherence and thermalization of the electron and hole gas at a high temperature due to the excitation of the carriers high in the conduction or valence band. This usually happens on a 60 - 100 fs time scale. On a 300fs - 1ps time scale, the hot carrier gas interacts with the lattice mainly by emitting LO-phonons (37 meV in GaAs). The carrier gas cools down to lattice temperature. After the thermalization and cooling processes, the carriers are at the bottom of the conduction and valence band,

respectively. The carriers vanish (III) either by getting trapped in impurity states, which can happen on a 100 fs - 100 ps time scale, or recombine over recombination centers or by radiation on a nanosecond time-scale. Carrier-lifetimes in III-VI semiconductors can reach several tens of nanoseconds and in indirect semiconductors like silicon or germanium lifetimes can be in the millisecond range. The carrier lifetime can be engineered over a large range of values from 100 fs - 30ns, depending on the growth conditions and purity of the material. Special low-temperature growth that leads to the formation or trapping and recombination centers as well as ion-bombardment can result in very short lifetimes [9]. Figure 8.5 shows a typical pump probe response of a semiconductor saturable absorber when excited with a 100 fs long pulse. The typical bi-temporal behavior stems from the fast thermalization (spectral hole-burning)[7] and carrier cooling and the slow trapping and recombination processes.

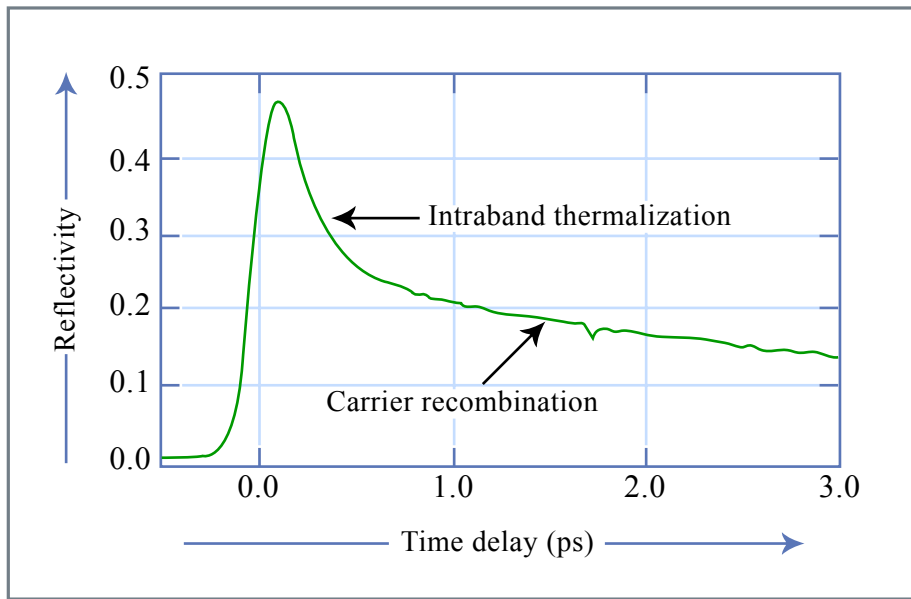


Figure 8.5: Pump probe response of a semiconductor saturable absorber mirror with a multiple-quantum well InGaAs saturable absorber grown at low temperature [3].

Figure by MIT OCW.

With the formula for the saturation intensity of a two-level system Eq. (2.145), we can estimate a typical value for the saturation fluence F_s (saturation energy density) of a semiconductor absorber for interband transitions. The saturation fluence F_A , also related to the absorption cross-section σ_A , is

then given by

$$F_A = \frac{hf}{\sigma_A} = I_A \tau_A = \frac{\hbar^2}{2T_2 Z_F |\vec{M}|^2} \quad (8.1)$$

$$= \frac{\hbar^2 n_0}{2T_2 Z_{F0} |\vec{M}|^2} \quad (8.2)$$

The value for the dipole moment for interband transitions in III-V semiconductors is about $d = 0.5$ nm with little variation for the different materials. Together with the a dephasing time on the order of $T_2 = 20$ fs and a linear refractive index $n_0 = 3$, we obtain

$$F_A = \frac{\hbar^2 n_0}{2T_2 Z_{F0} |\vec{M}|^2} = 35 \frac{\mu J}{cm^2} \quad (8.3)$$

Figure 8.6 shows the saturation fluence measurement and pump probe trace with 10 fs excitation pulses at 800 nm on a broadband GaAs semiconductor saturable absorber based on a metal mirror shown in Figure 8.7 [11]. The pump probe trace shows a 50 fs thermalization time and long time bleaching of the absorption recovering on a 50 ps time scale due to trapping and recombination.

Image removed due to copyright restrictions.

Please see:

Jung, I. D., et al. "Semiconductor saturable absorber mirrors supporting sub-10 fs pulses." *Applied Physics B* 65 (1997): 137-150.

Figure 8.6: Saturation fluence and pump probe measurements with 10 fs pulses on a broadband metal mirror based GaAs saturable absorber. The dots are measured values and the solid line is the fit to a two-level saturation characteristic [11].

A typical value for the fluence at which damage is observed on an absorber is on the order of a few mJ/cm^2 . Saturating an absorber by a factor of 10 without damaging it is still possible. The damage threshold is strongly dependent on the growth, design, fabrication and mounting (heat sinking) of the absorber.

Image removed due to copyright restrictions.

Please see:

Fluck, R., et al. "Broadband saturable absorber for 10 fs pulse generation." *Optics Letters* 21 (1996): 743-745.

Figure 8.7: GaAs saturable absorber grown on a GaAs wafer and transferred onto a metal mirror by post growth processing [10].

8.2 High Fluence Effects

To avoid Q-switched mode-locking caused by a semiconductor saturable absorber, the absorber very often is operated far above the saturation fluence or enters this regime during Q-switched operation. Therefore it is also important to understand the nonlinear optical processes occurring at high excitation levels [13]. Figure 8.8 shows differential pump probe measurements on a semiconductor saturable absorber mirror similar to Figure 8.2 but adapted to the $1.55 \mu\text{m}$ range for the development of pulsed laser sources for optical

communication. The structure is a GaAs/AlAs-Bragg-mirror with an InP half-wave layer and an embedded InGaAsP quantum well absorber with a band edge at $1.530 \mu\text{m}$. The mirror is matched to air with an Al_2O_3 single-layer Ar-coating. At low fluence ($5.6 \mu\text{J}$) the bleaching dynamics of the QWs are dominant. At higher fluences, two-photon absorption (TPA) and free carrier absorption (FCA) in the InP half-wave layer develop and eventually dominate [13].

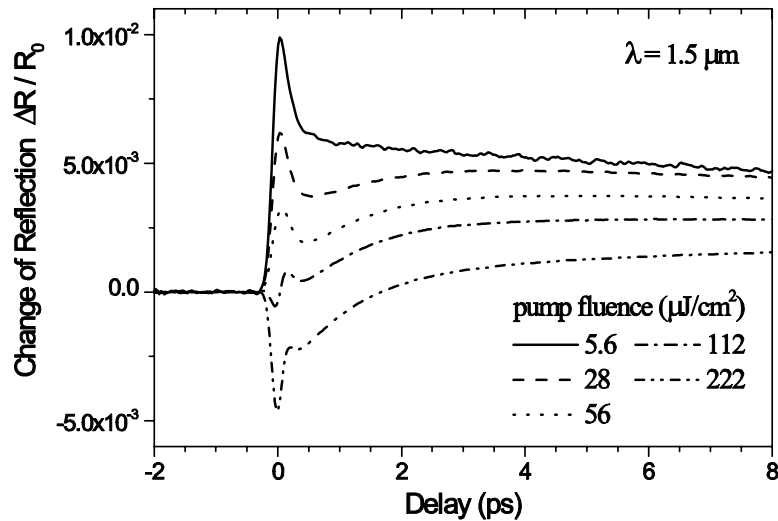


Figure 8.8: Differential reflectivity measurements of a semiconductor saturable absorber mirror (GaAs/AlAs-Bragg-mirror and InP half-wave layer with embedded InGaAsP quantum well absorber for the $1.55 \mu\text{m}$ range. The mirror is matched to air with an Al_2O_3 single-layer ar-coating). At low fluence the bleaching dynamics of the QWs are dominant. At higher fluences, TPA and FCA develop and eventually dominate [13].

Langlois, P. et al. "High fluence ultrafast dynamics of semiconductor saturable absorber mirrors." *Applied Physics Letters* 75 (1999): 3841-3483. Used with permission.

The assumption that TPA and FCA are responsible for this behaviour has been verified experimentally. Figure 8.9 shows differential reflectivity measurements under high fluence excitation at $1.56 \mu\text{m}$ for a saturable absorber mirror structure in which absorption bleaching is negligible (solid curve). The quantum well was placed close to a null of the field. A strong TPA peak is followed by induced FCA with a single $\sim 5\text{ps}$ decay for FCA. Both of these dynamics do not significantly depend on the wavelength of the excitation, as long as the excitation remains below the band gap. The $\sim 5\text{ps}$ decay is

attributed to carrier diffusion across the InP half-wave layer [13]. The dashed curve shows the differential absorption of a $\sim 350 \mu\text{m}$ thick InP substrate in which a standing-wave pattern is not formed and the $\sim 5\text{ps}$ decay is absent. The inset in Figure 8.9 shows the power dependence of TPA and FCA. As expected, TPA and FCA vary linearly and quadratically, respectively, with pump power. The pump-induced absorption of the probe (TPA) is linearly dependent on the pump power. Since FCA is produced by carriers that are generated by the pump alone via TPA, FCA scales with the square of the pump power.

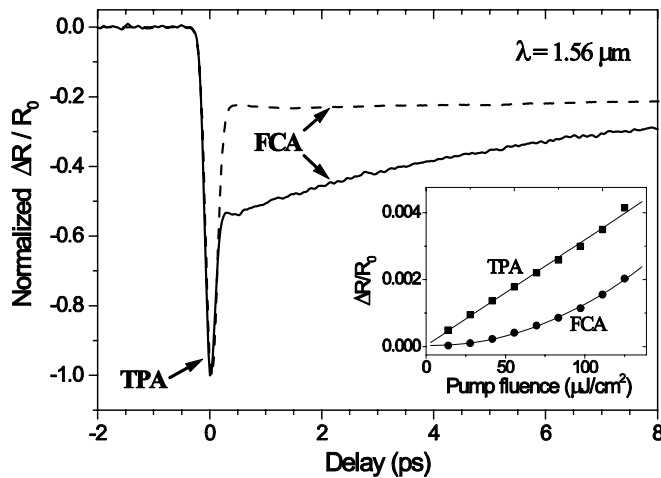


Figure 8.9: Differential reflectivity measurements under high fluence excitation at $1.56 \mu\text{m}$ for a saturable absorber mirror structure in which absorption bleaching is negligible (solid curve). The $\sim 5\text{ps}$ decay for FCA is attributed to carrier diffusion across the InP half-wave layer. The dashed curve shows the differential absorption of a $\sim 350 \mu\text{m}$ thick InP substrate in which a standing-wave pattern is not formed. (Inset) Linear and quadratic fluence dependence of the TPA and FCA components, respectively.

Langlois, P. et al. "High fluence ultrafast dynamics of semiconductor saturable absorber mirrors." *Applied Physics Letters* 75 (1999): 3841-3483. Used with permission.

These high fluence effects lead to strong modifications of the saturation characteristics of a saturable absorber. The importance of the high fluence effects was first recognized in resonant absorbers (see Figure 8.10). The field inside the absorber is enhanced by adding a top reflector and a proper spacer layer. This leads to an effective lower saturation fluence when viewed with

respect to the intracavity fluence or intensity. Therefore, high fluence effects are already reached at low intracavity intensities (see Figure 8.9).

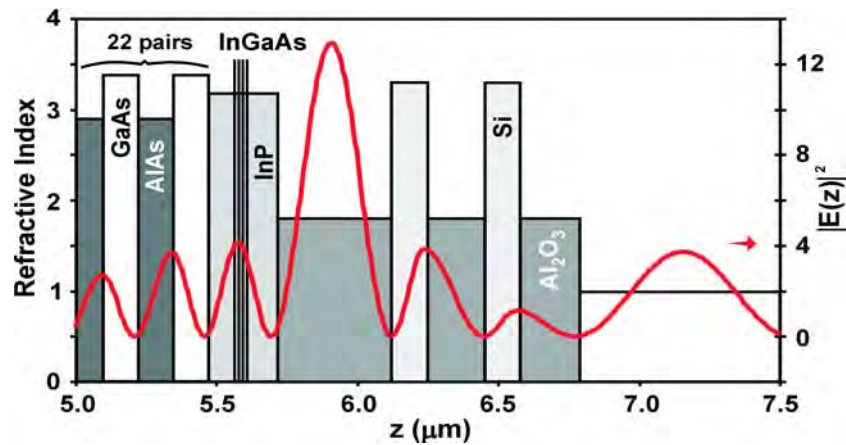


Figure 8.10: A top reflector is added to the semiconductor saturable absorber such that the field in the quantum well is resonantly enhanced by about a factor of 10 in comparison to the non resonant case.

Theon, E. R., et al. "Two-photon absorption in semiconductor saturable absorber mirrors." *Applied Physics Letters* 74 (1999): 3927-3929. Used with permission.

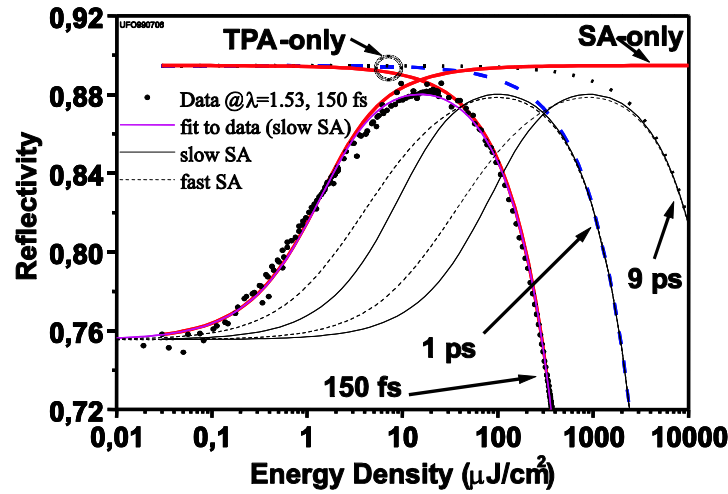


Figure 8.11: Saturation fluence measurement (dots) of the resonant absorber shown in Figure 8.10 with 150 fs pulses at $1.53 \mu\text{m}$. Fits are shown using a fast or slow saturable absorber and TPA. Also the scaled saturation characteristics of the absorber are shown when used in a laser with longer pulse durations.

Theon, E. R., et al. "Two-photon absorption in semiconductor saturable absorber mirrors." *Applied Physics Letters* 74 (1999): 3927-3929. Used with permission.

The roll-over of the saturation characteristics has positive and negative consequences for mode locking. First, if the roll-over can be reached with the available intracavity pulse energy, Q-switching can be suppressed. Second if the roll-over occurs too early, the pulses break up into multiple pulses to optimize the net gain for the overall pulse stream.

8.3 Break-up into Multiple Pulses

In the treatment of mode locking with fast and slow saturable absorbers we only concentrated on stability against energy fluctuations (Q-switched mode locking) and against break through of cw-radiation or continuum. Another often observed instability is the break-up into multiple pulses. The existence of such a mechanism is obvious if soliton pulse shaping processes are present. If we assume that the pulse is completely shaped by the solitonlike pulse shaping processes, the FWHM pulse width is given by

$$\tau_{FWHM} = 1.76 \frac{4|D_2|}{\delta W}. \quad (8.4)$$

where W denotes the pulse energy. D_2 the negative dispersion and δ the self-phase modulation coefficient. With increasing pulse energy, of course the absorber becomes more strongly saturated, which leads to shorter pulses according to the saturable absorber and the soliton formula. At a certain point, the absorber will saturate and can not provide any further pulse stabilization. However, the Kerr nonlinearity may not yet saturate and, therefore, the soliton formula dictates an ever decreasing pulse width for increasing pulse energy. Such a process continues, until either the continuum breaks through, because the soliton loss becomes larger than the continuum loss, or the pulse breaks up into two pulses. The pulses will have reduced energy per pulse and each one will be longer and experiences a reduced loss due to the finite gain bandwidth. Due to the reduced pulse energy, each of the pulses will suffer increased losses in the absorber, since it is not any longer as strongly saturated as before. However, once the absorber is already over saturated by the single pulse solution, it will also be strongly saturated for the double-pulse solution. The filter loss due to the finite gain bandwidth is heavily reduced for the double-pulse solution. As a result, the pulse will break up into double-pulses. To find the transition point where the break-up into multiple pulses occurs, we write down the round-trip loss due to the gain and filter losses and the saturable absorber according to 6.35

$$l_m = \frac{D_f}{3\tau_m^2} + q_s(W_m), \quad (8.5)$$

where, $q_s(W_m)$ is the saturation loss experienced by the pulse when it propagates through the saturable absorber. This saturation loss is given by

$$q_s(W) = \frac{1}{W} \int_{-\infty}^{+\infty} q(T, t) |A_s(t)|^2 dt. \quad (8.6)$$

This expression can be easily evaluated for the case of a sech-shaped steady state pulse in the fast saturable absorber model with

$$q_{fast}(t) = \frac{q_0}{1 + \frac{|A(t)|^2}{P_A}}, \quad \text{where } P_A = \frac{E_A}{\tau_A}. \quad (8.7)$$

and the slow saturable absorber model, where the relaxation term can be neglected because of $\tau_A \gg \tau$.

$$q_{slow}(t) = q_0 \exp \left[-\frac{1}{E_A} \int_{-\infty}^t |A_s(t')|^2 dt' \right]. \quad (8.8)$$

For the slow absorber 8.8 the absorber losses (8.6) can be evaluated independent of pulse shape to be

$$q_{s,slow}(W) = q_0 \frac{1 - \exp\left[-\frac{W}{E_A}\right]}{\frac{W}{E_A}}. \quad (8.9)$$

Thus for a slow absorber the losses depend only on pulse energy. In contrast, for a fast absorber, the pulse shape must be taken into account and, for a sech-shaped pulse, one obtains [14]

$$q_{s,fast}(W) = q_0 \sqrt{\frac{1}{\alpha(1+\alpha)}} \tanh^{-1} \left[\sqrt{\frac{\alpha}{1+\alpha}} \right], \quad \text{with } \alpha = \frac{W}{2P_A\tau}, \quad (8.10)$$

and the pulse energy of one pulse of the multiple pulse solution. The energy is determined from the total gain loss balance

$$\frac{g_0}{1 + \frac{mW_m}{P_L T_R}} = l + l_m. \quad (8.11)$$

Most often, the saturable absorber losses are much smaller than the losses due to the output coupler. In that case the total losses are fixed independent of the absorber saturation and the filter losses. Then the average power does not depend on the number of pulses in the cavity. If this is the case, one pulse of the double pulse solution has about half of the energy of the single pulse solution, and, therefore, the width of the double pulse is twice as large as that of the single pulse according to (8.4). Then the filter and absorber losses for the single and double pulse solution are given by

$$l_1 = \frac{D_f}{3\tau_1^2} + q_s(W_1), \quad (8.12)$$

$$l_2 = \frac{D_f}{12\tau_1^2} + q_s\left(\frac{W_1}{2}\right). \quad (8.13)$$

The single pulse solution is stable against break-up into double pulses as long as

$$l_1 \leq l_2 \quad (8.14)$$

is fulfilled. This is the case, if the difference in the filter losses between the single and double pulse solution is smaller than the difference in the saturable absorber losses

$$\frac{D_f}{4\tau_1^2} < \Delta q_s(W) = q_s\left(\frac{W}{2}\right) - q_s(W). \quad (8.15)$$

Figure 8.12 shows the difference in the saturable absorption for a single pulse and a double pulse solution as a function of the ratio between the single pulse peak power and saturation power for a fast absorber and as a function of the ratio between the single pulse energy and saturation energy for a slow absorber. Thus, for both cases the optimum saturation ratio, at which the largest discrimination between single and double pulses occurs and, therefore, the shortest pulse before break-up into multiple pulses occurs, is about 3. Note, that to arrive at this absolute number, we assumed that the amount of saturable absorption is negligible in comparison with the other intracavity losses, so that the saturated gain level and the gain and filter dispersion are fixed.

Image removed due to copyright restrictions.

Please see:

Kartner, F. X., J. A. d. Au, and U. Keller. "Mode-Locking with Slow and Fast Saturable Absorbers--What's the Difference." *Selected Topics in Quantum Electronics 4* (1998): 159.

Figure 8.12: Difference in loss experienced by a sech-shaped pulse in a slow (- -) and a fast (____) saturable absorber for a given pulse energy or peak power, respectively.

At this optimum operation point, the discrimination against multiple break-up of a fast absorber is about 50% larger than the value of the slow absorber. Since the minimum pulsewidth scales with the square root of $\Delta q_s(W)$, see Eq. (8.15), the minimum pulsewidth of the slow absorber is only about 22% longer than with an equally strong fast saturable absorber. Figure 8.12 also predicts that a laser modelocked by a fast saturable absorber is much more stable against multiple pulse break-up than a slow saturable absorber if it is oversaturated. This is due to the fact that a fast saturable absorber saturates with the peak power of the pulse in comparison with a slow saturable absorber, which saturates with the pulse energy. When the pulse breaks up into a pulse twice as long with half energy in each, the peak power of the

individual pulses changes by a factor of four. Therefore, the discrimination between long and short pulses is larger in the case of a fast saturable absorber, especially for strong saturation. Note that Fig. 8.12 is based on the simple saturation formulas for fast and slow saturable absorbers Eqs. (8.9) and (8.10). We compare these predictions with numerical simulations and experimental observations made with a Nd:glass laser [15][16].

The Nd:glass laser described in ref. [15] was modelocked by a saturable absorber which showed a fast recovery time of $\tau_A = 200$ fs, a modulation depth of $q_0 = 0.005$ and a saturation energy of $E_A = 17$ nJ. The other laser parameters can be found in [16]. Without the solitonlike pulse formation (GDD and SPM is switched off), the laser is predicted to produce about 200 fs short pulses with a single pulse per round-trip, very similar to what was discussed in the fast saturable absorber mode locking in Chapter 6. The dynamics becomes very much different if the negative GDD and positive SPM are included in the simulation, (see Figure 8.13)

Image removed due to copyright restrictions.

Please see:

Kartner, F. X., J. A. d. Au, and U. Keller. "Mode-Locking with Slow and Fast Saturable Absorbers--What's the Difference." *Selected Topics in Quantum Electronics 4* (1998): 159.

Figure 8.13: Each trace shows the pulse intensity profile obtained after 20,000 cavity round-trips in a diode-pumped Nd:glass laser according to [15]. When the laser reaches the double-pulse regime the multiple pulses are in constant motion with respect to each other. The resulting pulse train is not any longer stationary in any sense.

With increasing small signal gain, i. e. increasing pulse energy, the soliton shortens to 80 fs due to the solitonlike pulse shaping, (Figure 8.13).

Image removed due to copyright restrictions.

Please see:

Kartner, F. X., J. A. d. Au, and U. Keller. "Mode-Locking with Slow and Fast Saturable Absorbers--What's the Difference." *Selected Topics in Quantum Electronics* 4 (1998): 159.

Figure 8.14: Steady state pulse width (\circledR) and time-bandwidth product (\circ) for a Nd:glass laser modelocked by a saturable absorber with a 200 fs recovery time with GDD and SPM included, shown as a function of the intracavity pulse energy. The time-bandwidth product is only meaningful in the single pulse regime, where it is shown. The pulses are almost transform limited sech-pulses. The pulse width in the multiple pulse regime is only unique in the parameter region where multiple pulses of similar height and width are achieved. The pulses break up into multiple pulses when the absorber is about three times saturated.

The pulse width follows nicely the soliton relation (8.4), (dash-dotted line). The pulses become shorter, by about a factor of 2.5, than without GDD and SPM before the pulse breaks up into longer double-pulses. The pulse break-up into double-pulses occurs when the absorber is about two times saturated, close to the point where the shortest pulse can be expected according to the discussion above. Figure 8.13 shows, that the break-up point for the double pulses is also very close to the instability for continuum break-through. Indeed the first pulse train after break-up at a small signal gain of $g_0 = 0.09$ shows the coexistence of a longer and a shorter pulse, which indicates continuum break-through. But the following five traces are double pulses of equal height and energy. For even stronger saturation of the

absorber the double-pulses break-up into triple pulses and so on. Then the dynamics becomes even more complex. This behavior has been observed in detail in a Nd:glass laser [15], (see Figure 8.15), as well as in Cr⁴⁺:YAG lasers [17]. The simulations just discussed match the parameters of the Nd:glass experiments.

Image removed due to copyright restrictions.

Please see:

Kartner, F. X., J. A. d. Au, and U. Keller. "Mode-Locking with Slow and Fast Saturable Absorbers--What's the Difference." *Selected Topics in Quantum Electronics* 4 (1998): 159.

Figure 8.15: Pulselwidth in a Nd:glass laser [15] as a function of intracavity stored energy, i.e. pulse energy for a single pulse per round-trip. Dots measured values and solid line fits for a single and double-pulse solitonlike pulse stream.

Figure 8.15 clearly shows the scaling of the observed pulse width according to the soliton formula until the pulses break up at a saturation ratio of about 2. Notice, that the absorber recovery time of 200 fs is not much shorter than the pulse width achieved. Nevertheless, the optimum saturation ratio is close to the expected one of about 3. The break-up into pure double and triple pulses can be observed more clearly if the absorber recovery time is chosen to be shorter, so that continuum break-through is avoided. Figure 8.16 shows the final simulation results obtained after 20,000 round-trips in the cavity, if we reduce the absorber recovery time from 200 fs to 100 fs, again for different small signal gain, e.g. intracavity power levels and pulse energies. Now, we observe a clean break-up of the single-pulse solution into double-pulses and at even higher intracavity power levels the break-up into triple pulses without continuum generation in between. Note that the spacing between the pulses is very much different from what has been observed for the 200 fs response time. This spacing will depend on the details of the absorber and may also

be influenced by the dynamic gain saturation even if it is only a very small effect in this case [17].

Image removed due to copyright restrictions.

Please see:

Kartner, F. X., J. A. d. Au, and U. Keller. "Mode-Locking with Slow and Fast Saturable Absorbers--What's the Difference." *Selected Topics in Quantum Electronics* 4 (1998): 159.

Figure 8.16: Each trace shows the pulse intensity profile obtained after 20,000 cavity round-trips for an absorber with a response time $\tau_A = 100$ fs for different values of the small-signal gain. The simulations are always started with a 1 ps initial pulse shown as the first trace. Note that only the single pulse solutions are stationary.

8.4 Summary

Real absorbers do have the advantage of providing direct amplitude modulation and do not exploit additional cavities or operation of the resonator close to its stability boundary to achieve effective phase to amplitude conversion. Especially in compact resonator designs, as necessary for high-repetition rate lasers in the GHz range, semiconductor saturable absorbers with their low saturation energies and compactness offer unique solutions to this important technological challenge.

Bibliography

- [1] M. N. Islam, E. R. Sunderman, C. E. Soccolich, I. Bar-Joseph, N. Sauer, T. Y. Chang, and B. I. Miller: "Color Center Lasers Passively Mode Locked by Quantum Wells," *IEEE J. Quantum Electronics*. **25**, 2454-2463 (1989).
- [2] S. Tsuda, W. H. Knox, E. A. de Souza, W. Y. Jan, and J. E. Cunningham, "Mode-Locking Ultrafast Solid-State Lasers with Saturable-Bragg Reflectors," *IEEE J. Sel. Top. Quantum Electronics* **2**, 454-464 (1996).
- [3] U. Keller, "Semiconductor nonlinearities for solid-state laser modelocking and Q-switching," in *Semiconductors and Semimetals*, Vol. **59A**, edited by A. Kost and E. Garmire, Academic Press, Boston 1999.
- [4] J. Shah, "Ultrafast Spectroscopy of Semiconductors and Semiconductor Nanostructures," *Series in Solid-State Sciences* **115**, Springer Verlag, Berlin (1996).
- [5] E. O. Goebel, "Ultrafast Spectroscopy of Semiconductors," in *Advances in Solid State Physics* **30**, pp. 269 – 294 (1990).
- [6] W. H. Knox, R. L. Fork, M. C. Downer, D. A. B. Miller, D. S. Chemla and C. V. Shank, "Femtosecond Excitation of Nonthermal Carrier Populations in GaAs Quantum Wells," *Phys. Rev. Lett.* **54**, pp. 1306 – 1309 (1985).
- [7] J. L. Oudar, D. Hulin, A. Migus, A. Antonetti, F. Alexandre, "Subpicosecond Spectral Hole Burning Due to Nonthermalized Photoexcited Carriers in GaAs," *Phys. Rev. Lett.* **55**, pp. 2074 – 2076 (1985).
- [8] W. H. Knox, C. Hirlimann, D. A. B. Miller, J. Shah, D. S. Chemla and C. V. Shank, "Femtosecond Dynamics of Resonantly Excited Excitons in

- Room-Temperature GaAs Quantum Wells," *Phys. Rev. Lett.* **56**, 1191 – 1193 (1986).
- [9] G. L. Witt, R. Calawa, U. Mishra, E. Weber, Eds., "Low Temperature (LT) GaAs and Related Materials," **241**, Pittsburgh, (1992).
- [10] R. Fluck, I. D. Jung, G. Zhang, F. X. Kärtner, and U. Keller, "Broadband saturable absorber for 10 fs pulse generation," *Opt. Lett.* **21**, 743-745 (1996).
- [11] I. D. Jung, F. X. Kärtner, N. Matuschek, D. H. Sutter, F. Morier-Genoud, Z. Shi, V. Scheuer, M. Tilsch, T. Tschudi, U. Keller, "Semiconductor saturable absorber mirrors supporting sub-10 fs pulses," *Appl. Phys. B* **65**, pp. 137-150 (1997).
- [12] E. R. Thoen, E. M. Koontz, M. Joschko, P. Langlois, T. R. Schibli, F. X. Kärtner, E. P. Ippen, and L. A. Kolodziejski, "Two-photon absorption in semiconductor saturable absorber mirrors," *Appl. Phys. Lett.* **74**, 3927-3929, (1999).
- [13] P. Langlois, M. Joschko, E. R. Thoen, E. M. Koontz, F. X. Kärtner, E. P. Ippen, and L. A. Kolodziejski, "High fluence ultrafast dynamics of semiconductor saturable absorber mirrors," *Appl. Phys. Lett.* **75**, 3841-3843, (1999).
- [14] T. R. Schibli, E. R. Thoen, F. X. Kaertner, E. P. Ippen, "Suppression of Q-switched mode-locking and break-up into multiple pulses by inverse saturable absorption," *App. Phys. B* **70**, 41-49 (2000).
- [15] J. Aus der Au, D. Kopf, F. Morier-Genoud, M. Moser and U. Keller, "60-fs pulses from a diode-pumped Nd:glass laser," *Opt. Lett.* **22**, 207-309 (1997).
- [16] F.X. Kärtner, J. A. d. Au, U. Keller, "Mode-Locking with Slow and Fast Saturable Absorbers-What's the Difference," *Sel. Top. Quantum Electron.* **4**, 159 (1998).
- [17] B. C. Collings, K. Bergman, W. H. Knox, "Truely fundamental solitons in a passively mode-locked short cavity Cr⁴⁺:YAG laser.," *Opt. Lett.*, **22**,1098-1100 (1997).

Chapter 9

Noise and Frequency Control

So far we only considered the deterministic steady state pulse formation in ultrashort pulse laser systems due to the most important pulse shaping mechanisms prevailing in today's femtosecond lasers. Due to the recent interest in using modelocked lasers for frequency metrology and high-resolution laser spectroscopy as well as phase sensitive nonlinear optics the noise and tuning properties of mode combs emitted by modelocked lasers is of much current interest. Soliton-perturbation theory is well suited to successfully predict the noise behavior of many solid-state and fiber laser systems [1] as well as changes in group- and phase velocity in modelocked lasers due to intracavity nonlinear effects [5]. We start off by reconsidering the derivation of the master equation for describing the pulse shaping effects in a mode-locked laser. We assume that in steady-state the laser generates at some position z (for example at the point of the output coupler) inside the laser a sequence of pulses with the envelope $a(T = mT_r, t)$. These envelopes are the solutions of the corresponding master equation, where the dynamics per roundtrip is described on a slow time scale $T = mT_R$. Then the pulse train emitted from the laser including the carrier is

$$A(T, t) = \sum_{m=-\infty}^{+\infty} a(T = mT_r, t) e^{j[\omega_c(t - mT_R + (\frac{1}{v_g} - \frac{1}{v_p})2mL)]}. \quad (9.1)$$

with repetition rate $f_R = 1/T_R$ and center frequency ω_c . Both are in general subject to slow drifts due to mirror vibrations, changes in intracavity pulse energy that might be further converted into phase and group velocity changes. Note, the center frequency and repetition rate are only defined for times long

compared to the roundtrip time in the laser. Usually, they only change on a time scale three orders of magnitude longer than the expectation value of the repetition rate.

9.1 The Mode Comb

Lets suppose the pulse envelope, repetition rate, and center frequency do not change any more. Then the corresponding time domain signal is sketched in Figure 9.1.

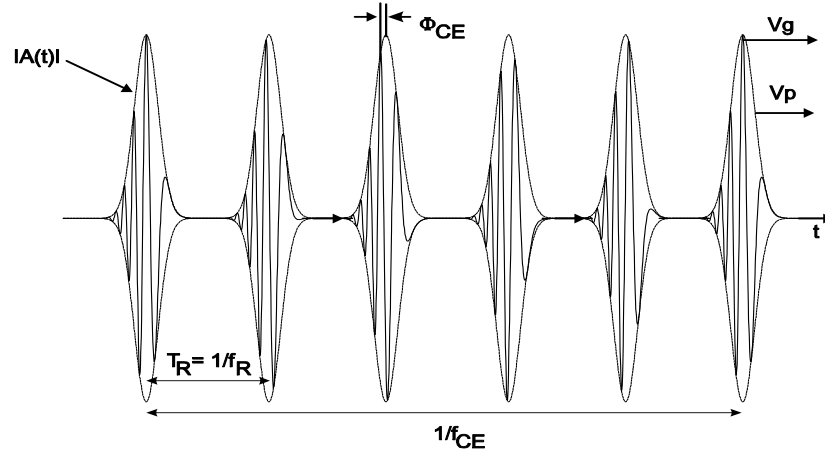


Figure 9.1: Pulse train emitted from a noise free mode-locked laser. The pulses can have chirp. The intensity envelope repeats itself with repetition rate f_R . The electric field is only periodic with the rate f_{CE} if it is related to the repetition rate by a rational number.

The pulse $a(T = mT_r, t)$ is the steady state solution of the master equation describing the laser system, as studied in chapter 6. Let's assume that the steady state solution is a perturbed soliton according to equation (6.64).

$$a(t, T) = \left(A_0 \operatorname{sech}\left(\frac{t - t_0}{\tau}\right) + a_c(T, t) \right) e^{-j\phi_0 \frac{T}{T_R}} \quad (9.2)$$

with the soliton phase shift

$$\phi_0 = \frac{1}{2} \delta A_0^2 = \frac{|D|}{\tau^2} \quad (9.3)$$

Thus, there is a carrier envelope phase shift $\Delta\phi_{CE}$ from pulse to pulse given by

$$\begin{aligned}\Delta\phi_{CE} &= \left. \left(\frac{1}{v_g} - \frac{1}{v_p} \right) \right|_{\omega_c} 2L - \phi_0 + \text{mod}(2\pi) \\ &= \omega_c T_R \left(1 - \frac{v_g}{v_p} \right) - \phi_0 + \text{mod}(2\pi)\end{aligned}\quad (9.4)$$

The Fourier transform of the unperturbed pulse train is

$$\begin{aligned}\hat{A}(\omega) &= \hat{a}(\omega - \omega_c) \sum_{m=-\infty}^{+\infty} e^{j(\Delta\phi_{CE} - (\omega - \omega_c)T_R)m} \\ &= \hat{a}(\omega - \omega_c) \sum_{n=-\infty}^{+\infty} e^{jmT_R \left(\frac{\Delta\phi_{CE}}{T_R} - \omega \right)} \\ &= \hat{a}(\omega - \omega_c) \sum_{n=-\infty}^{+\infty} T_R \delta \left(\omega - \left(\frac{\Delta\phi_{CE}}{T_R} + n\omega_R \right) \right)\end{aligned}\quad (9.5)$$

which is shown in Figure 9.2. Each comb line is shifted by the carrier-envelope offset frequency $f_{CE} = \frac{\Delta\phi_{CE}}{2\pi T_R}$ from the origin

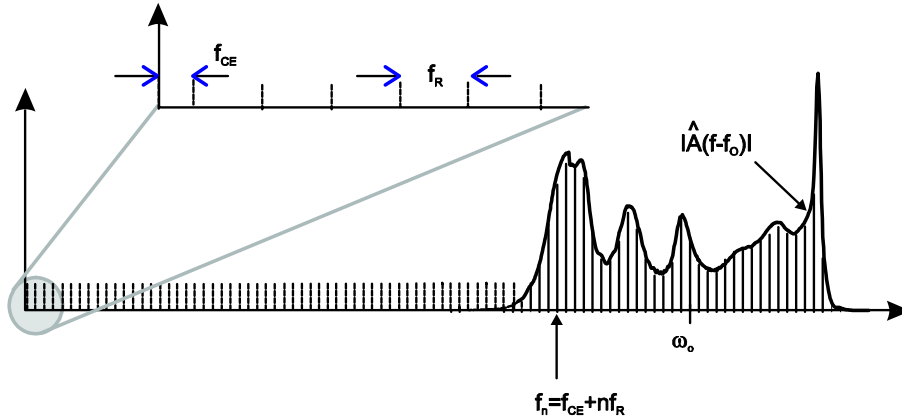


Figure 9.2: Optical mode comb of a mode-locked laser output.

To obtain self-consistent equations for the repetition rate, center frequency and the other pulse parameters we employ soliton-perturbation theory. This is justified for the case, where the steady state pulse is close to a

soliton, i.e. for the fast saturable absorber case, this is the chirp free solution, occurring when the ratio of gain filtering to dispersion is equal to the ratio of SAM action to self-phase modulation, see Eq. (6.61). Then the pulse solution in the m -th roundtrip is a solution of the nonlinear Schrödinger Equation stabilized by the irreversible dynamics and subject to additional perturbations

$$T_R \frac{\partial}{\partial T} A = jD \frac{\partial^2}{\partial t^2} A - j\delta |A|^2 A + (g - l)A + D_f \frac{\partial^2}{\partial t^2} A + \gamma |A|^2 A + L_{\text{pert}} \quad (9.6)$$

Due to the irreversible processes and the perturbations the solution to (9.6) is a soliton like pulse with perturbations in amplitude, phase, frequency and timing plus some continuum

$$A(t, T) = [(A_o + \Delta A_o) \text{sech}[(t - \Delta t)/\tau] + a_c(T, t)] e^{-j\phi_o T/T_R} e^{j\Delta p(T)t} e^{-j\theta_0} \quad (9.7)$$

with pulse energy $w_0 = 2A_o^2\tau$.

The perturbations cause fluctuations in amplitude, phase, center frequency and timing of the soliton and generate background radiation, i.e. continuum

$$\Delta A(T, t) = \Delta w(T) f_w(t) + \Delta \theta(T) f_\theta(t) + \Delta p(T) f_p(t) + \Delta t(T) f_t(t) + a_c(T, t). \quad (9.8)$$

where, we rewrote the amplitude perturbation as an energy perturbation. The dynamics of the pulse parameters due to the perturbed Nonlinear Schrödinger Equation (9.6) can be projected out from the perturbation using the adjoint basis and the orthogonality relation, see Chapter 3.5. Note, that the f_i correspond to the first component of the vector in Eqs.(3.22) - (3.25). The dynamics of the pulse parameters due to the perturbed Nonlinear Schrödinger Equation (9.6) can be projected out from the perturbation using the adjoint basis \bar{f}_i^* corresponding to the first component of the vector in Eqs.(3.44) - (3.47) and the new orthogonality relation

$$\text{Re} \left\{ \int_{-\infty}^{+\infty} \bar{f}_i^*(t) f_j(t) dt \right\} = \delta_{i,j}. \quad (9.9)$$

We obtain

$$\frac{\partial}{\partial T} \Delta w = -\frac{1}{\tau_w} \Delta w + \frac{1}{T_R} \operatorname{Re} \left\{ \int_{-\infty}^{+\infty} \bar{f}_w^*(t) L_{\text{pert}}(T, t) dt \right\} \quad (9.10)$$

$$\frac{\partial}{\partial T} \Delta \theta(T) = \frac{2\phi_o}{T_R} \frac{\Delta w}{w_o} + \frac{1}{T_R} \operatorname{Re} \left\{ \int_{-\infty}^{+\infty} \bar{f}_\theta^*(t) L_{\text{pert}}(T, t) dt \right\} \quad (9.11)$$

$$\frac{\partial}{\partial T} \Delta p(T) = -\frac{1}{\tau_p} \Delta p + \frac{1}{T_R} \operatorname{Re} \left\{ \int_{-\infty}^{+\infty} \bar{f}_p^*(t) L_{\text{pert}}(T, t) dt \right\} \quad (9.12)$$

$$\frac{\partial}{\partial T} \Delta t = \frac{-2|D|}{T_R} \Delta \omega + \frac{1}{T_R} \operatorname{Re} \left\{ \int_{-\infty}^{+\infty} \bar{f}_t^*(t) L_{\text{pert}}(T, t) dt \right\} \quad (9.13)$$

Note, that the irreversible dynamics does couple back the generated continuum to the soliton parameters. Here, we assume that this coupling is small and neglect it in the following, see [1]. Due to gain saturation and the parabolic filter pulse energy and center frequency fluctuations are damped with normalized decay constants

$$\frac{1}{\tau_w} = (2g_d - 2\gamma A_o^2) \quad (9.14)$$

$$\frac{1}{\tau_p} = \frac{4}{3} \frac{g_s}{\Omega_g^2 \tau^2} \frac{1}{T_R} \quad (9.15)$$

Here, g_s is the saturated gain and g_d is related to the differential gain by

$$g_s = \frac{g_o}{1 + \frac{w_o}{P_L T_R}} \quad (9.16)$$

$$g_d = \frac{dg_s}{dw_o} \cdot w_o \quad (9.17)$$

Note, in this model we assumed that the gain instantaneously follows the intracavity average power or pulse energy, which is not true in general. However, it is straight forward to include the relaxation of the gain by adding a dynamical gain model to the perturbation equations. For simplicity we shall neglect this here. Since the system is autonomous, there is no retiming and rephasing in the free running system.

9.2 Noise in Mode-locked Lasers

Within this framework the response of the laser to noise can be easily included. The spontaneous emission noise due to the amplifying medium with saturated gain g_s and excess noise factor Θ leads to additive white noise in the perturbed master equation (9.6) with $L_{\text{pert}} = \xi(t, T)$, where ξ is a white Gaussian noise source with autocorrelation function

$$\langle \xi(t', T') \xi(t, T) \rangle = T_R^2 P_n \delta(t - t') \delta(T - T') \quad (9.18)$$

where the spontaneous emission noise energy $P_n \cdot T_R$ with

$$P_n = \Theta \frac{2g_s}{T_R} \hbar \omega_c = \Theta \frac{\hbar \omega_c}{\tau_p} \quad (9.19)$$

is added to the pulse within each roundtrip in the laser. τ_p is the cavity decay time or photon lifetime in the cavity. Note, that the noise is approximated by white noise, i.e. uncorrelated noise on both time scales t, T . The noise between different round-trips is certainly uncorrelated. However, white noise on the fast time scale t , assumes a flat gain, which is an approximation. By projecting out the equations of motion for the pulse parameters in the presence of this noise according to (9.8)–(9.13), we obtain the additional noise sources which are driving the energy, center frequency, timing and phase fluctuations in the mode-locked laser

$$\frac{\partial}{\partial T} \Delta w = -\frac{1}{\tau_w} \Delta w + S_w(T), \quad (9.20)$$

$$\frac{\partial}{\partial T} \Delta \theta(T) = \frac{2\phi_o}{T_R} \frac{\Delta w}{w_o} + S_\theta(T), \quad (9.21)$$

$$\frac{\partial}{\partial T} \Delta p(T) = -\frac{1}{\tau_p} \Delta p + S_p(T), \quad (9.22)$$

$$\frac{\partial}{\partial T} \Delta t = \frac{-2|D|}{T_R} \Delta p + S_t(T), \quad (9.23)$$

with

$$S_w(T) = \frac{1}{T_R} \text{Re} \left\{ \int_{-\infty}^{+\infty} \bar{f}_w^*(t) \xi(T, t) dt \right\}, \quad (9.24)$$

$$S_\theta(T) = \frac{1}{T_R} \text{Re} \left\{ \int_{-\infty}^{+\infty} \bar{f}_\theta^*(t) \xi(T, t) dt \right\}, \quad (9.25)$$

$$S_p(T) = \frac{1}{T_R} \text{Re} \left\{ \int_{-\infty}^{+\infty} \bar{f}_p^*(t) \xi(T, t) dt \right\}, \quad (9.26)$$

$$S_t(T) = \frac{1}{T_R} \text{Re} \left\{ \int_{-\infty}^{+\infty} \bar{f}_t^*(t) \xi(T, t) dt \right\}. \quad (9.27)$$

The new reduced noise sources obey the correlation functions

$$\langle S_w(T') S_w(T) \rangle = \frac{P_n}{4w_0} \delta(T - T'), \quad (9.28)$$

$$\langle S_\theta(T') S_\theta(T) \rangle = \frac{4}{3} \left(1 + \frac{\pi^2}{12} \right) \frac{P_n}{w_o} \delta(T - T'), \quad (9.29)$$

$$\langle S_p(T') S_p(T) \rangle = \frac{4}{3} \frac{P_n}{w_o} \delta(T - T'), \quad (9.30)$$

$$\langle S_t(T') S_t(T) \rangle = \frac{\pi^2}{3} \frac{P_n}{w_o} \delta(T - T'), \quad (9.31)$$

$$\langle S_i(T') S_j(T) \rangle = 0 \text{ for } i \neq j. \quad (9.32)$$

The power spectra of amplitude, phase, frequency and timing fluctuations are defined via the Fourier transforms of the autocorrelation functions

$$|\Delta \hat{w}(\Omega)|^2 = \int_{-\infty}^{+\infty} \langle \Delta \hat{w}(T + \tau) \Delta \hat{w}(T) \rangle e^{-j\Omega\tau} d\tau, \text{ etc.} \quad (9.33)$$

After a short calculation, the power spectra due to amplifier noise are

$$\left| \frac{\Delta \hat{w}(\Omega)}{w_o} \right|^2 = \frac{4}{1/\tau_w^2 + \Omega^2} \frac{P_n}{w_o}, \quad (9.34)$$

$$|\Delta \hat{\theta}(\Omega)|^2 = \frac{1}{\Omega^2} \left[\frac{4}{3} \left(1 + \frac{\pi^2}{12} \right) \frac{P_n}{w_o} + \frac{16}{(1/\tau_p^2 + \Omega^2)} \frac{\phi_o^2}{T_R^2} \frac{P_n}{w_o} \right], \quad (9.35)$$

$$|\Delta \hat{p}(\Omega) \tau|^2 = \frac{1}{1/\tau_p^2 + \Omega^2} \frac{4}{3} \frac{P_n}{w_o}, \quad (9.36)$$

$$\left| \frac{\Delta \hat{t}(\Omega)}{\tau} \right|^2 = \frac{1}{\Omega^2} \left[\frac{\pi^2}{3} \frac{P_n}{w_o} + \frac{1}{(1/\tau_w^2 + \Omega^2)} \frac{4}{3} \frac{|D|^2}{T_R^2 \tau^4} \frac{P_n}{w_o} \right]. \quad (9.37)$$

These equations indicate, that energy and center frequency fluctuations become stationary with mean square fluctuations

$$\left\langle \left(\frac{\Delta w}{w_o} \right)^2 \right\rangle = 2 \frac{P_n \tau_w}{w_o} \quad (9.38)$$

$$\langle (\Delta \omega \tau)^2 \rangle = \frac{2}{3} \frac{P_n \tau_p^2}{w_o} \quad (9.39)$$

whereas the phase and timing undergo a random walk with variances

$$\begin{aligned} \sigma_\theta(T) &= \langle (\Delta\theta(T) - \Delta\theta(0))^2 \rangle = \frac{4}{3} \left(1 + \frac{\pi^2}{12} \right) \frac{P_n}{w_o} |T| \quad (9.40) \\ &+ 16 \frac{\phi_o^2}{T_R^2} \frac{P_n}{w_o} \tau_p^3 \left(\exp \left[-\frac{|T|}{\tau_p} \right] - 1 + \frac{|T|}{\tau_p} \right) \end{aligned}$$

$$\begin{aligned} \sigma_t(T) &= \left\langle \left(\frac{\Delta t(T) - \Delta t(0)}{\tau} \right)^2 \right\rangle = \frac{\pi^2}{3} \frac{P_n}{w_o} |T| \quad (9.41) \\ &+ \frac{4}{3} \frac{|D|^2}{T_R^2 \tau^4} \frac{P_n}{w_o} \tau_p^3 \left(\exp \left[-\frac{|T|}{\tau_p} \right] - 1 + \frac{|T|}{\tau_p} \right) \end{aligned}$$

The phase noise causes the fundamental finite width of every line of the mode-locked comb in the optical domain. The timing jitter leads to a finite linewidth of the detected microwave signal, which is equivalent to the lasers fundamental fluctuations in repetition rate. In the strict sense, phase and timing in a free running mode-locked laser (or autonomous oscillator) are not anymore stationary processes. Nevertheless, since we know these are Gaussian distributed variables, we can compute the amplitude spectra of phasors undergoing phase diffusion processes rather easily. The phase difference $\varphi = \Delta\theta(T) - \Delta\theta(0)$ is a Gaussian distributed variable with variance σ and propability distribution

$$p(\varphi) = \frac{1}{\sqrt{2\pi\sigma}} e^{-\frac{\varphi^2}{2\sigma}}, \text{ with } \sigma = \langle \varphi^2 \rangle. \quad (9.42)$$

Therefore, the expectation value of a phasor with phase φ is

$$\begin{aligned} \langle e^{j\varphi} \rangle &= \frac{1}{\sqrt{2\pi\sigma}} \int_{-\infty}^{+\infty} e^{-\frac{\varphi^2}{2\sigma}} e^{j\varphi} d\varphi \quad (9.43) \\ &= e^{-\frac{1}{2}\sigma}. \end{aligned}$$

9.2.1 The Optical Spectrum

$$a(t, T) = \left(A_0 \operatorname{sech}\left(\frac{t-t_0}{\tau}\right) + a_c(T, t) \right) e^{-j\phi_0 \frac{T}{\tau}} \quad (9.44)$$

In the presence of noise the laser output changes from eq.(9.1) to a random process. Neglecting the background continuum we obtain:

$$A(t, T = mT_R) = \sum_{m=-\infty}^{+\infty} (A_0 + \Delta A(mT_R)) \operatorname{sech} \left(\frac{t - mT_R - \Delta t(mT_R)}{\tau} \right) \quad (9.45)$$

$$e^{j\Delta\phi_{CE} \cdot m} e^{j(\omega_c + \Delta p(mT_R))t} e^{-j\Delta\theta(mT_R)}$$

For simplicity, we will neglect in the following amplitude and carrier frequency fluctuations in Eq.(9.45), because they are bounded and become only important at large offsets from the comb. However, we keep them in the expressions for the phase and timing jitter Eqs.(9.34) and (9.36). We assume a stationary process, so that the optical power spectrum can be computed from

$$S(\omega) = \lim_{T=2NT_R \rightarrow \infty} \frac{1}{T} \langle \hat{A}_T^*(\omega) \hat{A}_T(\omega) \rangle \quad (9.46)$$

with the spectra related to a finite time interval

$$\hat{A}_T(\omega) = \int_{-T}^T A(t) e^{-j\omega t} dt = \hat{a}_0(\omega - \omega_c) \sum_{m=-N}^N e^{jmT_R \left(\frac{\Delta\phi_{CE}}{T_R} - \omega \right)} \quad (9.47)$$

$$e^{-j[(\omega - \omega_c)\Delta t(mT_R) + \Delta\theta(mT_R)]}$$

where $\hat{a}_0(\omega)$ is the Fourier transform of the pulse shape. In this case

$$\hat{a}_0(\omega) = \int_{-\infty}^{\infty} A_0 \operatorname{sech} \left(\frac{t}{\tau} \right) e^{-j\omega t} dt = A_0 \pi \tau \operatorname{sech} \left(\frac{\pi}{2} \omega \tau \right) \quad (9.48)$$

With (9.46) the optical spectrum of the laser is given by

$$S(\omega) = \lim_{N \rightarrow \infty} |\hat{a}_0(\omega - \omega_c)|^2 \frac{1}{2NT_R} \sum_{m'=-N}^N \sum_{m=-N}^M e^{jT_R \left(\frac{\phi_{CE}}{T_R} - \omega \right) (m-m')} \quad (9.49)$$

$$\langle e^{+j[2\pi(f-f_c)(\Delta t(mT_R) - \Delta t(m'T_R)) - (\theta(mT_R) - \theta(m'T_R))]} \rangle$$

Note, that the difference between the phases and the timing only depends on the difference $k = m - m'$. In the current model phase and timing fluctuations are uncorrelated. Therefore, for $N \rightarrow \infty$ we obtain

$$S(\omega) = |\hat{a}_0(\omega - \omega_c)|^2 \frac{1}{T_R} \sum_{k'=-\infty}^{\infty} e^{jT_R(\frac{\Delta\phi_{CE}}{T_R} - \omega)k} \langle e^{+j[2\pi(\omega - \omega_0)(\Delta t((m+k)T_R) - \Delta t(mT_R))]} \rangle \langle e^{-j(\theta((m+k)T_R) - \theta(mT_R))} \rangle. \quad (9.50)$$

The expectation values are exactly of the type calculated in (9.43), which leads to

$$S(\omega) = \frac{|\hat{a}_0(\omega - \omega_c)|^2}{T_R} \sum_{k'=-\infty}^{\infty} e^{jT_R(\frac{\phi_{CE}}{T_R} - \omega)k} e^{-\frac{1}{2}\sigma_\theta(kT_R)} e^{-\frac{1}{2}[(\omega - \omega_c)\tau]^2\sigma_t(kT_R)} \quad (9.51)$$

Most often we are interested in the noise very close to the lines at frequency offsets much smaller than the inverse energy and frequency relaxation times τ_w and τ_p . This is determined by the long term behavior of the variances, which grow linearly in $|T|$

$$\sigma_\theta(T) = \frac{4}{3} \left(1 + \frac{\pi^2}{12} + 16 \frac{\tau_w^2}{T_R^2} \phi_o^2 \right) \frac{P_n}{w_o} |T| = 2\Delta\omega_\phi |T|, \quad (9.52)$$

$$\sigma_t(T) = \frac{1}{3} \left(\pi^2 + \frac{\tau_p^2}{T_R^2} \left(\frac{D}{\tau^2} \right)^2 \right) \frac{P_n}{w_o} |T| = 4\Delta\omega_t |T|. \quad (9.53)$$

with the rates

$$\Delta\omega_\phi = \frac{2}{3} \left(1 + \frac{\pi^2}{12} + 16 \frac{\tau_w^2}{T_R^2} \phi_o^2 \right) \frac{P_n}{w_o}, \quad (9.54)$$

$$\Delta\omega_t = \frac{1}{6} \left(\pi^2 + \frac{\tau_p^2}{T_R^2} \left(\frac{D}{\tau^2} \right)^2 \right) \frac{P_n}{w_o}. \quad (9.55)$$

From the Poisson formula

$$\sum_{k=-\infty}^{+\infty} h[k] e^{-jkx} = \sum_{n=-\infty}^{+\infty} G(x + 2n\pi) \quad (9.56)$$

where

$$G(x) = \int_{-\infty}^{+\infty} h[k]e^{-jkx} dk, \quad (9.57)$$

and Eqs.(9.51) to (9.55) we finally arrive at the optical line spectrum of the mode-locked laser

$$S(\omega) = \frac{|\hat{a}_0(\omega - \omega_c)|^2}{T_R^2} \sum_{n=-\infty}^{+\infty} \frac{2\Delta\omega_n}{(\omega - \omega_n)^2 + \Delta\omega_n^2} \quad (9.58)$$

which are Lorentzian lines at the mode comb positions

$$\omega_n = \omega_c + n\omega_R - \frac{\Delta\phi_{CE}}{T_R}, \quad (9.59)$$

$$= \frac{\Delta\phi_{CE}}{T_R} + n'_R\omega, \quad (9.60)$$

with a half width at half maximum of

$$\Delta\omega_n = \Delta\omega_\phi + [\tau(\omega_n - \omega_c)]^2 \Delta\omega_t. \quad (9.61)$$

Estimating the number of modes M included in the comb by

$$M = \frac{T_R}{\tau}, \quad (9.62)$$

we see that the contribution of the timing fluctuations to the linewidth of the comb lines in the center of the comb is negligible. Thus the linewidth of the comb in the center is given by 9.54

$$\Delta\omega_\phi = \frac{2}{3} \left(1 + \frac{\pi^2}{12} + 16 \frac{\tau_w^2}{T_R^2} \phi_o^2 \right) \frac{\Theta 2g_s}{N_0 T_R} \quad (9.63)$$

$$= \frac{2}{3} \left(1 + \frac{\pi^2}{12} + 16 \frac{\tau_w^2}{T_R^2} \phi_o^2 \right) \frac{\Theta}{N_0 \tau_p} \quad (9.64)$$

where $N_0 = \frac{w_o}{\hbar\omega_c}$ is the number of photons in the cavity and $\tau_p = T_R/(2l)$ is the photon lifetime in the cavity. Note that this result for the mode-locked laser is closely related to the Schawlow-Townes linewidth of a continuous wave laser which is $\Delta f_\phi = \frac{\Theta}{2\pi N_0 \tau_p}$. For a solid-state laser at around $1\mu m$ wavelength with a typical intracavity pulse energy of 50 nJ corresponding to $N_0 = 2.5 \cdot 10^{11}$ photons and 100 MHz repetition rate with a 10% output coupler and an

excess noise figure of $\Theta = 2$, we obtain $\Delta f_\phi \sim \frac{\Theta}{3\pi N_0 \tau_p} = 8\mu\text{Hz}$ without the amplitude to phase conversion term depending on the nonlinear phase shift ϕ_o . These intrinsic linewidths are due to fluctuations happening on a time scale faster than the round-trip time and, therefore, can not be compensated by external servo control mechanisms. For sub-10 fs lasers, the spectra fill up the full gain bandwidth and the KLM is rather strong, so that the amplitude and center frequency relaxation times are on the order of 10-100 cavity roundtrips. In very short pulse Ti:sapphire lasers nonlinear phase shifts are on the order of 1 rad per roundtrip. Then most of the fluctuations are due to amplitude fluctuations converted into phase jitter. This contributions can increase the linewidth by a factor of 100-10000, which may bring the linewidth to the mHz and Hz level.

9.2.2 The Microwave Spectrum

Not only the optical spectrum is of interest als the spectrum of the photo detected output of the laser is of intrest. Simple photo detection can convert the low jitter optical pulse stream into a comb of extremely low phase noise microwave signals. The photo detector current is proportional to the output power of the laser. From Eq.(9.45) we find

$$I(t) = \eta \frac{e}{\hbar\omega_c} |A(T, t)|^2 = \eta \frac{e}{\hbar\omega_c \tau} \sum_{m=-\infty}^{+\infty} (w_0 + \Delta w(mT_R)) \frac{1}{2} \text{sech}^2 \left(\frac{t - mT_R - \Delta t(mT_R)}{\tau} \right), \quad (9.65)$$

where η is the quantum efficiency. For simplicity we neglect again the amplitude noise and consider only the consequences due to the timing jitter. Then we obtain for the Fourier Transform of the photo current

$$\hat{I}_T(\omega) = \eta \frac{e w_0}{\hbar\omega_0 \tau} |a_0|^2(\omega) \sum_{m=-N}^{+N} e^{-j\omega(mT_R + \Delta t(mT_R))}, \quad (9.66)$$

$$|a_0|^2(\omega) = \int_{-\infty}^{\infty} \frac{1}{2} \text{sech}^2(x) e^{-j\omega\tau x} dx \quad (9.67)$$

$$= \frac{\pi\omega\tau}{\sinh(\frac{\pi}{2}\omega\tau)}, \quad (9.68)$$

and its power spectrum according to Eq.(9.46)

$$\begin{aligned}
 S_I(\omega) &= \frac{(\eta e N_0)^2}{T_R} \left| |a_0|^2(\omega) \right|^2 \sum_{k=-\infty}^{+\infty} e^{-j\omega k T_R} \langle e^{-j\omega(\Delta t(k T_R) - \Delta t(0))} \rangle, \\
 &= \frac{(\eta e N_0)^2}{T_R} \left| |a_0|^2(\omega) \right|^2 \sum_{k=-\infty}^{+\infty} e^{-j\omega k T_R} e^{-\frac{1}{2}[(\omega \tau)^2 \sigma_t(k T_R)]} \quad (9.69)
 \end{aligned}$$

Using the Poisson formula again results in

$$\begin{aligned}
 S_I(\omega) &= \frac{(\eta e N_0)^2}{T_R} \left| |a_0|^2(\omega) \right|^2 \sum_{k=-\infty}^{+\infty} e^{-j\omega k T_R} e^{-j\omega(\Delta t(k T_R) - \Delta t(0))}, \\
 &= \frac{(\eta e N_0)^2}{T_R^2} \left| |a_0|^2(\omega) \right|^2 \sum_{n=-\infty}^{+\infty} \frac{2\Delta\omega_{I,n}}{(\omega - n\omega_R)^2 + \Delta\omega_{I,n}^2} \quad (9.70)
 \end{aligned}$$

with the linewidth $\Delta\omega_{I,n}$ of the n-th harmonic

$$\begin{aligned}
 \Delta\omega_{I,n} &= \left(2\pi n \frac{\tau}{T_R} \right)^2 \Delta\omega_t \\
 &= \left(\frac{2\pi n}{M} \right)^2 \Delta\omega_t. \quad (9.71)
 \end{aligned}$$

The fundamental line ($n = 1$) of the microwave spectrum has a width which is M^2 -times smaller than the optical linewidth. For a 10-fs laser with 100 MHz repetition rate, the number of modes M is about a million.

9.2.3 Example: Yb-fiber laser:

Figure 9.3 shows the schematic of a stretched pulse modelocked laser operating close to zero dispersion. Therefore, the contribution of the Gordon-Haus jitter should be minimized. Infact, it has been shown and discussed that these types of lasers reach minimum jitter levels [2][3][4].

The timing jitter of the stretched pulse laser shown in Figure is computed in table 9.1.

The theoretical results above are derived with soliton perturbation theory. The stretched pulse modelocked laser in Figure 9.3 is actually far from being a soliton laser, see [3][4]. The pulse is breathing considerably during

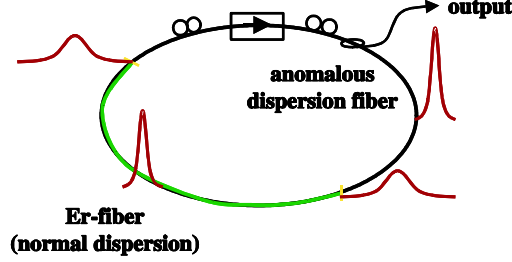


Figure 9.3: Schematic of a stretched pulse modelocked laser.

Gain Half-Width Half Maximum	$\Omega_g = 2\pi \cdot \frac{0.3\mu\text{m}/\text{fs}}{(1.\mu\text{m})^2} 0.02\mu\text{m} = 38\text{THz}$
Saturated gain	$g_s = 1.2$
Pulse width	$\tau_{FWHM} = 50\text{fs}, \tau = \tau_{FWHM}/1.76 = 30\text{fs}$
Pulse repetition time	$T_R = 12\text{ns}$
Decay time for center freq. fluctuations	$\frac{1}{\tau_p} = \frac{4}{3} \frac{g_s}{\Omega_g^2 \tau^2 T_R} = \frac{4}{3} \frac{1}{T_R}$
Intracavity power	$P = 100\text{mW}$
Intra cavity pulse energy / photon number	$w_o = 1.2\text{nJ}, N_0 = 0.6 \cdot 10^{10}$
Noise power spectral density	$P_n = \Theta \frac{2g_s}{T_R} \hbar\omega_o$
Amplifier excess noise factor	$\Theta = 10$
ASE noise	$\frac{P_n}{w_o} = \Theta \frac{2g_s}{T_R N_0} = \frac{1}{3}\text{Hz}$
Dispersion	5000fs^2
Frequency-to-timing conv.	$\frac{4}{\pi^2} \frac{4 D ^2}{\tau^4} \frac{\tau_p^2}{T_R^2} = \left(\frac{2}{\pi} \frac{3 \cdot 10000}{4 \cdot 1000}\right)^2 = (3.7)^2$
Timing jitter density	$\left \frac{\Delta\hat{t}(\Omega)}{\tau}\right ^2 = \frac{1}{\Omega^2} \frac{\pi^2}{3} \frac{P_n}{w_o} \left(1 + \frac{4}{\pi^2} \frac{4 D ^2}{\tau^4} \frac{1}{(T_R^2/\tau_p^2 + T_R^2\Omega^2)}\right)$
Timing jitter $[f_{\min}, f_{\max}]$ for $f_{\min} \ll 1/\tau_p$, $f_{\min} = 10\text{kHz}, D = 5000\text{fs}^2$	$\Delta t = \tau \sqrt{\frac{1}{12 \cdot f_{\min}} \frac{P_n}{w_o} \left(1 + \frac{4}{\pi^2} \frac{4 D ^2}{\tau^4} \frac{\tau_p^2}{T_R^2}\right)} = 0.2\text{fs}$

Table 9.1: Parameters for the stretched pulse modelocked laser of Figure 9.3.

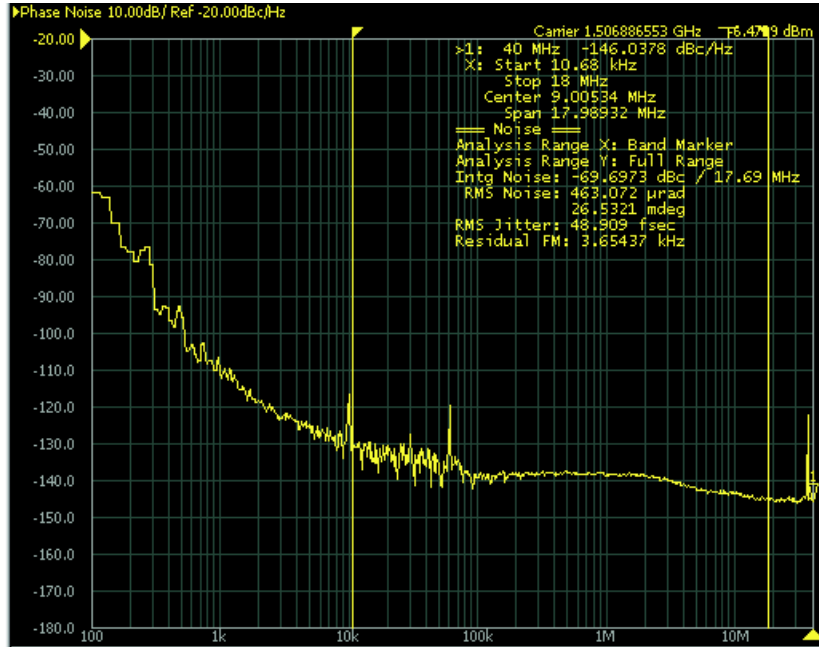


Figure 9.4: Timing jitter measurement of the output from the stretched pulse modelocked laser measured with a HP 5504 signal analyzer.

passage through the cavity up to a factor of 10. Therefore, the theory should take that into account by assuming an average pulse width when the noise is added in the cavity. For more details see [3][4]. In reality, these quantum limited (ASE) and rather small optical and microwave linewidths are difficult to observe, because they are most often swamped by technical noise such as fluctuations in pump power, which may cause gain fluctuations, or mirror vibrations, air-density fluctuations or thermal drifts, which directly cause changes in the laser's repetition rate. Figure 9.4 shows the single-sideband phase noise spectrum $L(f)$ of the $N=32$ nd harmonic of the fundamental repetition rate, i.e. 1.3 GHz, in the photocurrent spectrum 9.70. The phase of the $N=32$ nd harmonic of the photocurrent 9.65 is directly related to the timing jitter by

$$\Delta\varphi(T) = 2\pi N f_R \Delta t(T) \quad (9.72)$$

The single-sideband phase noise is the power spectral density of these phase fluctuations defined in the same way as the power spectral density of the

photocurrent itself, i.e.

$$L(f) = 2\pi S_{\Delta\varphi}(\omega) \quad (9.73)$$

The phase fluctuations in a certain frequency intervall can then be easily evaluated by

$$\Delta\varphi^2 = 2 \int_{f_{\min}}^{f_{\max}} L(f) df. \quad (9.74)$$

And the timing jitter is then

$$\Delta t = \frac{1}{2\pi N f_R} \sqrt{2 \int_{f_{\min}}^{f_{\max}} L(f) df}. \quad (9.75)$$

For the measurements shown in Figure 9.4 we obtain for the integrated timing jitter from 10kHz to 20 MHz of 50 fs. This is about 200 times larger than the limits derived in table 9.1. This discrepancy comes from several effects, most notable amplitude to phase conversion in the photodetector during photodetection, an effect not yet well understood as well as other noise sources we might not have modelled, such as noise from the pump laser. However, these noise sources can be eliminated in principle by careful design and feedback loops. Therefore, it is important to understand the dependence of the group and phase velocity on the intracavity power or pulse energy at least within the current basic model. Additional linear and nonlinear effects due to higher order linear dispersion or nonlinearities may cause additional changes in group and phase velocity, which might also create unusual dependencies of group and phase velocity on intracavity pulse energy. Here we discuss as an example the impact of the instantaneous Kerr effect on group and phase velocity of a soliton like pulse.

9.3 Group- and Phase Velocity of Solitons

The Kerr-effect leads to a change of phase velocity of the pulse, resulting in the self-phase shift of the soliton, ϕ_o , per round-trip. A change in group velocity does not appear explicitly in the solution of the NLSE. Self-steepening which becomes important for ultrashort pulses leads to an additional term in the NLSE and therefore to an additional term in the master equation (9.6)

$$L_{\text{pert}} = -\frac{\delta}{\omega_c} \frac{\partial}{\partial t} (|a(T, t)|^2 a(T, t)). \quad (9.76)$$

The impact of this term is expected to be small of the order of $1/(\omega_o\tau)$ and therefore only important for few-cycle pulses. However, it turns out that this term alters the phase and group velocity of the soliton like pulse as much as the nonlinear phase shift itself. We take his term into account in form of a perturbation. This perturbation term is odd and real and therefore only leads to a timing shift, when substituted into Eq.(9.6).

$$\begin{aligned} T_R \frac{\partial \Delta t(T)}{\partial T} \Big|_{sst} &= -\frac{\delta}{\omega_c} A_0^3 \operatorname{Re} \left\{ \int_{-\infty}^{+\infty} \bar{f}_t^*(t) \frac{\partial}{\partial t} \left(\operatorname{sech}^3 \left(\frac{t}{\tau} \right) \right) dt \right\} \\ &= \frac{\delta}{\omega_c} A_0^2 = \frac{2\phi_0}{\omega_c}. \end{aligned} \quad (9.77)$$

$$(9.78)$$

This timing shift or group delay per round-trip, together with the nonlinear phase shift leads to a phase change between carrier and envelope per roundtrip given by

$$\Delta\phi_{CE} = -\phi_0 + \omega_o T_R \frac{\partial}{\partial T} \Delta t(T) \Big|_{selfsteep} = -\frac{1}{2} \delta A_0^2 + \delta A_0^2 = \frac{1}{2} \delta A_0^2. \quad (9.79)$$

The compound effect of this phase delay per round-trip in the carrier versus envelope leads to a carrier-envelope frequency

$$f_{CE} = \frac{\Delta\phi_{CE}}{2\pi} f_R = \frac{\phi_0}{2\pi} f_R. \quad (9.80)$$

The group delay also changes the optical cavity length of the laser and therefore alters the repetition rate according to

$$\Delta f_R = -f_R^2 \Delta t(T) \Big|_{selfsteep} = -2\phi_0 \frac{f_R}{\omega_o} f_R = -\frac{2}{m_0} f_{CE}, \quad (9.81)$$

where m_0 is the mode number of the carrier wave. Eqs.(9.80) and (9.81) together determine the shift of the m-th line of the optical comb $f_m = f_{CE} + m f_R$ due to an intracavity pulse energy modulation and a change in cavity length by

$$\Delta f_m = \Delta f_{CE} + m \Delta f_R = f_{CE} \left(1 - \frac{2m}{m_0} \right) \frac{\Delta w}{w_0} - m f_R \frac{\Delta L}{L_0}. \quad (9.82)$$

Specifically, Eq. (9.82) predicts, that the mode with number $m = m_0/2$, i.e. the mode at half the center frequency, does not change its frequency

as a function of intracavity pulse energy. Of course, one has to remember, that this model is so far based on self-phase modulation and self-steepening as the cause of a power dependent carrier-envelope offset frequency. There may be other mechanisms that cause a power dependent carrier envelope offset frequency. One such effect is the group delay caused by the laser gain medium another one is the carrier-envelope change due to a change in carrier frequency, which gives most likely a very strong additional dependence on pump power. Nevertheless, the formula 9.82 can be used for the control of the optical frequency comb of a femtosecond laser by controlling the cavity length and the intracavity pulse energy, via the pump power.

9.4 Femtosecond Laser Frequency Combs

Nevertheless, the formula (9.82) can be used for the control of the optical frequency comb of a femtosecond laser by controlling the cavity length and the intracavity pulse energy, via the pump power. According to Fig. 9.2 every line of the optical comb determined by

$$f_m = f_{CE} + mf_R. \quad (9.83)$$

Note, if the femtosecond laser emits a spectrum covering more than one octave, then one can frequency double part of the comb at low frequencies and beat it with the corresponding high frequency part of the comb on a photo detector, see Fig. 9.5 The result is a photodetector beat signal that consists of discrete lines at the beat frequencies

$$f_k = kf_R \pm f_{CE} \quad (9.84)$$

This method for determining the carrier-envelope offset frequency is called f-to-2f interferometry. The carrier-envelope offset frequency can be extracted with filters and synchronized to a local oscillator or to a fraction of the repetition rate of the laser, for example $f_R/4$.

Figure 9.6 shows the setup of an octave spanning 200 MHz Ti:sapphire laser where the carrier envelope offset frequency f_{CE} is locked to a local oscillator at 36 MHz using the f-to-2f self-referencing method [6]

The spectral output of this laser is shown in Figure 9.7 The spectral components at 1140 are properly delayed in a chirped mirror delay line against the spectral components at 570 nm. The 1140 nm range is frequency doubled in a 1mm BBO crystal and the frequency doubled light together with

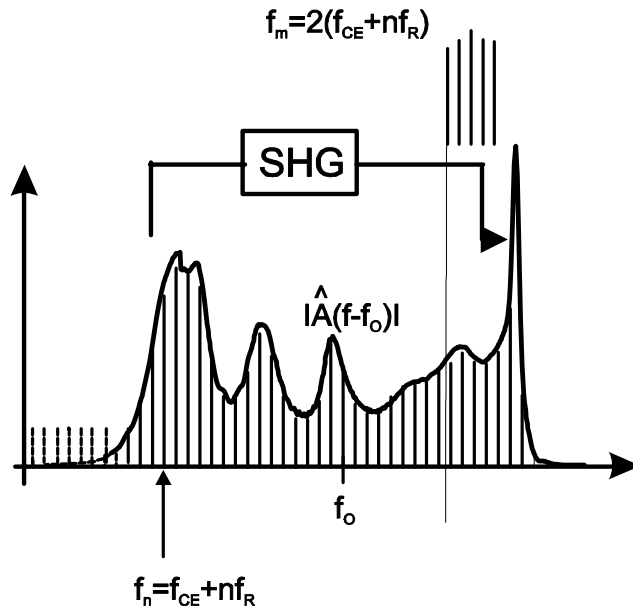


Figure 9.5: f-to-2f interferometry to determine the carrier-envelope offset frequency.

Image removed due to copyright restrictions.

Please see:

Mucke, Oliver, et al. "Self-Referenced 200 MHz Octave-Spanning Ti: Sapphire Laser with 50 Attosecond Carrier-Envelope Phase Jitter." *Optics Express* 13, no. 13 (June 2005): 5163-5169.

Figure 9.6: Carrier-envelope phase stabilized 200 MHz octave-spanning Ti:sapphire laser. The femtosecond laser itself is located inside the grey area. AOM, acousto-optical modulator; S, silver end mirror; OC, output coupling mirror; PBS, polarizing beam splitter cube; PMT, photomultiplier tube; PD, digital phase detector; LF, loop filter; VSA, vector signal analyzer. The carrier-envelope frequency is phase locked to 36 MHz.

Image removed due to copyright restrictions.

Please see:

Mucke, Oliver, et al. "Self-Referenced 200 MHz Octave-Spanning Ti: Sapphire Laser with 50 Attosecond Carrier-Envelope Phase Jitter." *Optics Express* 13, no. 13 (June 2005): 5163-5169. Used with permission.

Figure 9.7: Output spectrum of the Ti:sapphire laser on a linear (black curve) and on a logarithmic scale (grey curve). The wavelengths 570 and 1140 nm used for self-referencing are indicated by two dashed lines.

the fundamental at 570 nm is projected into the same polarization via a polarizing beam splitter. The signal is then filtered through a 10nm wide filter and detected with a photomultiplier tube (PMT). A typical signal from the PMT is shown in Figure 9.8. Phase locking is achieved by a phase-locked loop (PLL) by feeding the error signal from the digital phase detector to an AOM placed in the pump beam (see Fig. 9.6) which modulates the pump power and thus changes the carrier-envelope frequency via Eq.(9.82). A bandpass filter is used to select the carrier-envelope beat signal at 170 MHz. This signal is amplified, divided by 16 in frequency, and compared with a reference frequency f_{LO} supplied by a signal generator (Agilent 33250A) using a digital phase detector. The carrier-envelope beat signal is divided by 16 to enhance the locking range of the PLL. The phase detector acts as a frequency discriminator when the loop is open, the output is thus the difference frequency between the carrier-envelope frequency and the designated locking frequency. The output signal is amplified in the loop filter, which in our case is a proportional and integral controller, and fed back to the AOM, closing the loop. The output of the phase detector is proportional to the remaining jitter between the carrier-envelope phase evolution and the local oscillator reduced by the division ratio 16. The power spectral density (PSD) of the carrier-envelope phase fluctuations are measured with a vector signal analyzer (VSA) at the output of the phase detector. After proper rescaling by the division factor the phase error PSD is shown in Fig. 9.9. The measure-

Image removed due to copyright restrictions.

Please see:

Mucke, Oliver, et al. "Self-Referenced 200 MHz Octave-Spanning Ti: Sapphire Laser with 50 Attosecond Carrier-Envelope Phase Jitter." *Optics Express* 13, no. 13 (June 2005): 5163-5169.

Figure 9.8: Radio-frequency power spectrum measured with a 100 kHz resolution bandwidth (RBW). The peak at the carrier-envelope frequency offset frequency exhibits a signal-to-noise ratio of ~ 35 dB.

ment was taken in steps with an equal amount of points per decade. The PSD of the carrier-envelope phase fluctuations can be integrated to obtain the total phase error. In the range above 1 MHz (see Fig. 9.9), the accuracy of this measurement is limited by the noise floor of the vector signal analyzer. We obtain an integrated carrier-envelope phase jitter of about 0.1 radian over the measured frequency range. The major contribution to the phase noise comes from low frequency fluctuations < 10 kHz. If in addition to the carrier-envelope frequency also the repetition rate of the laser is locked to a frequency standard, such as for example a Cesium clock, the femtosecond laser frequency comb in the optical domain is completely determined with microwave precision and can be used for optical frequency measurements [6].

Image removed due to copyright restrictions.

Please see:

Mucke, Oliver, et al. "Self-Referenced 200 MHz Octave-Spanning Ti: Sapphire Laser with 50 Attosecond Carrier-Envelope Phase Jitter." *Optics Express* 13, no. 13 (June 2005): 5163-5169.

Figure 9.9: Carrier-envelope phase noise power spectral density (left) and integrated phase jitter (right) resulting in only 45 as accumulated carrier-envelope timing jitter.

Bibliography

- [1] H.A. Haus and A. Mecozzi: Noise of mode-locked lasers, *IEEE J. Quantum Electron.* **29**, 983-996 (1993).
- [2] S. Namiki and H. A. Haus: "Observation of nearly quantum-limited timing jitter in a P-APM all fiber ring laser", *J. of the Opt. Soc. of Am. B.*, **13**, 2817-2823 (1996).
- [3] S. Namiki and H. A. Haus: "Noise of the stretched pulse fiber ring laser: Part I—Theory", *IEEE J. of Quantum Electronics*, **33**, 640-659 (1997).
- [4] Ch. Xu, S. Namiki, H. A. Haus: "Noise in the Stretched Pulse Fiber Laser: Part II – Experiments", *IEEE J. of Quantum Electronics*, **33**, 660-668 (1997).
- [5] H.A. Haus and E.P. Ippen: Group velocity of solitons, *Opt. Lett.* **26**, 1654-1656 (2001)
- [6] D. J. Jones, S. A. Diddams, J. K. Ranka, R. S. Windeler, J. L. Hall, and S. T. Cundiff, *Science* **288**, 635 (2000).

Chapter 10

Pulse Characterization

Characterization of ultrashort laser pulses with pulse widths greater than 20 ps can be directly performed electronically using high speed photo detectors and sampling scopes. Photo detectors with bandwidth of 100 GHz are available. For shorter pulses usually some type of autocorrelation or cross-correlation in the optical domain using nonlinear optical effects has to be performed, i.e. the pulse itself has to be used to measure its width, because there are no other controllable events available on such short time scales.

10.1 Intensity Autocorrelation

Pulse duration measurements using second-harmonic intensity autocorrelation is a standard method for pulse characterisation. Figure 10.1 shows the setup for a background free intensity autocorrelation. The input pulse is split in two, and one of the pulses is delayed by τ . The two pulses are focussed into a nonlinear optical crystal in a non-collinear fashion. The nonlinear optical crystal is designed for efficient second harmonic generation over the full bandwidth of the pulse, i.e. it has a large second order nonlinear optical susceptibility and is phase matched for the specific wavelength range. We do not consider the z -dependence of the electric field and phase-matching effects. To simplify notation, we omit normalization factors. The induced nonlinear polarization is expressed as a convolution of two interfering electric-fields $E_1(t)$, $E_2(t)$ with the nonlinear response function of the medium, the

second order nonlinear susceptibility $\chi^{(2)}$.

$$P^{(2)}(t) \propto \iint_{-\infty}^{\infty} \chi^{(2)}(t - t_1, t - t_2) \cdot E_1(t_1) \cdot E_2(t_2) dt_1 dt_2$$

Image removed due to copyright restrictions.

Please see:

Keller, U., Ultrafast Laser Physics, Institute of Quantum Electronics, Swiss Federal Institute of Technology, ETH Hönggerberg—HPT, CH-8093 Zurich, Switzerland.

Figure 10.1: Setup for a background free intensity autocorrelation. To avoid dispersion and pulse distortions in the autocorrelator reflective optics can be used and a thin crystal has to be used for measuring very short, typically sub-100 fs pulses.

We assume the material response is instantaneous and replace $\chi^{(2)}(t - t_1, t - t_2)$ by a Dirac delta-function $\chi^{(2)} \cdot \delta(t - t_1) \cdot \delta(t - t_2)$ which leads to

$$P^{(2)}(t) \propto E_1(t) \cdot E_2(t) \tag{10.1}$$

Due to momentum conservation, see Figure 10.1, we may separate the product $E(t) \cdot E(t - \tau)$ geometrically and suppress a possible background coming from simple SHG of the individual pulses alone. The signal is zero if the pulses don't overlap.

$$P^{(2)}(t) \propto E(t) \cdot E(t - \tau). \tag{10.2}$$

Image removed due to copyright restrictions.

Please see:

Keller, U., Ultrafast Laser Physics, Institute of Quantum Electronics, Swiss Federal Institute of Technology, ETH Honggerberg—HPT, CH-8093 Zurich, Switzerland.

Table 10.1: Pulse shapes and its deconvolution factors relating FWHM, τ_p , of the pulse to FWHM, τ_A , of the intensity autocorrelationfunction.

The electric field of the second harmonic radiation is directly proportional to the polarization, assuming a nondepleted fundamental radiation and the use of thin crystals. Due to momentum conservation, see Figure 10.1, we find

$$I_{AC}(\tau) \propto \int_{-\infty}^{\infty} |A(t)A(t-\tau)|^2 dt. \quad (10.3)$$

$$\propto \int_{-\infty}^{\infty} I(t)I(t-\tau) dt, \quad (10.4)$$

with the complex envelope $A(t)$ and intensity $I(t) = |A(t)|^2$ of the input pulse. The photo detector integrates because its response is usually much slower than the pulsewidth. Note, that the intensity autocorrelation is symmetric by construction

$$I_{AC}(\tau) = I_{AC}(-\tau). \quad (10.5)$$

It is obvious from Eq.(10.3) that the intensity autocorrelation does not contain full information about the electric field of the pulse, since the phase of the pulse in the time domain is completely lost. However, if the pulse shape is known the pulse width can be extracted by deconvolution of the correlation function. Table 10.1 gives the deconvolution factors for some often used pulse shapes.

10.2 Interferometric Autocorrelation (IAC)

A pulse characterization method, that also reveals the phase of the pulse is the interferometric autocorrelation introduced by J. C. Diels [2], (Figure 10.2 a). The input beam is again split into two and one of them is delayed. However, now the two pulses are sent colinearly into the nonlinear crystal. Only the SHG component is detected after the filter.

Image removed due to copyright restrictions.

Please see:

Keller, U., Ultrafast Laser Physics, Institute of Quantum Electronics, Swiss Federal Institute of Technology, ETH Hönggerberg—HPT, CH-8093 Zurich, Switzerland.

Figure 10.2: (a) Setup for an interferometric autocorrelation. (b) Delay stage, so that both beams are reflected from the same air/medium interface imposing the same phase shifts on both pulses.

The total field $E(t, \tau)$ after the Michelson-Interferometer is given by the two identical pulses delayed by τ with respect to each other

$$E(t, \tau) = E(t + \tau) + E(t) \quad (10.6)$$

$$= A(t + \tau)e^{j\omega_c(t+\tau)}e^{j\phi_{CE}} + A(t)e^{j\omega_c t}e^{j\phi_{CE}}. \quad (10.7)$$

$A(t)$ is the complex amplitude, the term $e^{j\omega_0 t}$ describes the oscillation with the carrier frequency ω_0 and ϕ_{CE} is the carrier-envelope phase. Eq. (10.1) writes

$$P^{(2)}(t, \tau) \propto (A(t + \tau)e^{j\omega_c(t+\tau)}e^{j\phi_{CE}} + A(t)e^{j\omega_c t}e^{j\phi_{CE}})^2 \quad (10.8)$$

This is only ideally the case if the paths for both beams are identical. If for example dielectric or metal beamsplitters are used, there are different reflections involved in the Michelson-Interferometer shown in Fig. 10.2 (a) leading to a differential phase shift between the two pulses. This can be avoided by an exactly symmetric delay stage as shown in Fig. 10.1 (b).

Again, the radiated second harmonic electric field is proportional to the polarization

$$E(t, \tau) \propto (A(t + \tau)e^{j\omega_c(t+\tau)}e^{j\phi_{CE}} + A(t)e^{j\omega_c t}e^{j\phi_{CE}})^2. \quad (10.9)$$

The photo-detector (or photomultiplier) integrates over the envelope of each individual pulse

$$\begin{aligned} I(\tau) &\propto \int_{-\infty}^{\infty} \left| (A(t + \tau)e^{j\omega_c(t+\tau)} + A(t)e^{j\omega_c t})^2 \right|^2 dt. \\ &\propto \int_{-\infty}^{\infty} \left| A^2(t + \tau)e^{j2\omega_c(t+\tau)} \right. \\ &\quad \left. + 2A(t + \tau)A(t)e^{j\omega_c(t+\tau)}e^{j\omega_c t} \right. \\ &\quad \left. + A^2(t)e^{j2\omega_c t} \right|^2 dt. \end{aligned} \quad (10.10)$$

Evaluation of the absolute square leads to the following expression

$$\begin{aligned} I(\tau) &\propto \int_{-\infty}^{\infty} \left[|A(t + \tau)|^4 + 4|A(t + \tau)|^2|A(t)|^2 + |A(t)|^4 \right. \\ &\quad \left. + 2A(t + \tau)|A(t)|^2A^*(t)e^{j\omega_c \tau} + \text{c.c.} \right. \\ &\quad \left. + 2A(t)|A(t + \tau)|^2A^*(t + \tau)e^{-j\omega_c \tau} + \text{c.c.} \right. \\ &\quad \left. + A^2(t + \tau)(A^*(t))^2e^{j2\omega_c \tau} + \text{c.c.} \right] dt. \end{aligned} \quad (10.11)$$

The carrier-envelope phase ϕ_{CE} drops out since it is identical to both pulses. The interferometric autocorrelation function is composed of the following terms

$$I(\tau) = I_{back} + I_{int}(\tau) + I_{\omega}(\tau) + I_{2\omega}(\tau). \quad (10.12)$$

Background signal I_{back} :

$$I_{back} = \int_{-\infty}^{\infty} (|A(t+\tau)|^4 + |A(t)|^4) dt = 2 \int_{-\infty}^{\infty} I^2(t) dt \quad (10.13)$$

Intensity autocorrelation $I_{int}(\tau)$:

$$I_{int}(\tau) = 4 \int_{-\infty}^{\infty} |A(t+\tau)|^2 |A(t)|^2 dt = 4 \int_{-\infty}^{\infty} I(t+\tau) \cdot I(t) dt \quad (10.14)$$

Coherence term oscillating with ω_c : $I_{\omega}(\tau)$:

$$I_{\omega}(\tau) = 4 \int_{-\infty}^{\infty} \text{Re} \left[\left(I(t) + I(t+\tau) \right) A^*(t) A(t+\tau) e^{j\omega\tau} \right] dt \quad (10.15)$$

Coherence term oscillating with $2\omega_c$: $I_{2\omega}(\tau)$:

$$I_{2\omega}(\tau) = 2 \int_{-\infty}^{\infty} \text{Re} \left[A^2(t) (A^*(t+\tau))^2 e^{j2\omega\tau} \right] dt \quad (10.16)$$

Eq. (10.12) is often normalized relative to the background intensity I_{back} resulting in the interferometric autocorrelation trace

$$I_{IAC}(\tau) = 1 + \frac{I_{int}(\tau)}{I_{back}} + \frac{I_{\omega}(\tau)}{I_{back}} + \frac{I_{2\omega}(\tau)}{I_{back}}. \quad (10.17)$$

Eq. (10.17) is the final equation for the normalized interferometric autocorrelation. The term $I_{int}(\tau)$ is the intensity autocorrelation, measured by non-colinear second harmonic generation as discussed before. Therefore, the averaged interferometric autocorrelation results in the intensity autocorrelation sitting on a background of 1.

Fig. 10.3 shows a calculated and measured IAC for a sech-shaped pulse.

Image removed due to copyright restrictions.

Please see:

Keller, U., Ultrafast Laser Physics, Institute of Quantum Electronics, Swiss Federal Institute of Technology, ETH Honggerberg—HPT, CH-8093 Zurich, Switzerland.

Figure 10.3: Computed and measured interferometric autocorrelation traces for a 10 fs long sech-shaped pulse.

As with the intensity autocorrelation, by construction the interferometric autocorrelation has to be also symmetric:

$$I_{IAC}(\tau) = I_{IAC}(-\tau) \quad (10.18)$$

This is only true if the beam path between the two replicas in the setup are completely identical, i.e. there is not even a phase shift between the two pulses. A phase shift would lead to a shift in the fringe pattern, which shows up very strongly in few-cycle long pulses. To avoid such a symmetry breaking, one has to arrange the delay line as shown in Figure 10.2 b so that each pulse travels through the same amount of substrate material and undergoes the same reflections.

At $\tau = 0$, all integrals are identical

$$\begin{aligned}
 I_{back} &\equiv 2 \int |A(t)|^4 dt \\
 I_{int}(\tau = 0) &\equiv 2 \int |A^2(t)|^2 dt = 2 \int |A(t)|^4 dt = I_{back} \\
 I_{\omega}(\tau = 0) &\equiv 2 \int |A(t)|^2 A(t) A^*(t) dt = 2 \int |A(t)|^4 dt = I_{back} \\
 I_{2\omega}(\tau = 0) &\equiv 2 \int A^2(t) (A^2(t))^* dt = 2 \int |A(t)|^4 dt = I_{back}
 \end{aligned} \tag{10.19}$$

Then, we obtain for the interferometric autocorrelation at zero time delay

$$\begin{aligned}
 I_{IAC}(\tau)|_{\max} &= I_{IAC}(0) = 8 \\
 I_{IAC}(\tau \rightarrow \pm\infty) &= 1 \\
 I_{IAC}(\tau)|_{\min} &= 0
 \end{aligned} \tag{10.20}$$

This is the important 1:8 ratio between the wings and the pick of the IAC, which is a good guide for proper alignment of an interferometric autocorrelator. For a chirped pulse the envelope is not any longer real. A chirp in the pulse results in nodes in the IAC. Figure 10.4 shows the IAC of a chirped sech-pulse

$$A(t) = \left(\operatorname{sech} \left(\frac{t}{\tau_p} \right) \right)^{(1+j\beta)}$$

for different chirps.

Image removed due to copyright restrictions.

Please see:

Keller, U., Ultrafast Laser Physics, Institute of Quantum Electronics, Swiss Federal Institute of Technology, ETH Hönggerberg—HPT, CH-8093 Zurich, Switzerland.

Figure 10.4: Influence of increasing chirp on the IAC.

10.2.1 Interferometric Autocorrelation of an Unchirped Sech-Pulse

Envelope of an unchirped sech-pulse

$$A(t) = \operatorname{sech}(t/\tau_p) \quad (10.21)$$

Interferometric autocorrelation of a sech-pulse

$$I_{IAC}(\tau) = 1 + \{2 + \cos(2\omega_c\tau)\} \frac{3 \left(\left(\frac{\tau}{\tau_p} \right) \cosh \left(\frac{\tau}{\tau_p} \right) - \sinh \left(\frac{\tau}{\tau_p} \right) \right)}{\sinh^3 \left(\frac{\tau}{\tau_p} \right)} + \frac{3 \left(\sinh \left(\frac{2\tau}{\tau_p} \right) - \left(\frac{2\tau}{\tau_p} \right) \right)}{\sinh^3 \left(\frac{\tau}{\tau_p} \right)} \cos(\omega_c\tau) \quad (10.22)$$

10.2.2 Interferometric Autocorrelation of a Chirped Gaussian Pulse

Complex envelope of a Gaussian pulse

$$A(t) = \exp \left[-\frac{1}{2} \left(\frac{t}{t_p} \right)^2 (1 + j\beta) \right]. \quad (10.23)$$

Interferometric autocorrelation of a Gaussian pulse

$$\begin{aligned} I_{IAC}(\tau) = & 1 + \left\{ 2 + e^{-\frac{\beta^2}{2} \left(\frac{\tau}{\tau_p} \right)^2} \cos(2\omega_c \tau) \right\} e^{-\frac{1}{2} \left(\frac{\tau}{\tau_p} \right)^2} \\ & + 4e^{-\frac{3+\beta^2}{8} \left(\frac{\tau}{\tau_p} \right)^2} \cos \left(\frac{\beta}{4} \left(\frac{\tau}{\tau_p} \right)^2 \right) \cos(\omega_c \tau). \end{aligned} \quad (10.24)$$

10.2.3 Second Order Dispersion

It is fairly simple to compute in the Fourier domain what happens in the presence of dispersion.

$$E(t) = A(t)e^{j\omega_c t} \xrightarrow{F} \tilde{E}(\omega) \quad (10.25)$$

After propagation through a dispersive medium we obtain in the Fourier domain.

$$\tilde{E}'(\omega) = \tilde{E}(\omega)e^{-i\Phi(\omega)}$$

and

$$E'(t) = A'(t)e^{j\omega_c t}$$

Figure 10.5 shows the pulse amplitude before and after propagation through a medium with second order dispersion. The pulse broadens due to the dispersion. If the dispersion is further increased the broadening increases and the interferometric autocorrelation traces shown in Figure 10.5 develop a characteristic pedestal due to the term I_{int} . The width of the interferometrically sensitive part remains the same and is more related to the coherence time in the pulse, that is proportional to the inverse spectral width and does not change.

Image removed due to copyright restrictions.

Please see:

Keller, U., Ultrafast Laser Physics, Institute of Quantum Electronics, Swiss Federal Institute of Technology, ETH Hönggerberg—HPT, CH-8093 Zurich, Switzerland.

Figure 10.5: Effect of various amounts of second order dispersion on a transform limited 10 fs Sech-pulse.

10.2.4 Third Order Dispersion

We expect, that third order dispersion affects the pulse significantly for

$$\frac{D_3}{\tau^3} > 1$$

which is for a 10fs sech-pulse $D_3 > \left(\frac{10 \text{ fs}}{1.76}\right)^3 \sim 183 \text{ fs}^3$. Figure 10.6 and 10.7 show the impact on pulse shape and interferometric autocorrelation. The odd dispersion term generates asymmetry in the pulse. The interferometric autocorrelation develops characteristic nodes in the wings.

Image removed due to copyright restrictions.

Please see:

Keller, U., Ultrafast Laser Physics, Institute of Quantum Electronics, Swiss Federal Institute of Technology, ETH Hönggerberg—HPT, CH-8093 Zurich, Switzerland.

Figure 10.6: Impact of 200 fs^3 third order dispersion on a 10 fs pulse at a center wavelength of 800 nm. and its interferometric autocorrelation.

Image removed due to copyright restrictions.

Please see:

Keller, U., Ultrafast Laser Physics, Institute of Quantum Electronics, Swiss Federal Institute of Technology, ETH Hönggerberg—HPT, CH-8093 Zurich, Switzerland.

Figure 10.7: Changes due to increasing third order Dispersion from 100-1000 fs^3 on a 10 fs pulse at a center wavelength of 800 nm.

10.2.5 Self-Phase Modulation

Self-phase modulation without compensation by proper negative dispersion generates a phase over the pulse in the time domain. This phase is invisible in the intensity autocorrelation, however it shows up clearly in the IAC, see Figure 10.8 for a Gaussian pulse with a peak nonlinear phase shift $\phi_0 = \delta A_0^2 = 2$ and Figure 10.8 for a nonlinear phase shift $\phi_0 = 3$.

Image removed due to copyright restrictions.

Please see:

Keller, U., Ultrafast Laser Physics, Institute of Quantum Electronics, Swiss Federal Institute of Technology, ETH Hönggerberg—HPT, CH-8093 Zurich, Switzerland.

Figure 10.8: Change in pulse shape and interferometric autocorrelation in a 10 fs pulse at 800 nm subject to pure self-phase modulation leading to a nonlinear phase shift of $\phi_0 = 2$.

Image removed due to copyright restrictions.

Please see:

Keller, U., *Ultrafast Laser Physics*, Institute of Quantum Electronics, Swiss Federal Institute of Technology, ETH Hönggerberg—HPT, CH-8093 Zurich, Switzerland.

Figure 10.9: Change in pulse shape and interferometric autocorrelation in a 10 fs pulse at 800 nm subject to pure self-phase modulation leading to a nonlinear phase shift of $\phi_0 = 3$.

From the experience gained by looking at the above IAC-traces for pulses undergoing second and third order dispersions as well as self-phase modulation we conclude that it is in general impossible to predict purely by looking at the IAC what phase perturbations a pulse might have. Therefore, it was always a wish to reconstruct uniquely the electrical field with respect to amplitude and phase from the measured data. In fact one can show rigorously, that amplitude and phase of a pulse can be derived uniquely from the IAC and the measured spectrum up to a time reversal ambiguity [1]. Furthermore, it has been shown that a cross-correlation of the pulse with a replica

chirped in a known medium and the pulse spectrum is enough to reconstruct the pulse [3]. Since the spectrum of the pulse is already given only the phase has to be determined. If a certain phase is assumed, the electric field and the measured cross-correlation or IAC can be computed. Minimization of the error between the measured cross-correlation or IAC will give the desired spectral phase. This procedure has been dubbed PICASO (Phase and Intensity from Cross Correlation and Spectrum Only).

Note, also instead of measuring the autocorrelation and interferometric autocorrelation with SHG one can also use two-photon absorption or higher order absorption in a semiconductor material (Laser or LED) [4].

However today, the two widely used pulse characterization techniques are Frequency Resolved Optical Gating (FROG) and Spectral Phase Interferometry for Direct Electric Field Reconstruction (SPIDER)

10.3 Frequency Resolved Optical Gating (FROG)

We follow closely the book of the FROG inventor Rich Trebino. In frequency resolved optical gating, the pulse to be characterized is gated by another ultrashort pulse [5]. The gating is no simple linear sampling technique, but the pulses are crossed in a medium with an instantaneous nonlinearity ($\chi^{(2)}$ or $\chi^{(3)}$) in the same way as in an autocorrelation measurement (Figures 10.1 and 10.10). The FROG-signal is a convolution of the unknown electric-field $E(t)$ with the gating-field $g(t)$ (often a copy of the unknown pulse itself). However, after the interaction of the pulse to be measured and the gate pulse, the emitted nonlinear optical radiation is not put into a simple photo detector, but is instead spectrally resolved detected. The general form of the frequency-resolved intensity, or Spectrogram $S_F(\tau, \omega)$ is given by

$$S_F(\tau, \omega) \propto \left| \int_{-\infty}^{\infty} E(t) \cdot g(t - \tau) e^{-j\omega t} dt \right|^2. \quad (10.26)$$

Image removed due to copyright considerations.

Figure 10.10: The spectrogram of a waveform $E(t)$ tells the intensity and frequency in a given time interval [5].

Representations of signals, or waveforms in general, by time-frequency distributions has a long history. Most notably musical scores are a temporal sequence of tones giving its frequency and volume, see Fig. 10.11.

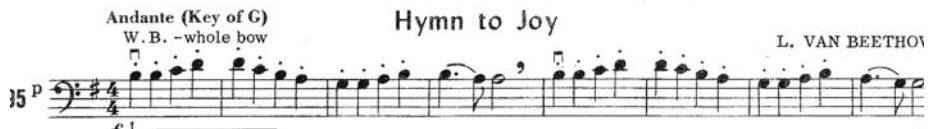


Figure 10.11: A musical score is a time-frequency representation of the signal to be played.

Time-frequency representations are well known in the radar community, signal processing and quantum mechanics [9] (Spectrogram, Wigner-Distribution, Husimi-Distribution, ...), Figure 10.12 shows the spectrogram of differently chirped pulses. Like a musical score, the spectrogram visually displays the frequency vs. time.

Image removed due to copyright considerations.

Figure 10.12: Like a musical score, the spectrogram visually displays the frequency vs. time [5].

Note, that the gate pulse in the FROG measurement technique does not to be very short. In fact if we have

$$g(t) \equiv \delta(t) \quad (10.27)$$

then

$$S_F(\tau, \omega) = |E(\tau)|^2 \quad (10.28)$$

and the phase information is completely lost. There is no need for short gate pulses. A gate length of the order of the pulse length is sufficient. It temporally resolves the slow components and spectrally the fast components.

10.3.1 Polarization Gate FROG

Figure 10.13 shows the setup [6][7]. FROG is based on the generation of a well defined gate pulse, eventually not yet known. This can be achieved by using the pulse to be measured and an ultrafast nonlinear interaction. For example the electronic Kerr effect can be used to induce an ultrafast polarization modulation, that can gate the pulse with a copy of the same pulse.

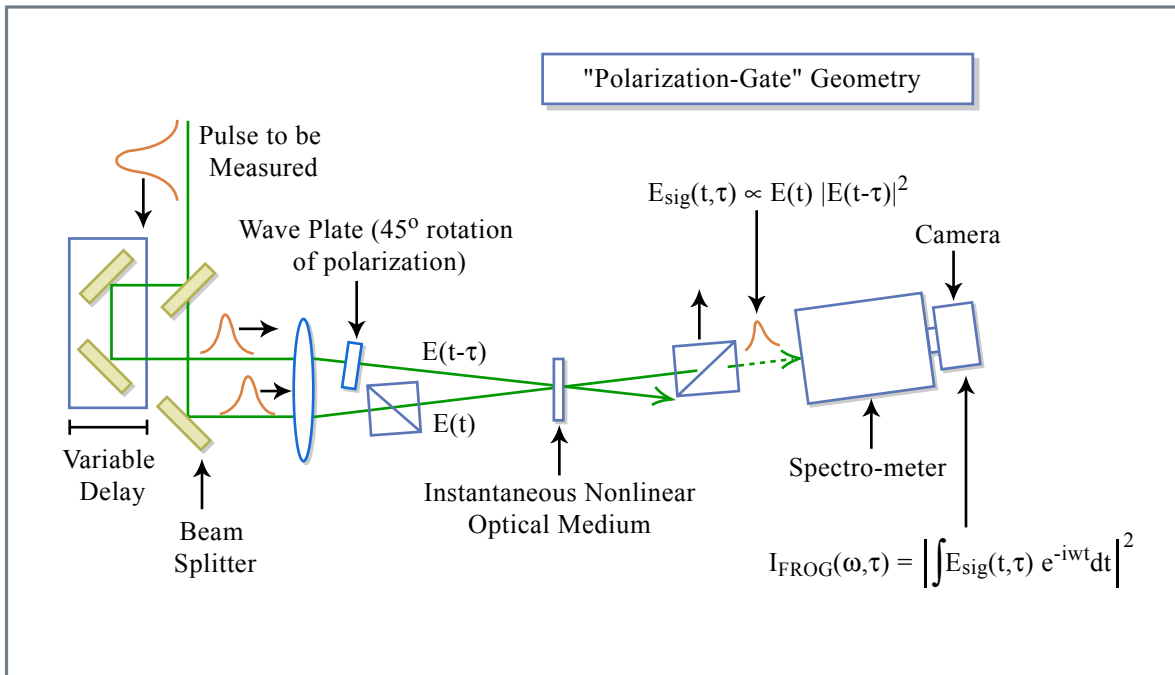


Figure 10.13: Polarization Gate FROG setup. The instantaneous Kerr-effect is used to rotate the polarization of the signal pulse $E(t)$ during the presence of the gate pulse $E(t - \tau)$ proportional to the intensity of the gate pulse [5].

Figure by MIT OCW.

The signal analyzed in the FROG trace is, see Figure 10.14,

$$E_{sig}(t, \tau) = E(t) |E(t - \tau)|^2 \quad (10.29)$$

Image removed due to copyright considerations.

Figure 10.14: The signal pulse reflects the color of the gated pulse at the time $2\tau/3$ [5]

The FROG traces generated from a PG-FROG for chirped pulses is identical to Fig. 10.12. Figure 10.15 shows FROG traces of more complicated pulses

Image removed due to copyright considerations.

Figure 10.15: FROG traces of more complicated pulses.

10.3.2 FROG Inversion Algorithm

Spectrogram inversion algorithms need to know the gate function $g(t - \tau)$, which in the given case is related to the yet unknown pulse. So how do we get from the FROG trace to the pulse shape with respect to amplitude and phase? If there is such an algorithm, which produces solutions, the question of uniqueness of this solution arises. To get insight into these issues, we realize, that the FROG trace can be written as

$$I_{FROG}(\tau, \omega) \propto \left| \int_{-\infty}^{\infty} E_{sig}(t, \tau) e^{-j\omega t} dt \right|^2 \quad (10.30)$$

Writing the signal field as a Fourier transform in the time variable, i.e.

$$E_{sig}(t, \tau) = \int_{-\infty}^{\infty} \hat{E}_{sig}(t, \Omega) e^{-j\Omega \tau} d\Omega \quad (10.31)$$

yields

$$I_{FROG}(\tau, \omega) \propto \left| \int_{-\infty}^{\infty} \int_{-\infty}^{\infty} \hat{E}_{sig}(t, \Omega) e^{-j\omega t - j\Omega \tau} dt d\Omega \right|^2. \quad (10.32)$$

This equation shows that the FROG-trace is the magnitude square of a two-dimensional Fourier transform related to the signal field $E_{sig}(t, \tau)$. The inversion of Eq.(10.32) is known as the 2D-phase retrieval problem. Fortunately algorithms for this inversion exist [8] and it is known that the magnitude (or magnitude square) of a 2D-Fourier transform (FT) essentially uniquely determines also its phase, if additional conditions, such as finite support or the relationship (10.29) is given. Essentially unique means, that there are ambiguities but they are not dense in the function space of possible 2D-transforms, i.e. they have probability zero to occur.

Furthermore, the unknown pulse $E(t)$ can be easily obtained from the modified signal field $\hat{E}_{sig}(t, \Omega)$ because

$$\hat{E}_{sig}(t, \Omega) = \int_{-\infty}^{\infty} E_{sig}(t, \tau) e^{j\Omega \tau} d\tau \quad (10.33)$$

$$= \int_{-\infty}^{\infty} E(t) g(t - \tau) e^{-j\Omega \tau} d\tau \quad (10.34)$$

$$= E(t) G^*(\Omega) e^{-j\Omega t} \quad (10.35)$$

with

$$G(\Omega) = \int_{-\infty}^{\infty} g(\tau) e^{-j\Omega \tau} d\tau. \quad (10.36)$$

Thus there is

$$E(t) \propto \hat{E}_{sig}(t, 0). \quad (10.37)$$

The only condition is that the gate function should be chosen such that $G(\Omega) \neq 0$. This is very powerful.

Fourier Transform Algorithm

The Fourier transform algorithm also commonly used in other phase retrieval problems is schematically shown in Fig. 10.16

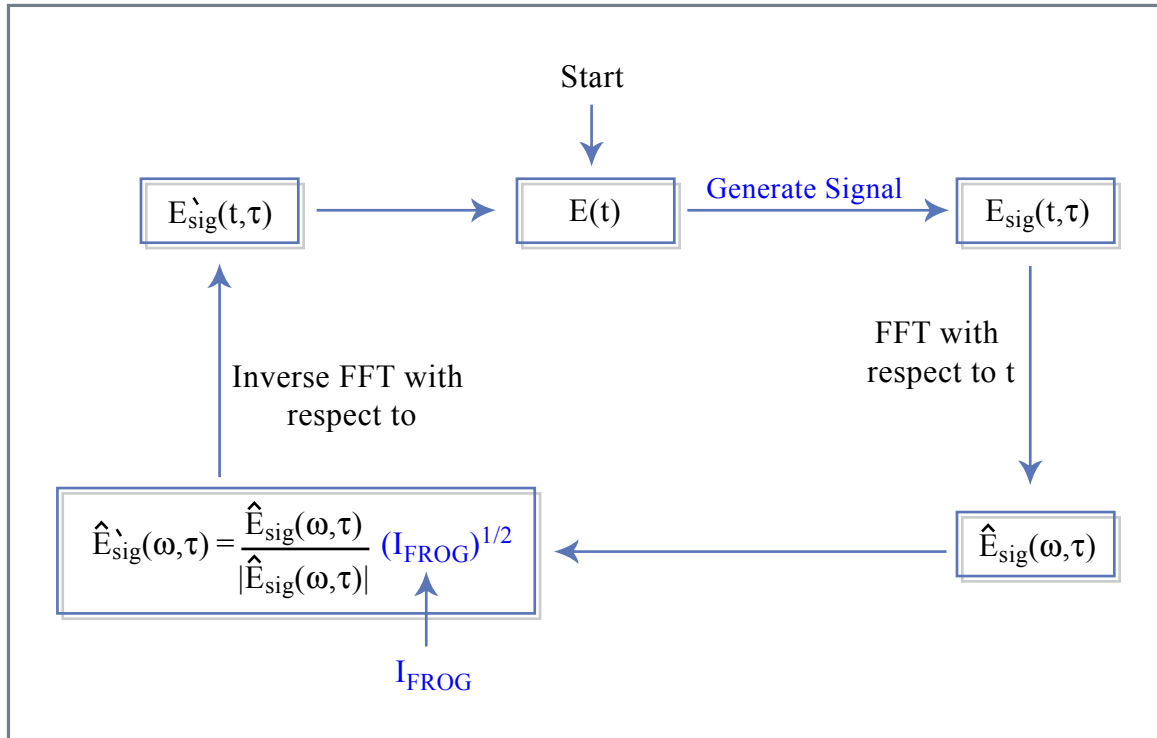


Figure 10.16: Fourier transform algorithm for FROG trace inversion. The blue operations indicate the constraints due to the gating technique used and the FROG data [5]
 Figure by MIT OCW.

Generalized Projections

The signal field $E_{sig}(t, \tau)$ has to fulfill two constraints, which define sets see Fig. 10.17. The intersection between both sets results in yields $E(t)$. Moving to the closest point in one constraint set and then the other yields convergence to the solution, if the two sets or convex. Unfortunately, the FROG constraints are not convex. Nevertheless the algorithm works surprisingly well. For more information consult with reference [5].

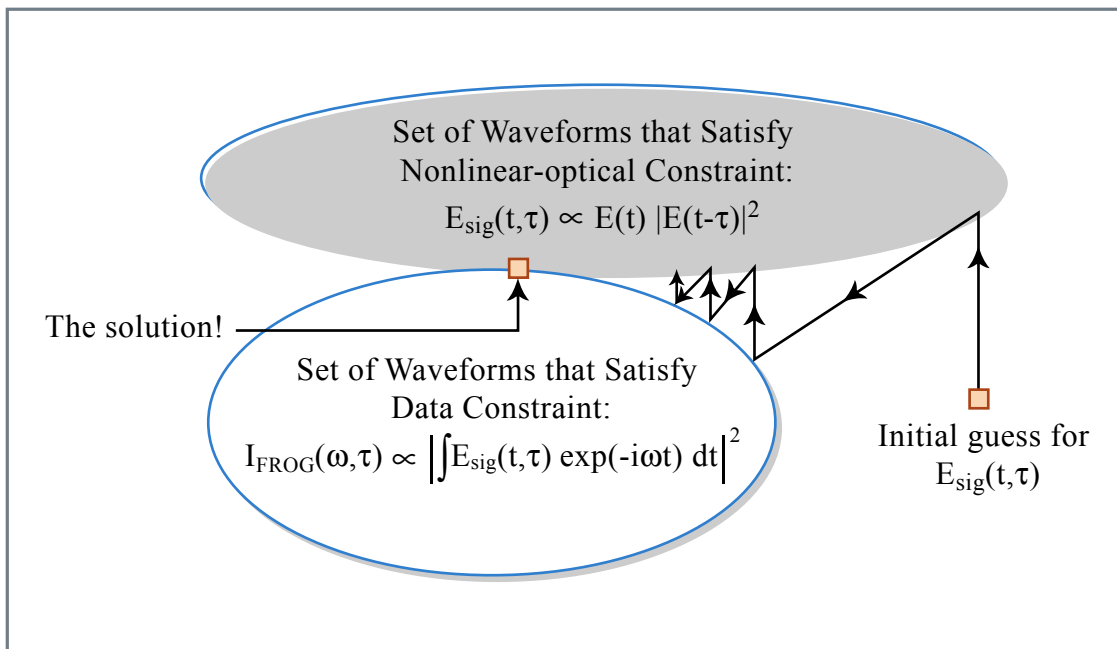


Figure 10.17: Generalized Projections applied to FROG [5].

10.3.3 Second Harmonic FROG

So far we only discussed PG-FROG. However, if we choose a $\chi^{(2)}$ nonlinearity, e.g. SHG, and set the gating-field equal to a copy of the pulse $g(t) \equiv E(t)$, we are measuring in eq.(10.26) the spectrally resolved autocorrelation signal. The marginals of the measured FROG-trace do have the following properties

$$\int_{-\infty}^{\infty} S_F(\tau, \omega) d\omega \propto \int_{-\infty}^{\infty} |E(t)|^2 \cdot |g(t - \tau)|^2 dt = I_{AC}(\tau). \quad (10.38)$$

$$\int_{-\infty}^{\infty} S_F(\tau, \omega) d\tau \propto \left| \int_{-\infty}^{\infty} \hat{E}(\omega) \cdot \hat{G}(\omega - \omega')^2 d\omega' \right| = \left| \hat{E}_{2\omega}(\omega) \right|^2. \quad (10.39)$$

For the case, where $g(t) \equiv E(t)$, we obtain

$$\int_{-\infty}^{\infty} S_F(\tau, \omega) d\omega \propto I_{AC}(\tau). \quad (10.40)$$

$$\int_{-\infty}^{\infty} S_F(\tau, \omega) d\tau \propto \left| \hat{E}_{2\omega}(\omega) \right|^2. \quad (10.41)$$

The setup to measure the Frog-trace is identical with the setup to measure the intensity autocorrelation function (Figure 10.1) only the photodiode for the second harmonic is replaced by a spectrometer (Figure 10.18).

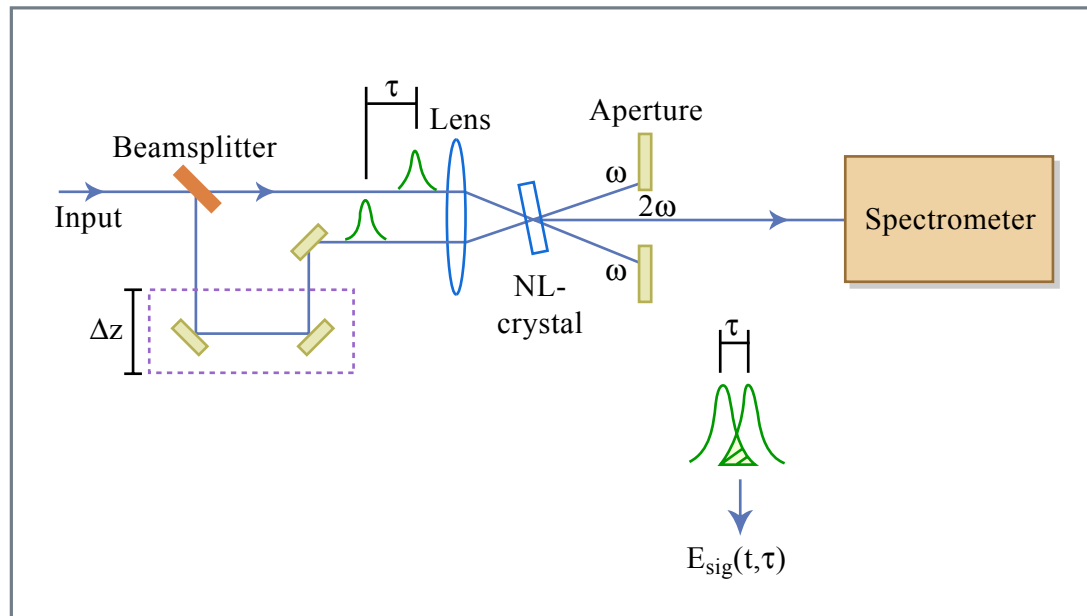


Figure 10.18: SHG-FROG setup.

Figure by MIT OCW.

Since the intensity autocorrelation function and the integrated spectrum can be measured simultaneously, this gives redundancy to check the correctness of all measurements via the marginals (10.38, 10.39). Figure 10.19 shows the SHG-FROG trace of the shortest pulses measured so far with FROG.

Image removed due to copyright restrictions.

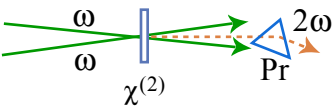
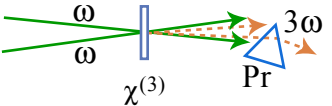
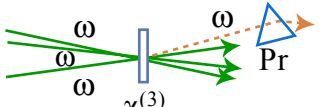
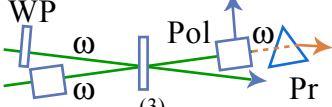
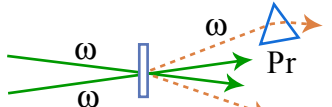
Please see:

Baltuska, Pshenichnikov, and Wiersma. *Journal of Quantum Electronics* 35 (1999): 459.

Figure 10.19: FROG measurement of a 4.5 fs laser pulse.

10.3.4 FROG Geometries

The Frog-signal E_{sig} can also be generated by a nonlinear interaction different from SHG or PG, see table 10.20[5].

FROG Geometries: Pros and Cons			
	Sensitivity	Ambiguities	
SHG 	.001 nJ	Direction of time; Rel. phase of multiple pulses	Most sensitive; most accurate
THG 	1 nJ	Relative phase of multiple pulses	Tightly focused beams
TG 	10 nJ	None	Useful for UV and transient-grating experiments
PG 	100 nJ	None	Simple, intuitive, best scheme for amplified pulses
SD 	1000 nJ	None	Useful for UV

SHG = Second-harmonic generation THG = Third-harmonic generation TG = Transient-grating
 PG = Polarization-gate SD = Self-diffraction

Figure 10.20: FROG geometries and their pros and cons.

Figure by MIT OCW.

10.4 Spectral Interferometry and SPIDER

Spectral Phase Interferometry for Direct Electric-Field Reconstruction (SPIDER) avoids iterative reconstruction of the phase profile. Iterative Fourier transform algorithms do have the disadvantage of sometimes being rather time consuming, preventing real-time pulse characterization. In addition, for "pathological" pulse forms, reconstruction is difficult or even impossible. It is mathematically not proven that the retrieval algorithms are unambiguous especially in the presence of noise.

Spectral shearing interferometry provides an elegant method to overcome these disadvantages. This technique has been first introduced by C. Iaconis and I.A. Walmsley in 1999 [11] and called spectral phase interferometry for direct electric-field reconstruction – SPIDER. Before we discuss SPIDER let's look at spectral interferometry in general

10.4.1 Spectral Interferometry

The spectrum of a pulse can easily be measured with a spectrometer. The pulse would be completely known, if we could determine the phase across the spectrum. To determine this unknown phase spectral interferometry for pulse measurement has been proposed early on by Froehly and others [12]. If we would have a well referenced pulse with field $E_R(t)$, superimpose the unknown electric field $E_S(t)$ delayed with the reference pulse and interfere them in a spectrometer, see Figure 10.21, we obtain for the spectrometer output

$$E_I(t) = E_R(t) + E_S(t - \tau) \quad (10.42)$$

$$\hat{S}(\omega) = \left| \int_{-\infty}^{+\infty} E_I(t) e^{-j\omega t} dt \right|^2 = \left| \hat{E}_R(\omega) + \hat{E}_S(\omega) e^{-j\omega\tau} \right|^2 \quad (10.43)$$

$$= \hat{S}_{DC}(\omega) + \hat{S}^{(-)}(\omega) e^{j\omega\tau} + \hat{S}^{(+)}(\omega) e^{-j\omega\tau} \quad (10.44)$$

with

$$\hat{S}^{(+)}(\omega) = \hat{E}_R^*(\omega) \hat{E}_S(\omega) \quad (10.45)$$

$$\hat{S}^{(-)}(\omega) = \hat{S}^{(+)*}(\omega) \quad (10.46)$$

Where (+) and (-) indicate as before, well separated positive and negative "frequency" signals, where "frequency" is now related to τ rather than ω .

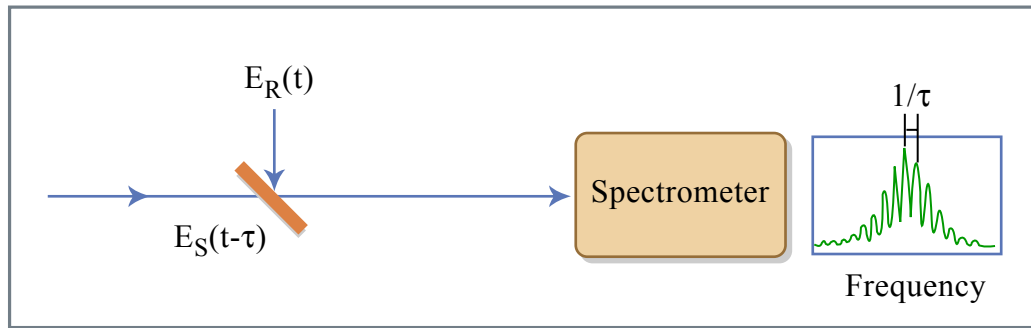


Figure 10.21: Spectral Interferometry of a signal pulse with a reference pulse.

Figure by MIT OCW.

If τ is chosen large enough, the inverse Fourier transformed spectrum $S(t) = F^{-1}\{\hat{S}(\omega)\}$ results in well separated signals, see Figure 10.22.

$$S(t) = S_{DC}(t) + S^{(-)}(t + \tau) + \hat{S}^{(+)}(t - \tau) \quad (10.47)$$

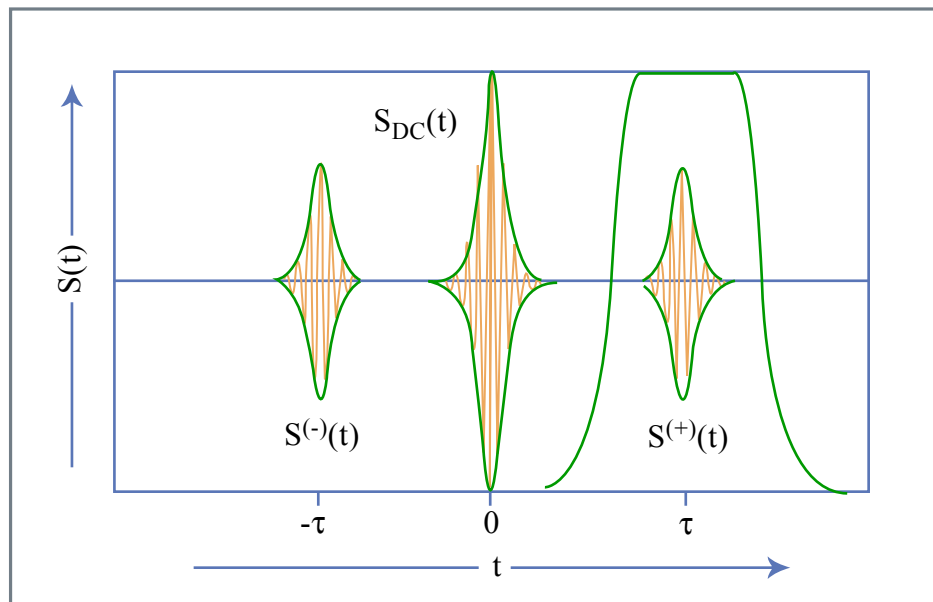


Figure 10.22: Decomposition of SPIDER signal.

Figure by MIT OCW.

We can isolate either the positive or negative frequency term with a filter in the time domain. Back transformation of the corresponding term to the frequency domain and computation of the spectral phase of one of the terms results in the spectral phase of the signal up to the known phase of the reference pulse and a linear phase contribution from the delay.

$$\Phi^{(+)}(\omega) = \arg\{\hat{S}^{(+)}(\omega)e^{j\omega\tau}\} = \varphi_S(\omega) - \varphi_R(\omega) + \omega\tau \quad (10.48)$$

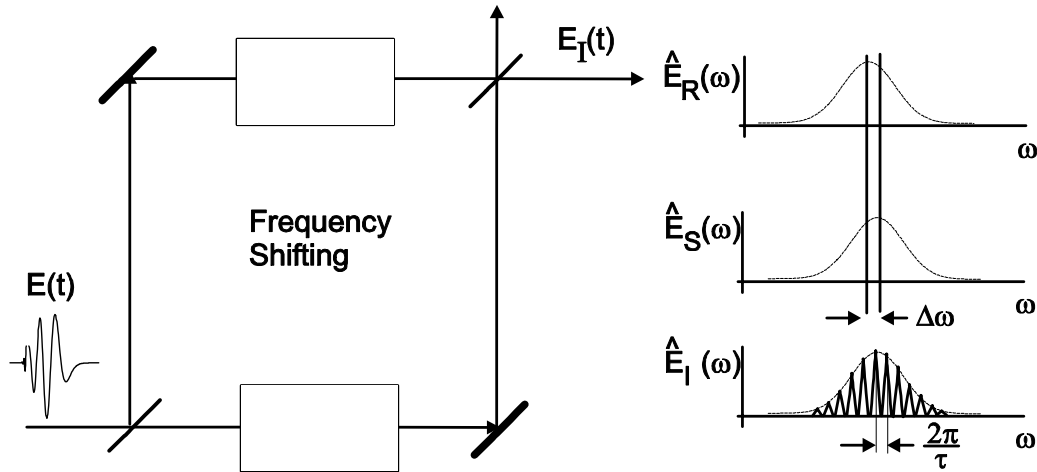


Figure 10.23: The principle of operation of SPIDER.

Adapted from F. X. Kaertner. *Few-Cycle Laser Pulse Generation and its Applications*. New York, NY: Springer-Verlag, 2004.

10.4.2 SPIDER

What can we do if we don't have a well characterized reference pulse? C. Iaconis and I.A. Walmsley [?] came up with the idea of generating two up-converted spectra slightly shifted in frequency and to investigate the spectral interference of these two copies, see Figure 10.23. We use

$$E_R(t) = E(t)e^{j\omega_s t} \quad (10.49)$$

$$E_S(t) = E(t - \tau)e^{j(\omega_s + \Omega)t} \quad (10.50)$$

$$E_I(t) = E_R(t) + E_S(t) \quad (10.51)$$

where ω_s and $\omega_s + \Omega$ are the two frequencies used for upconversion and Ω is called the spectral shear between the two pulses. $E(t)$ is the unknown electric field with spectrum

$$\hat{E}(\omega) = \left| \hat{E}(\omega) \right| e^{j\varphi(\omega)} \quad (10.52)$$

Spectral interferometry using these specially constructed signal and reference pulses results in

$$\hat{S}(\omega) = \left| \int_{-\infty}^{+\infty} E_I(t)e^{-j\omega t} dt \right|^2 = \hat{S}_{DC}(\omega) + \hat{S}^{(-)}(\omega)e^{j\omega\tau} + \hat{S}^{(+)}(\omega)e^{-j\omega\tau} \quad (10.53)$$

$$\hat{S}^{(+)}(\omega) = \hat{E}_R^*(\omega)\hat{E}_S(\omega) = \hat{E}^*(\omega - \omega_s)\hat{E}(\omega - \omega_s - \Omega) \quad (10.54)$$

$$\hat{S}^{(-)}(\omega) = \hat{S}^{(+)*}(\omega) \quad (10.55)$$

The phase $\psi(\omega) = \arg[\hat{S}^{(+)}(\omega)e^{-j\omega\tau}]$ derived from the isolated positive spectral component is

$$\psi(\omega) = \varphi(\omega - \omega_s - \Omega) - \varphi(\omega - \omega_s) - \omega\tau. \quad (10.56)$$

The linear phase $\omega\tau$ can be subtracted off after independent determination of the time delay τ . It is obvious that the spectral shear Ω has to be small compared to the spectral bandwidth $\Delta\omega$ of the pulse, see Fig. 10.23. Then the phase difference in Eq.(10.56) is proportional to the group delay in the pulse, i.e.

$$-\Omega \frac{d\varphi}{d\omega} = \psi(\omega), \quad (10.57)$$

or

$$\varphi(\omega) = -\frac{1}{\Omega} \int_0^\omega \psi(\omega') d\omega'. \quad (10.58)$$

Note, an error $\Delta\tau$ in the calibration of the time delay τ results in an error in the chirp of the pulse

$$\Delta\varphi(\omega) = -\frac{\omega^2}{2\Omega} \Delta\tau. \quad (10.59)$$

Thus it is important to chose a spectral shear Ω that is not too small. How small does it need to be? We essentially sample the phase with a sample spacing Ω . The Nyquist theorem states that we can uniquely resolve a pulse in the time domain if it is only nonzero over a length $[-T, T]$, where $T = \pi/\Omega$. On the other side the shear Ω has to be large enough so that the fringes in the spectrum can be resolved with the available spectrometer.

SPIDER Setup

We follow the work of Gallmann et al. [?] that can be used for characterization of pulses only a few optical cycles in duration. The setup is shown in Figure 10.24.

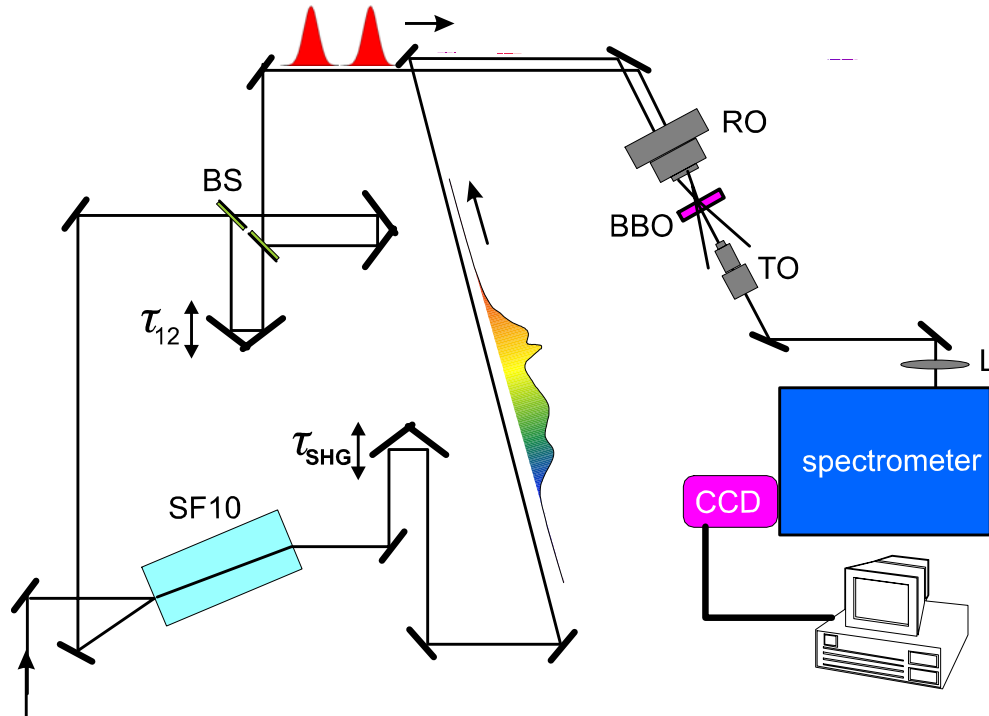


Figure 10.24: SPIDER setup; SF10: 65 mm glass block ($GDD/z \approx 160 \text{ fs}^2/\text{mm}$), BS: metallic beam splitters ($\approx 200 \mu\text{m}$, Cr–Ni coating 100 nm), τ : adjustable delay between the unchirped replica, τ_{SHG} : delay between unchirped pulses and strongly chirp pulse, RO: reflective objective (Ealing–Coherent, x35, NA=0.5, $f=5.4 \text{ mm}$), TO: refractive objective, L: lens, spectrometer: Lot-Oriel MS260i, grating: 4001/mm, Blaze–angle 350 nm, CCD: Andor DU420 CCI 010, 1024 x 255 pixels, $26 \mu\text{m}/\text{pixel}$ [13].

Courtesy of Richard Ell. Used with permission.

Generation of two replica without additional chirp:

A Michelson–type interferometer generates two unchirped replicas. The beam–splitters BS have to be broadband, not to distort the pulses. The delay τ between the two replica has to be properly chosen, i.e. in the setup shown it was about 400–500 fs corresponding to 120–150 μm distance in space.

Spectral shearing:

The spectrally sheared copies of the pulse are generated by sum-frequency generation (SFG) with quasi-monochromatic beams at frequencies ω_s and $\omega_s + \Omega$. These quasi monochromatic signals are generated by strong chirping of a third replica (cf. Fig. 10.24) of the signal pulse that propagates through a strongly dispersive glass slab. For the current setup we estimate for the broadening of a Gaussian pulse due to the glass dispersion from 5 fs to approximately 6 ps. Such a stretching of more than a factor of thousand assures that SFG occurs within an optical bandwidth less than 1 nm, a quasi-monochromatic signal. Adjustment of the temporal overlap τ_{SHG} with the two unchirped replica is possible by a second delay line. The stretched pulse can be computed by propagation of the signal pulse $E(t)$ through the strongly dispersive medium with transfer characteristic

$$H_{glass}(\omega) = e^{-jD_{glass}(\omega-\omega_c)^2/2} \quad (10.60)$$

neglecting linear group delay and higher order dispersion terms. We obtain for the analytic part of the electric field of the stretched pulse leaving the glass block by convolution with the transfer characteristic

$$\begin{aligned} E_{stretch}(t) &= \int_{-\infty}^{+\infty} \hat{E}(\omega) e^{-jD_{glass}(\omega-\omega_c)^2/2} e^{j\omega t} d\omega = \\ &= e^{jt^2/(2D_{glass})} e^{j\omega_c t} \int_{-\infty}^{+\infty} \hat{E}(\omega) e^{-jD_{glass}((\omega-\omega_c)-t/D_{glass})^2/2} d\omega \end{aligned} \quad (10.61)$$

If the spectrum of the pulse is smooth enough, the stationary phase method can be applied for evaluation of the integral and we obtain

$$E_{stretch}(t) \propto e^{j\omega_c(t+t^2/(2D_{glass}))} \hat{E}(\omega = \omega_c + t/D_{glass}) \quad (10.63)$$

Thus the field strength at the position where the instantaneous frequency is

$$\omega_{inst} = \frac{d}{dt} \omega_c(t + t^2/(2D_{glass})) = \omega_c + t/D_{glass} \quad (10.64)$$

is given by the spectral amplitude at that frequency, $\hat{E}(\omega = \omega_c + t/D_{glass})$. For large stretching, i.e.

$$|\tau_p/D_{glass}| \ll |\Omega| \quad (10.65)$$

the up-conversion can be assumed to be quasi monochromatic.

SFG:

A BBO crystal (wedged 10–50 μm) is used for type I phase-matched SFG. Type II phase-matching would allow for higher acceptance bandwidths. The pulses are focused into the BBO-crystal by a reflective objective composed of curved mirrors. The signal is collimated by another objective. Due to SFG with the chirped pulse the spectral shear is related to the delay between both pulses, τ , determined by Eq.(10.64) to be

$$\Omega = -\tau/D_{glass}. \quad (10.66)$$

Note, that conditions (10.65) and (10.66) are consistent with the fact that the delay between the two pulses should be much larger than the pulse width τ_p which also enables the separation of the spectra in Fig.10.22 to determine the spectral phase using the Fourier transform method. For characterization of sub-10fs pulses a crystal thickness around 30 μm is a good compromise. Efficiency is still high enough for common cooled CCD-cameras, dispersion is already sufficiently low and the phase matching bandwidth large enough.

Signal detection and phase reconstruction:

An additional lens focuses the SPIDER signal into a spectrometer with a CCD camera at the exit plane. Data registration and analysis is performed with a computer. The initial search for a SPIDER signal is performed by chopping and Lock-In detection. The chopper wheel is placed in a way that the unchirped pulses are modulated by the external part of the wheel and the chirped pulse by the inner part of the wheel. Outer and inner part have different slit frequencies. A SPIDER signal is then modulated by the difference (and sum) frequency which is discriminated by the Lock-In amplifier. Once a signal is measured, further optimization can be obtained by improving the spatial and temporal overlap of the beams in the BBO-crystal.

One of the advantages of SPIDER is that only the missing phase information is extracted from the measured data. Due to the limited phase-matching bandwidth of the nonlinear crystal and the spectral response of grating and CCD, the fundamental spectrum is not imaged in its original form but rather with reduced intensity in the spectral wings. But as long as the interference fringes are visible any damping in the spectral wings and deformation of the spectrum does not impact the phase reconstruction process the SPIDER

technique delivers the correct information. The SPIDER trace is then generated by detecting the spectral interference of the pulses

$$E_R(t) = E(t)\hat{E}(\omega_s)e^{j\omega_s t} \quad (10.67)$$

$$E_S(t) = E(t - \tau)\hat{E}(\omega_s + \Omega)e^{j(\omega_s + \Omega)t} \quad (10.68)$$

$$E_I(t) = E_R(t) + E_S(t) \quad (10.69)$$

The positive and negative frequency components of the SPIDER trace are then according to Eqs.(10.55)

$$\begin{aligned} \hat{S}^{(+)}(\omega) &= \hat{E}_R^*(\omega)\hat{E}_S(\omega) = \hat{E}^*(\omega - \omega_s)\hat{E}(\omega - \omega_s - \Omega)\hat{E}^*(\omega_s)\hat{E}(\omega_s + \Omega) \\ \hat{S}^{(-)}(\omega) &= \hat{S}^{(+)*}(\omega) \end{aligned} \quad (10.71)$$

and the phase $\psi(\omega) = \arg[\hat{S}^{(+)}(\omega)e^{-j\omega\tau}]$ derived from the isolated positive spectral component subtraction already the linear phase offset is

$$\psi(\omega) = \varphi(\omega - \omega_s - \Omega) - \varphi(\omega - \omega_s) - \varphi(\omega_s + \Omega) + \varphi(\omega_s). \quad (10.72)$$

Thus up to an additional constant it delivers the group delay within the pulse to be characterized. A constant group delay is of no physical significance.

SPIDER-Calibration

This is the most critical part of the SPIDER measurement. There are three quantities to be determined with high accuracy and reproducibility:

- delay τ
- shift ω_s
- shear Ω

Delay τ :

The delay τ is the temporal shift between the unchirped pulses. It appears as a frequency dependent phase term in the SPIDER phase, Eqs. (10.56) and leads to an error in the pulse chirp if not properly subtracted out, see Eq.(10.59).

A determination of τ should preferentially be done with the pulses detected by the spectrometer but without the spectral shear so that the observed fringes are all exactly spaced by $1/\tau$. Such an interferogram may

be obtained by blocking the chirped pulse and overlapping of the individual SHG signals from the two unchirped pulses. A Fourier transform of the interferogram delivers the desired delay τ . In practice, this technique might be difficult to use. Experiment and simulation show that already minor changes of τ (± 1 fs) significantly alter the reconstructed pulse duration ($\approx \pm 1 - 10\%$).

Another way for determination of τ is the following. As already mentioned, τ is accessible by a differentiation of the SPIDER phase with respect to ω . The delay τ therefore represents a constant GDD. An improper determination of τ is thus equivalent to a false GDD measurement. The real physical GDD of the pulse can be minimized by a simultaneous IAC measurement. Maximum signal level, respectively shortest IAC trace means an average GDD of zero. The pulse duration is then only limited by higher order dispersion not depending on τ . After the IAC measurement, the delay τ is chosen such that the SPIDER measurement provides the shortest pulse duration. This is justified because through the IAC we know that the pulse duration is only limited by higher order dispersion and not by the $\text{GDD} \propto \tau$. The disadvantage of this method is that an additional IAC setup is needed.

Shift ω_s :

The SFG process shifts the original spectrum by a frequency $\omega_s \approx 300$ THz towards higher frequencies equivalent to about 450 nm when Ti:sapphire pulses are characterized. If the SPIDER setup is well adjusted, the square of the SPIDER interferogram measured by the CCD is similar to the fundamental spectrum. A determination of the shift can be done by correlating both spectra with each other. Determination of ω_s only influences the frequency too which we assign a give phase value, which is not as critical.

Shear Ω :

The spectral shear is uncritical and can be estimated by the glass dispersion and the delay τ .

10.4.3 Characterization of Sub-Two-Cycle Ti:sapphire Laser Pulses

The setup and the data registration and processing can be optimized such that the SPIDER interferogram and the reconstructed phase, GDD and intensity envelope are displayed on a screen with update rates in the range of 0.5-1s.

Real-time SPIDER measurements enabled the optimization of external

dispersion compensation leading to 4.8 fs pulses directly from a laser [13], see Figure 10.25.

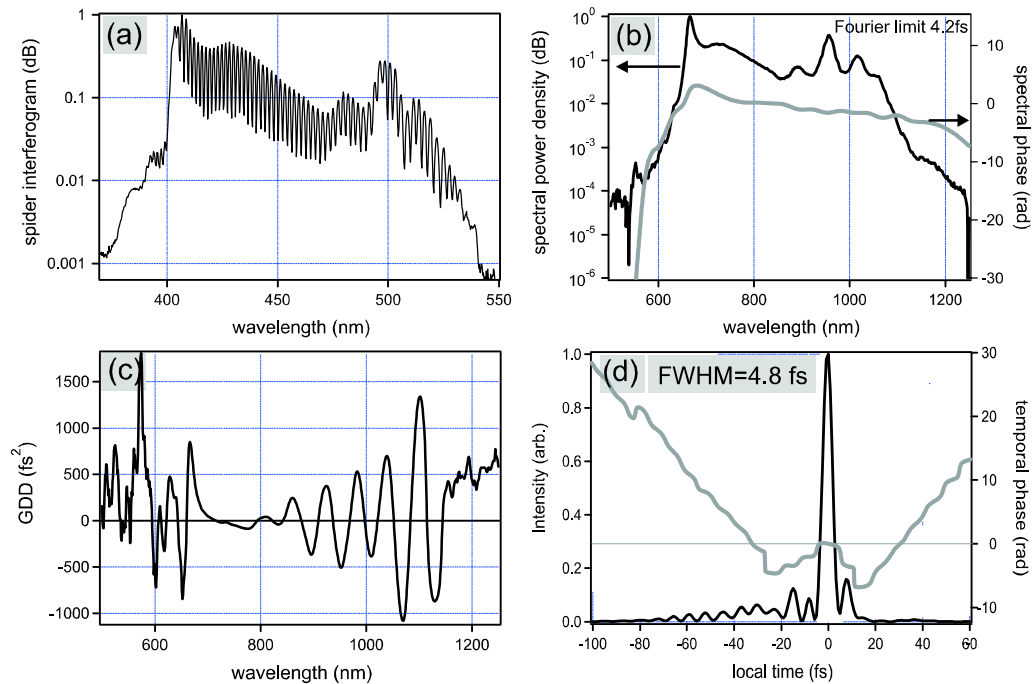


Figure 10.25: SPIDER measurement of a 4.8 fs Ti:sapphire laser pulse. (a) SPIDER interferogram on a logarithmic scale. (b) Spectral power density and spectral phase of the pulse. (c) Calculated GDD of the pulse. (d) Intensity envelope and temporal phase curve [13].

Courtesy of Richard Ell. Used with permission.

Figure 10.25(a) shows the SPIDER interferogram as detected by the CCD camera. The interferogram is modulated up to 90%, the resolutions limit in the displayed graphic can not resolve this. The large number of interference fringes assures reliable phase calculation. Figure (b) displays the laser spectrum registered by the optical spectrum analyzer on a logarithmic scale. The calculated spectral phase curve is added in this plot. The small slope of the phase curve corresponds to a constant GD which is an unimportant time shift. Fig. 10.25 (c) depicts the GDD obtained from the phase by two derivatives with respect to the angular frequency ω . The last Figure (d)

shows the intensity envelope with a FWHM pulse duration of 4.8 fs together with the temporal phase curve.

10.4.4 Pros and Cons of SPIDER

Advantages	Disadvantages
direct analytical phase extraction	complex experimental setup
no moving mirrors or other components	precise delay calibration necessary
possible real-time characterization	"compact" spectrum necessary (no zero-intensity intervals)
simple 1-D data acquisition	need for expensive CCD-camera
minor dependence on spectral response of nonlinear crystal and spectrometer	

Bibliography

- [1] K. Naganuma, K. Mogi, H. Yamada, "General method for ultrashort light pulse chirp measurement," *IEEE J. of Quant. Elec.* **25**, 1225 - 1233 (1989).
- [2] J. C. Diels, J. J. Fontaine, and F. Simoni, "Phase Sensitive Measurement of Femtosecond Laser Pulses From a Ring Cavity," in *Proceedings of the International Conf. on Lasers. 1983*, STS Press: McLean, VA, p. 348-355. J. C. Diels et al., "Control and measurement of Ultrashort Pulse Shapes (in Amplitude and Phase) with Femtosecond Accuracy," *Applied Optics* **24**, 1270-82 (1985).
- [3] J.W. Nicholson, J.Jasapara, W. Rudolph, F.G. Ometto and A.J. Taylor, "Full-field characterization of femtosecond pulses by spectrum and cross-correlation measurements," *Opt. Lett.* **24**, 1774 (1999).
- [4] D. T. Reid, et al., *Opt. Lett.* **22**, 233-235 (1997).
- [5] R. Trebino, "Frequency-Resolved Optical Gating: the Measurement of Ultrashort Laser Pulses," Kluwer Academic Press, Boston, (2000).
- [6] Trebino, et al., *Rev. Sci. Instr.*, **68**, 3277 (1997).
- [7] Kane and Trebino, *Opt. Lett.*, **18**, 823 (1993).
- [8] Stark, *Image Recovery*, Academic Press, 1987.
- [9] L. Cohen, "Time-frequency distributions-a review, " *Proceedings of the IEEE*, **77**, 941 - 981 (1989).

- [10] L. Gallmann, D. H. Sutter, N. Matuschek, G. Steinmeyer and U. Keller, "Characterization of sub-6fs optical pulses with spectral phase interferometry for direct electric-field reconstruction," *Opt. Lett.* **24**, 1314 (1999).
- [11] C. Iaconis and I. A. Walmsley, Self-Referencing Spectral Interferometry for Measuring Ultrashort Optical Pulses, *IEEE J. of Quant. Elec.* **35**, 501 (1999).
- [12] C. Froehly, A. Lacourt, J. C. Vienot, "Notions de reponse impulsionelle et de fonction de tranfert temporelles des pupilles opticques, justifications experimentales et applications," *Nouv. Rev. Optique* 4, **18** (1973).
- [13] Richard Ell, "Sub-Two Cycle Ti:sapphire Laser and Phase Sensitive Nonlinear Optics," PhD-Thesis, University of Karlsruhe (TH), (2003).

Chapter 11

Ultrafast Measurement Techniques

11.1 Pump Probe Measurements

11.1.1 Non-Colinear Pump-Probe Measurement:

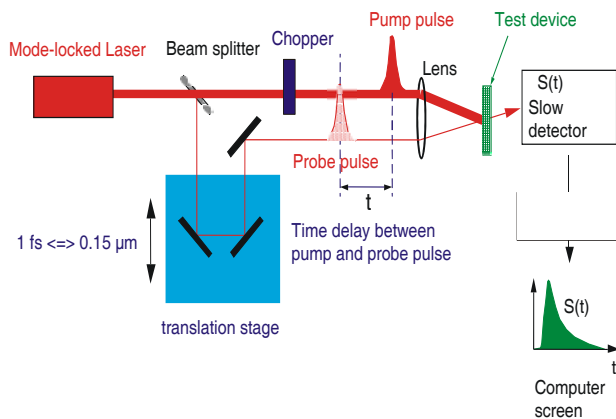


Figure 11.1: Non-colinear pump-probe setup with co-polarized pump-probe beams.

Adapted from U. Keller.

Figure 11.1 shows a non-colinear pump-probe measurement setup. To suppress background light and low frequency noise of the probe beam the pump

beam is chopped. Typical chopper frequencies of regular mechanical choppers are $f_{ch} = 100Hz - 2kHz$. Mechanical choppers up to 20kHz have been built. With acousto-optic modulators or electro-optic modulators chopper frequencies up to several hundred MHz are possible.

Lets denote $S_{in} = S_0 + \delta S$ as the probe pulse energy, where S_0 is the average value and δs a low frequency noise of the pulse source and $S(t)$ is the probe signal transmitted through the test device. Then the detected signal transmitted through the test device can be written as

$$\begin{aligned} S(t) &= T(P(t))S_{in} \\ &= T_0S_{in} + \frac{dT}{dP}(P_0m(t)) \end{aligned} \quad (11.1)$$

where T_0 is the transmission without pump pulse, P_0 is the pump pulse energy and $m(t)$ the chopper modulation function. It is obvious that if the noise of the probe laser δS is of low frequency, then the signal can be shifted away from this noise floor by choosing an appropriately large chopper frequency in $m(t)$. Ideally, the chopper frequency is chosen large enough to enable shot noise limited detection.

Sometimes the test devices or samples have a rough surface and pump light scattered from the surface might hit the detector. This can be partially suppressed by orthogonal pump and probe polarization

This is a standard technique to understand relaxation dynamics in condensed matter, such as carrier relaxation processes in semiconductors for example.

11.1.2 Colinear Pump-Probe Measurement:

Sometimes pump and probe pulses have to be collinear, for example when pump probe measurements of waveguide devices have to be performed. Then pump and probe pulse, which might both be at the same center wavelength have to be made separable. This can be achieved by using orthogonal pump and probe polarization as shown in Figure 11.2 or by chopping pump and probe at different frequencies and detecting at the difference frequency, see Figure 11.3.

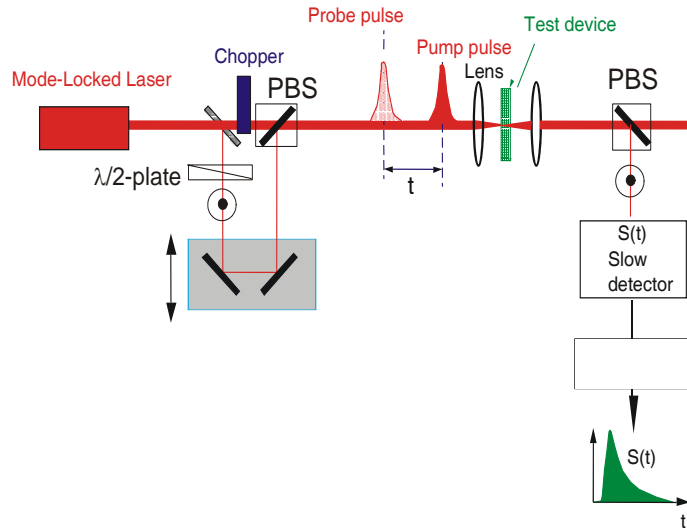


Figure 11.2: Colinear pump-probe with orthogonally polarized pump and probe beams.
Adapted from U. Keller.

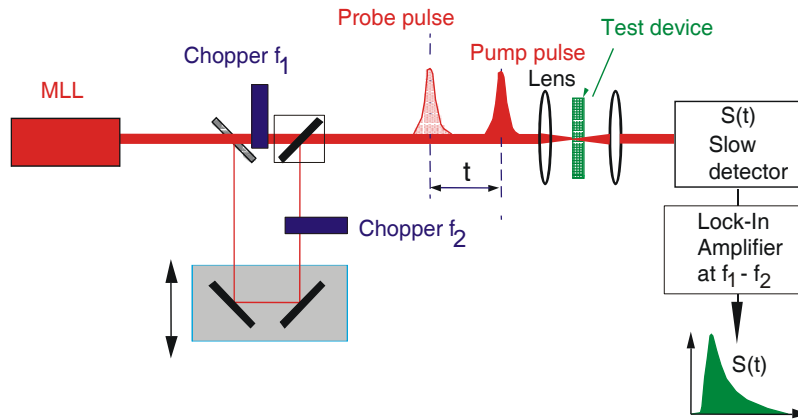


Figure 11.3: Colinear pump probe with chopping of pump and probe and lock-in detection at the difference frequency.
Adapted from U. Keller.

11.1.3 Heterodyne Pump Probe

The lock-in detection is greatly improved if the difference frequency at which the detection occurs can be chosen higher and the signal can be filtered much better using a heterodyne receiver. This is shown in Figure 11.4, where AOM's are used to prepare a probe and reference pulse shifted by 39 and 40 MHz respectively. The pump beam is chopped at 1kHz. After the test device the probe and reference pulse are overlaid with each other by delaying the reference pulse in a Michelson-Interferometer. The beat note at 1MHz is downconverted to base band with a receiver.

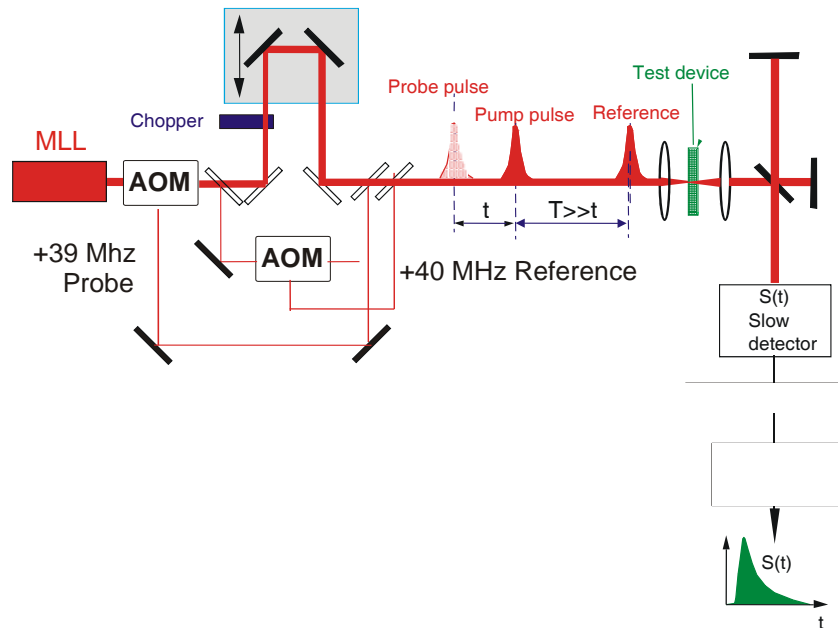


Figure 11.4: Colinear pump probe measurement with parallel polarization and large difference frequency.

Adapted from U. Keller.

If a AM or FM receiver is used and the interferometers generating the reference and probe pulse are interferometrically stable, both amplitude and phase nonlinearities can be detected with high signal to noise.

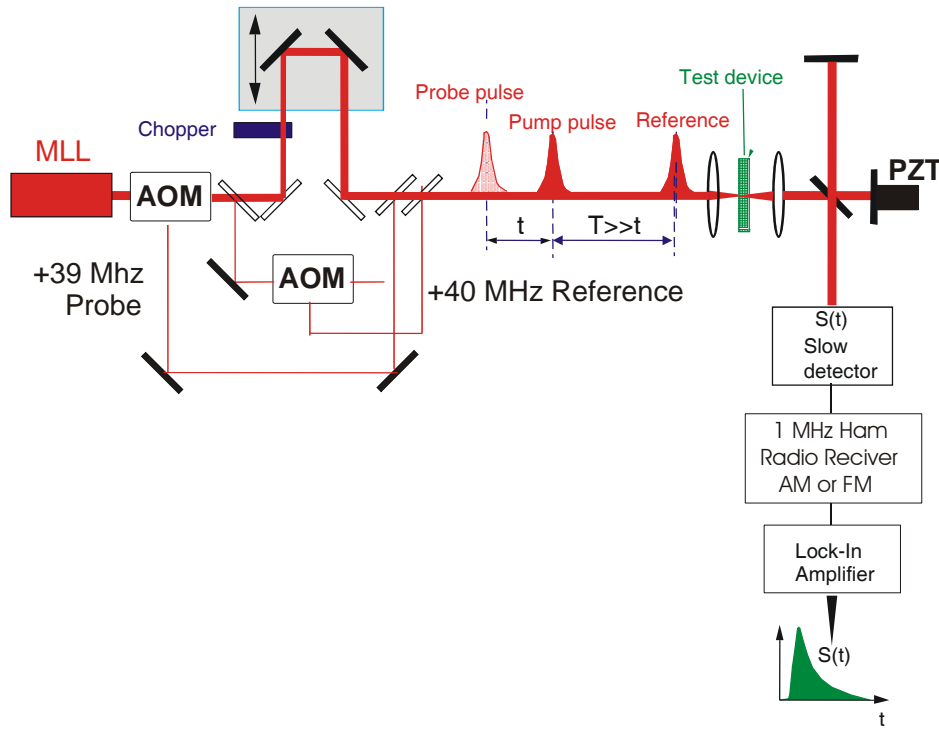


Figure 11.5: Heterodyne pump probe using AM and FM receiver to detect amplitude and phase nonlinearities.

Adapted from U. Keller.

11.2 Electro-Optic Sampling:

Electro-Optic Sampling was invented by Valdmanis and Mourou in the early 1980's [8][5]. It is based on polarization rotation of a short laser pulse when propagating in a medium showing a linear electro-optic effect. The polarization rotation is due to an applied electric field, i.e. the optical pulse samples the instantaneous electric field, see Fig.11.6

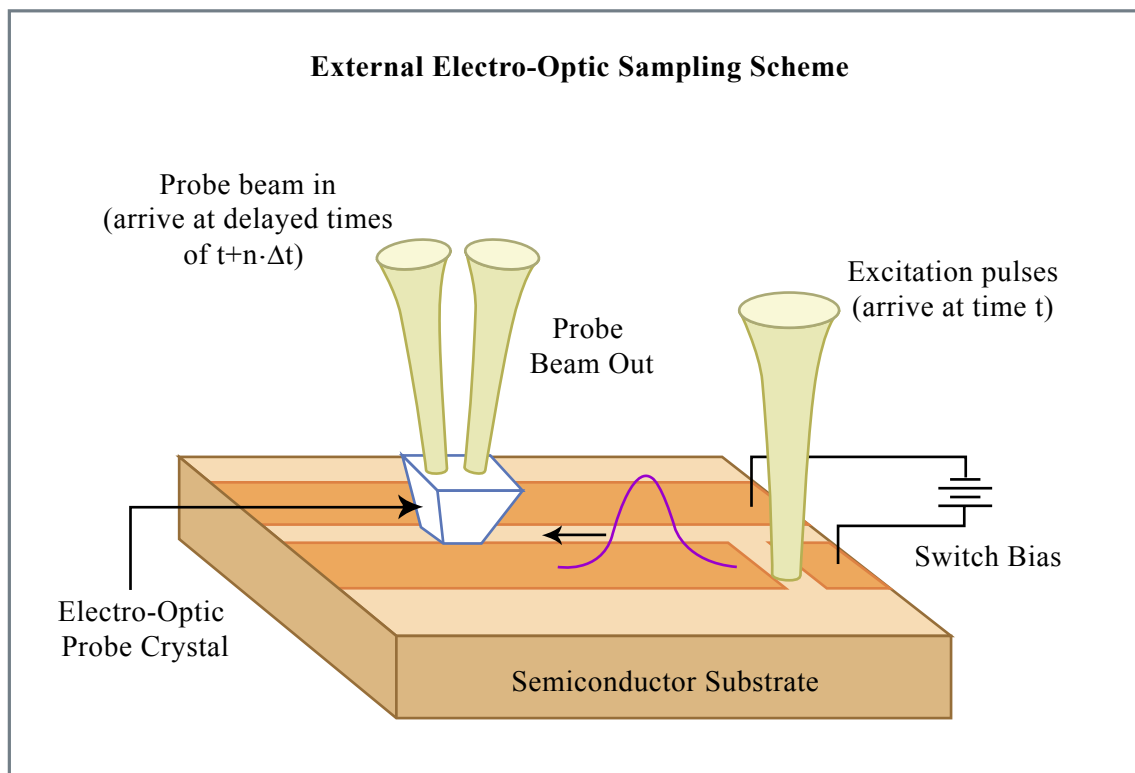


Figure 11.6: Electro-optic sampling scheme according to J. Whitaker, Univ. of Michigan, Ann Arbor.

Figure by MIT OCW.

In Fig. 11.6 a electric transient is generated with a photo-conductive switch activated by a femtosecond laser pulse. A delayed pulse samples the transient electronic pulse with an electro-optic probe as shown in Fig. 11.7.

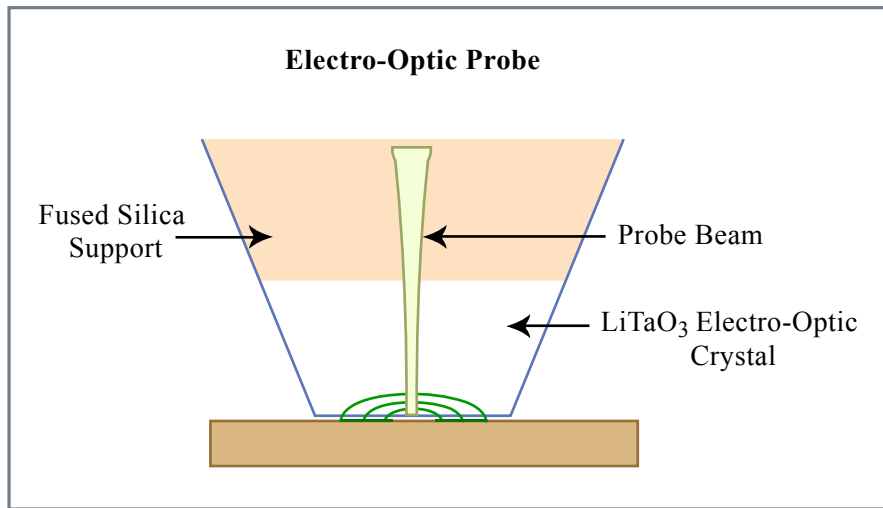


Figure 11.7: LiTaO₃–Electro-Optic Probe according to J. Whitaker, Univ. Michigan.

Figure by MIT OCW.

Fig. 11.8 shows an overall version of an electro-optic sampling system according to J. Whitaker, Univ. of Michigan [6]

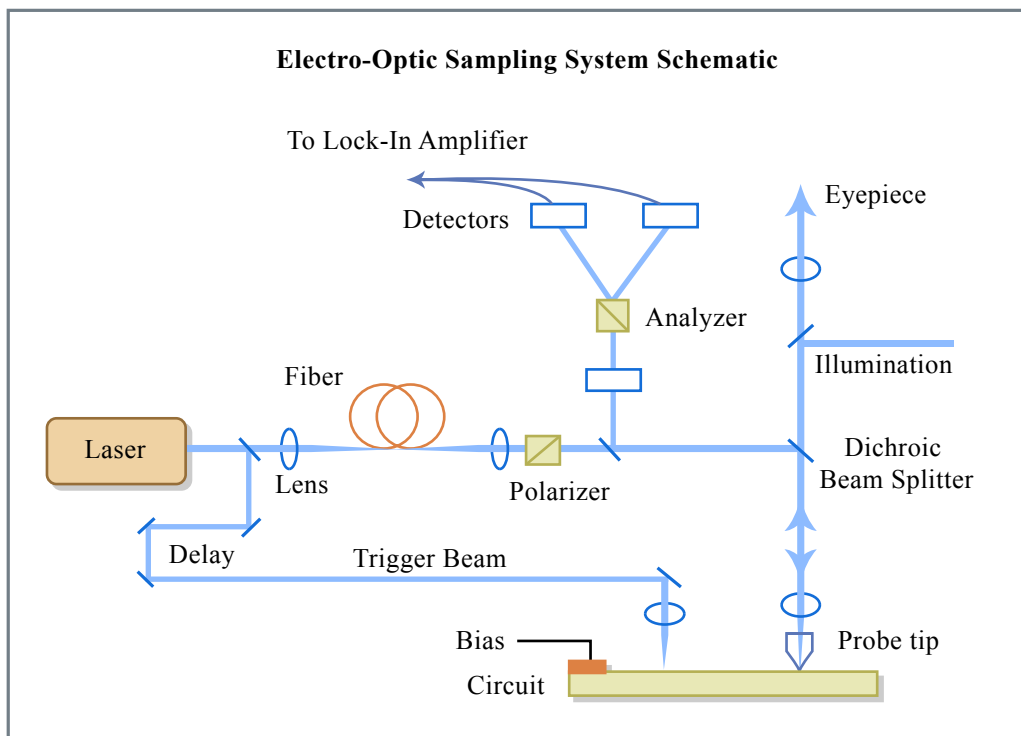


Figure 11.8: Electro-Optic Sampling System according to J. Whitaker, Univ. Michigan.

Figure by MIT OCW.

11.3 THz Spectroscopy and Imaging

Photo-conductive switches activated by sub-100 fs pulses or optical rectification with sub-100 fs pulses leads to the generation of THz electro-magnetic impulses, that can be received with similar photo-conductive receivers or by electro-optic sampling [8][9]. This technique was pioneered by Ch. Fattinger and D. Grischkowsky [7].

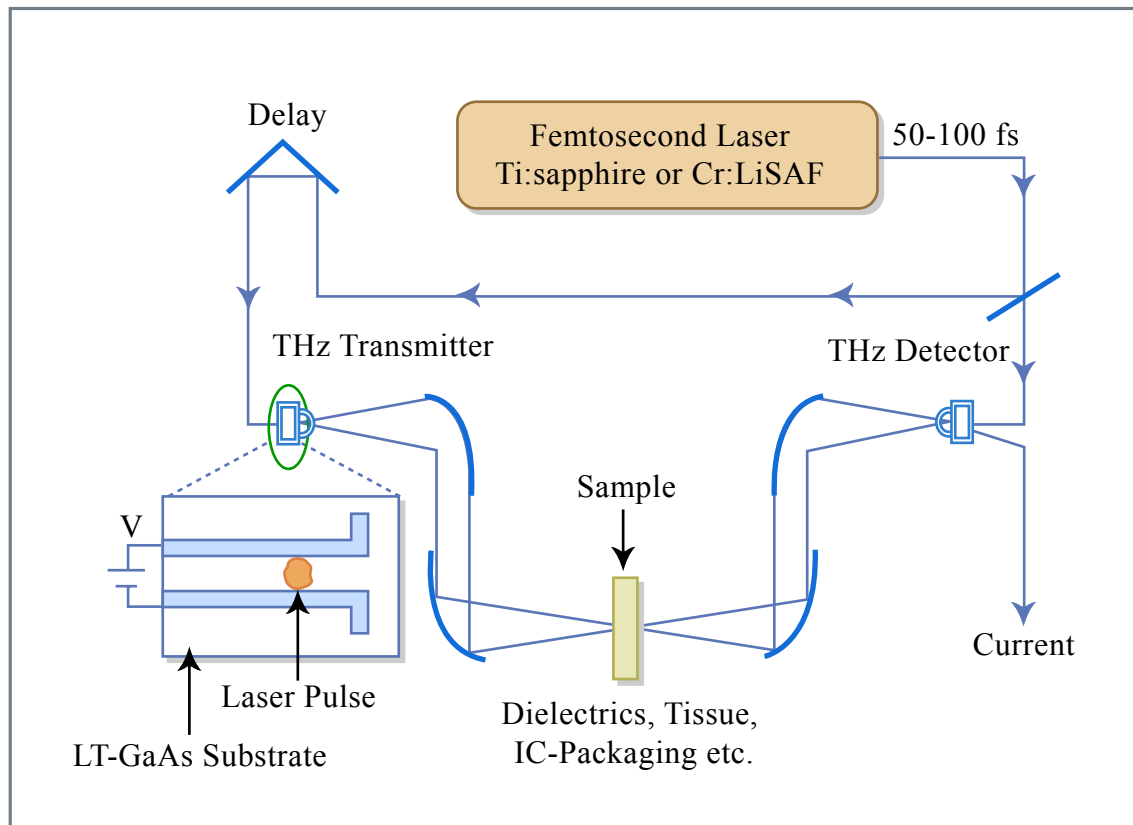


Figure 11.9: THz Time Domain Spectroscopy according to [8]

Figure by MIT OCW.

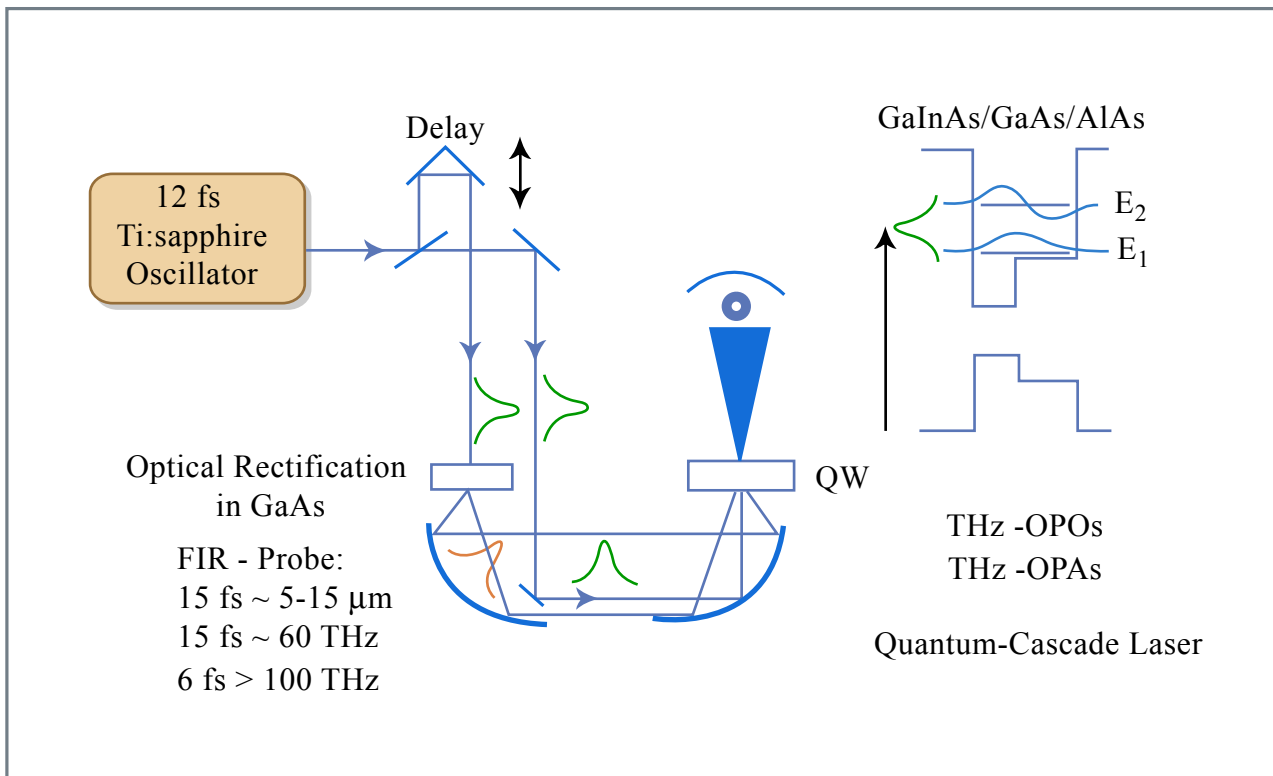


Figure 11.10: THz Time Domain Spectroscopy using optical rectification in GaAs [9].

Figure by MIT OCW.

Figure 11.11: Terahertz waveforms modified by passage through (a) a 10mm block of styacast and (b) a chinese fortune cookie. The dashed lines show the shape of the input waveform multiplied by 0.5 in (a) and by 0.1 in 9b). In *a(the transmitted plse exhibits a strong "chirp" due to frequency-dependent index, while in (b), pulse broadening indicates preferential absorption of high frequencies [8].

Figure 11.11 shows typical generated THz waveforms and distortions due to propagation through materials.

11.4 Four-Wave Mixing

A more advanced ultrafast spectroscopy technique than pump-probe is four-wave mixing (FWM). It enables to investigate not only energy relaxation processes, as is the case in pump-probe measurements, but also dephasing processes in homogenous as well as inhomogenously broadened materials. The typical set-up is shown in Fig. 11.12

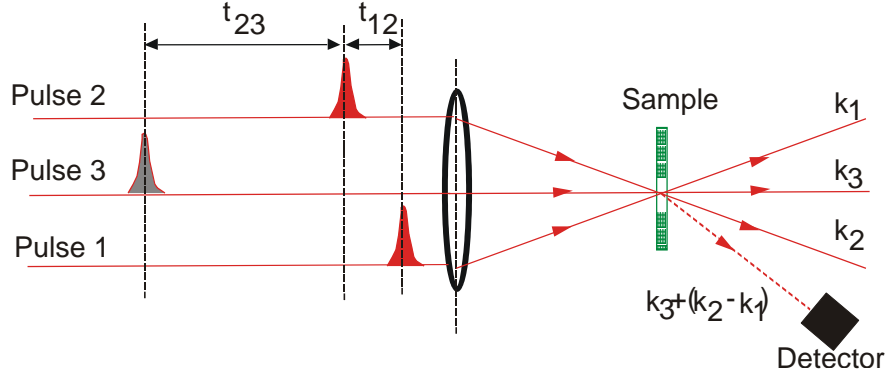


Figure 11.12: Typical Four-Wave-Mixing (FWM) beam geometry.

Lets assume these pulses interact resonantly with a two-level system modelled by the Bloch Equations derived in chapter 2 (2.1592.162).

$$\left(\Delta - \frac{1}{c_0^2} \frac{\partial^2}{\partial t^2} \right) \vec{E}^{(+)}(z, t) = \mu_0 \frac{\partial^2}{\partial t^2} \vec{P}^{(+)}(z, t), \quad (11.2)$$

$$\vec{P}^{(+)}(z, t) = -2N\vec{M}^*d(z, t) \quad (11.3)$$

$$\dot{d}(z, t) = -\left(\frac{1}{T_2} - j\omega_{eg} \right) d + \frac{1}{2j\hbar} \vec{M} \vec{E}^{(+)} w, \quad (11.4)$$

$$\dot{w}(z, t) = -\frac{w - w_0}{T_1} + \frac{1}{j\hbar} (\vec{M}^* \vec{E}^{(-)} d - \vec{M} \vec{E}^{(+)} d^*) \quad (11.5)$$

The two-level system, located at $z = 0$, will be in the ground state, i.e. $d(t = 0) = 0$ and $w(t = 0) = -1$, before arrival of the first pulses. That is, no polarization is yet present. Lets assume the pulse interacting with the two-level system are weak and we can apply perturbation theory. Then the arrival of the first pulse with the complex field

$$\vec{E}^{(+)}(\vec{x}, t) = \vec{E}_0^{(+)} \delta(t) e^{j(\omega_{eg}t - j\vec{k}_1 \vec{x})} \quad (11.6)$$

will generate a polarization wave according to the Bloch-equations

$$d(\vec{x}, t) = -\frac{\vec{M}\vec{E}_0^{(+)}}{2j\hbar} e^{j(\omega_{eg}-1/T_2)t} e^{-j\vec{k}_1\vec{x}} \delta(z), \quad (11.7)$$

which will decay with time. Once a polarization is created the second pulse will change the population and induce a weak population grating

$$\Delta w(\vec{x}, t) = \frac{|\vec{M}\vec{E}_0^{(+)}|^2}{\hbar^2} e^{-t_{12}/T_2} e^{-j(\vec{k}_1-\vec{k}_2)\vec{x}} e^{-(t-t_2)/T_1} \delta(z) + c.c., \quad (11.8)$$

When the third pulse comes, it will scatter of from this population grating, i.e. it will induce a polarization, that radiates a wave into the direction $\vec{k}_3 + \vec{k}_2 - \vec{k}_1$ according to

$$d(\vec{x}, t) = \frac{\vec{M}\vec{E}_0^{(+)}}{2j\hbar} \frac{|\vec{M}\vec{E}_0^{(+)}|^2}{\hbar^2} e^{-t_{12}/T_2} e^{-t_{32}/T_1} e^{-j(\vec{k}_3+\vec{k}_2-\vec{k}_1)\vec{x}} \delta(z) \quad (11.9)$$

Thus the signal detected in this direction, see Fig. 11.12, which is proportional to the square of the radiating dipole layer

$$S(t) \sim |d(\vec{x}, t)|^2 \sim e^{-2t_{12}/T_2} e^{-2t_{32}/T_1} \quad (11.10)$$

will decay on two time scales. If the time delay between pulses 1 and 2, t_{12} , is only varied it will decay with the dephasing time $T_2/2$. If the time delay between pulses 2 and 3 is varied, t_{32} , the signal strength will decay with the energy relaxation time $T_1/2$

Bibliography

- [1] K. L. Hall, G. Lenz, E. P. Ippen, and G. Raybon, "Heterodyne pump-probe technique for time-domain studies of optical nonlinearities in waveguides," *Opt. Lett.* **17**, p.874-876, (1992).
- [2] K. L. Hall, A. M. Darwish, E. P. Ippen, U. Koren and G. Raybon, "Femtosecond index nonlinearities in InGaAsP optical amplifiers," *App. Phys. Lett.* **62**, p.1320-1322, (1993).
- [3] K. L. Hall, G. Lenz, A. M. Darwish, E. P. Ippen, "Subpicosecond gain and index nonlinearities in InGaAsP diode lasers," *Opt. Comm.* **111**, p.589-612 (1994).
- [4] J. A. Valdmanis, G. Mourou, and C. W. Gabel, "Picosecond electro-optic sampling system," *Appl. Phys. Lett.* **41**, p. 211-212 (1982).
- [5] B. H. Kolner and D. M. Bloom, "Electrooptic Sampling in GaAs Integrated Circuits," *IEEE J. Quantum Elect.* **22**, 79-93 (1986).
- [6] S. Gupta, M. Y. Frankel, J. A. Valdmanis, J. F. Whitaker, G. A. Mourou, F. W. Smith and A. R. Calaw , "Subpicosecond carrier lifetime in GaAs grown by molecular beam epitaxy at low temperatures," *App. Phys. Lett.* **59**, pp. 3276-3278 91991)
- [7] Ch. Fattinger, D. Grischkowsky, "Terahertz beams," *Appl. Phys. Lett.* **54**, pp.490-492 (1989)
- [8] D. M. Mittleman, R. H. Jacobsen, and M. Nuss, "T-Ray Imaging," *IEEE JSTQE* **2**, 679-698 (1996)
- [9] A. Bonvalet, J. Nagle, V. Berger, A. Migus, JL Martin, and M. Joffre, "Ultrafast Dynamic Control of Spin and Charge Density Oscillations in a GaAs Quantum Well," *Phys. Rev. Lett.* **76**, 4392 (1996).

Chapter 12

Pulse Amplification

We use a presentation mostly developed by

Francois Salin
Center for Intense Lasers
and Applications (CELIA)
Université Bordeaux I, FRANCE
www.celia.u-bordeaux.fr

and extended by Rick Trebino.

The slides can be downloaded from Rick Trebinos web pages and his Ultrafast Optics Course:

<http://www.physics.gatech.edu/gcuo/UltrafastOptics/>

MIT OpenCourseWare
<https://ocw.mit.edu/>

6.977 Ultrafast Optics
Spring 2005

For information about citing these materials or our Terms of Use, visit: <https://ocw.mit.edu/terms>.